

This item was submitted to [Loughborough's Research Repository](#) by the author.  
Items in Figshare are protected by copyright, with all rights reserved, unless otherwise indicated.

## **Binder-free LiCoO<sub>2</sub>-based composite cathodes produced by cold sintering for lithium-ion batteries**

PLEASE CITE THE PUBLISHED VERSION

PUBLISHER

Loughborough University

LICENCE

CC BY-NC-ND 4.0

REPOSITORY RECORD

Wu, Jason. 2021. "Binder-free LiCoO<sub>2</sub>-based Composite Cathodes Produced by Cold Sintering for Lithium-ion Batteries". Loughborough University. <https://doi.org/10.26174/thesis.lboro.13515239.v1>.

**Binder-free  $\text{LiCoO}_2$  Based Composite Cathodes  
Produced by Cold Sintering for Lithium-ion Batteries**

**By**

**Jianshen Wu**

A Doctoral Thesis Submitted in Partial Fulfilment of the Requirements for  
the Award of Doctor of Philosophy of Loughborough University

Project Supervisors:

Dr. Hongtao Zhang

Prof. Bala Vaidhyanathan

Dr. Xujin Bao



# Abstract

Renewable energy sources, such as solar energy, tide energy, and hydroelectric energy, are attracting numerous attentions on the grounds that they are able to effectively alleviate the effect of global warming induced by CO<sub>2</sub> emission. Owing to the intermittent nature of these renewable energy sources, energy storage devices are needed to store surplus energy and release the energy in demand. Lithium-ion batteries (LIBs) as energy storage devices have stimulated a surge of interests due to the high energy density, extended longevity, and low-discharge rate. LiCoO<sub>2</sub>(LCO)-graphite is the first commercialised materials system for LIBs and is being widely used. However, most of the current research endeavours focus on improving the power density of LIB rather than energy density, especially volumetric energy density. This thesis presents an account of a novel sintering technique, termed cold sintering process (CSP), leading to the fabrication of high-performance LCO/graphene composite cathodes which significantly improve the volumetric energy density of LIBs whilst still maintain its appealing electrochemical properties, such as high working potential and promising rate capability.

In this thesis, the concept of CSP feasibility on densification of monolithic LCO ceramics via a dissolution-precipitation process at ultralow temperature and high pressure with appropriate processing time was first verified. CSP variables were investigated and optimised in achieving high bulk density and preferable materials properties for CSP-ed LCO. With the integration of multi-walled carbon nanotubes (CNTs) or microwave reduced graphene oxide (MWrGO) into CSP-ed LCO matrix, a thick binder-free composite cathode was achieved in one-step synthesis at temperature as low as 250 °C for the first time, which is impossible to realise in conventional high-temperature

sintering methodology because of inevitable carbon decomposition. The abovementioned MWrGO was synthesised from graphene oxide using microwave irradiation at a super-fast heating rate (within seconds) and was incorporated in the dense CSP-ed LCO body to compensate the adverse effects induced by sintered ceramics, such as intrinsically low electrical conductivity, rigid LCO matrix and slow  $\text{Li}^+$  ion diffusion in dense ceramics, due to its high electrical conductivity, planar character and porous structure. With the systematic investigation in this project, the property-structure relationship of MWrGO was thoroughly elucidated and found that the quality of MWrGO can be carefully tuned by controlling microwave power and inert atmosphere to meet the specific expectation of high-performance electrode for LIBs.

The merits of MWrGO to the electrochemical performance of thick LCO composite cathode were demonstrated as compared to CNTs. The addition of 1 wt% MWrGO in LCO matrix (LCO/1%MWrGO) provided a comparable electrical conductivity to the addition of 3 wt% CNTs (LCO/3%CNTs). Owing to less addition of carbon materials and absence of binder/current collector, the LCO/1%MWrGO cathodes delivered a superior volumetric discharge capacity of  $\sim 501.5 \text{ mAh cm}^{-3}$  in the first cycle and a promising capacity retention of 80.9% after 40 cycles with respect to  $\sim 459 \text{ mAh cm}^{-3}$  and 62% retention after 40 cycles for LCO/3%CNTs. More notably, the LCO/1%MWrGO cathodes can still afford  $\sim 50 \text{ mAh g}^{-1}$  at 1 C and  $\sim 30 \text{ mAh g}^{-1}$  at 2 C, whereas no capacities were attained for LCO/3%CNTs cathodes at current rates  $> 1 \text{ C}$ .

This research ultimately advances the understanding of the processing of pressure-assisted sintered electrode composites for use in LIBs. The main scientific and technical contributions of this project are as follows:

1. The concept of CSP feasibility on fabrication of LCO-based electrode expands the materials spectrum of CSP applicability.
2. The realisation of high energy density without compromising other electrochemical properties expands the field for binder-free electrode fabrication exploration beyond conventional strategies and structural motifs. This promising electrochemical performance of binder-free electrodes is expected to bring them a step closer to use in practical LIBs.
3. The versatility of CSP opens up the possibility of ‘all-in-one-step’ densification of two materials with substantial dissimilar physical properties to produce advanced functional devices (such as solar panel, supercapacitors, and sensors) but not limiting to LIBs, demonstrating CSP is a valuable asset within ceramic processing toolbox for both research and industrial production.

**Key words:** cold sintering process; lithium-ion batteries;  $\text{LiCoO}_2$ ; microwave-assisted synthesis; graphene; high volumetric energy density; binder-free cathode; annealing treatment; microwave arcing; coagulation bath.

## Acknowledgements

Traditionally, the Acknowledgement Section is the last bit to be done to finalise the PhD thesis and it typically symbolises as the full stop mark to the PhD journey. So do I. It is now the New Year Eve with the clock ticking down toward 2021. Sitting by a snapping fireplace, I am starting with a separate blank page in a peaceful British village of Caldecote at this very special moment.

First and foremost, I would like to express my special appreciation and sincere gratitude to my supervisory team, Dr. Hongtao Zhang, Prof. Bala Vaidhyanathan, and Dr. Xujin Bao, for offering me the opportunity to undertake research on the promising fields of lithium-ion battery and graphene. I would like to thank them for guiding me with their valuable ideas into the subject matter which steered me towards the right path. I would particularly like to single out my esteemed supervisor, Prof. Bala Vaidhyanathan, for his invaluable supervision, support, and nurturing during the course of my PhD study, especially for his confidence in me. He consistently and patiently provided encouragement and was always willing and enthusiastic to assist in any way he could at every stage of the research project. His thoughtful insight/advice on both research methodology and my life, have been invaluable and has significantly influenced me, which I believe will keep working for the rest of my life.

I would like to take this opportunity here to recognise the professional trainings and assistances I received from Loughborough Materials Characterisation Centre (LMCC) on the use of materials characterisation facilities. First, my thanks are due to Dr. Zhaoxia Zhou who instructed me a lot on HR-TEM characterisation. Next, a special gratitude must go to Dr. Keith Yendall for helping me with the use of experimental equipment (FEGSEM

and XRD etc.) and technical troubleshooting during the running of this project. Additionally, more thanks are extended to the members in the Advanced Ceramics Group who always gave me all sorts of incredible supports and their willingness to impart their knowledge while I was working in laboratory. It is their kind help and accompanies that have made my study and life in the UK a cherished time. I cannot leave Loughborough University without mentioning Dr. Jiawei Zhao, who never wavered in his constructive support to overcome many troubles throughout the duration of my project.

Furthermore, I would like to immensely appreciate my parents for their unconditional love, wise counsel, tremendous understanding, and selfless encouragement. You have been always standing behind me no matter what troubles I came across and made numerous sacrifices to help me get to this point. Your contributions have shaped my values and made me the man that I am today. Ultimately, I am delighted that I have made this milestone in my life journey which you are proud of.

Lastly, I would like to acknowledge Loughborough University for the scholarship financial support, without it all would not have been possible. For those who I have not yet mentioned above but also offered frequent help, you really does deserve the greatest of thanks. There is no doubt that the days would have passed far more slowly without all of you, both at Loughborough University and around Leicester.

Thanks again to everyone and everything that made me possible and stronger.

# Contents

<b>Abstract .....</b>	<b>I</b>
<b>Acknowledgements .....</b>	<b>IV</b>
<b>Contents .....</b>	<b>VI</b>
<b>List of Tables .....</b>	<b>X</b>
<b>List of Figures .....</b>	<b>XII</b>
<b>List of Abbreviation &amp; Symbols .....</b>	<b>XXII</b>
<b>Chapter 1. Introduction .....</b>	<b>1</b>
1.1. The energy dilemma.....	1
1.2. Thesis structure .....	6
<b>Chapter 2. Literature review .....</b>	<b>8</b>
2.1. Lithium-ion batteries .....	8
2.1.1. Underlying electrochemistry for LIBs .....	12
2.1.2. Anode .....	20
2.1.3. Electrolyte .....	23
2.1.4. Cathode.....	26
2.2. Cold sintering process .....	32
2.2.1. CSP mechanism.....	32
2.2.2. Processing variables of CSP.....	36
2.2.2.1. CSP temperature/pressure/holding time .....	36
2.2.2.2. Selection of transient liquid solution.....	36
2.2.2.3. Physical characteristics of starting materials.....	37
2.2.2.4. Post-CSP annealing treatment .....	38
2.2.3. CSP application for LIBs .....	44
2.3. Microwave-assisted reduction of graphene oxide.....	49

2.3.1.	Introduction to graphene .....	49
2.3.2.	Graphene production methods .....	53
2.3.3.	Microwave-assisted reduction of GO.....	57
2.3.4.	Microwave-induced arcing & hot-spots.....	69
2.4.	The use of CNTs and graphene in LIBs.....	78
2.4.1.	CNTs as conductive filler.....	83
2.4.2.	Graphene as conductive filler.....	86
2.4.3.	Choice: CNT or graphene?.....	91
2.5.	Aims and objectives of the project.....	93
<b>Chapter 3.</b>	<b>Experimental details .....</b>	<b>95</b>
3.1.	Materials and reagents list.....	97
3.2.	Cold sintering process of LiCoO <sub>2</sub> and LiCoO <sub>2</sub> /xCNTs pellets .....	98
3.2.1.	Synthesis of LCO powder .....	99
3.2.2.	Preparation of LCO/xCNTs powder.....	100
3.2.3.	Cold sintering process and post-CSP annealing.....	101
3.2.4.	Materials characterisation .....	103
3.2.5.	Electrochemical measurements .....	105
3.2.5.1.	Coin cell assembly.....	105
3.2.5.2.	Electrochemical evaluation .....	107
3.2.5.3.	Calculations for electrochemical data .....	108
3.2.5.4.	Post-mortem characterisation .....	110
3.3.	Microwave-assisted reduction of graphene oxide.....	112
3.3.1.	Synthesis of graphite oxide .....	113
3.3.2.	Coagulation bath of GO .....	115
3.3.3.	Synthesis of MWrGO.....	116
3.3.4.	Materials characterisations of MWrGO .....	118

3.3.5. Electrochemical measurements .....	121
3.3.5.1. MWrGO anode preparation .....	121
3.3.5.2. Cathode preparation.....	122
3.3.5.3. Coin cell assembly.....	124
3.3.5.4. Electrochemical evaluation .....	124
3.4. Cold sintering process of LiCoO <sub>2</sub> /MWrGO.....	126
3.4.1. Preparation of LCO/xMWrGO powder.....	127
3.4.2. Cold sintering process and post-CSP annealing.....	128
3.4.3. Materials Characterisation.....	129
3.4.4. Electrochemical measurements .....	130
<b>Chapter 4. Cold sintering process and electrochemical evaluation of LiCoO<sub>2</sub>/CNTs composite electrode with high volumetric capacity .....</b>	<b>132</b>
4.1. The CSP of monolithic LCO pellets .....	133
4.2. Effect of CNTs content on electrical conductivity of composite cathode..	145
4.3. The effect of post-CSP annealing treatment .....	149
4.4. Electrochemical characterisation.....	152
4.5. Chapter conclusions .....	161
<b>Chapter 5. Rapid microwave-assisted bulk production and characterisation of reduced graphene oxide synthesised under tuneable microwave powers for Li-ion battery application.....</b>	<b>164</b>
5.1. Coagulation bath of GO .....	165
5.2. The enhanced microwave absorption of GO by annealing treatment .....	172
5.3. MWrGO characterisation .....	178
5.4. The application of MWrGO in lithium-ion batteries .....	203
5.4.1. 800W/10min MWrGO in anode for LIBs.....	204
5.4.2. 800W/10min MWrGO in cathode for LIBs .....	210



5.5. Chapter conclusions .....	215
<b>Chapter 6. Cold sintering process and electrochemical evaluation of high-performance LiCoO<sub>2</sub>-matrix cathode with MWrGO as conductive filler .....</b>	<b>218</b>
6.1. Microstructural characterisation of LCO/xMWrGO composites .....	220
6.2. The effect of graphene content on electrical conductivity of composite cathode.....	224
6.3. The effect of post-CSP annealing treatment .....	227
6.4. Electrochemical characterisation.....	231
6.5. Chapter conclusions .....	250
<b>Chapter 7. Thesis conclusions .....</b>	<b>252</b>
<b>Chapter 8. Future work .....</b>	<b>255</b>
<b>References.....</b>	<b>257</b>
<b>Publication.....</b>	<b>285</b>

## List of Tables

<b>Table 2-1.</b> Standard electrode potentials of redox reactions taking place at 25 °C [31].	14
<b>Table 2-2.</b> Electrochemical properties of the common intercalation-type cathode compounds [65].	27
<b>Table 2-3.</b> Overview of microwave-assisted reduction of solid-state GO at a fixed frequency of 2.45 GHz.	68
<b>Table 3-1.</b> The materials list of the chemical formula, the chemical name, the chemical grade, and the materials supplier used in this project.	97
<b>Table 3-2.</b> The formula, current collector, counter electrode, separator, electrolyte volume, and galvanostatic test conditions of LCO/3%CNTs pellets produced by CSP, LCO/1%MWrGO pellets produced by CSP, MWrGO anode, CNTs-containing cathode, and MWrGO-containing cathode.	111
<b>Table 3-3.</b> The sample denotation of all the MWrGO synthesised with various microwave powers and argon flushing times.	117
<b>Table 4-1.</b> Literature survey of the electrical conductivities of LCO pellets produced by conventional sintering.	146
<b>Table 4-2.</b> Electrochemical performance of densified LiCoO <sub>2</sub> cathodes prepared by different methods.	160
<b>Table 5-1.</b> Calculated Raman spectral features of pristine graphite, graphite oxide, annealed GO, and MWrGO synthesised at different conditions (based on the data extracted from Fig. 5-11).	184
<b>Table 5-2.</b> The assignment of FTIR peaks for pristine graphite, graphite oxide, annealed GO, and 800W/10min MWrGO.	190
<b>Table 5-3.</b> Quantative analysis of oxygen functional groups on pristine graphite, graphite oxide, annealed GO and 800W/10min MWrGO.	195
<b>Table 5-4.</b> The evolution of XPS C1s spectra of MWrGO synthesised with various argon flushing times at the microwave power of 800 W.	196
<b>Table 5-5.</b> The evolution of XPS C1s spectra of MWrGO synthesised with various microwave powers with the argon flushing time of 10 min.	197
<b>Table 5-6.</b> Summary of electrical conductivities of rGO reduced by various chemical agents.	199

<b>Table 6-1.</b> The calculated DCIR values for LCO/1%MWrGO pellet and LCO/3%CNTs at different SOC.....	234
<b>Table 6-2.</b> Independent components of the LCO/1wt%MWrGO and LCO/3wt%CNTs electrodes deduced from the modelling of EIS data with the value uncertainty. ....	245

## List of Figures

<b>Fig. 2-1.</b> The evolution of gravimetric/volumetric energy density with the development of commercial batteries [26].	10
<b>Fig. 2-2.</b> The representation of different commercial LIBs configurations: <b>(a)</b> cylindrical, <b>(b)</b> coin, <b>(c)</b> prismatic, and <b>(d)</b> film [27].	10
<b>Fig. 2-3.</b> The comparison of each component of commercial LIBs in terms of <b>(a)</b> volume, <b>(b)</b> mass, and <b>(c)</b> cost [28].	11
<b>Fig. 2-4.</b> Schematic representation of the intercalation/deintercalation process of Li ions between cathode and anode for LIBs [29].	12
<b>Fig. 2-5.</b> The illustration of the effect of various polarisations on discharge behaviour of LIBs [30].	16
<b>Fig. 2-6.</b> <b>(a)</b> The presence of nanovoids on graphene permits extra lithium ions to be accommodated and released, and <b>(b)</b> the surface defects give a higher surface area and thus result in formation of substantial SEI [56].	22
<b>Fig. 2-7.</b> Commonly used non-aqueous solvents for LIBs, along with their physical properties. $\epsilon$ : Dielectric constant, M.P.: melting point, B. P.: Boiling point (The physical data were obtained from [31, 59, 60]).	24
<b>Fig. 2-8.</b> Schematic illustration of LiCoO <sub>2</sub> crystal structure with R3m space group [68].	27
<b>Fig. 2-9.</b> Schematic representation of <b>(a)</b> the primary stages involved in the course of CSP at macroscopic level, and <b>(b)</b> the interaction of liquid phase with particles surfaces during CSP at microscopic level [99, 101].	34
<b>Fig. 2-10.</b> The comparison of Gibbs free energy change of each processing pathway taking place in CSP and conventional sintering.	35
<b>Fig. 2-11.</b> CV curves of LiCoO <sub>2</sub> thin films prepared on Al/Au substrate by spray pyrolysis <b>(a)</b> without annealing and <b>(b)</b> with annealing [110].	41
<b>Fig. 2-12.</b> The effect of annealing treatment on the evolution of accessible capacities of LiCoO <sub>2</sub> thin films prepared on Al/Au substrate by spray pyrolysis over extended cycles [110].	41
<b>Fig. 2-13.</b> <b>(a)</b> XRD spectra of LiFePO <sub>4</sub> before and after CSP, <b>(b)</b> TEM images of amorphous LiFePO <sub>4</sub> phase, <b>(c-e)</b> electrochemical properties of LiFePO <sub>4</sub> composite cathode.	46

<b>Fig. 2-14. (a)</b> TEM images of amorphous $\text{LiFePO}_4$ phase on grain boundary, <b>(b-d)</b> Electrochemical properties of bulk $\text{LiFePO}_4$ composite cathode produced by CSP [17].	47
<b>Fig. 2-15.</b> Schematic representation of graphitic structure in the forms of fullerenes, carbon nanotubes, and graphite [124].	50
<b>Fig. 2-16.</b> Schematic summary of typical synthesis methods of graphene in terms of bottom-up and top-down methods [150].	53
<b>Fig. 2-17.</b> Schematic illustration of Lerf-Klinowski model of GO with the presence of oxygen-containing functional groups on carbon basal plane and along plane edges [160]	56
<b>Fig. 2-18. (a)</b> FTIR spectra, <b>(b)</b> TGA plots, <b>(c)</b> XPS spectra, and <b>(d)</b> Raman spectra of GO and rGO treated with microwave irradiation for different times (MWG1 for 1 min, MWG2 for 2 min, MWG3 for 3 min, and MWG4 for 10 min) [178].	60
<b>Fig. 2-19.</b> The Raman spectra of microwave-reduced GO which were vacuum-dried at varying temperatures [188].	64
<b>Fig. 2-20. (a-c)</b> Raman spectra, XPS spectra and the plotting of $I_{2D}/I_G$ vs $L_a$ for graphite, GO, HOPG, graphene samples prepared using CVD, microwave-assisted thermal reduction, and mechanical exfoliation. <b>(d)</b> HR-TEM of A) single-layer rGO containing high concentration density, B) Bi-layer and C) tri-layer graphene exhibiting higher carbon crystallinity. <b>(e)</b> Digital images of the intensive arcing happened during microwave irradiation [153].	65
<b>Fig. 2-21. (a)</b> Schematic representation of rGO film on GO “paper” during microwave irradiation, <b>(b-d)</b> XPS spectra, Raman spectra, and the plotting of $I_{2D}/I_G$ vs $L_a$ for GO, rGO, HOPG, graphene prepared using CVD and microwave-assisted thermal reduction, <b>(e)</b> Raman spectra of graphene at different positions away from the secondary rGO susceptor [184].	67
<b>Fig. 2-22. (a)</b> the changes of electrical conductivity and oxygen content with varying oxidation degrees of GO, <b>(b)</b> the microwave-induced heating of GO with different oxidation degrees, <b>(c)</b> schematic representation of the development of conjugate networks with oxidation treatment. (The $x$ in $\text{GO-}x$ represents the mass ratio of $\text{KMnO}_4$ to graphite) [136].	70

<b>Fig. 2-23.</b> Schematic diagram of the microwave-matter interaction and light emission of GO after being subjected to microwave irradiation (black colour for the GO and yellowish colour for the light-emission areas [172]).	71
<b>Fig. 2-24.</b> (a) TGA/DSC scan of wet GO, (b) FTIR absorbance spectrum of the decomposed gas (the peaks at $2350\text{ cm}^{-1}$ and $670\text{ cm}^{-1}$ are assigned for $\text{CO}_2$ , the regions from $1400\text{--}1800\text{ cm}^{-1}$ and $3500\text{--}3900\text{ cm}^{-1}$ are assigned for water vapour [146]), (c) mass-spectra of outlet gas produced at explosion of GO ( $\text{CO}$ : $m/z=28$ , $\text{CO}_2$ : $m/z=44$ , water: $m/z=18$ , $[\text{SO}]^+$ : $m/z=48$ and $[\text{SO}_2]^+$ : $m/z=64$ ) [190].	73
<b>Fig. 2-25.</b> Schematic representation of reduction of GO induced by plasma collision mechanism [194].	74
<b>Fig. 2-26.</b> Scanning force microscopy images of the array of iron nanoparticles. A significant degradation of the monolayer <i>n</i> -octadecyltrichlorosilane was detected after microwave irradiation. (a) height image, (b) phase image, and (c) line profile of the corresponding height image [196].	76
<b>Fig. 2-27.</b> The reduction temperatures of GO as a function of microwave irradiation time in a vacuum [197].	77
<b>Fig. 2-28.</b> The typical “S” curve describes the relation between electrical conductivity of composite and the filler fraction. $\sigma_1$ and $\sigma_2$ represent intrinsic electrical conductivities of the major phase and the conductive filler, respectively. $s$ and $t$ are the critical exponents below and above the percolation threshold for the major phase and the conductive filler, respectively [204].	81
<b>Fig. 2-29.</b> (a) SEM image of cross-sectioned $\text{LiCoO}_2\text{-SACNT}$ . (b) life cycle of $\text{LiCoO}_2\text{-SACNT}$ at $0.1\text{ C}$ and (c) the rate capability of $\text{LiCoO}_2\text{-SACNT}$ at different C rate [222].	86
<b>Fig. 2-30.</b> (a) Life cycle and (b) galvanostatic curves of $2.0\text{ Ah}$ Li ion cells containing $2\text{ wt\%}$ graphene, and $7\text{ wt\%}$ carbon black + $3\text{ wt\%}$ conductive graphite.	88
<b>Fig. 2-31.</b> Schematic illustration of the Li ion diffusion across electroactive materials with different particle sizes relative to same size graphene sheets. “plane-to-point” contact mode facilitates the electrical conduction, whilst the planar characteristic of graphene flake impedes the diffusion of Li ions when the particle sizes of graphene sheets are apparently larger than those of active materials [235].	89
<b>Fig. 2-32.</b> Schematic representation of different electroactive materials/graphene sheets assembly models.	90

<b>Fig. 3-1.</b> The flow chart of the overall experimental works to make monolithic LCO pellets produced by CSP, dry-pressed LCO/xCNTs pellets and LCO/xCNTs pellets produced by CSP. ....	98
<b>Fig. 3-2.</b> The photograph of Fritsch Pulverisette-6 planetary ball milling machine used in this project. ....	99
<b>Fig. 3-3.</b> The experimental setup for cold sintering process includes a hydraulic press, a mould and a heater jacket which wraps around the mould and is electrically controlled by the heat controller. ....	101
<b>Fig. 3-4.</b> Typical top-down digital images of LCO/3%CNTs pellet produced by CSP <b>(a)</b> before polish and <b>(b)</b> after polish process. ....	102
<b>Fig. 3-5.</b> FEGSEM image of the fractured LCO/3%CNTs pellet produced by CSP, revealing features such as the thickness and the surface flatness of the polished pellet. ....	106
<b>Fig. 3-6.</b> FEGSEM image of Celgard <sup>®</sup> 2325 membrane used for all coin cell assembly, showing the pore size and pore distribution. ....	106
<b>Fig. 3-7.</b> Schematic illustration of all constituent parts used in 2032 type coin cell and the typical assembly configuration for LIBs (The anode is lithium metal disc in half cell configuration) [249]. ....	107
<b>Fig. 3-8.</b> The flow chart of the overall experimental work starting from raw materials to microwave reduction of graphene oxide, along with the materials characterisation techniques. ....	112
<b>Fig. 3-9.</b> Photographs of GO beads formed in 1wt% CaCl <sub>2</sub> coagulation bath after 24 hours immersion, depicting that <b>(a)</b> the GO beads are robust enough and <b>(b)</b> the bead diameter of GO beads is about 6 mm. ....	115
<b>Fig. 3-10.</b> Schematic illustration of microwave-assisted reduction of GO apparatus in which microwave arcing takes place on the surface of the annealed GO in argon atmosphere. ....	117
<b>Fig. 3-11.</b> Instantaneous photographs of the occurrence of arcing upon microwave irradiation of annealed GO. <b>(a)</b> Before microwave irradiation of 800 W, <b>(b)</b> Heating up of annealed GO samples by microwave irradiation, <b>(c)</b> The initiation of arcing from the annealed GO surface, and <b>(d)</b> The development of strong arcing with extended microwave irradiation. ....	118

<b>Fig. 3-12.</b> Typical FEGSEM image of cross-sectioned MWrGO anode which has been dried and roll pressed, along with the copper current collector.....	122
<b>Fig. 3-13.</b> Typical FEGSEM image of cross-sectioned LCO-MWrGO cathode which has been dried and roll pressed, along with the aluminium current collector.....	123
<b>Fig. 3-14.</b> The flow chart of the overall experimental works to make dry-pressed LCO/xMWrGO pellets and LCO/xMWrGO pellets produced by CSP, along with materials characterisation. ....	126
<b>Fig. 4-1.</b> XRD patterns of as-calcinated LCO, as-milled LCO, and monolithic LCO pellet produced by CSP. ....	133
<b>Fig. 4-2.</b> FEGSEM images of <b>(a)</b> as-calcinated LCO powder and <b>(b)</b> as-milled LCO powder. ....	136
<b>Fig. 4-3.</b> The particle size comparison of as-calcinated LCO powder and as-milled LCO powder. ....	137
<b>Fig. 4-4.</b> Nitrogen adsorption/desorption hysteresis loops of as-calcinated LCO powder and as-milled LCO powder, revealing the specific surface areas based on Branauer-Emmett-Teller (BET) method. ....	137
<b>Fig. 4-5.</b> The effects of CSP processing conditions on the relative densities of monolithic LCO pellets: <b>(a)</b> Relative density as a function of CSP pressures at the temperature of 250 °C for 60 min; <b>(b)</b> Relative density as a function of CSP temperatures at the pressure of 250 MPa for 60 min; <b>(c)</b> Relative density as a function of CSP duration times at 250 °C and at 250 MPa. 20 wt% LiOH solution was used in all cases. ....	142
<b>Fig. 4-6.</b> FEGSEM images of <b>(a)</b> monolithic LCO pellet cold-sintered at 250 °C and 250 MPa for 60 min and <b>(b)</b> LCO pellets dry-pressed at 250 MPa. ....	144
<b>Fig. 4-7.</b> The dependency of the electrical conductivities on the conductive CNTs content for LCO/xCNTs pellets prepared at the CSP condition of 250 °C and 250 MPa for 60 min. ....	146
<b>Fig. 4-8.</b> X-ray diffractograms of LCO/3%CNTs pellet produced by CSP, together to those related to as-calcinated LCO, as-milled LCO and monolithic LCO pellet. ....	148
<b>Fig. 4-9.</b> FEGSEM image of the fractured surface of LCO/3%CNTs pellets produced by CSP.....	148
<b>Fig. 4-10.</b> The plots of <b>(a)</b> relative density and <b>(b)</b> electrical conductivity of LCO/3%CNTs pellets produced by CSP and dry-pressed LCO/3%CNTs pellets as a	



function of annealing temperatures in comparison with as-CSPed LCO/3%CNTs pellets and as-dry-pressed LCO/3%CNTs pellets.....	151
<b>Fig. 4-11.</b> The cyclic voltammogram of LCO/3%CNTs pellet for the initial cycle recorded at the sweep rate of $0.1 \text{ mV s}^{-1}$ . ....	154
<b>Fig. 4-12.</b> The cyclic voltammetry curves of LCO/3%CNTs pellet for the first three cycles at the sweep rate of $0.1 \text{ mV s}^{-1}$ . ....	154
<b>Fig. 4-13.</b> Galvanostatic charge/discharge curves of LCO/3%CNTs pellet for 1 <sup>st</sup> , 2 <sup>nd</sup> , 5 <sup>th</sup> , 10 <sup>th</sup> , and 20 <sup>th</sup> cycles at the current rate of 0.1 C (inset: the magnified region of polarisation spike appearing in the first charge cycle). ....	156
<b>Fig. 4-14.</b> The cycling performance of LCO/3%CNTs pellet between 3.0 V and 4.2 V at the constant rate of 0.1 C. ....	157
<b>Fig. 4-15.</b> FEGSEM images of LCO/3%CNTs pellet (a) before and (b) after 40 galvanostatic cycles (the micro-cracks were marked in cyan circles). ....	158
<b>Fig. 4-16.</b> The discharge rate capabilities of LCO/3%CNTs pellet every five cycles at various current rates. ....	159
<b>Fig. 5-1.</b> The evolutions of the GO beads soaking in 0 wt% $\text{CaCl}_2$ solution (de-ionised water) after (a) 1 min, (b) 30 min, and (c) 60 min. ....	166
<b>Fig. 5-2.</b> The photographs of the GO beads which have been soaked in (a) 1 wt% $\text{CaCl}_2$ and (b) 3 wt% $\text{CaCl}_2$ after 24 hours. ....	166
<b>Fig. 5-3.</b> XRD spectra of the GO beads which have been soaked in 1 wt% and 3 wt% $\text{CaCl}_2$ solutions after 24 hours. ....	168
<b>Fig. 5-4.</b> EDS compositional mapping of the GO beads which have been soaked in 3 wt% $\text{CaCl}_2$ solution after 24 hours (Au elemental mapping was caused by the conductive coating on sample surface). ....	169
<b>Fig. 5-5.</b> Schematic illustration of (a) the core-shell structure of GO bead formed in coagulation bath and (b) the development of GO shell in $\text{CaCl}_2$ -containing coagulation bath [283]. ....	171
<b>Fig. 5-6.</b> Typical FEGSEM micrographs of (a) as-prepared GO and (b) annealed GO which has been subjected to annealing at $250^\circ\text{C}$ . ....	173
<b>Fig. 5-7.</b> Photos of 100 mg of (left) as-prepared GO and (right) fluffy annealed GO, showing the large volume expansion (almost doubles the apparent volume) upon annealing treatment at $250^\circ\text{C}$ in argon atmosphere. ....	173

<b>Fig. 5-8.</b> A comparison of time-temperature profiles of annealed GO and unannealed GO upon irradiation by 800 W microwaves with the argon flushing time of 10 min. The heating rate is $\sim 30\,000\text{ }^{\circ}\text{C min}^{-1}$ for annealed GO and $\sim 150\text{ }^{\circ}\text{C s}^{-1}$ for unannealed GO. The temperature records were extracted from Video S2.....	175
<b>Fig. 5-9.</b> Typical FEGSEM image of 800W/10min MWrGO. The graphene sheets were efficiently exfoliated and showed a wrinkled surface morphology.....	176
<b>Fig. 5-10.</b> A schematic illustration of microwave-induced hotspots and arcing on graphene flake.....	177
<b>Fig. 5-11.</b> Raman spectra of MWrGO synthesised <b>(a)</b> at various microwave powers after 10 min of constant argon flushing and <b>(b)</b> under various argon flushing times at the microwave power of 800 W in comparison with pristine graphite, graphite oxide, and annealed GO. ....	180
<b>Fig. 5-12.</b> A quintessential example of peak fitting of $G_{\text{App}}$ peak in the Raman spectrum of 800W/10min MWrGO (The peak fitting analysis was carried out using PeakFit V4.12 software. The peak fitting was analysed using Voigt deconvolution function till Chi-square is not less than 0.98).....	182
<b>Fig. 5-13.</b> XRD patterns of pristine graphite, graphite oxide, and 800W/10min MWrGO. ....	186
<b>Fig. 5-14.</b> <b>(a)</b> XRD patterns of MWrGO synthesised with various argon flushing times at the constant microwave power of 800 W and <b>(b)</b> The enlarged XRD plot of $20^{\circ} - 30^{\circ}$ showing the changes in position of (002) peak. ....	187
<b>Fig. 5-15.</b> <b>(a)</b> XRD patterns of MWrGO synthesised with various microwave powers after 10 min of constant argon flushing and <b>(b)</b> The enlarged XRD plot of $20^{\circ} - 30^{\circ}$ showing the changes in position of (002) peak. ....	188
<b>Fig. 5-16.</b> FTIR spectra of pristine graphite, graphite oxide, annealed GO, and 800W/10min MWrGO.....	190
<b>Fig. 5-17.</b> <b>(a)</b> Normalised TGA plots and <b>(b)</b> DTG plots for graphite oxide, annealed GO, and 800W/10min MWrGO over the temperature range from $25\text{ }^{\circ}\text{C}$ to $800\text{ }^{\circ}\text{C}$ at the heating rate of $5\text{ }^{\circ}\text{C min}^{-1}$ . ....	193
<b>Fig. 5-18.</b> The dynamic evolution of high-resolution XPS C1s photoemission spectra of <b>(a)</b> pristine graphite, <b>(b)</b> graphite oxide, <b>(c)</b> annealed GO, and <b>(d)</b> 800W/10min MWrGO. ....	195

<b>Fig. 5-19.</b> The bar chart of the electrical conductivities of pristine graphite, as-prepared GO, annealed GO, and 800W/10min MWrGO measured by four-probe method.....	198
<b>Fig. 5-20.</b> The plot of C/O ratios and electrical conductivities of pristine graphite, as-prepared GO, annealed GO and 800W/10min MWrGO, showing the strong relationship among them. ....	199
<b>Fig. 5-21.</b> Nitrogen adsorption/desorption hysteresis loops of as-prepared GO, annealed GO and 800W/10min MWrGO, revealing (a) the specific surface area and (b) the pore size distribution based on Branauer-Emmett-Teller method (BET) and Barrer-Joyner-Halenda (BJH) methods, respectively. ....	201
<b>Fig. 5-22.</b> Typical aberration-corrected HR-TEM micrographs of 800W/10min MWrGO prepared by solid-state microwave irradiation method at (a) low magnification and (b) high magnification, and the electron diffraction pattern of 800W/10min MWrGO is given in the inset, along with the diffraction intensity profiles of (1120) and (1100). ....	202
<b>Fig. 5-23.</b> The galvanostatic charge/discharge curves of MWrGO anode for 1 <sup>st</sup> , 5 <sup>th</sup> , 20 <sup>th</sup> , 50 <sup>th</sup> and 100 <sup>th</sup> at the current density of 0.2 A g <sup>-1</sup> . The regions of the electrochemical cycling data that are attributed for the electrochemical lithiation/delithiation and Faradic capacitance are separated by a dash line. ....	205
<b>Fig. 5-24.</b> The cyclic voltammogram of 800W/10min MWrGO anode for the first 5 cycles taken at the sweep rate of 0.1 mV s <sup>-1</sup> .....	206
<b>Fig. 5-25.</b> The galvanostatic cycling performance and the coulombic efficiency of 800W/10min MWrGO half cell at the current density of 0.2 A g <sup>-1</sup> between 0.01 V and 2.5 V for 100 electrochemical cycles. ....	207
<b>Fig. 5-26.</b> Rate capability of MWrGO anode every ten cycles at the various current densities between 0.01 V and 2.5 V. ....	209
<b>Fig. 5-27.</b> The cycling performances of LCO-MWrGO and LCO-CNTs cathode over 100 electrochemical cycles between 3.0 V and 4.2 V at the current rate of 0.2 C.....	211
<b>Fig. 5-28.</b> FEGSEM images of LCO-MWrGO cathode at (a) lower magnification, (b) medium magnification, and (c) higher magnification, depicting the graphene-wrapping-LCO structural model in which the LCO particles were fully wrapped by a thin layer of graphene.....	212
<b>Fig. 5-29.</b> EDS compositional mapping of the LCO-MWrGO cathode along with EDS spectrum of the whole area. The Al signal in the spectrum is a result of the Al substrate used for current collector. ....	212

<b>Fig. 5-30.</b> The rate capability comparison of LCO-MWrGO and LCO-CNTs cathodes every five cycles at charge/discharge current rates from 0.1 C to 10 C between 3.0 V and 4.2 V. ....	214
<b>Fig. 6-1.</b> XRD patterns of as-milled LCO powder, MWrGO, and LCO/xMWrGO ( $x=0.5$ wt%, 1 wt%, 2 wt%, and 3 wt%) pellets produced by CSP. ....	220
<b>Fig. 6-2.</b> The enlarged XRD plots of $20^\circ - 30^\circ$ range as indicated in Fig. 6-1.....	221
<b>Fig. 6-3.</b> X-ray diffractograms of as-milled LCO powder, LCO/3%CNTs pellet produced by CSP, and LCO/1%MWrGO pellet produced by CSP.....	222
<b>Fig. 6-4.</b> FEGSEM images of fractured surface of LCO/1%MWrGO pellet produced by CSP. ....	223
<b>Fig. 6-5.</b> FEGSEM image of the fractured surface of LCO/1%MWrGO pellet produced by CSP. ....	223
<b>Fig. 6-6.</b> The effect of MWrGO content on the electrical conductivities of LCO/xMWrGO pellets prepared at CSP conditions of $250^\circ\text{C}$ , 250 MPa, and 60 min. ....	225
<b>Fig. 6-7.</b> The comparison of electrical conductivities of LCO/xMWrGO pellets produced by CSP and LCO/xCNTs pellets produced by CSP with respect to the varied contents of 800W/10min MWrGO and CNTs, respectively. ....	226
<b>Fig. 6-8.</b> Nitrogen adsorption/desorption hysteresis loops of MWrGO and CNTs.....	226
<b>Fig. 6-9.</b> The plot of relative densities of LCO/1%MWrGO pellets produced by CSP and dry-pressed LCO/1%MWrGO pellets as a function of annealing temperatures in comparison with as-CSPed LCO/1%MWrGO pellets and as-dry-pressed LCO/1%MWrGO pellets. ....	229
<b>Fig. 6-10.</b> The plot of electrical conductivities of LCO/1%MWrGO pellets produced by CSP and dry-pressed LCO/1%MWrGO pellets as a function of annealing temperatures in comparison with as-CSPed LCO/1%MWrGO pellets and as-dry-pressed LCO/1%MWrGO pellets. ....	229
<b>Fig. 6-11.</b> The cyclic voltammogram of a half-cell consisted of LCO/1%MWrGO pellet for the initial cycle recorded at the sweep rate of $0.1\text{ mV s}^{-1}$ .....	232
<b>Fig. 6-12.</b> The comparison for initial-cycle CV plots of LCO/1%MWrGO pellet and LCO/3%CNTs pellet at the sweep rate of $0.1\text{ mV s}^{-1}$ .....	233
<b>Fig. 6-13.</b> The DCIR profiles of LCO/1%MWrGO pellet and LCO/3%CNTs pellet performed at the same state of charge (SOC). ....	233

<b>Fig. 6-14. (a)</b> Sweep rate dependence of cyclic voltammogram for LCO/1%MWrGO pellet produced by CSP, <b>(b)</b> The relationship between the square root of the sweep rates for the LCO/1%MWrGO pellet and anodic/cathodic peak currents. ....	235
<b>Fig. 6-15.</b> The galvanostatic cycling curves of LCO/1%MWrGO pellet for 1 <sup>st</sup> , 2 <sup>nd</sup> , 5 <sup>th</sup> , 10 <sup>th</sup> , and 20 <sup>th</sup> cycles at the current rate of 0.1 C. ....	237
<b>Fig. 6-16.</b> Cyclability comparison of LCO/1%MWrGO pellet and LCO/3%CNTs pellet between 3.0 V and 4.2 V over 40 cycles at the constant rate of 0.1 C. ....	238
<b>Fig. 6-17.</b> X-ray diffractograms of <b>(a)</b> LCO/1%MWrGO cathode and <b>(b)</b> LCO/3%CNTs cathode at pristine state and after 40 cycles at full discharge state. The insets show the magnified view of (003) peak of each XRD result.....	239
<b>Fig. 6-18. (a)</b> Rate capability comparison of LCO/1%MWrGO pellet produced by CSP and LCO/3%CNTs pellet produced by CSP. <b>(b)</b> The dependency of capacity retention on C-rate of LCO/1%MWrGO pellet and LCO/3%CNTs pellets in semi-logarithmic plots (normalised to first-cycle capacity). ....	241
<b>Fig. 6-19. (a)</b> The electrochemical charge/discharge curves of the LCO/1%MWrGO composite cathode at varying current rates, <b>(b)</b> The plot of discharge potential versus current rates plot for the LCO/1%MWrGO cathode. ....	243
<b>Fig. 6-20.</b> Nyquist plots of LCO/1%MWrGO pellet and LCO/3%CNTs pellet before and after 40 cycles with the equivalent circuit in the inset, where $R_s$ represents the electrolyte resistance, $R_{ct}$ represents the charge transfer resistance, CPE stands for constant phase element for the electrode-electrolyte interface and $Z_w$ is often referred to the Warburg impedance, which arises from the Li diffusion in LCO particles.....	245
<b>Fig. 6-21.</b> The plots of $Z_{re}$ and the reciprocal square root of frequency for LCO/1wt%MWrGO and LCO/3wt%CNTs pellets produced by CSP. ....	246
<b>Fig. 6-22.</b> The schematic representation of the architecture of LCO particles and <b>(a)</b> CNTs and <b>(b)</b> MWrGO. ....	249

## List of Abbreviation & Symbols

BET	Branauer-Emmett-Teller method
BJH	Barrer-Joyner-Halenda method
CSP	Cold sintering process
CNTs	Carbon nanotubes
CV	Cyclic voltammetry
CVD	Chemical vapour deposition
$D_{Li}$	Lithium ion diffusion coefficient
DMC	Dimethyl carbonate
$E^0$	Theoretical chemical potential
EC	Ethylene carbonate
EDAX	Energy dispersive X-ray analysis
EIS	Electrochemical impedance spectroscopy
F	Faraday's constant
FEGSEM	Field emission gun scanning electron microscope
FTIR	Fourier-transform infrared spectroscopy
FWHM	Full width at half maximum
GO	Graphene oxide
HOPG	Highly ordered pyrolytic graphite
HR-TEM	High-resolution transmission electron microscopy
IR	Ohmic loss
JCPDS	Joint Committee for Powder Diffraction Studies
$L_a$	Crystalline domains
LCO	$LiCoO_2$
Pb-acid batteries	Lead-acid batteries
LIBs	Lithium-ion batteries
$M_w$	Molecular weight
MCMB	Mesocarbon Microbeads
MWrGO	Microwave reduced graphene oxide
Nickel-Cadmium	Ni-Cd
Nickel-Metal hydride	Ni-MH
NMP	<i>N</i> -methyl pyrrolidinone
OCV	Open-circuit voltage
PVdF	Polyvinylidene difluoride
rGO	Reduced graphene oxide
RMD	Reactive molecular dynamics

SAED	Selected area electron diffraction
SEI	Solid electrolyte interface
SIBs	Sodium ion batteries
TGA	Thermogravimetric analysis
XRD	X-ray diffraction
XPS	X-ray photoelectron spectroscopy
$\Delta G^0$	Gibbs free energy

# Chapter 1. Introduction

## 1.1. The energy dilemma

The carbon dioxide emission caused by combustion of fossil fuel in vehicles and power plants has been recognised as one major sources towards the greenhouse effect across the world. It is reported that 34% of the world's total primary energy consumption was generated from oil and it was responsible for 40% of the total carbon dioxide emission [1]. According to the figures quoted in World Meteorological Organisation (WMO) Bulletin, the long-lasting greenhouse gases resulted in a 43% increase in total radiative forcing, which is the warming effect on the climate, in the past 3 decades [2]. Among the common greenhouse gases, carbon dioxide is responsible for the 81% of the increase, leading to the rapid temperature rising and the sea level rising. However, it is predicted that the energy demand will far overtake the energy supplies by the mid-term of 21 century and thus the preservation of a consistent energy supply is a formidable challenge. The ambition to alleviate the environmental impact of CO<sub>2</sub> emission and the upcoming power shortage will together lead to an energy dilemma in short future [3].

In efforts to tackle these impending “energy crisis”, some major technological actions should be immediately taken: (i) to exploit renewable energy sources to reduce the reliance on the fossil fuels, such as crude oil, coals and natural gas; and (ii) to store the renewable energies in electrochemical energy devices which can be later used to power up the world. There are, however, numerous challenges found for the exploitation and the storage of the renewable energies generated. Many alternative renewable energy sources can be the potential contenders to replace fossil-fuel energy, such as solar energy, wind



energy, tide energy and geothermal energy, *etc.* Albeit that they do not produce any greenhouse gases during exploitation, the intermittent nature plagues their wide applications. For example, solar energy is solely generated during the daytime when the sunlight is accessible for only 8-12 hours which depends on the geographic location. Additionally, the intensity of the sunlight is affected to a great extent by the weather and the environment. Thus, the generation of electricity from solar energy is not stable. On the other hand, solar power devices and plants are unable to store the excess electricity generated during the daytime and supply it in peak times at night or in weak sunlight condition. Similar problems can also be identified for other renewable energy sources during exploitation and storage other than solar energy.

To surmount these problems, electrochemical energy storage devices/systems are demanded for improving the energy resilience because they can soak up excess energies in chemical form and release them when needed. The common electrochemical energy storage devices/systems include primary/secondary batteries, (super)capacitor and fuel cell, *etc.* Among them, primary/secondary batteries, such as Zinc-carbon/air, lead-acid (Pb-acid), Nickel-Cadmium (Ni-Cd), Nickel-Metal hydride (Ni-MH), lithium-ion batteries (LIBs), and sodium ion batteries (SIBs), have garnered enormous attentions in terms of the reliability, the cost and the performance. They are suitable for various storage applications, from small-scale format cells for portable electronic devices, to medium-scale format batteries for electric vehicles/trains, and further to large-scale format for stationary energy storage devices/uninterrupted power sources [4-6]. The global battery market is estimated to be > \$30 billion in 2020 and its growth is drastically driven by the burgeoning demand for electric vehicles and stationary energy storage devices [7]. To meet the scope of this thesis, we primarily focus on the evolution, fundamentals, and

challenges of LIBs because they exhibit apparent advantages over the counterparts, like high energy density, lightweight, long cycle life, low self-discharge rate, and environmental benign.

Since the first market introduction of LIBs in 1991, the electrochemical performances in terms of gravimetric/volumetric energy densities have been greatly improved as they were promoted by the rapid development of portable devices in which the weight and volume of LIBs are seriously concerned. A typical example that deserves the special attentions is the evolutions of LiCoO<sub>2</sub>-carbon rechargeable LIBs developed by Sony Corporation. By replacing the soft carbon (first generation) with hard carbon (second generation) as anode, a significant electrochemical improvement was observed in terms of gravimetric energy density (80 Wh kg<sup>-1</sup> → 120 Wh kg<sup>-1</sup>) and volumetric energy density (200 Wh L<sup>-1</sup> → 295 Wh L<sup>-1</sup>) [8-10]. Following that, with the newly designed mesocarbon microbeads (MCMB) and bespoke electrolyte recipe, the gravimetric and volumetric energy densities were further raised to 155 Wh kg<sup>-1</sup> and 400 Wh L<sup>-1</sup>, respectively [9].

In recent years, the majority focus of research to improve the electrochemical performances of LiCoO<sub>2</sub>-carbon batteries lies in increasing the gravimetric energy density by increasing the specific capacity and the operating voltage of the LiCoO<sub>2</sub> (LCO) cathode materials. However, if the operating voltage is raised beyond 4.2 V to achieve a higher capacity (> 140 mAh g<sup>-1</sup>), the LCO-based electrodes likely suffer many problems, such as large crystallographic volume change, decomposition of organic electrolyte and fast capacity decay. To ameliorate these problems, some approaches have been adopted, such as coating LCO particles with passivation layers, developing new high-voltage electrolyte, *etc.* These approaches have been reported to effectively optimise the gravimetric energy density. However, the volumetric energy density is neglected in many

previously published papers to emphasize their superior gravimetric energy density. In some cases where the volumetric energy densities were reported, it did not consider the occupations of electrochemically inactive components, such as conductive additives, polymeric binder, current collector and probably dispersant agents, leading to an overestimated value. It is a common sense that the volumetric energy density metric is becoming more critical when rechargeable batteries for portable electronic devices and electricity-driven vehicles have to be installed in a limited space. Therefore, the volumetric energy density needs to be appropriately assessed to provide a valuable estimation.

It is widely accepted that the usage of conductive additives, polymeric binder and current collector should be minimised to achieve the highest energy output of conventional electrode (*i.e.*, thin-filmed electrode). However, there seems to have little room for further improvement. In efforts to achieve a high volumetric energy density without the expense of rate performance, a bulk electrode prototype with high density and high electrical conductivity should be developed. Many techniques have been employed for this purpose, including conventional sintering [11], co-extrusion [12] and rotating magnetic field method [13], to produce thicker bulk  $\text{LiCoO}_2$  electrodes. However, their reversible capacities suffered from a rapid degradation at high current density due to the absence of conductive fillers, which normally is carbonaceous materials, in the LCO matrix. It should point out that the carbonaceous materials in LCO matrix are readily decomposed at the high sintering temperature during conventional sintering, resulting in a poor electrical conductivity. Therefore, a novel sintering technique which can consolidate bulk LCO composite electrode at low temperature is needed.

Inspired by a hydrothermal-assisted hot pressing technique in which high-density

ceramics (> 90% relative density) can be fabricated via combining hydrothermal synthesis with uniaxial pressing, an innovative cold sintering process (CSP) is recently proposed by C. A. Randal's group [14-16]. The densification induced by CSP is typically achieved via a mediated dissolution-precipitation process in which an appropriate aqueous solution (*e.g.*, water, acid or base) is incorporated to dissolve the sharp edges of ceramic particles under reduced temperatures (from ambient temperature to 300 °C) and then densify the ceramic body after evaporation. CSP has been successfully utilised to fabricate bulk composite cathodes, such as  $\text{LiFePO}_4$  [17, 18], which have achieved superior electrochemical performances in terms of the volumetric energy density. However, the densification of LCO using CSP and its most eminent application for LIBs remains insufficiently studied, which needs to be explored.

Last but not least, the rate performance of bulk LCO-based composite cathode cannot be compromised by minimising the conductive additive to achieve a higher volumetric energy density. Henceforth, a conductive additive with high electrical conductivity, such as carbon nanotube and graphene, is required for LCO-based composite cathode produced by CSP.

## 1.2. Thesis structure

This thesis first starts with a literature review in Chapter 2 which covers the following fundamental aspects: (i) a brief introduction of the principles and the developments of LIBs; (ii) the densification mechanism for cold sintering process (CSP) of ceramics; (iii) the influences of CSP processing variables, including temperature, pressure, holding time, transient liquid, particle size of starting materials, and post-CSP annealing treatment; (iv) an up-to-date review of CSP application for LIBs; (v) graphene properties and production methods; (vi) a critical review of graphene produced via microwave-assisted reduction method; and (vii) the percolation theory of conductive fillers, mainly CNTs and graphene, in electrode.

Chapter 3 details the experimental procedures to fabricate (i) bulk  $\text{LiCoO}_2$  cathode via CSP method and (ii) high-quality graphene via microwave-assisted reduction method, including processing procedures, materials characterisation techniques, and electrochemical studies.

Chapter 4 is devoted to proving the successful application of CSP to fabricate bulk  $\text{LiCoO}_2$  cathode composite with multi-walled carbon nanotubes as conductive filler, along with its electrochemical performance.

Chapter 5 presents an ultra-fast production method to fabricate high-quality graphene via microwave irradiation and preliminarily demonstrates its potential use in conventional LIBs.

Chapter 6 demonstrates the improvement of microwave-synthesised graphene to the electrochemical performances of bulk  $\text{LiCoO}_2$  cathode prepared by CSP.

The project conclusions are then provided in Chapter 7 and finally the future developments that can be continued in the lines of this project are given Chapter 8.

## Chapter 2. Literature review

### 2.1. Lithium-ion batteries

A battery can be classified as primary or secondary batteries based on whether it is repeatedly chargeable or not. Primary batteries store energies once manufactured and will be disposed once drained. While secondary batteries can be recharged back to original chemical state even after the stored energies are completely consumed up. The best-known primary battery is based on zinc-carbon system. However, this initial battery prototype has been soon replaced by secondary battery, such as lead-acid battery which was invented by Plante in 1859 [19]. It is nowadays still widely used in vehicles to ignite the fuel engines due to its excellent power density at low temperature conditions. However, owing to the heavy package of lead-acid batteries, alkaline Ni-Cd batteries were then invented and used on some occasions where portability is the main concern. Since then, Ni-Cd batteries were used for a few decades, but engineers still managed to find alternative batteries because of the pollution-related issues and low capacity caused by the cadmium element. Metal hydride was then proved to be an excellent substitution to cadmium electrode and formed Ni-MH batteries. In comparison with the energy density (20-50 Wh kg<sup>-1</sup>) of Ni-Cd battery system, Ni-MH batteries are able to deliver improved energy density of 70-100 Wh kg<sup>-1</sup> for batteries of the same size [20, 21]. However, with the ambitions to drive vehicles in a longer range, even Ni-MH batteries are unable to supply sufficient energy density. More importantly, the memory effect of Ni-Cd and Ni-MH batteries further reduces the practical battery capacity and thus the energy density if the batteries are repeatedly subjected to shallow-depth discharge [22]. Therefore, a more advanced battery system is needed to fulfil the increasing demand for high energy density, affordable price, and practical usage.

Developed by Asahi Kasei Company in Japan, lithium-ion batteries (LIBs) was then first commercialised by Sony Corporation for practical purpose in 1991. Soon after, LIBs gained a big part of energy storage markets as diverse as laptops, mobile phones, electric/hybrid vehicles and even grid systems. The increasing growth of LIBs in energy storage market is believed to be related to the high energy density ( $80 \text{ Wh kg}^{-1}$ ;  $200 \text{ Wh L}^{-1}$  [21]) and lightweight. This is ascribed to lithium being the lightest metal element and also lithium being the electronegative metal ( $-3.04 \text{ V}$  vs standard hydrogen reference electrode [23]). In Fig. 2-1, the performances of the abovementioned battery systems have been assessed in terms of gravimetric energy density and volumetric energy density, indicating the overwhelming superiority of LIBs [24]. In addition, LIBs can be manufactured with different commercial configurations/designs which can flexibly tailor to the needs of industry and customers due to the differences in the volume utilisation in housing case and in the packing density in battery module/system, as shown in Fig. 2-2. Among them, the coin and cylindrical cells possess the higher volume occupancy in housing case due to less accessories, whereas the pouch and prismatic cells are now prevalently adopted due to the efficient packing arrangement [25].



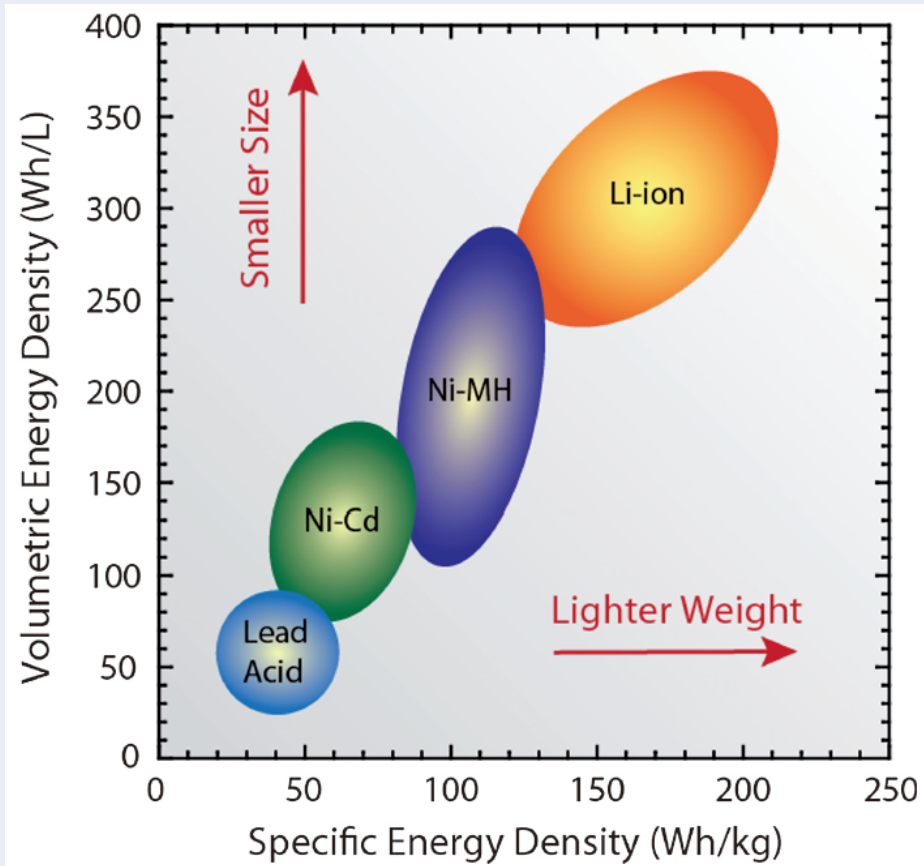


**Fig. 2-1.** The evolution of gravimetric/volumetric energy density with the development of commercial batteries [26].

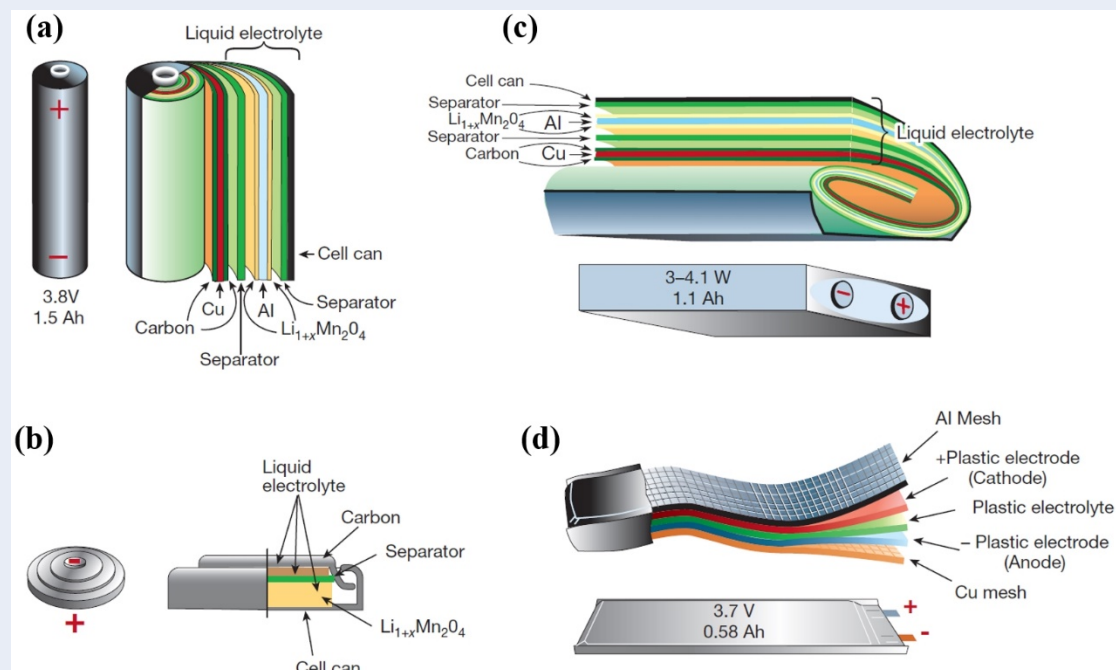


**Fig. 2-2.** The representation of different commercial LIBs configurations: (a) cylindrical, (b) coin, (c) prismatic, and (d) film [27].

A typical commercial LIB consists of three major components (cathode, anode, and electrolyte), along with other essential components, such as current collectors, separators, polymeric binder, and conductive fillers. The relative volume, relative mass and relative costs of each component are given for comparison in Fig. 2-3. However, the performances of a given battery are mainly dependent on the properties of cathode, anode, and electrolyte. This is why they receive immense attentions from academic community and industry. Note that special attention should be given to the volume breakdown of porosity/electrolyte which takes up around 1/3 of the total volume in Fig. 2-3.

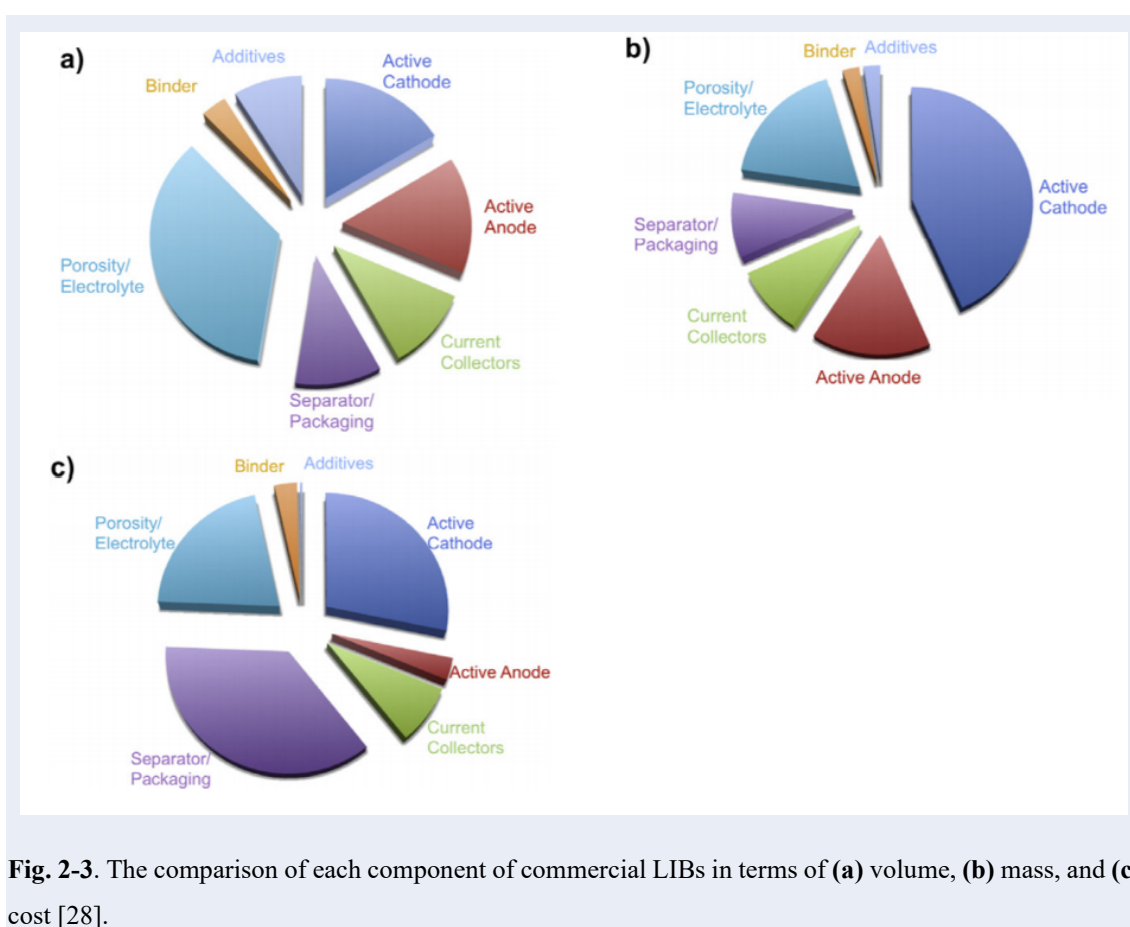


**Fig. 2-3.** The comparison of each component of commercial LIBs in terms of (a) volume, (b) mass, and (c) cost [28].

### 2.1.1. Underlying electrochemistry for LIBs

Prior to discussing how LIBs work to supply energy to external loadings, it is necessary to elaborate the basic electrochemistry behind the LIBs as well as how the voltage and the electrochemical capacity of a typical LIBs are derived. Afterwards, the intrinsic factors that can affect the kinetics of LIBs are also discussed to fully understand the working mechanism of LIBs, which can guide the future work to optimise the design of LIBs. To fully rationalise the working mechanism of LIBs, LiCoO<sub>2</sub>-graphite system (Fig. 2-4) is exemplified in this thesis on the grounds that it is the first breakthrough commercial LIBs and it has been being widely used.

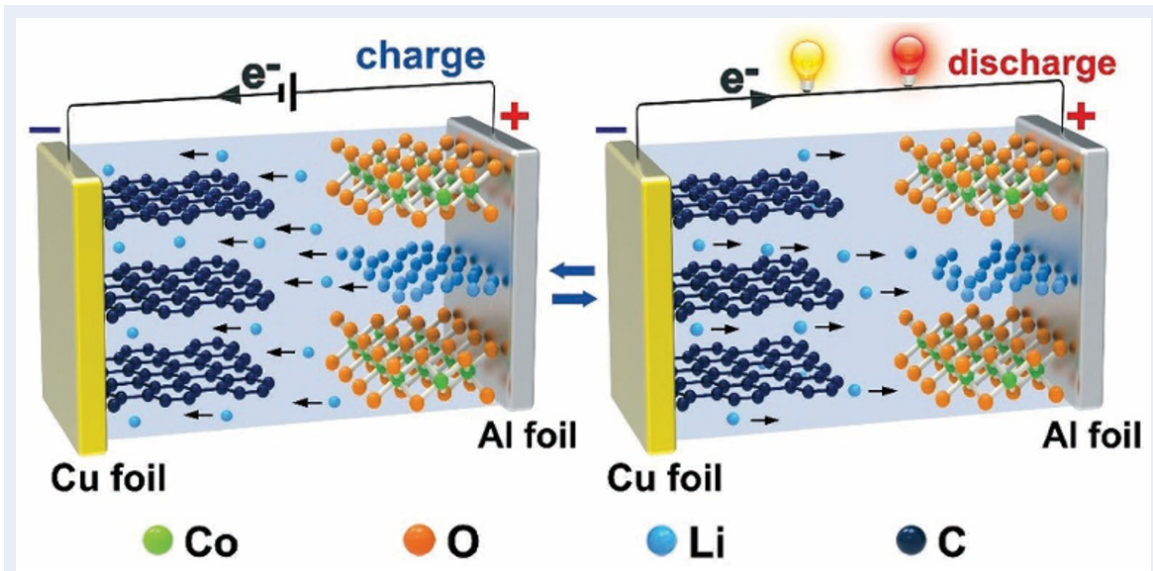
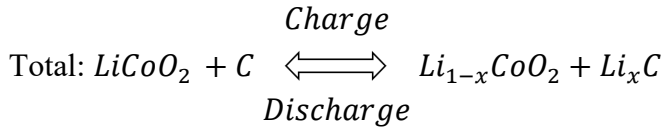
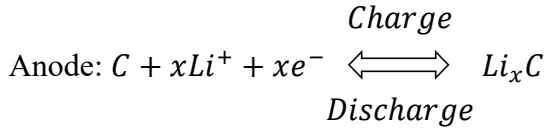
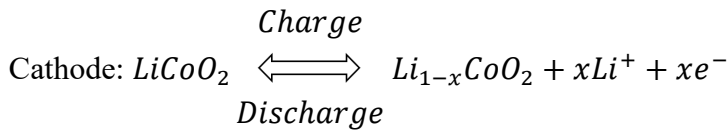


**Fig. 2-4.** Schematic representation of the intercalation/deintercalation process of Li ions between cathode and anode for LIBs [29].

The commercial LiCoO<sub>2</sub> and graphite are typically intercalation/deintercalation-type materials in which Li ions are able to insert and extract from the layered structure without causing structural collapsing. Specifically, during charging, the Li ions are released from “lithium source” cathode matrix and travel to “lithium sink” anode via electrolyte and separator, forming a Li-ion flow from the cathode to anode. Simultaneously, the free electrons are forced to travel from cathode to anode via the external load and form a

complete circuit with the Li-ion flow. Upon discharging process, the electrochemical reaction reversely takes place with the Li ions traveling from the anode to the cathode. Also, the current flow proceeds in a reverse way and drives the external loading to work. Owing to this unique working mechanism, LIBs are collectively known as rocking-chair cell. The electrochemical reactions taking place on cathode and anode are shown below, together with the overall electrochemical reaction:



Generally speaking, the theoretical chemical potential of a battery system is determined by the Gibbs free energy ( $\Delta G^0$ ) difference between positive electrode and negative electrode based on the following equation [30]:

$$\Delta G^0 = -nFE^0 \text{ [Equation 1]}$$

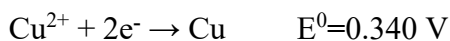
Where, n is the transfer number of electrons involved in the electrochemical reaction  
F is the Faraday's constant, 96485.33 C mol<sup>-1</sup>.  
E<sup>0</sup> is the theoretical chemical potential.

The standard electrode potentials of various electrode reactions are summarised in Table 2-1. Among them, the battery system of Cu/Zn in acid electrolyte, also called Daniel cell, is the well-known electrochemical storage device which was discovered in 1836.

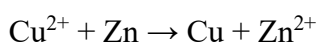
**Table 2-1.** Standard electrode potentials of redox reactions taking place at 25 °C [31].

Electrode reaction	$E^0$ , V	Electrode reaction	$E^0$ , V
$\text{Li}^+ + e \rightleftharpoons \text{Li}$	-3.01	$\text{Tl}^+ + e \rightleftharpoons \text{Tl}$	-0.34
$\text{Rb}^+ + e \rightleftharpoons \text{Rb}$	-2.98	$\text{Co}^{2+} + 2e \rightleftharpoons \text{Co}$	-0.27
$\text{Cs}^+ + e \rightleftharpoons \text{Cs}$	-2.92	$\text{Ni}^{2+} + 2e \rightleftharpoons \text{Ni}$	-0.23
$\text{K}^+ + e \rightleftharpoons \text{K}$	-2.92	$\text{Sn}^{2+} + 2e \rightleftharpoons \text{Sn}$	-0.14
$\text{Ba}^{2+} + 2e \rightleftharpoons \text{Ba}$	-2.92	$\text{Pb}^{2+} + 2e \rightleftharpoons \text{Pb}$	-0.13
$\text{Sr}^{2+} + 2e \rightleftharpoons \text{Sr}$	-2.89	$\text{D}^+ + e \rightleftharpoons \frac{1}{2}\text{D}_2$	-0.003
$\text{Ca}^{2+} + 2e \rightleftharpoons \text{Ca}$	-2.84	$\text{H}^+ + e \rightleftharpoons \frac{1}{2}\text{H}_2$	0.000
$\text{Na}^+ + e \rightleftharpoons \text{Na}$	-2.71	$\text{Cu}^{2+} + 2e \rightleftharpoons \text{Cu}$	0.34
$\text{Mg}^{2+} + 2e \rightleftharpoons \text{Mg}$	-2.38	$\frac{1}{2}\text{O}_2 + \text{H}_2\text{O} + 2e \rightleftharpoons 2\text{OH}^-$	0.40
$\text{Ti}^+ + 2e \rightleftharpoons \text{Ti}$	-1.75	$\text{Cu}^+ + e \rightleftharpoons \text{Cu}$	0.52
$\text{Be}^{2+} + 2e \rightleftharpoons \text{Be}$	-1.70	$\text{Hg}^{2+} + 2e \rightleftharpoons 2\text{Hg}$	0.80
$\text{Al}^{3+} + 3e \rightleftharpoons \text{Al}$	-1.66	$\text{Ag}^+ + e \rightleftharpoons \text{Ag}$	0.80
$\text{Mn}^{2+} + 2e \rightleftharpoons \text{Mn}$	-1.05	$\text{Pd}^{2+} + 2e \rightleftharpoons \text{Pd}$	0.83
$\text{Zn}^{2+} + 2e \rightleftharpoons \text{Zn}$	-0.76	$\text{Ir}^{3+} + 3e \rightleftharpoons \text{Ir}$	1.00
$\text{Ga}^{3+} + 3e \rightleftharpoons \text{Ga}$	-0.52	$\text{Br}_2 + 2e \rightleftharpoons 2\text{Br}^-$	1.07
$\text{Fe}^{2+} + 2e \rightleftharpoons \text{Fe}$	-0.44	$\text{O}_2 + 4\text{H}^+ + 4e \rightleftharpoons 2\text{H}_2\text{O}$	1.23
$\text{Cd}^{2+} + 2e \rightleftharpoons \text{Cd}$	-0.40	$\text{Cl}_2 + 2e \rightleftharpoons 2\text{Cl}^-$	1.36
$\text{In}^{3+} + 3e \rightleftharpoons \text{In}$	-0.34	$\text{F}_2 + 2e \rightleftharpoons 2\text{F}^-$	2.87

The corresponding redox half reactions that occur on the positive and the negative electrodes are given:



The overall redox reaction for the Cu/Zn battery system is:



Therefore, the overall electrochemical potential of Cu/Zn battery system can be simply obtained from the potential difference between positive electrode and negative electrode according to the following equation:

$$\Delta V = E_{positive}^0 - E_{negative}^0 \quad [\text{Equation 2}]$$

It is worth noting that the standard chemical potentials shown above are the values given

at 298.15 K, 191.325 KPa and the concentrations of products and reactants have to be 1 *M*. Henceforth, the standard overall electrochemical potential of Cu/Zn battery system is  $E^0 = 1.103$  V. However, the electrochemical reactions are virtually hard to satisfy the standard conditions for temperature and pressure. Also, the concentrations of products and reactants usually deviate away from 1 *M*. Those factors can alter the chemical potentials of electrochemical reactions and Nernst equation distinctly tells the relationship amongst them, as shown below:

$$E = E^0 - \frac{RT}{nF} \ln \frac{(products)Cu.Zn^{2+}}{(Reactants)ZnCu^{2+}} \quad [\text{Equation 3}]$$

Where *E* is the real electrochemical potential

$E^0$  is the standard electrochemical potential, 1.103 V for Cu/Zn battery system

*R* is the gas constant; 8.3145 J mol<sup>-1</sup> K<sup>-1</sup>

*n* represents the number of transfer electrons involved in the electrochemical reaction

*F* is the Faraday's constant, 96485.33 C mol<sup>-1</sup>

*T* is the absolute temperature in the unit of K.

Apart from the variations in temperature, pressure and product/reactant concentrations, there are a few practical factors which can deviate the battery potential from the ideal value. It can be explained from the view of reaction polarisations and they are illustrated in Fig. 2-5. The polarisations for a battery are very complex but they can be identified in terms of three important sources: (i) activation polarisation; (ii) ohmic polarisation; and (iii) concentration polarisation. The activation polarisation is ascribed to the charge-transfer electrochemical reactions occurring on the electrode surfaces and is greatly influenced by the electroactive materials itself and the surface physical properties of electrode, such as porosity, surface areas, and tortuosity [31]. By appropriate surface

manipulation to increase the surface areas and improve the tortuosity, it can reduce the microstructurally-induced activation polarisation and thus lead to a uniform current flow across the electrode surfaces [32]. The ohmic polarisation is closely related to the intrinsic resistance of each constituent in the battery and the contact/interfacial impedances between constituents. The concentration polarisation is largely attributed to the kinetics of mass transport of chargers in electrolyte and it may become significant at reaction sites where it is difficult for the liquid electrolyte to reach, especially at the core part of dense electrode. These aforementioned polarisations are nonlinear and become significant at tough current rates, which result in large IR drop, lower potential plateau, and premature termination of charge/discharge process [33].

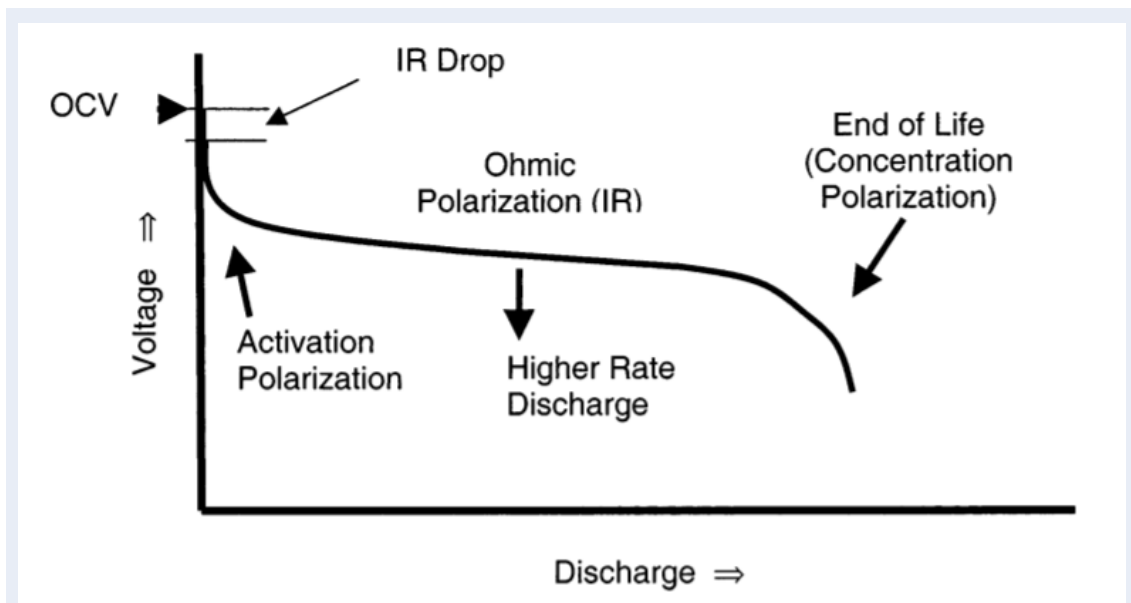


**Fig. 2-5.** The illustration of the effect of various polarisations on discharge behaviour of LIBs [30].

To reduce the detrimental effect of polarisations on LIBs, a number of approaches have been pursued to fully utilise the performance of battery:

- Conductive fillers with higher electrical conductivity and larger surface area, such as carbon nanotubes and graphene, can greatly lower the ohmic polarisation by building up 3D electrical network and providing more contact points [34]

- The non-conductive polymeric binder which is typically employed to “glue” together electrode particles can be completely eliminated from the electrode as long as the electrode particles are capable to “bond” together themselves, such as via sintering process
- An electrode with large surface areas and optimised structure will benefit the mass transport and the formation of homogeneous current density
- An electrolyte with lower viscosity and higher ionic conductivity can reduce both the ohmic polarisation and concentration polarisation [35]
- An electrolyte with large potential window can avoid the undesired side reaction taking place at the interfaces of electrode and electrolyte, which may substantially increase the activation polarisation [31]
- The separator with high porosity can uptake sufficient electrolyte to facilitate the rapid transportation of lithium ion between positive and negative terminals [36]
- The current collectors should be chemically stable in the battery potential window and cannot react with any electrolyte to become corroded [37]. Also, the lower ohmic resistance is beneficial to reduce the overall ohmic resistance of the whole battery

After discussing the fundamentals of chemical potentials of a battery system as well as the associated factors affecting the performance of battery, the theoretical capacity of electroactive materials needs to be discussed. Normally, the overall capacity of a battery is highly restrained by the quantity of electroactive materials used in a battery. Thus, for reliable comparison, the specific capacity should be calculated in terms of either gravimetric or volumetric unit. The theoretical specific gravimetric capacity of a given battery can be obtained using the following equation [38, 39]:

$$Q = \frac{n F}{M} \quad [\text{Equation 4}]$$

Where, Q is the theoretical specific gravimetric capacity for a given electroactive material (mAh g<sup>-1</sup>)

n represents the number of transfer electrons involved in the electrochemical reaction

F is the Faraday’s constant, 96485.33 C mol<sup>-1</sup>

M is the molecular weight of the electroactive materials (g mol<sup>-1</sup>).



Let us take LiCoO<sub>2</sub> for example because it is the most widely commercial cathode materials for use in LIBs. It has the molecular weight of 97.87 g mol<sup>-1</sup> and it releases one electron during charging/discharge process, representing that n is 1.

$$Q = \frac{n(1) F \left( 96485 \frac{C}{mol} \times \frac{A \cdot s}{C} \times \frac{1h}{3600s} \right)}{M \left( 97.87 \frac{g}{mol} \right)} = 274 \text{ mAh g}^{-1}$$

Even though LiCoO<sub>2</sub> exhibits a superior theoretical gravimetric capacity (274 mAh g<sup>-1</sup>) in comparison with other commercial spinel-type LiMn<sub>2</sub>O<sub>4</sub> (148 mAh g<sup>-1</sup> [40]) and olivine-type LiFePO<sub>4</sub> (170 mAh g<sup>-1</sup> [41]), it can only deliver a practically reversible capacity of ~140 mAh g<sup>-1</sup> up to 4.2 V due to the structural instability. The more details regarding the relationship between microstructure and practical capacity will be discussed in this thesis. It is worth noting that the chemical potential and capacity are all essential battery metrics because they altogether determine the overall gravimetric energy density (in Wh kg<sup>-1</sup>) of a given battery.

$$\text{Energy density} = \frac{E_{pos} - E_{neg}}{\frac{1}{C_{pos}} + \frac{1}{C_{neg}}}$$

Where,  $E$  represents the equilibrium potential (in V) and  $C$  represents the specific capacity (in Ah kg<sup>-1</sup>) [33].

The specific gravimetric capacity and gravimetric energy above can be readily converted to the corresponding specific volumetric capacity and volumetric energy density as long as the density is provided. When it comes to the calculation of electrode density, all the components involved in the electrode need to be taken into consideration, even for those electrochemically inactive materials, such as conductive filler, polymeric binder, current

collector, or probably dispersant agents. As the major component in electrode formulation, the crystallographic density of electroactive materials plays a pivotal role in determining the volumetric energy density and the crystallographic densities of common intercalation-type lithium transition-metal oxides vary in the order  $density_{(layer)} > density_{(spinel)} > density_{(olivine)}$  [42]. It suggests that the layered  $LiCoO_2$  can provide higher energy density per volume unit among the three intercalation-type compounds. Volumetric energy density metric is becoming more critical when LIBs are used in grid-scale energy storage system, portable electronic devices and electricity-driven vehicles [42].

### 2.1.2. Anode

In the early development of LIBs, lithium metal has long been considered the “holy grail” in lithium battery research, due to its superhigh specific capacity ( $3\,860\text{ mAh g}^{-1}$ ;  $2\,047\text{ mAh cm}^{-3}$  [43]) and the lowest potential amongst all lithium anode materials [44]. However, the lithium metal was then quickly phased out following the observation of Li dendrites formed on the surface. The occurrence of Li dendrites is ascribed to the ununiform deposition of  $\text{Li}^+$  ions extracted from the cathode terminal on lithium metal surfaces during charging process. Upon repetitious galvanostatic (dis)charging process, the Li dendrites may grow and eventually penetrate the polymeric separator and short-circuit the battery, leading to the vigorous dissipation of a large amount of heat and even explosion. Consequently, the Li metal anode was initially replaced by coke ( $250\text{ mAh g}^{-1}$ ) from the view of safety concern [45]. However, coke was quickly withdrawn as a result of low capacity and was soon replaced by Mesocarbon Microbeads (MCMB) ( $300\text{ mAh g}^{-1}$ ). Afterwards, graphite started to garner recognition as anode-active materials in commercial LIBs due to the higher capacity ( $372\text{ mAh g}^{-1}$ ), better structural stability, high electrical conductivity (bandgap of  $\approx 0.4\text{ eV}$ ), and lower cost [31].

Graphite has an interlayer spacing of  $0.337\text{ nm}$  and is believed to freely accommodate Li ions ( $0.76\text{ \AA}$ ) to form stoichiometric substance  $\text{LiC}_6$  via a “staging” intercalation mechanism in which Li ions are likely to reside in the distant graphene layers before in the neighbour graphene layers [46]. This reversible intercalation process ultimately yields a promising capacity of  $372\text{ mAh g}^{-1}$ . Nevertheless, the intercalation process of Li ions in graphite is also accompanied with the inevitable formation of solid electrolyte interface (SEI) at low potential ( $<0.1\text{ V vs Li}^+/\text{Li}$ ) when in contact with many commonly used carbonate solvents. Even though the formation of SEI reduces the first cycle coulombic

efficiency and increases the interfacial resistance between graphite and electrolyte, the presence of SEI prevents the further decomposition of electrolyte but is still permeable for the transport of Li ions, enabling the safe operation of graphite anode (because  $\text{LiC}_6$  is a strong reducing agent). It has been proved that the thickness of SEI may greatly affect the performance of LIBs in terms of rate capability [47, 48]. Thus, the formation of controllable thickness of SEI has attracted increasing attentions and was achieved with the introduction of electrolyte additives, such as  $\text{NaNO}_3$ , 12-crown-4, 15-crown-5, azoethers, and boranes [35]. The formation of SEI is correlated to the reduction reaction of electrolyte solvents with lithium, mainly ethylene carbonate (EC). Sanyo's group [49] first reported the successful lithium intercalation of graphite in EC-based electrolyte and Dahn [50] proved that EC was prone to generate a graphite intercalation compound with high anion population, such as  $\text{PF}_6^-$ , in  $\text{Li}^+$  solvation shell, resulting in high F-containing SEI compositions, whose energy gap is wide enough to insulate the electron tunnelling. Since then, EC became an indispensable solvent for carbon-based anode in LIBs. It is believed that the main compositions of naturally formed SEI are  $\text{LiF}$ ,  $\text{Li}_2\text{CO}_3$ ,  $\text{Li}_2\text{O}$ ,  $\text{ROLi}$ ,  $\text{ROCO}_2\text{Li}$ , *etc.*, which are all electrically insulated but ionically conductive [51, 52]. It is readily predicted that without the spatial separation of SEI the graphite would continue to consume the electrolyte and eventually result in the failure of LIBS in just few cycles.

With the ambition to further increase the energy density of LIBs, researchers are enthusiastic to find out carbonaceous active materials with higher capacity. In this sense, many carbonaceous materials with different dimensions were proposed and investigated. 1D carbon materials, such as carbon nanotubes, carbon fibre and carbon nanowires, are developed. Their unique physical properties (large surface area and high aspect ratio) offer promising capacity of  $> 372 \text{ mAh g}^{-1}$  [53, 54]. Additionally, two-dimensional

carbon, *i.e.* graphene, has a carbon hexagonal structure and is able to accommodate Li ions on both sides of every single layer, yielding a theoretical capacity of  $744 \text{ mAh g}^{-1}$  [55]. Furthermore, this capacity value can be further increased with the presence of structural defects, such as nanovoids, disorders and plane edges. These structural defects can serve as additional active sites to store Li ions and thus contribute to an improved capacity, as shown in Fig. 2-6 (a). Encouraged by the defect-enhanced theory, graphene with defects that were purposely produced by electron beam irradiation and low-temperature pyrolysis surprisingly exhibited  $1013\sim 1054 \text{ mAh g}^{-1}$  [56]. However, it is believed that the presence of structural defects has high chemical reactivity and tend to decompose the contacting electrolyte, leading to a thick SEI and a reduced first-cycle efficiency, as depicted in Fig. 2-6 (b) [57, 58]. In this thesis, high-quality graphene was synthesised using a microwave-assisted thermal reduction method and it had proved to possess less structural defects. It was used as electroactive materials in anode for LIBs and the electrochemical properties were evaluated in half cell, which will be discussed in detail below.

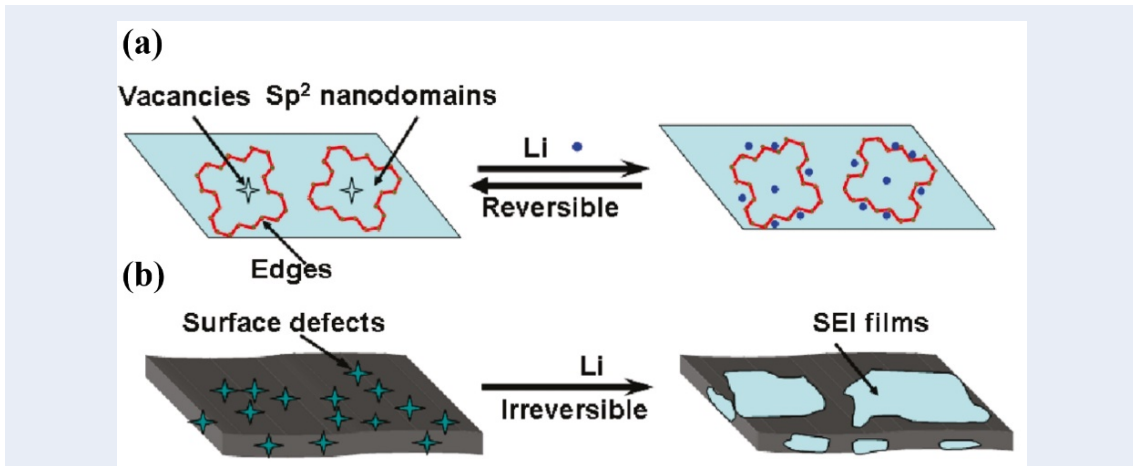


**Fig. 2-6.** (a) The presence of nanovoids on graphene permits extra lithium ions to be accommodated and released, and (b) the surface defects give a higher surface area and thus result in formation of substantial SEI [56].

### 2.1.3. Electrolyte

An electrolyte is made of a blend of organic carbonate solvents with Li salts dissolved. The existence of electrolyte is quite essential in battery as it serves as a medium to transport lithium ions between negative and positive electrodes upon charging/discharging. Therefore, an electrolyte with high ionic conductivity is preferable in efforts to alleviate the concentration polarisation as discussed above. The common Li-containing salts used in electrolyte include Lithium Perchlorate ( $\text{LiClO}_4$ ), Lithium Hexafluoroarsenate ( $\text{LiAsF}_6$ ), Lithium Trifluoromethanesulfonate ( $\text{LiTf}$ ), Lithium Trifluoromethanesulfonate ( $\text{LiCF}_3\text{SO}_3$ ), Lithium Tetrafluoroborate ( $\text{LiBF}_4$ ), and Lithium Hexafluorophosphate ( $\text{LiPF}_6$ ) [35]. Among them,  $\text{LiPF}_6$  is the most widely used Li-containing salt and overperforms the other Li-containing salts in terms of high ionic conductivity ( $> 10^{-3} \text{ S cm}^{-1}$ ), high lithium ion transference number ( $\sim 0.35$ ), promising thermal stability, and stable chemical stability [31]. Previously, aqueous electrolyte was used in some specific types of battery because it has higher conductivity than its non-aqueous peer. However, aqueous electrolyte is not suitable in LIBs with Li metal being anode because it is chemically reactive to Li metal and its derived products. Also, the high working potential of LIBs ( $> 3.0 \text{ V}$ ) will decompose the water in aqueous electrolyte.

Upon selecting proper electrolyte solvents to dissolve Li salts, carbonate solvents gain the priority because they have a high dielectric constant which is able to solvate lithium salt to a high concentration ( $> 1 \text{ M}$ ) [31]. Fig. 2-7 shows the commercially available organic solvents used in LIBs, along with their structures and physical properties. It is clearly seen that an appropriate solvent is typically assessed in terms of viscosity, dielectric constant, melting point and boiling point [35].

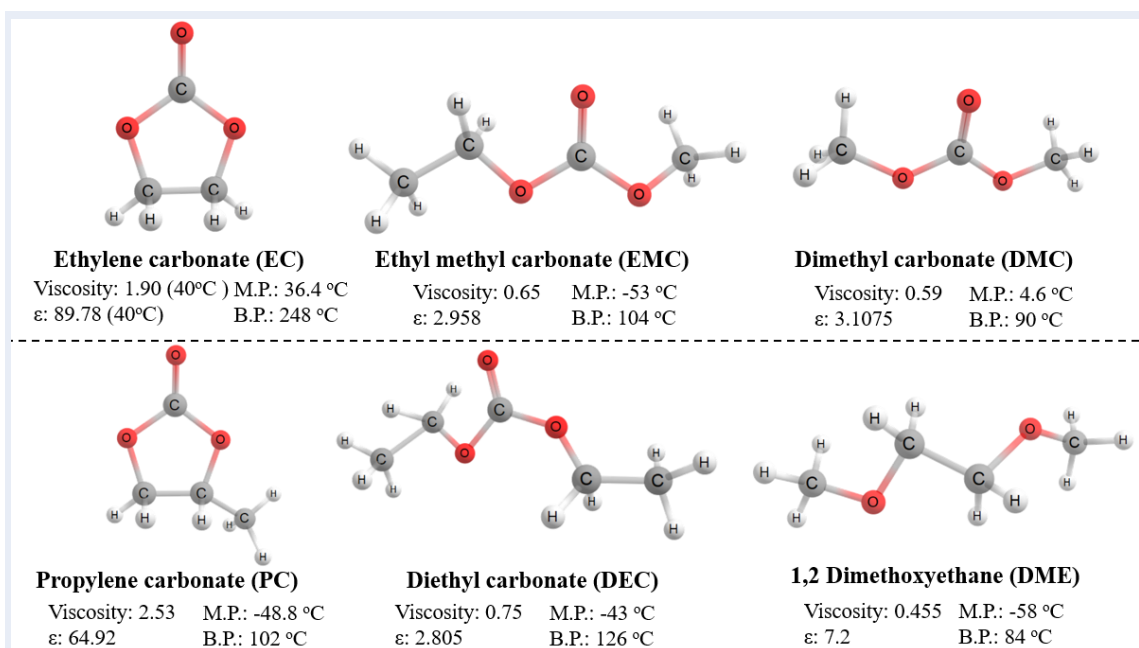


**Fig. 2-7.** Commonly used non-aqueous solvents for LIBs, along with their physical properties.  $\epsilon$ : Dielectric constant, M.P.: melting point, B. P.: Boiling point (The physical data were obtained from [31, 59, 60]).

The basic principle in selecting solvents for LIBs is low viscosity, high dielectric constant, low melting point and high boiling point which can give a highest ionic conductivity no matter at low temperature and high temperature. From this sense, the binary solvents of EC and PC were initially proposed in preference to others, but the high viscosity reduced the Li ion mobility. Additionally, it was reported that PC had a tendency to react with lithiated carbon-based materials because the curving chain structure of PC's reductive product is likely to form loose deposits with weak cohesion on the carbon particles [61]. Therefore, it resulted in graphite exfoliation and deteriorated the electrochemical properties, especially poor cycle life [31, 35]. Henceforth, in order to take advantage of extremely high dielectric constant and low capacity fade of EC, the PC is normally replaced by DME or DMC that have rather low viscosity. Even though the dielectric constants of DME and DMC are relatively low, the melting points are rather attractive. And they can be used to dissolve EC which is in solid state at ambient condition. However, the DME is not widely accepted since the SEI layer formed by reduction of DME with Li

metal is not stable, which may result in premature death of LIBs [35]. By varying the relative ratio between EC and DMC, one can obtain specific-purpose electrolyte to be used in different environment [62]. There is no universal electrolyte and the choice is dependent on the electrochemical system of interest. Therefore, the electrolyte of 1 *M* LiPF<sub>6</sub> dissolved in EC/DMC (50 vol%:50 vol%) which is the most common formulation in the community of LIBs, was used throughout this project.

In summary, a promising electrolyte should consider the following aspects:

- Wide electrochemical window ( $> 4.6$  V for most commercial LIBs)
- High ionic conductivity ( $> 10^{-4}$  S cm<sup>-1</sup>) and high transfer number to minimise concentration polarisation [63]
- Formation of stable SEI layer with suitable thickness
- Environmentally friendly and low cost
- Low safety concern



#### 2.1.4. Cathode

From the view of development of LIBs, MoS<sub>2</sub> was the first cathode used in commercial LIBs. In nature, the MoS<sub>2</sub> is abundant in the earth so as that the price is quite affordable. Moreover, the synthesis process of MoS<sub>2</sub> is facile, making the manufacturing process cost effective. Nevertheless, MoS<sub>2</sub> was quickly withdrawn from the market because the low chemical potential and low capacity, thereby giving a low energy density [31]. Afterwards, MoS<sub>2</sub> was substituted by intercalation-type cathode materials, such as titanium disulfide (TiS<sub>2</sub>). TiS<sub>2</sub> maintains a stable microstructure upon charging/discharging, thereby giving a stable voltage platform [27]. However, the high production cost of TiS<sub>2</sub> imposes a hurdle during commercialisation. Even so, the successful utilisation of intercalation-type cathode materials shed a light on investigating this group of material because it can deliver a promising capacity with an intact microstructure. Following that, other intercalation-type cathodes, chiefly lithium transition metal oxides, were developed for use in LIBs, including LiCoO<sub>2</sub>, LiMn<sub>2</sub>O<sub>4</sub>, and LiFePO<sub>4</sub>. This type of cathode materials exhibits high energy density as a result of both high working potential and high capacity, which are mainly ascribed to the highly oxidised Co<sup>3+/4+</sup>, Mn<sup>3+/4+</sup>, and Fe<sup>3+/4+</sup> redox couples [24]. The electrochemical properties of these three cathode materials and their derivatives are compared in Table 2-2. Among them, LiCoO<sub>2</sub> is more well-known than the other two due to the high practical capacity and high working potential. The other two are typically needed on the demand for higher safety and fast discharge as well as the cost is the main concern. Li-Co chemistry was first suggested as intercalation-type cathode in rechargeable LIBs by Mizushima and Goodenough *et al.* in 1980 [64]. Nevertheless, until 1991, the first successful commercialisation of LiCoO<sub>2</sub> was accomplished by SONY Corp. with its integration in classical LiCoO<sub>2</sub>/graphite battery system.

**Table 2-2.** Electrochemical properties of the common intercalation-type cathode compounds [65].

Framework	Compound	Specific capacity <sup>a</sup> (mAh g <sup>-1</sup> )	Average potential (V vs. Li <sup>0</sup> /Li <sup>+</sup> )
Layered	LiCoO <sub>2</sub>	272 (140)	4.2
	LiNi <sub>1/3</sub> Mn <sub>1/3</sub> Co <sub>1/3</sub> O <sub>2</sub>	272 (200)	4.0
Spinel	LiMn <sub>2</sub> O <sub>4</sub>	148 (120)	4.1
	LiMn <sub>3/2</sub> Ni <sub>1/2</sub> O <sub>4</sub>	148 (120)	4.7
Olivine	LiFePO <sub>4</sub>	170 (160)	3.45
	LiFe <sub>1/2</sub> Mn <sub>1/2</sub> PO <sub>4</sub>	170 (160)	3.4/4.1

<sup>a</sup> Value in parenthesis indicates the practical specific capacity of electrode.

LiCoO<sub>2</sub> exhibits a layered structure with the rhombohedral  $R\bar{3}m$  space group and is isostructural to  $\alpha$ -NaFeO<sub>2</sub> in which Co atoms take up octahedral  $3c$  sites and oxygen atoms surround the Co atoms with Li atoms occupying  $3b$  sites in the alternate layers [66, 67], as schematically illustrated in Fig. 2-8. The adjacent CoO<sub>2</sub> layers are separated by a Li layer in which the positively charged Li<sup>+</sup> ions effectively screen and stabilise the negatively charged CoO<sub>2</sub> skeletal structure [67]. It is clearly seen that Li ions can be freely intercalated/deintercalated in a 2-dimensional pathway between two strongly bonded CoO<sub>2</sub> slabs. However, with the deintercalation process of electrostatically stabilised Li<sup>+</sup> ions, the adjacent CoO<sub>2</sub> layers electrostatically repulse each other, leading to a volume swelling along  $c$  direction and volume shrinkage along  $a$  direction [67].

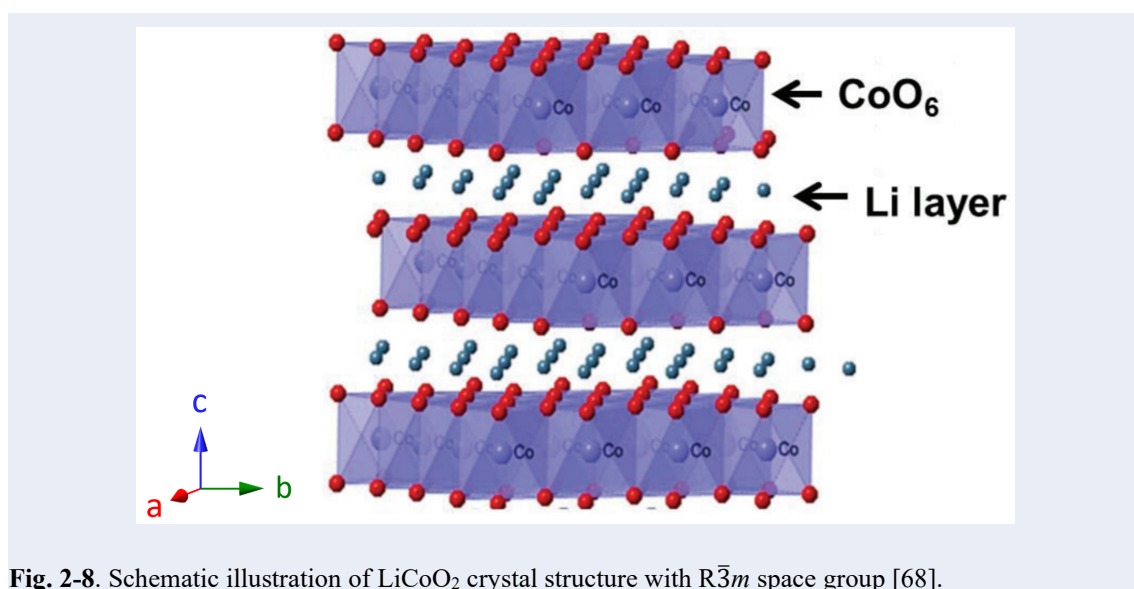


**Fig. 2-8.** Schematic illustration of LiCoO<sub>2</sub> crystal structure with  $R\bar{3}m$  space group [68].

With the desire to develop LiCoO<sub>2</sub> electrode with high volumetric energy density, two approaches have been generally employed, by (i) increasing the practical capacity and/or working voltage of LiCoO<sub>2</sub>, and/or (ii) decreasing the overall volume of electrode.

As calculated above, LiCoO<sub>2</sub> is able to provide a high theoretical capacity of 274 mAh g<sup>-1</sup> in the case where one Li ion is extracted from each unit of LiCoO<sub>2</sub> cell. However, with the removal of Li ions from the layered structure, the delithiated LiCoO<sub>2</sub> compound undergoes anisotropic changes along the *c* direction and *a* direction due to the increases in the electrostatic repulsion between O-Co-O sheets and cobalt oxidation, respectively [69]. This anisotropic host lattice changes accompanied with volume changes of LiCoO<sub>2</sub> structure generally result in ‘electrochemical grinding’ of the LiCoO<sub>2</sub> particles, thereby leading to the formation of micro-cracks and related structural instability [70]. Based on extensive studies on the relationship between practical capacity and structural stability, it has been accepted that Li<sub>x</sub>CoO<sub>2</sub> (0.5 < *x* < 1) can still maintain a stable microstructure over extending galvanostatic cycling, yielding a reversible capacity of only 140 mAh g<sup>-1</sup> at the corresponding voltage of 4.2 V [67, 71-75]. If the operating voltage is raised beyond 4.2 V, higher capacity (> 140 mAh g<sup>-1</sup>) can be achieved but it may bring about additional issues, such as larger crystallographic volume change induced by phase transition in LiCoO<sub>2</sub> and decomposition of carbonate-based electrolyte at the particle surface [76].

To mitigate the phase transition, the approach to coat LiCoO<sub>2</sub> particles with passivation layers, such as ZrO<sub>2</sub> [77], CeF<sub>3</sub> [78], Al<sub>2</sub>O<sub>3</sub> [79, 80], MgO [81] and ternary layer containing Li, Al, and F elements [82], has been widely adopted. These coated LiCoO<sub>2</sub> particles exhibited better electrochemical performances in terms of reduced capacity degradation when being operated up to 4.6 V. The high cut-off voltage was ascribed to the modification to the surface chemistry of the LiCoO<sub>2</sub> particles [81]. Despite that some

successes have been achieved for various oxides coating, the presence of the electrochemically inactive layer on  $\text{LiCoO}_2$  particles increases the overall volume of particles and therefore compromises the volumetric energy density of LIBs.

In order to improve the volumetric energy density of LIBs, the most effective way is to reduce the overall volume of electrode, including lowering the volume fraction of the inactive components and/or increasing the pack density of electrode. A close looking on the recipe of traditionally tape-cast  $\text{LiCoO}_2$  electrodes ( $\text{LiCoO}_2$  + polymeric binders + conductive fillers + metallic current collector) may readily lead to the awareness that the volumetric energy density of electrode could be greatly degraded by the increasing occupation of low-density battery accessories, such as polymeric binders, current collector, and even conductive fillers. It has been reported that the conventional calendered tape-cast electrode structure is consisted of < 50% electroactive materials loading by volume if the thickness of electrode goes down to 100  $\mu\text{m}$  or less [12, 83]. Henceforth, the removal of electrochemically inactive components, *i.e.*, conductive fillers, polymeric binders and current collector, would be an alternative strategy to effectively improve the volumetric capacity of LIBs.

Given that the electrical conductivity of  $\text{LiCoO}_2$  is relatively low ( $\sim 10^{-4} \text{ S m}^{-1}$ ) [84], the incorporation of conductive filler is essential. However, it is practical to employ conductive fillers with higher electrical conductivity, such as carbon nanotubes (CNTs) or graphene, in LIBs to reduce the dosage. They possess large surface area and distinct morphology, which enable to form an electrically conductive network at lower percolation content. Even though LCO electrode without the addition of conductive filler has been produced by taking advantage of its intrinsic semiconductor-metal structural transition (band gap  $E_g=2.7 \text{ eV}$  [85, 86]), the rate performance was inferior at high current

rate and it can be only used in niche application, such as microdevices where power density of LIBs is less concerned [11]. With regard to polymeric binder and metallic current collector, it has been reported that they can be completely removed away if LCO is produced in the form of bulk electrodes because high compactness of LCO electrode can guarantee the mechanical handling [11].

In addition to providing sufficient electrical conductivity and mechanical strength, a rational design of bulk LCO electrodes should consider the mobility of ionic species [87]. A bulk LCO electrode with too high density ( $> 90\%$  relative density) is generally not pursued because of the poor kinetics caused by high tortuosity and long ionic diffusion paths. Both of them impede the transportation of electrolyte ions, mainly solvated  $\text{Li}^+$  ions, across bulk electrodes and results in high concentration polarisation at tough charge/discharge rate [88, 89], which increases the proportion of electroactive materials that become inaccessible to Li ions during battery operation, especially the core part of electrode.

So far, bulk  $\text{LiCoO}_2$  electrodes have been produced by a wide range of techniques, such as radio frequency (RF) magnetron sputtering [90], screen printing [91], pulsed laser deposition [92, 93], electrostatic spray pyrolysis [94] and sol-gel [95]. Despite that the resultant bulk  $\text{LiCoO}_2$  electrodes can attain high volumetric energy density and promising rate performance, the electrode preparations generally require a layer of substrate or current collector to support the electrode, which apparently leads to a sacrifice in the volumetric energy density of individual electrode. Additionally, the thickness of  $\text{LiCoO}_2$  electrodes produced above were generally less than  $10\text{ }\mu\text{m}$ , which implied that a low electrode/current collector ratio per stack volume was required for LIBs with large-capacity design.

Fabricating thick electrodes with high areal loading of electroactive materials is believed to tactfully increase the energy density of LIBs on the fact that the energy capacity scales linearly with the electrode thickness for a given areal footprint [96]. To produce thicker bulk  $\text{LiCoO}_2$  electrodes, many other techniques have been also employed, including conventional sintering [11], co-extrusion [12] and rotating magnetic field method [13]. The resultant bulk  $\text{LiCoO}_2$  electrodes possessed the thickness of  $> 100 \mu\text{m}$ , and the current collector have been even eliminated on some occasions due to the sufficient mechanical strength of thick electrodes. However, their reversible capacity suffered from a rapid degradation at high current density due to the absence of conductive fillers in the LCO matrix which resulted in high resistance from point contacts between adjacent particles in the electrode. Their works suggested that it was not wise to pursue high volumetric energy density at the expense of rate performance.

As discussed above, the high tortuosity and ohmic polarisation may result in low accessible capacity of  $\text{LiCoO}_2$ . In order to reduce both effects, the electrode density should be carefully tuned and the electrical conductivity of bulk  $\text{LiCoO}_2$  electrode must be improved by introducing conductive fillers. In this project, we are going to introduce a novel densification technique, termed cold sintering process (CSP), to consolidate  $\text{LiCoO}_2$  composite cathode which contains minimum conductive fillers to simultaneously improve the volumetric energy density and rate performance of bulk LCO composite electrode.

## 2.2. Cold sintering process

### 2.2.1. CSP mechanism

Inspired by a hydrothermal assisted hot pressing technique in which ceramics with high density ( $> 90\%$  relative density) can be fabricated via combining hydrothermal synthesis with uniaxial pressing, an innovative CSP is recently proposed by C. A. Randal's group to densify ceramics at a much lower temperature and high uniaxial pressure with the aid of transient liquid [14-16]. The densification by CSP is typically achieved via a mediated dissolution-precipitation process in which an appropriate aqueous solution (*e.g.*, water, acid, or base) is incorporated to dissolve the sharp edges of ceramic particles under reduced processing temperatures (from ambient temperature to  $300\text{ }^{\circ}\text{C}$ ) and to assist the rearrangement of the particles to a compact configuration under high uniaxial pressure (from 100 to 500 MPa) [14, 97, 98]. Owing to the low processing temperatures used, CSP not only enables the densification of pure ceramics, but also the densification of ceramics/polymer composites in which both constituents show substantial dissimilar physical properties, like melting temperatures and thermal expansion coefficient, etc. This is typically not achieved in conventional high-temperature sintering. However, to enable the densification of composite, at least one constituent should be soluble to trigger the dissolving process. The detailed CSP mechanism can be elucidated in macroscopic and microscopic perspectives, as schematically shown in Fig. 2-9.

Macroscopically speaking, multiple stages can be identified in the course of CSP, including (i) particle compaction, (ii) dissolution of materials, (iii) hydrothermal crystal growth or formation of intermediate phases, and (iv) recrystallisation of intermediate phase, which are depicted in Fig. 2-9 (a) [99]. Initially, a liquid phase is introduced and

mixed with ceramic powders to obtain homogeneously lubricated particle surfaces. The presence of liquid phase on the particle surfaces would conduce to the subsequent particle rearrangement and dissolution of sharp edges of ceramic powders under the effect of external pressure. The dissolved shape edges, therefore, confer more interstitial spaces for surrounding particle sliding to achieve an initial compaction. Simultaneously, the liquid phase with dissolved species is “pushed” to fill up the pores among particles by the external pressure. Due to the pressure-induced interaction of liquid phase with particles, three possible mechanisms are proposed to account for the particle compaction and the improved mass transport, including (i) liquid-enhanced creep at the solid-solid interface, (ii) Marangoni flow at the liquid-liquid interface, and (iii) diffusiophoresis at the solid-liquid interface. It is accepted that the particle compaction arises from the combination of mechanical-chemical coupling effects and it plays a beneficial role in the subsequent particle densification process [99].

Next, the liquid phase which contains the dissolved species becomes supersaturated as the system temperature is raised right above the boiling point of the liquid to evaporate the liquid. In this case, the ceramics ensemble system has a high Gibbs free energy and is thermodynamically unfavourable. The Gibbs free energy tends to reduce by precipitation of the dissolved species in two routes: (i) direct precipitation on particle sites with lower surface energies, leading to the epitaxial crystal growth on the outer surfaces of particles and further Ostwald Ripening crystal growth; and (ii) the nucleation of amorphous phase on the grain boundaries when its nucleation rate exceeds that of the crystalline counterpart [99]. Even though the formation of amorphous phase is an undesired parasitic reaction, especially upon fast cooling, it can be overcome by re-crystallisation via a post-CSP thermal treatment, which will be further discussed in this chapter [99].



From the microscopic perspective, the dissolution-precipitation process is very identical to that in the macroscopic perspective. As illustrated in Fig. 2-9 (b), after the liquid phase is introduced on the particle surfaces, the ionic species and/or atomic clusters on the very outer surfaces of particles start to dissolve under an applied external pressure [98]. The dissolution effect becomes more significant on the surface sites with large curvature, such as sharp edges or protrusion, and high system temperature can enhance this process. Meanwhile, with the influence of capillary pressure, the liquid phase dissolved with ionic species and/or atomic clusters redistributes itself and precipitates on particles at sites away from stressed contact areas, which have least surface energies. Consequently, an amorphous phase is formed on the grain boundaries, but its presence is shown to hinder the grain boundary diffusion or mobility as well as inhibit the grain growth [98, 100].

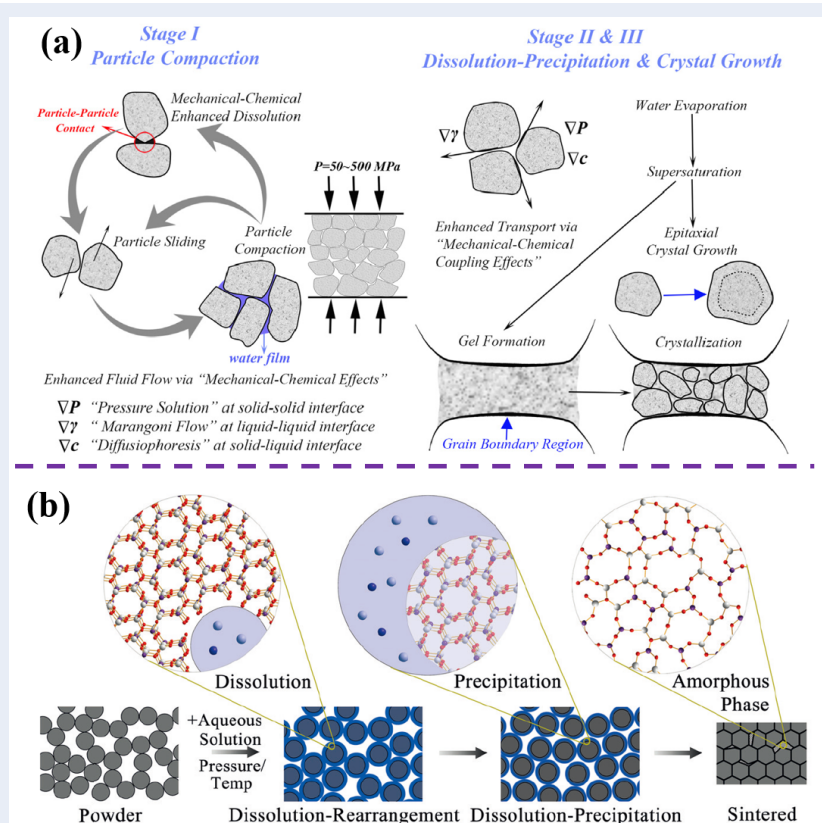


**Fig. 2-9.** Schematic representation of (a) the primary stages involved in the course of CSP at macroscopic level, and (b) the interaction of liquid phase with particles surfaces during CSP at microscopic level [99, 101].

As clearly seen from the above discussion, the CSP is apparently a multiple-step sintering process which mainly includes dissolution, precipitation, and grain growth. Randall's group attributed the successful densification of ceramics powders at reduced temperature to the smaller free energy barrier of each sub-step, as manifested in Fig. 2-10. In sharp contrast with huge energy barrier ( $\Delta G$ ) to overcome in conventional sintering, the requirement of free energy barriers reduction for each sub-step ( $\Delta g$ ) in CSP is far smaller and the sum is far smaller than  $\Delta G$  [99]. Therefore, they also deduced the natural formation of pearl and rock may adopt a CSP-like sintering process, disclosing the beauty of CSP [99].

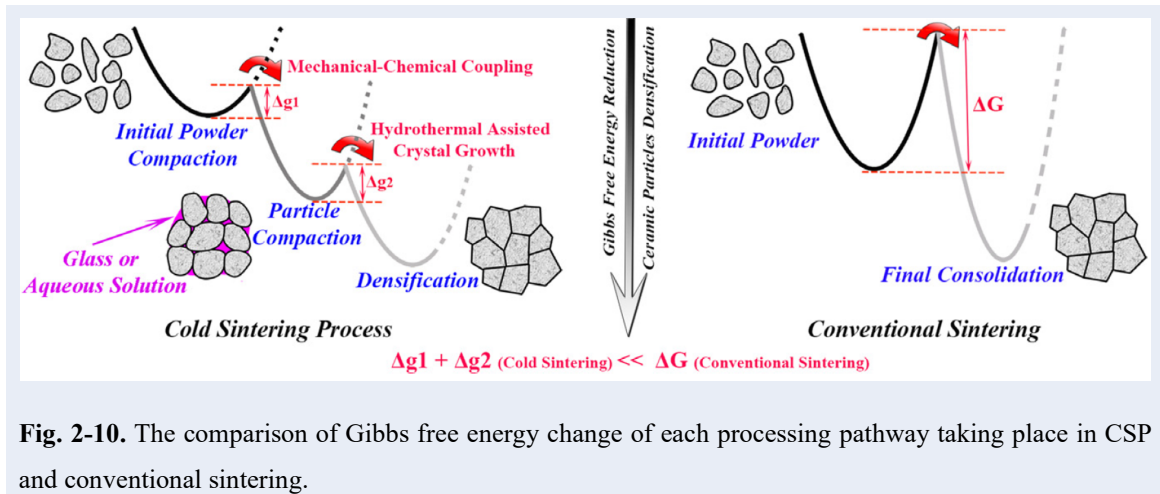


**Fig. 2-10.** The comparison of Gibbs free energy change of each processing pathway taking place in CSP and conventional sintering.

### 2.2.2. Processing variables of CSP

Apparently, the densification by CSP is strongly affected by many chemical and physical factors, such as CSP temperature/pressure/holding time, the selection of transient liquid solution, the physical characteristics of the starting materials, and post-CSP annealing treatment. Each factor has different densification mechanisms at different stages of CSP. Understanding of the influence of each factor plays an important role in elucidating CSP mechanism and therefore improving the performance of CSP-prepared materials.

#### 2.2.2.1. CSP temperature/pressure/holding time

It is easy to understand that the increases in CSP temperature/pressure can improve the solubility of dissolved species in liquid phase and enhance the liquid-enhanced creep effect at grain contact under stress [97]. On the other hand, the prolonged holding time can ensure (i) the establishment of equilibrium state of solid-liquid mixture phase at early stage of CSP; and (ii) the completed precipitation process of dissolved ionic species and/or atomic clusters on grain boundaries. This is why the effects of CSP temperature/pressure/holding time on densification of various ceramics powder were studied in numerous published papers with the intention to figure out the optimal CSP condition for the subsequent processing [18, 102-105].

#### 2.2.2.2. Selection of transient liquid solution

To achieve a high consolidation of ceramics powders, the choice of an appropriate transient liquid solution needs to be carefully made. The solubilities of various ceramic powders drastically vary, and their dissolution can be divided into two types: congruent and incongruent dissolution. With regard to congruent, the composition of the materials

stays at the same composition since the dissolved species have the same stoichiometry as the parent phase. Whereas incongruent dissolution leads in a solid that exhibited a changed stoichiometry/composition as compared to the parent phase. The dissolving process can be categorised into 3 different situations. (i) With regard to ceramic powders with high solubilities, such as hygroscopic compounds, the CSP is simply accomplished via a straightforward approach; (ii) As to ceramic powders with incongruent solubility, like  $\text{BaTiO}_3$  which has a passivation layer on the particle surfaces to hinder the dissolution process, a saturated liquid phase with required stoichiometric ratios is demanded [97]. (iii) In instance where ceramic powders have negligible solubility, the preparation of a liquid phase containing the corresponding chemical moieties is considered. In efforts to fabricate bulk  $\text{LiCoO}_2$  electrodes through CSP in this project, a judicious selection of basic aqueous  $\text{LiOH}$  solution with high mole concentration is considered because it has the mutual  $\text{Li}^+$  species. The 2 M  $\text{LiOH}$  transient liquid has been successfully reported to densify another Li-containing transition-metal cathode, *i.e.*  $\text{LiFePO}_4$  [18], which lights up the forward way to densify  $\text{LiCoO}_2$  electrodes. Following this inspiration, the 2 M  $\text{LiOH}$  transient liquid is determined to consolidate  $\text{LiCoO}_2$  electrodes for LIBs in this project.

#### 2.2.2.3. Physical characteristics of starting materials

Bear in mind that the solubility of  $\text{LiCoO}_2$  in 2 M  $\text{LiOH}$  solution is still far below the expectation. Therefore, the physical characteristics of starting  $\text{LiCoO}_2$  powder should be tuned, mainly in terms of surface area. By reducing the particle size of starting  $\text{LiCoO}_2$  powder, the surface area of  $\text{LiCoO}_2$  powder can be expected to drastically increase. The advantages brought about by the increased surface area of  $\text{LiCoO}_2$  powder can be cogently explained from 3 aspects. (i) From the thermodynamic perspective, the surface

Gibbs free energy is typically determined by  $\Delta G = A\bar{\gamma}$ , in which A is the surface area and  $\bar{\gamma}$  is the average interfacial energy.  $\bar{\gamma}$  is assumed to remain unchanged to any particles size. Therefore, after particle size reduction, more accessible surface areas are introduced to contact with liquid phase, which results in increases in solute content under applied pressure [97]; (ii) Kinetically speaking, the densification by CSP is largely determined by both dissolution process and mass transport process which in tandem significantly affect the subsequent precipitation process. Among them, the dissolution process is greatly promoted by the aforementioned liquid phase creep which only occurs at the contact points under stress. Henceforth, the increased surface areas by particle size reduction is believed to introduce more contact points between smaller particles, leading to a prominent liquid phase creep enhanced dissolution process. Additionally, the particles with smaller size generate more tiny channels in the ceramic ensemble, which substantially enhances the capillary effect to redistributes the liquid phase and thus enhances mass transport [97]; (iii) Particles with reduced size are able to assist in the particle compaction under applied pressure and the binding of large-size particles through diffusion bonding [97]. For this purpose, a high-energy planetary ball-milling process will be used in this project to reduce the particle size and increase the surface areas of LiCoO<sub>2</sub> powder for the sake of its simplicity, high efficiency, and process economy.

#### 2.2.2.4. Post-CSP annealing treatment

As discussed in Section 2.2.1, the ceramic ensemble fabricated by CSP has a common issue related to the presence of amorphous phase on the grain boundaries which deteriorate the desired properties of functional ceramics. The formation of this metastable phase is the resultant precipitation process of dissolve ionic species/clusters upon fast cooling and is recognised as a low-kinetic process of crystallisation. Therefore, a post-

CSP annealing treatment, at temperature lower than that is needed for the conventional sintering, is required to crystallise the amorphous phase to restore the properties of functional ceramics.

Since the invention of CSP by Randall's group in year 2017, a wide range of functional ceramics and ceramics-polymer composites have been prepared by CSP, including BaTiO<sub>3</sub> [16, 97], V<sub>2</sub>O<sub>5</sub> composite [106], Na<sub>3.256</sub>Mg<sub>0.128</sub>Zr<sub>1.872</sub>Si<sub>2</sub>PO<sub>12</sub> solid electrolyte [102], Li<sub>1.5</sub>Al<sub>0.5</sub>Ge<sub>1.5</sub>(PO<sub>4</sub>)<sub>3</sub> solid electrolyte [105], ZrO<sub>2</sub> and ZrO<sub>2</sub>-based composite [104, 107, 108]. However, their properties, such as electronic/ionic conductivities and dielectric properties, have been deteriorated by the amorphous by-product on the grain boundaries, but they have been restored via a post-CSP thermal treatment at a reduced temperature for a short period of time. As a further example, through a comparative study in which cold-sintered and conventionally dry-pressed Na<sub>3.256</sub>Mg<sub>0.128</sub>Zr<sub>1.872</sub>Si<sub>2</sub>PO<sub>12</sub> solid electrolytes were treated at the identical annealing condition, Leng *et al.* [102] concluded that the improvement in ionic conductivity for cold-sintered solid electrolyte was convincingly attributed to the re-crystallisation of the deleterious amorphous phase, whereas the improved ionic conductivity for dry-pressed solid electrolyte was very limited and was simply pertained to the increased contact surfaces amongst particles. Furthermore, as a direct result of post-annealing treatment, the density evolution of Na<sub>3.256</sub>Mg<sub>0.128</sub>Zr<sub>1.872</sub>Si<sub>2</sub>PO<sub>12</sub> solid electrolytes produced by CSP was found to increase because the structural transition from amorphous (glassy) phase to crystalline phase resulted in a more compacted atomic configuration and thus volume shrinkage. Another physical property restoration by post-CSP annealing treatment was reported by Jing *et al* [109]. The electrical conductivity of ZnO ceramics was as low as 0.0005 S cm<sup>-1</sup> after it was cold sintered at 250 °C and 350 MPa for 1 h. Interestingly, its electrical conductivity

was increased to  $16.4 \text{ S cm}^{-1}$  after ZnO was annealed at  $500^\circ\text{C}$  in argon atmosphere and the authors attributed the improvement in electrical conductivity to the increase in crystallinity of ZnO induced by post-CSP annealing treatment. The above two studies illuminated and provided insights that both ionic conductivity and electrical conductivity of CSP-prepared ceramics could be restored by post-CSP annealing treatment, which pave the way to improve the two most essential properties of high-performance electrode for use in LIBs.

Looking back to the fabrication of bulk  $\text{LiCoO}_2$  electrodes using RF magnetron sputtering [90], pulsed laser deposition [92, 93], electrostatic spray pyrolysis [94], and sol-gel [95] methods, it has been identified that the amorphous  $\text{LiCoO}_2$  was present and it resulted in deteriorative electrochemical properties of  $\text{LiCoO}_2$ . A thin-film  $\text{LiCoO}_2$  deposited by spray pyrolysis was exemplified for the electrochemical effect of amorphous  $\text{LiCoO}_2$  [110]. After being exposed to an annealing treatment, the electrical conductivity of amorphous  $\text{LiCoO}_2$  was substantially increased from  $2 \times 10^{-4} \text{ S cm}^{-1}$  to  $1.0 \text{ S cm}^{-1}$ . The slow-scan CV curves in Fig. 2-11 also showed distinctly different electrochemical behaviours with the broad anodic/cathodic peaks observed in amorphous  $\text{LiCoO}_2$  and the sharp anodic/cathodic peaks for well-crystallised  $\text{LiCoO}_2$ . Additionally, as compared to higher capacity retention of annealed  $\text{LiCoO}_2$ , amorphous  $\text{LiCoO}_2$  suffered from a rapid capacity loss in the first few cycles, as depicted in Fig. 2-12.

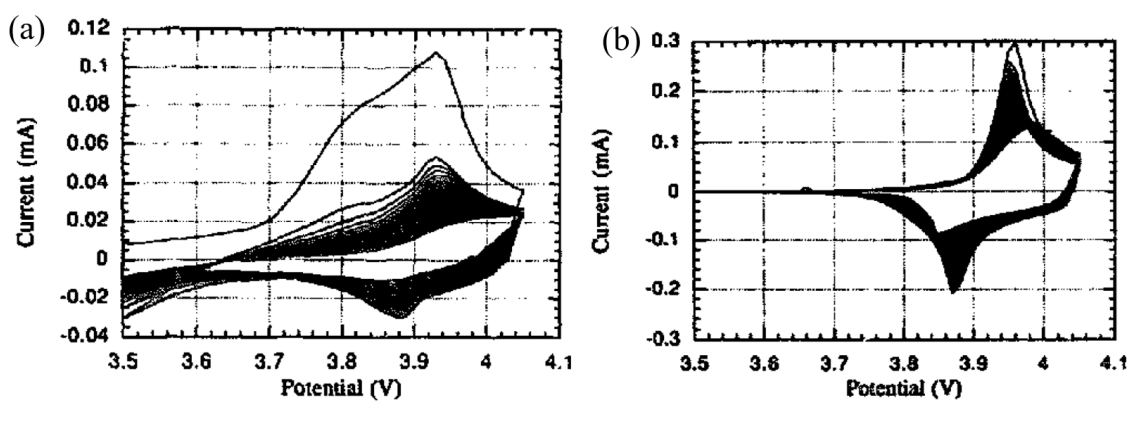


Fig. 2-11. CV curves of LiCoO<sub>2</sub> thin films prepared on Al/Au substrate by spray pyrolysis (a) without annealing and (b) with annealing [110].

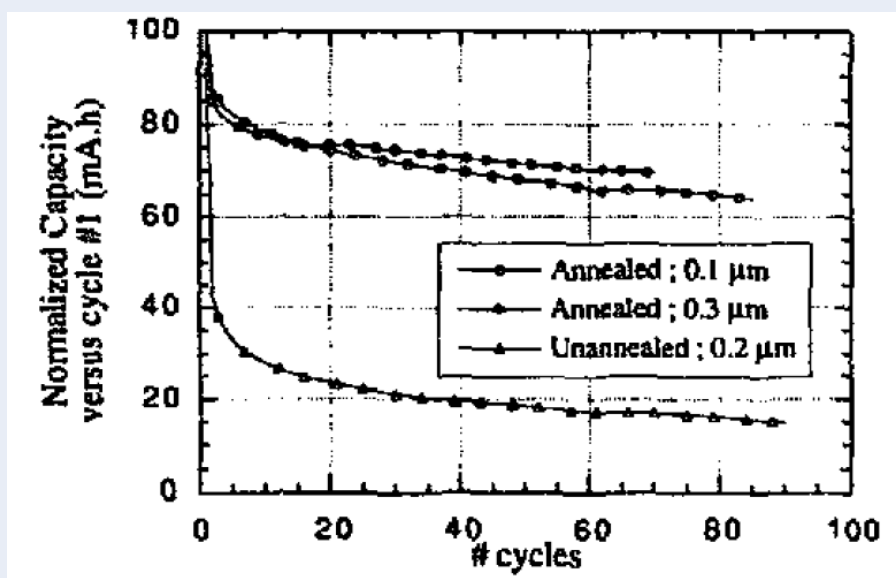


Fig. 2-12. The effect of annealing treatment on the evolution of accessible capacities of LiCoO<sub>2</sub> thin films prepared on Al/Au substrate by spray pyrolysis over extended cycles [110].

Based on the above discussion, it is essential to restore the electrochemical properties of thick LiCoO<sub>2</sub> electrodes produced by CSP via a post-annealing treatment. The effectiveness of crystallisation of amorphous LiCoO<sub>2</sub> phase is strongly dependent on the post-annealing treatment conditions, such as annealing temperature, annealing holding time, and annealing environment.

By combining transmission electron microscopy (TEM) and the corresponding selected



area electron diffraction (SAED) pattern of LiCoO<sub>2</sub> films annealed at 400-700 °C for 1 hour, Kim *et al.* found that the re-crystallisation process of amorphous LiCoO<sub>2</sub> phase started to happen at 400 °C and completed with larger crystallite at 500 °C [111]. With further raising the annealing temperature, the TEM images clearly showed the formation of intermittent voids between columnar crystallites at 600 °C and the intermittent voids became larger at 700 °C. The authors associated the formation of intermittent voids to the Kirkendall effect which described that intermittent voids were caused by different interdiffusion rates [111]. This study indicated that annealing treatment at extremely high temperature was not necessary because it may result in particle coarsening and other side effects, like formation of intermittent voids and inter-diffusion of species if metal substrates are used.

The annealing environment also plays a significant effect on the re-crystallisation of amorphous LiCoO<sub>2</sub> phase and its final electrochemical properties. LiCoO<sub>2</sub> films produced by RF magnetron sputtering were annealed at 650-900 °C for 30 min under an Ar or O<sub>2</sub> environments [112]. Through a systematic electrochemical characterisation, it is intriguing to find that the LiCoO<sub>2</sub> films annealed in O<sub>2</sub> ambient outperformed those annealed in Ar ambient, which was ascribed to the suppressed outdiffusion of oxygen from the LiCoO<sub>2</sub> lattice at a high oxygen vapour pressure induced by O<sub>2</sub> annealing environments [112].

A literature survey was also conducted to find that the annealing temperature used to eliminate amorphous LiCoO<sub>2</sub> phase ranged from 400 to 900 °C [111-115] for a timespan in the range of 540 seconds - 4 hours [110, 113, 114, 116, 117], which showed an extraordinary divergence. The determination of appropriate annealing conditions, *i.e.*, temperature, holding time and gas ambient, ought to be made based on the real

experimental condition, such as the decomposition temperature of secondary phase in the composite, the quantity of amorphous  $\text{LiCoO}_2$  phase, the process leading to the formation of amorphous  $\text{LiCoO}_2$  phase, and the particle size of  $\text{LiCoO}_2$  crystallites, *etc.*

### 2.2.3. CSP application for LIBs

To date, CSP has been successfully utilised to fabricate dense ceramics for the applications for LIBs, such as solid-state electrolytes [102, 105, 118-120] and intercalation-type cathode [17, 18, 106]. Among them, solid-state electrolytes have garnered enormous attentions, such as  $\text{Li}_{1.5}\text{Al}_{0.5}\text{Ge}_{1.5}(\text{PO}_4)_3$  [105],  $x\text{Li}_2\text{S} + (1-x)\text{P}_2\text{S}_5$  [119],  $\text{Na}_{3.4}\text{Sc}_{0.4}\text{Zr}_{1.6}\text{Si}_2\text{PO}_{12}$  [120], and  $\text{CsH}_2\text{PO}_4$  [118]. Little efforts, however, have been devoted to cathodes produced by CSP.

Very recently,  $\text{V}_2\text{O}_5$  which is a typical layered cathode material affordable for 294 mAh  $\text{g}^{-1}$  with 2  $\text{Li}^+$  ions intercalated/deintercalated in/from per formula unit [121], has been cold sintered at 120 °C and 350 MPa for 20 min [106]. With the assistance of TEM characterisation, the formation of amorphous  $\text{V}_2\text{O}_5$  phase was noticed on the grain boundaries, which delivered an electrical conductivity of only  $4.8 \times 10^{-3} \text{ S cm}^{-1}$ . Instead of increasing the electrical conductivity by post-CSP annealing treatment, the researchers improved the electrical conductivity of  $\text{V}_2\text{O}_5$  pellets to  $10^{-3} \sim 10^{-2} \text{ S cm}^{-1}$  by introducing a minor amount of conductive polymer PEDOT:PSS. The improvement in electrical conductivity promoted itself to potential application of  $\text{V}_2\text{O}_5$ -PEDOT:PSS composite for LIBs. Nevertheless, in their following publication, they studied the temperature dependence of electrical conductivity of 97vol%  $\text{V}_2\text{O}_5$  - 3vol% PEDOT:PSS and suggested it to be used in negative temperature coefficient devices [122]. But their works still highlighted the merit of CSP as a new route to densify composite containing constituents with large melting point gaps.

In another pioneering study, CSP was extended to consolidate  $\text{LiFePO}_4$  composite cathode for use in LIBs. The pure  $\text{LiFePO}_4$  was firstly homogenised with basic  $\text{LiOH}$

transient liquid to enhance the dissolution process in a high pH environment. Afterwards, the mixture was densified at 240 °C for 30 min at different applied pressures (30-750 MPa). A relative density of 85% ( $3.04 \text{ g cm}^{-3}$ ) was achieved for  $\text{LiFePO}_4$  composite cathode at 750 MPa. Albeit that no secondary phase could be identified in XRD spectrum of cold-sintered  $\text{LiFePO}_4$  pellets in Fig. 2-13 (a), the TEM images in Fig. 2-13 (b) distinctly showed the presence of amorphous  $\text{LiFePO}_4$  phase on the grain boundaries due to the small amount of amorphous  $\text{LiFePO}_4$  phase formed during CSP. Following that, a mixture of 80 wt%  $\text{LiFePO}_4$ , 10 wt% PVdF, and 10 wt% conductive carbon was cold sintered using the similar CSP condition and a composite pellet with the 89% relative density ( $2.70 \text{ g cm}^{-3}$ ) was obtained. This value was much greater than that obtained by conventional tape-casting method ( $1.90 \text{ g cm}^{-3}$ ), showing the CSP feasibility to densify ternary composite. As shown in Fig. 2-13 (c-e), cyclic voltammetry (CV) of  $\text{LiFePO}_4$  composite cathode produced by CSP was characterised with a pair of symmetrical redox peaks at  $\sim 3.45 \text{ V vs Li}^+/\text{Li}$ , indicating the excellent reversibility of electrochemical  $\text{Fe}^{3+/4+}$  reactions. The cold-sintered  $\text{LiFePO}_4$  composite cathode afforded a gravimetric capacity of  $155 \text{ mAh g}^{-1}$  and the corresponding volumetric capacity of  $340 \text{ mAh cm}^{-3}$  at 0.1 C, which was ascribed to the highly dense ceramic structure by CSP. Additionally, the thick  $\text{LiFePO}_4$  composite cathode displayed stable voltage plateaus up to 1 C and afforded a reasonable capacity retention of 87% after 40 cycles.

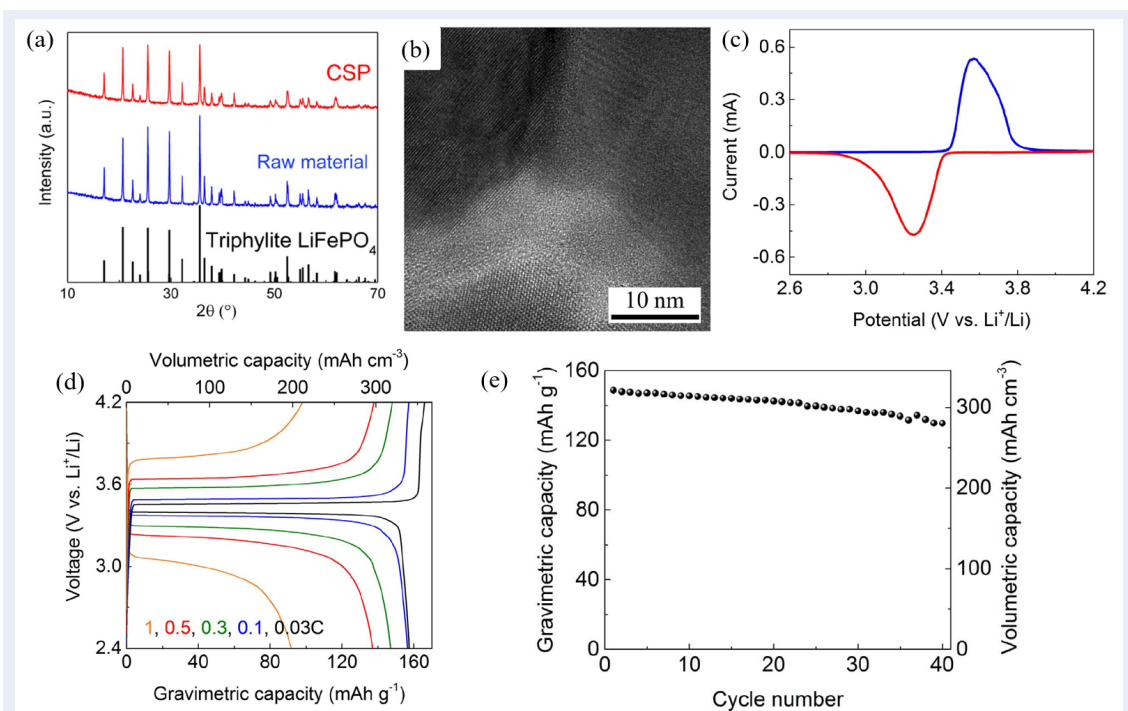


**Fig. 2-13.** (a) XRD spectra of  $\text{LiFePO}_4$  before and after CSP, (b) TEM images of amorphous  $\text{LiFePO}_4$  phase, (c-e) electrochemical properties of  $\text{LiFePO}_4$  composite cathode.

In the subsequent publication, the author attempted to improve the volumetric capacity of cold-sintered  $\text{LiFePO}_4$  composite cathode by removing the electrochemically inactive binder and substituting carbon black with less amount (6 wt% relative to the mass of  $\text{LiFePO}_4$ ) of carbon nanofiber which has higher electrical conductivity and distinct long-chain morphology [17]. After being humidified with the tape-casted cathode tape with steam, the densification was performed for the cathode tape on Al substrate at 180  $^\circ\text{C}$  and 240 MPa for only 10 min using CSP. Consequently, a dense cathode with the relative density of  $\sim 70\%$  ( $2.42 \text{ g cm}^{-3}$ ) and low porosity was obtained. Similarly, a minor amount of amorphous  $\text{LiFePO}_4$  phase was observed on the grain boundaries in Fig. 2-14 (a), which was a typical characteristic for ceramic ensemble produced by CSP. As compared with the previously cold-sintered  $\text{LiFePO}_4$  composite cathode which contained carbon black and polymer binder, the electrochemical characterisation in this study showed enhanced electrochemical figures of merit, as shown in Fig. 2-14 (b-d). More specifically,

the LiFePO<sub>4</sub> composite cathode offered an identical gravimetric capacity of 154 mAh g<sup>-1</sup> at 0.1 C, but the corresponding volumetric capacity was raised to 373 mAh cm<sup>-3</sup>, which was due to the significant change in cathode formulation. Even at high charge/discharge rate of 10 C, a high gravimetric and volumetric capacity of 102 mAh g<sup>-1</sup> and 247 mAh cm<sup>-3</sup> were retained with a flat voltage plateau [17]. Moreover, 90% and 93% of initial capacities were maintained at 1 C and 10 C, receptively, after 100 cycles. It should be noted, however, that the Al current collector was still used in this study but was not taken into consideration for the calculation of volumetric capacity, which artificially “increased” the volumetric capacity. Actually, in a commercial LIBs with full package, every single component should be incorporated in the calculation to give a reliable evaluation.

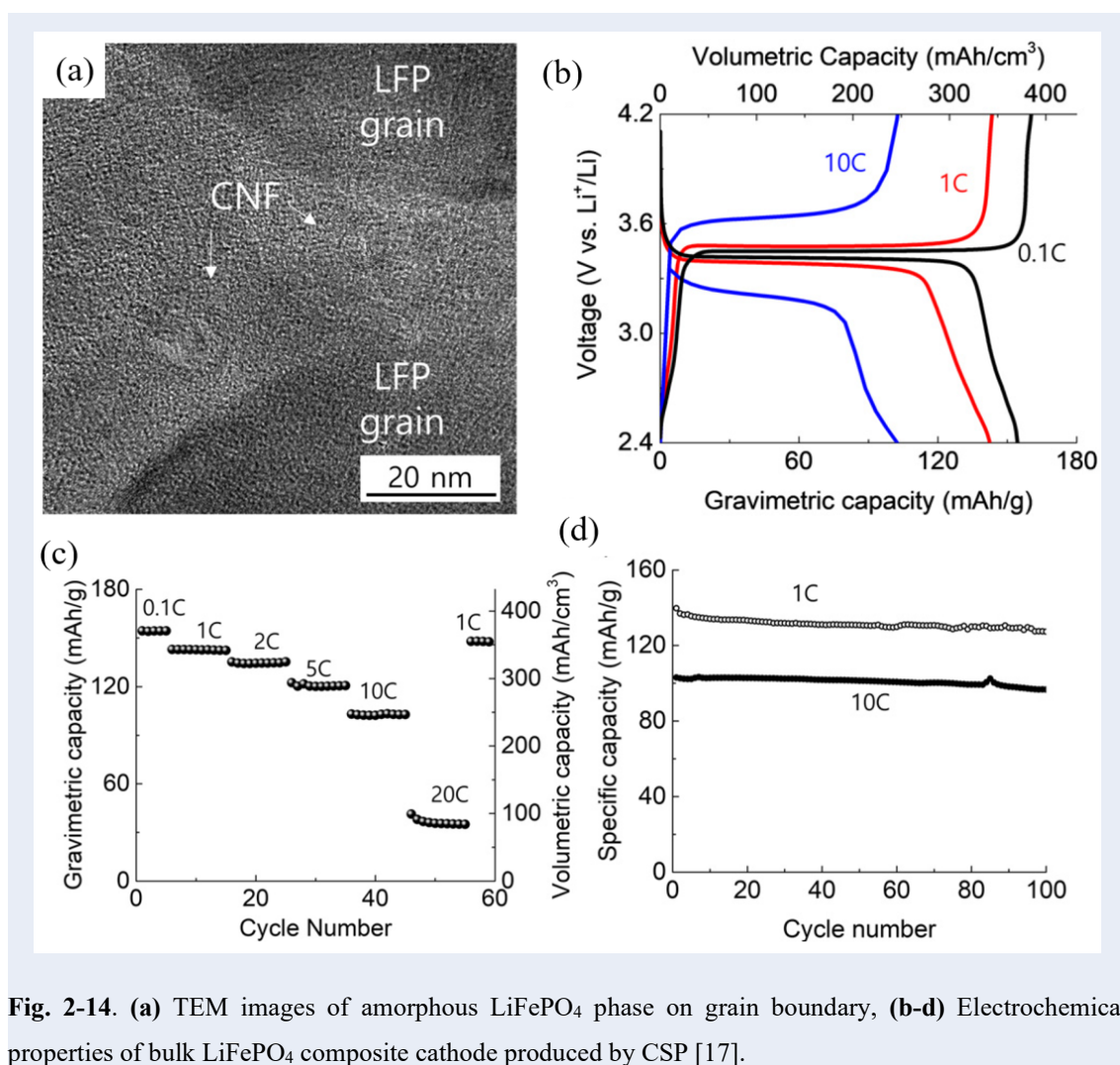


**Fig. 2-14.** (a) TEM images of amorphous LiFePO<sub>4</sub> phase on grain boundary, (b-d) Electrochemical properties of bulk LiFePO<sub>4</sub> composite cathode produced by CSP [17].

Through a comprehensive survey, to our best knowledge, the densification of LCO using CSP and its application for LIBs have not yet been reported, which leaves a research gap to study the feasibility to fabricate thick  $\text{LiCoO}_2$  composite cathode which contains least amount of conductive filler with total absence of polymer binder and current collector. In order to maximise the volumetric capacity/energy density of thick  $\text{LiCoO}_2$  composite cathode, the properties of conductive filler are critical to guarantee the success. As above mentioned, graphene and CNTs are strong candidates in this case due to their high electrical conductivity and distinct morphological character. However, the production of high-quality graphene, *e.g.*, large flake size, less structural defects, and less oxygen functional groups, still faces many specific challenges. Next, a simple and effective approach using microwave localised heating effect is reviewed, along with the underlying mechanisms involved in deoxygenation of oxygen functional groups and the formation of hot-spot/arcing. Finally, the unique effects of CNTs and graphene in advanced lithium batteries are discussed, along with their recent research progress.

## **2.3. Microwave-assisted reduction of graphene oxide**

### **2.3.1. Introduction to graphene**

Graphene is a 2D form of  $sp^2$ -hybridised carbons that are densely arranged in hexagonal (honeycomb) crystallographic structure with a distance of 0.142 nm between neighbouring carbon atoms. This hexagonal structure belongs to one of the five 2-D Bravais lattices [123]. It is another allotrope of carbon materials in atomic scale relative to fullerenes (0D), carbon nanotubes (1D), and graphite (3D) or charcoal (3D), as shown in Fig. 2-15 [124]. Even though graphite was discovered and used for decades, it was unlikely known to people until Bernal [125] revealed the lamellar structure by using X-ray diffraction (XRD) technique. Since then, significant research efforts to isolate single-layer graphite (graphene) by either mechanical methods or chemical methods were made, and many characterisation techniques were employed to study the tiny basic structure of graphite. Some groups proposed to mechanically isolate bulky lamellar-structure graphite with the ultimate aim of achieving mono-layer graphene with “perfect” electronic structure and thus its intrinsic properties. Unfortunately, multilayer graphene with less than 20 layers were not mechanically obtained until 2004 when two scientists, Andre Geim and Kostya Novoselov from The University of Manchester, successfully “pulled” mono-layer graphene out of bulky graphite using Scotch tape, which was later referred to as micromechanical cleavage or the Scotch tape technique [126, 127]. Although it was thought to be an extremely labour-intensive and unreliable method, it was the first time to mechanically extract mono-layer graphene from natural graphite. The mechanically exfoliated mono-layer graphene is shown to exhibit amazing mechanical properties and chemical properties, which then sparks the “the gold rush” of graphene world.



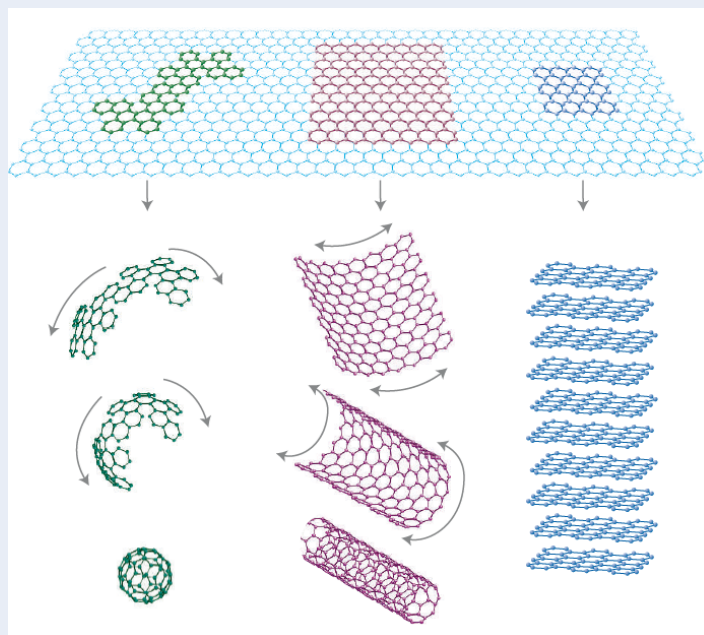


**Fig. 2-15.** Schematic representation of graphitic structure in the forms of fullerenes, carbon nanotubes, and graphite [124].

The 2D graphene which was ever predicted to be impossible to exist in the free state by scientists, came as a surprise to the world with its many properties superior than the other allotropes of carbon families, such as massive specific surface area [128, 129], highly flexible but mechanically robust structure [130, 131], optical transmittance (97.7%) [132], exceptional electrical conductivity ( $\sim 10^4$ - $10^5$  S m<sup>-1</sup>) [124, 133, 134], superior thermal conductivity ( $\approx 3\,000$  W mK<sup>-1</sup> at room temperature [135]), and chemical reactivity *etc.* Certainly, each of these promising properties is able to lead to a profound revolution in industries and engineering, such as energy generation/storage devices [136-138], catalysts [139], electronic devices [140, 141], composite materials with high specific strength [142], *etc.* Definitely, the aforementioned appealing properties of graphene can be explained from the viewpoint of its unique microstructure and electronic structure.

Monolayer graphene features huge theoretical specific surface area (SSA) of  $\sim 2\,630$  m<sup>2</sup> g<sup>-1</sup> [128, 129]. This value approaches that of activated carbon ( $\approx 3\,000$  m<sup>2</sup> g<sup>-1</sup>) which is

generally used, with varying successes, as conductive filler for LIBs/SIBs. It, therefore, indicates that graphene can be a potential candidate to replace the currently used activated carbon in energy storage devices from the perspective of SSA. However, the theoretical specific surface area of  $2\,630\text{ m}^2\text{ g}^{-1}$  is of difficulty to achieve in practice because it is highly restrained by processing methods. For instance, graphene produced from reduced graphene oxides (rGO) by hydrazine reduction only exhibited  $320\text{ m}^2\text{ g}^{-1}$  [143]. SSA of graphene was reported to be  $463\text{ m}^2\text{ g}^{-1}$  for microwave assisted exfoliation method [144],  $400\text{ m}^2\text{ g}^{-1}$  for low-temperature exfoliation [145] and  $700\text{ m}^2\text{ g}^{-1}$  for high-temperature exfoliation [146]. The values mentioned above were far lower than the theoretical value, which is chiefly attributed to (i) The oxygen functional groups on basal plane are extremely difficult to be completely eliminated; and (ii) The tendency of re-stacking of graphene flakes after processing. Compared with carbon black with small SSA, graphene with a high surface-to-volume ratio is always desirable in the LIB application since it can provide more contact points with electroactive materials, such as  $\text{LiCoO}_2$ , thereby improving the electrical conductivity of electrode.

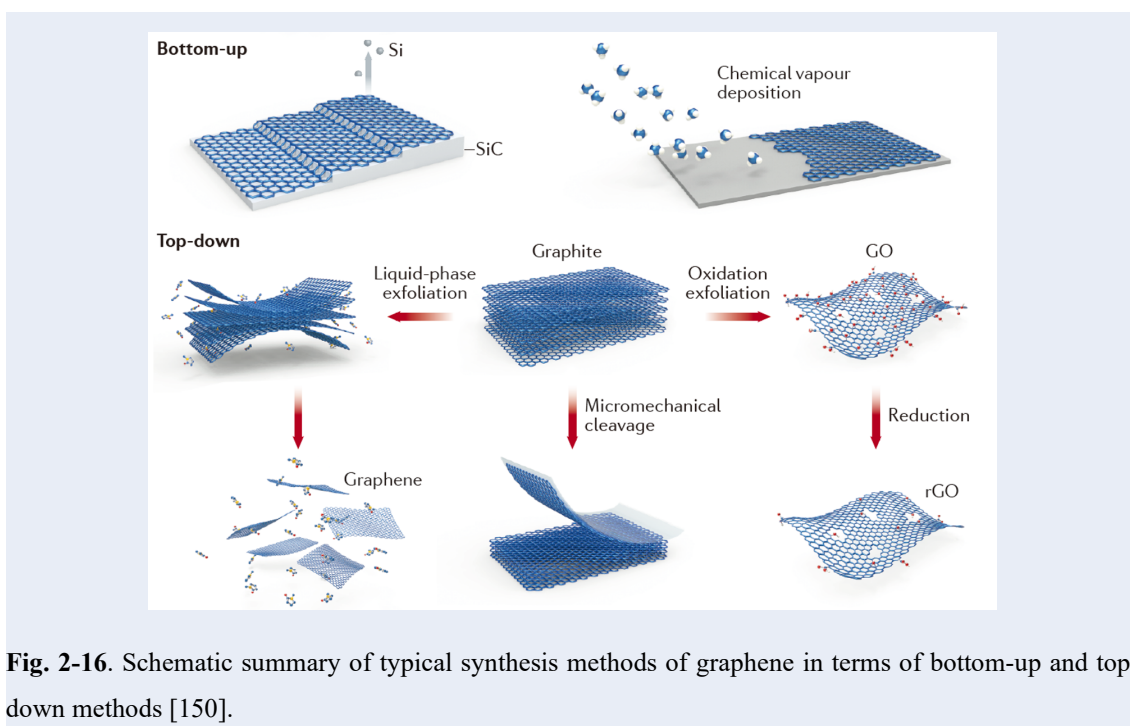
In addition, the high carrier mobility ( $\approx 15\,000\text{ cm}^2\text{ V}^{-1}\text{ s}^{-1}$  at 300 K and  $\approx 60\,000\text{ cm}^2\text{ V}^{-1}\text{ s}^{-1}$  at 4 K [127]) and the high charge carrier concentration ( $n = 10^{12}\text{ cm}^{-2}$  [147]) of graphene results in an exceptional electrical conductivity ( $\sim 2\,000\text{ S m}^{-1}$  [148]), which is very appealing to energy storage devices. Through a deep understanding of graphene's electronic structure, the high electron mobility originates primarily from the formation of  $\pi$ -bond. Each carbon atom located in graphene has 4 electrons in the outer orbital with 3 of them hybridizing in the form of  $\text{sp}^2$  hybridization, leaving one in  $\text{P}_z$  direction moving freely to constitute “Electron Sea” above and below the graphene sheet [149]. The high electrical conductivity, or more specifically the high carrier mobility, is a very essential

characteristic for microwave-induced heating effect, which will be discussed in Section 2.3.4.

Apart from the abovementioned SSA and electrical conductivity, the other properties of graphene endow it to be used for LIBs. The robust but flexible graphitic grid paves the way for wrapping electrode particles, which thus prevents electrode particles from disintegrating from current collector. The superior thermal stability provides its use in harsh environments. The chemical reactivity provides reaction sites with heterogenous atoms or oxygen functional groups, which can tune the electronic structure and the bandgap of graphene for specific LIB application.

### 2.3.2. Graphene production methods

Attracted by the outstanding properties of graphene, many scientists and engineers have come up with a number of production methods to produce high-quality graphene. However, the efficient mass production of graphene with less structural defects and large lateral dimensions is still remaining a grand challenge to research community and industry. To date, the proposed production methods can be briefly categorised into two groups, either as bottom-up routes or top-down routes, as schematically shown in Fig. 2-16 [150].



Generally speaking, the bottom-up routes are a carbon crosslinking process in which basic molecular units are built up on a metal substrate or on the previously formed carbon layers in a 2D carbon network. The most representative bottom-up routes are epitaxial growth on SiC and chemical vapour deposition (CVD), which are, currently, most widely used in laboratories because they can produce high-quality graphene with single layer, large size, and less defects. During CVD process,  $H_2/CH_4$  gas mixture, which serves as

carbonaceous precursor, is supplied into the high-temperature reactor wherein a transition metal substrate (Ni [151] or Cu [152]) is placed. Once the gas mixture contacts the hot substrate surface (normally 900-1000 °C), it is catalytically decomposed to radical species which have high chemical reactivity and tend to form single-layer graphene and multiple-layer graphene with virtually perfect hexagonal microstructure. It is, however, not suitable to be adopted in industry owing to the high capital cost, critical treatment conditions, and low production yield [153].

Alternatively, the top-down routes typically involve mechanical exfoliation process of graphite or chemical/thermal reduction process of initially oxidised graphitic precursors to fabricate graphene. The former is generally performed without participation of chemical reactions. The representative routes includes the birth-of-graphene Scotch tape, ball milling [154], ultrasonication [155], fluid dynamics [156], and supercritical fluid [157] methods, *etc.* Nevertheless, the latter is performed with participation of chemical reactions. Chemical oxidation reactions are first required to produce adequate large-size functional groups on the periphery of graphitic planes to expand graphene interspacing and reduce the Van der Waal force, which can lead to the efficient exfoliation of graphene oxide (GO) sheets. Following that, a chemical/thermal reduction process is needed to remove as much the chemically derived functional groups and structural disorders as possible. In contrast with CVD, the production method by chemically/thermally reducing GO exhibits two admirable advantages: (i) It is a cost-effective and high-yield strategy to fabricate graphene from extremely cheap raw graphite without any specialised equipment; and (ii) The presence of oxygen-containing polar functional groups endows GO with the high hydrophilicity, which enables to form stable aqueous suspension by simple mixing or sonication processes, both of which are significant for massive production. The

oxidation of graphite process and reduction of GO process will be discussed next with more details.

GO represents an classical precursor for the fabrication of graphene and is predominantly produced via a strategy proposed by Hummers in year 1958, in which pristine graphite was rigorously oxidised in concentrated oxidant mixtures of  $\text{H}_2\text{SO}_4$ ,  $\text{NaNO}_3$  and  $\text{KMnO}_4$  [158]. The layered structure can still be retained after oxidation process, but the colour becomes lighter than pristine graphite due to the disrupted electronic conjugation network by oxidation treatment [159]. Although the Hummers method has been modified in terms of different acid species, concentrations, and temperatures, the main oxidation mechanism still remains the same and they are all termed as modified Hummers methods. Albeit that the synthesis method of GO has been known for more than 50 years, the universal chemical composition of GO still remains unclear since the oxidation process is complicated and is highly dependent on the participation of oxidation agents and oxidation time/temperature. Owing to the amorphous nature and the complexity of GO, the most accepted structural model of GO was revised by Lerf and Kilnowski, in which they anticipated that only hydroxyl and epoxy functional groups locate at carbon basal plane, while hydroxyl, epoxy and carboxyl functional groups can decorate along the sheet edges, as shown in Fig. 2-17 [160].

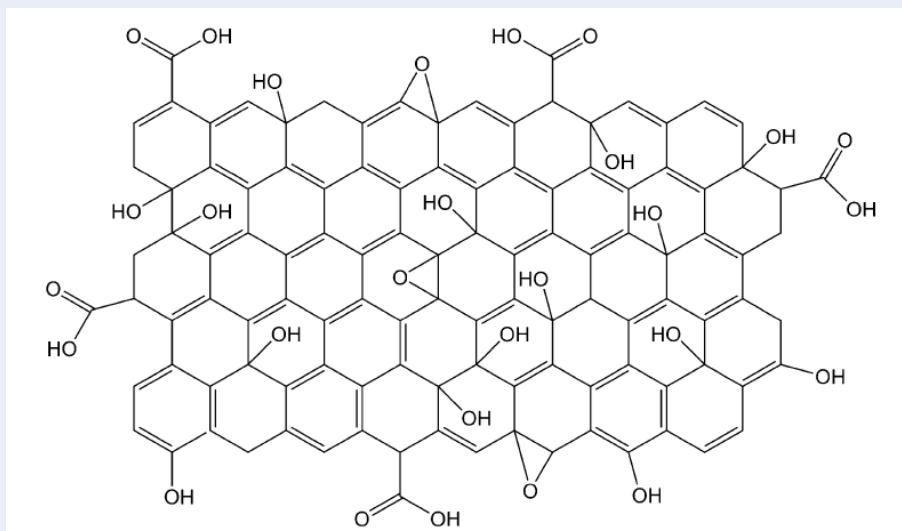


**Fig. 2-17.** Schematic illustration of Lerf-Klinowski model of GO with the presence of oxygen-containing functional groups on carbon basal plane and along plane edges [160]

Since the outstanding graphene properties, especially the electrical conductivity, are closely related to its perfect crystallographic lattice and long-range carbon conjugated microstructure, the GO is usually reduced using chemical reductants to restore the carbon microstructure, such as hydrazine [161],  $\text{NaBH}_4$  [162] and hydroiodic acid [163], *etc.* The chemical reduction process of GO is, however, generally slow. The resultant rGO also contains high-concentration functional groups, disordered graphitic regions and low carbon-to-oxygen atomic ratio (C/O), which distort the hexagonal lattice, change the conjugated network and consequently affect the electrical conductivity of rGO. More specifically, GO has been experimentally proven to be electrically insulated due to the disrupted carbon microstructure. But it becomes electrically conductive again once the functional groups coverage can reach below 25% of carbon planes, corresponding to 60% coverage of  $\text{sp}^2$  carbon bonding, which was computationally simulated by Boukhvalov *et al* [164]. Notably, rGO without any functional groups has not been experimentally obtained so far, which agrees with theoretical calculation that the reduction of GO is relatively easy from 75% to 6.25% coverage (C:O ratio = 16:1) but further reduction

seems to be rather difficult [164].

Even though chemical reduction of GO is accompanied with many shortcomings which are difficult to resolve and the quality of rGO varies from experiment to experiment, it is currently the predominant massive production method to prepare graphene. In order to remove more functional groups and heal structural defects to restore the graphene microstructure, considerable efforts have been expended to thermal reduction of GO, including conventional thermal annealing, microwave-assisted reduction [137] and photon-assisted reduction [165]. Among them, conventional thermal annealing is regarded to be promising for large scale production. However, the prolonged high-temperature annealing process not only increases the energy bill but also leads to fragmentation of graphene [166]. Comparatively, microwave-assisted reduction of GO is more attractive on the grounds that it simultaneously combines the advantages of high-yield production capability of GO by Hummer's method and super-fast volumetric reduction of GO by microwave Maxwell-Wagner effect [167].

### 2.3.3. Microwave-assisted reduction of GO

Microwave irradiation relies on the mechanism in which a material absorbs electromagnetic energy in the range of frequency from 300 MHz to 30 GHz, which correspond to the wavelength from 1 m to 0.01 m [168]. Amongst this wide frequency range, the operating frequencies of 915 MHz and 2.45 GHz are allotted by an international commission for industrial microwave ovens while only 2.45 (+/-0.05) GHz (12.25 cm wavelength) is prevalently adopted for domestic or lab microwave ovens [167, 169]. Due to the low energy of each photon, the microwave irradiation does not trigger the chemical reactions by breaking down the chemical bonds but actually accelerates the rotation of



dipoles and motivates the translation motion of free/bound charges in microwave-receptive materials without changing the molecular structure [170]. With regard to 2.45 GHz microwave irradiation, the electric field oscillates  $4.9 \times 10^9$  times within one second with the oscillation timescale approaching the relaxation time of permanent dipoles [169]. Therefore, the permanently polarised dipoles and charges pronouncedly couple with the electric field component of the microwaves by realigning themselves at a high speed. The vigorous dipole rotations result in molecular friction and random collisions, thereby generating a rapid temperature increase (termed as dielectric heating) [170]. In addition to the dielectric heating, magnetic heating also contributes to the microwave heating in magnetic materials in which the magnetic dipoles are responsive to the electromagnetic field of microwave [170]. To this end, unlike heat convection slowly transferring thermal energy from surface to core parts of materials in conventional heating, a uniform heating can be easily achieved by microwave irradiation on the grounds of the high penetration depths of microwaves. Henceforth, microwave-induced heating provides particularly advantageous basis, for instance, contactless heating, highly selective dielectric heating, instantaneous response, enhanced reaction rate as well as rapid energy transfer [167, 171, 172].

Initially, microwave-assisted synthesis of graphene was used to accelerate the reaction kinetics of GO reduced using chemical reductants, which normally required a long reaction time of 8 - 48 hours [173-176]. In addition to the prolonged reduction process, the resulting rGO exhibited low C/O ranging from only 1.5 to 5.6, implying the inefficient removal of labile functional groups by chemical reducing agents [175, 176]. A typical work was conducted to compare the qualities of rGO using conventional chemical reduction and microwave-assisted chemical reduction of GO using hydroiodic acid/acetic

acid as reducing agent [177]. Through an array of characterisation techniques, such as Raman, Fourier-transform infrared spectroscopy (FTIR) and TEM, the authors found that the quality of rGO treated with 4 h microwave irradiation was comparable to rGO prepared without microwave irradiation for 48 h.

Considering the toxicity and high cost of chemical reducing agents, huge efforts have been devoted to microwave irradiation of GO dispersed in organic solvents without any chemical reducing agents. Chen *et al.* reported microwave-assisted reduction of GO dispersed in *N,N*-dimethylacetamide and water (DMAc/H<sub>2</sub>O) [178]. With the microwave irradiation at 800 W under nitrogen purge, they found the amounts of oxygen functional groups were decreased and the thermal stabilities were increased with increasing irradiation times (1-10 min), as evidenced by FTIR and thermogravimetric analysis (TGA) in Fig. 2-18. However, due to the low boiling point of DMAc (165 °C), this mild thermal reduction induced by 10 min microwave irradiation cannot effectively remove oxygen functional groups and heal the carbon conjugated microstructure, yielding a low C/O ratio at 5.46 and an electrical conductivity of only 200 S m<sup>-1</sup>. The structural disorders induced by oxygen functional groups and defects were confirmed by the minor changes in  $I_D/I_G$  (0.95 for GO and 0.96 for rGO treated with microwave) in Raman spectra [178]. Besides, similar research works using microwave-assisted thermal reduction of GO have been performed in other organic media, such as dimethyl sulfoxide (DMSO) [179], *N*-methylpyrrolidone (NMP) [180], oleylamine [181], and *N,N*-dimethylformamide (DMF) [182]. However, the reduction degree of GO in organic media by microwave irradiation was inferior because of the low boiling points of organic media, which are generally less than 300 °C. It has been reported that the temperature required to effectively reduce GO was ~ 1050 °C in argon atmosphere [146] and could be alleviated to 800 °C in hydrogen

atmosphere [183], which were difficult to achieve in all organic media. In addition, after microwave irradiation, the reduced GO sheets precipitate out from the organic media and are prone to aggregate to large particulates upon drying due to intensive  $\pi$ - $\pi$  interactions between planar graphene sheets, which impaired the attainable properties of graphene.

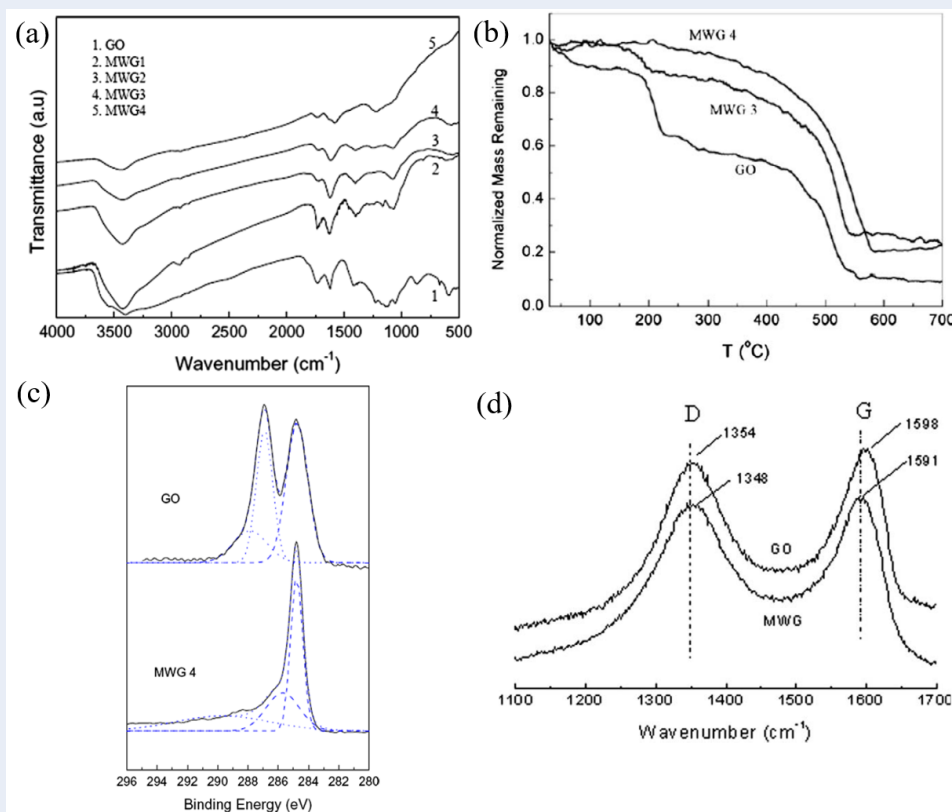


**Fig. 2-18.** (a) FTIR spectra, (b) TGA plots, (c) XPS spectra, and (d) Raman spectra of GO and rGO treated with microwave irradiation for different times (MWG1 for 1 min, MWG2 for 2 min, MWG3 for 3 min, and MWG4 for 10 min) [178].

To overcome the restrictions of the low boiling points of organic media and the aggregation of dried graphene, further research efforts have been expended to extending the microwave-assisted reduction process to GO in solid state powder form wherein the so-called ‘arcing discharge’ or ‘microplasma’ phenomena takes place within a matter of minutes [136, 137, 144, 180, 184, 185]. The first reported direct microwave-driven reduction of solid-state GO in ambient condition was achieved by Ruoff *et al.* in a multi-

mode domestic microwave oven [144]. In the work, they discovered that a minimum of 40% of the full power, *i.e.*, 280 W, was requested to reduce the GO precursor. It should be noted, however, that this minimum power value was unique to their microwave oven because many other factors can alter this value, such as mass/density of GO, the type of irradiation (single-/multi-mode), the size of reaction chamber, gas atmosphere as well as the age and condition of magnetron [170].

After 3 months, another microwave-assisted reduction of solid-state GO was reported by Li *et al.* who processed the GO suspension into a free-standing film prior to microwave irradiation [186]. With the radiation frequency of  $6.425 \pm 1.150$  GHz at the power of 500 W, the temperature showed little increase in the 1<sup>st</sup> second whereas it then experienced a drastic increase to 400 °C after the 2<sup>nd</sup> second. The increase in heating rate was attributed to the different couplings response of GO and rGO to the microwave. After microwave irradiation at this special frequency, the electrical conductivity increased from  $0.07 \text{ S m}^{-1}$  to  $1 \times 10^4 \text{ S m}^{-1}$ , which was comparable to that of high-temperature (1050 °C) exfoliated graphene. Additionally, the TGA results indicated improved thermal stability with increasing microwave exposure time and  $I_D/I_G$  in Raman spectra proved a decrease from 1 to 0.3. Comparatively, they attempted to reduce the GO at 1000 W using a domestic microwave oven which had a different frequency at 2.45 GHz. Even treated with a higher microwave power, the rGO reduced at 2.45 GHz seemed to exhibit a greater defect concentration than that at 6.425 GHz in terms of the  $I_D/I_G$  ratio in Raman spectra, indicating the significance of microwave frequency.

In addition to the microwave powers and the microwave frequency, the effect of microwave irradiation time on the quality of graphene was studied by Jiang *et al* [184]. Instead of using the well-known  $I_D/I_G$  ratio as quality indicator, the authors simply utilised

the intensity and the shape of 2D band, which is the overtone mode of D band, to estimate the reduction degree of GO. They concluded that the highest quality of graphene was obtained at 800 W when microwave irradiation was maintained extra 3-5 s from the onset of the microwave-induced arcing. Microwave irradiations which neither fell below 3 s nor exceeded 12 s from the beginning of the microwave-induced arcing resulted in deteriorated graphene, as confirmed by the weak 2D band.

The rGO freshly formed by microwave irradiation is believed to rather reactive to surrounding oxygen. Thus, different gas atmospheres, such as N<sub>2</sub> [172], Ar [187] and Ar/H<sub>2</sub> [185], have been created to render the freshly formed rGO from being re-oxidised and thus improve the graphene quality. Tang *et al.* [172] created an inert atmosphere by flushing the reaction chamber with high purity N<sub>2</sub> (> 99.999%) for 15 min. After microwave irradiation, the oxygen content was significantly reduced from 46 wt% for GO to only 1.2 wt% for rGO. Instead, Odedairo *et al.* attempted to improve the graphene quality by either creating a highly vacuum condition or a vacuum-argon condition [187]. Through a comparative study, the rGO which was microwave-assisted reduced in the presence of argon at 750 W was shown to exhibit larger surface area, greater pore volume, higher C/O ratio, higher electrical conductivity than its counterpart processed without the presence of argon (*i.e.*, only vacuum condition). The authors attributed the improved graphene properties to the larger amount of highly energetic electrons generated in microwave plasma, which could effectively deoxygenate the functional groups and exfoliate the GO sheets [187]. By mixing 10 vol% H<sub>2</sub> in argon gas, Park *et al.* found that the oxygen content was drastically reduced from 45.4 wt% in GO to 6.6 wt% in rGO [185]. This value was even lower than those of rGO samples which were microwave reduced in pure argon (9.85 wt%) atmosphere and in ambient air (26.2 wt%). Moreover,

the rGO prepared in H<sub>2</sub>/Ar gas mixture possessed smallest  $I_D/I_G$  ratio in Raman spectra (0.785 for H<sub>2</sub>/Ar vs 0.842 for Ar vs 0.853 for air) and highest electrical conductivity ( $1.25 \times 10^3 \text{ S m}^{-1}$  for H<sub>2</sub>/Ar vs  $7.41 \times 10^2 \text{ S m}^{-1}$  for Ar), which can be associated to the presence of less vacancies and defects in conjugated network [185]. Unlike deoxygenation achieved by high-temperature annealing or chemical reduction method, the oxygen moieties likely react with H<sub>2</sub> molecules to form H<sub>2</sub>O rather than CO/CO<sub>2</sub>. The latter originates from the carbon atoms underlying the oxygen functional groups, thereby resulting in formation of structural defects and deteriorated graphene properties.

Considering the low microwave coupling effect of GO in which the conjugated carbon network has been highly disrupted, an array of carbonaceous materials, such as graphene, carbon black or graphite, were used as microwave secondary susceptors to enhance microwave absorption and thus trigger super-heating to facilitate thermal reduction of surrounding GO powder [136, 137, 184]. However, it has been revealed that the super-heating by susceptor were mainly localised in places where the susceptor were present, thereby resulting in non-uniform thermal reduction of GO powder. Moreover, a preceding vacuum-drying step was adopted to remove the microwave-absorbable water to enhance the interaction of GO itself with microwave [188]. Through simply vacuum-drying at various temperatures, the exfoliation and reduction of GO can be improved to a certain extent, but it still yielded an apparent D peak in Raman spectra, as shown in Fig. 2-19.

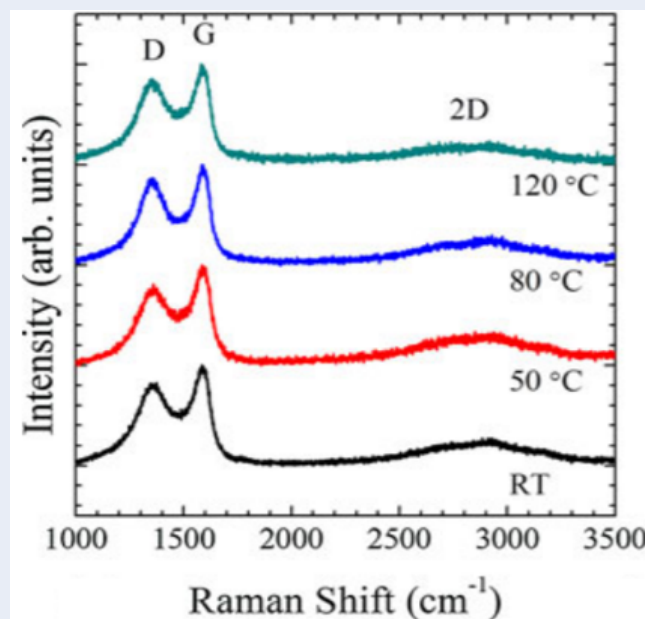


**Fig. 2-19.** The Raman spectra of microwave-reduced GO which were vacuum-dried at varying temperatures [188].

More recently, Voiry *et al.* optimised the microwave-assisted reduction process by exposing the GO powder to an thermal annealing process at 300 °C in argon atmosphere to obtain partially reduced GO prior to microwave irradiation, which converted entire GO from a poor microwave absorber to an extraordinary microwave absorber [153]. It has been identified that the partial restoration of the  $\pi$ - $\pi$  conjugated network of thermally annealed GO improved the electrical conductivity and concurrently enhanced the uniform microwave absorption, which led to intensive volumetric microwave heating and the formation of large arcing [136, 153, 184]. By means of this strategy, *i.e.*, annealing process, Voiry and collaborators were able to produce high-quality graphene nanosheets within few seconds using pulse microwaves (2.45 GHz at 1 000 W) in argon atmosphere and the quality was distinctively competitive to the counterparts synthesised by CVD in terms of Raman spectroscopy and X-ray photoelectron spectroscopy (XPS), as shown in Fig. 2-20. More specifically, the in-plane oxygen concentration was significantly reduced to 4 atomic% after microwave irradiations, which was smaller than the theoretically

predicted value (15-25%) for rGO annealed at 1 500 K [153]. Through an in-depth Raman analysis, the intensities of characteristic D peak and G peak were utilised to estimate the size of crystalline domains ( $L_a$ ) and the  $L_a$  was plotted against  $I_{2D}/I_G$  ratio, which explicitly disclosed the superior quality of rGO over other graphene prepared using different methods. This resulting high quality was further confirmed with the presence of a highly ordered carbon grid observed by aberration corrected HR-TEM, which may be attributed to the reorganisation of carbon bonds during microwave-induced microplasma, as shown in Fig. 2-20 (e) [153].

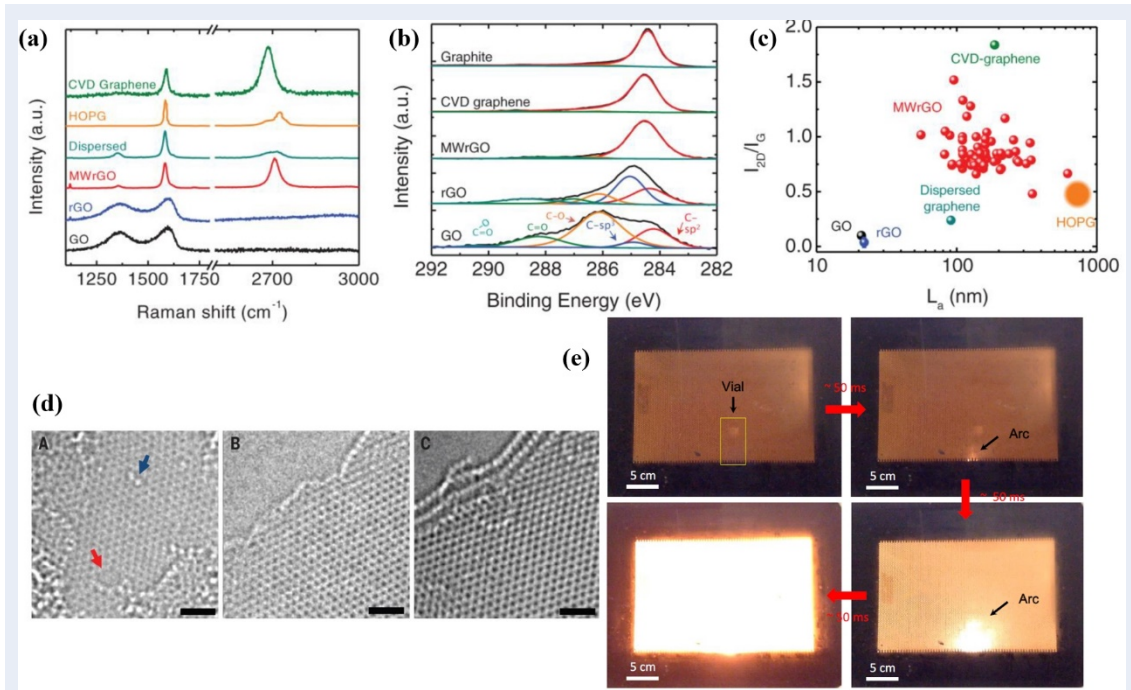


**Fig. 2-20.** (a-c) Raman spectra, XPS spectra and the plotting of  $I_{2D}/I_G$  vs  $L_a$  for graphite, GO, HOPG, graphene samples prepared using CVD, microwave-assisted thermal reduction, and mechanical exfoliation. (d) HR-TEM of A) single-layer rGO containing high concentration density, B) Bi-layer and C) tri-layer graphene exhibiting higher carbon crystallinity. (e) Digital images of the intensive arcing happened during microwave irradiation [153].

In contrast with pre-heating the GO at 300 °C before microwave irradiation, Jiang *et al.* slightly modified Voiry's experiment and produced high-quality graphene with a small piece of rGO film as microwave secondary susceptor [184]. Firstly, they used 1 wt%



CaCl<sub>2</sub> solution to coagulate GO “paper” on filter paper. Then, a small piece of rGO film was placed on the GO “paper” to effectively absorb the microwave energy and concurrently reduce the GO “paper”. After microwave irradiation at 800 W in air, the XPS spectra showed efficient elimination of labile oxygen functional groups and Raman spectra depicted CVD-like peaks for D band, G band and 2D band, as shown in Fig. 2-21. Additionally, the graphene sheet resistance was measured to be only 40  $\Omega \text{ cm}^{-2}$ , which was much less than 796  $\Omega \text{ cm}^{-2}$  of rGO annealed at 800 °C [184]. By analysing the Raman spectra of a microwave-synthesised graphene along the irradiation reduction direction in Fig. 2-21, they found that the highest quality of graphene was achieved at positions slightly away from where the secondary rGO was. Therefore, they surmised that the microwave-assisted reduction was the results of both microwave-assisted thermal heating and microwave-assisted arc discharge. Even though they claimed that no argon gas was needed in their work to obtain high quality graphene and the experiment was thus simplified, it should be noted that the graphene quality varied from position to position and was determined by the relative position to the secondary rGO [184].

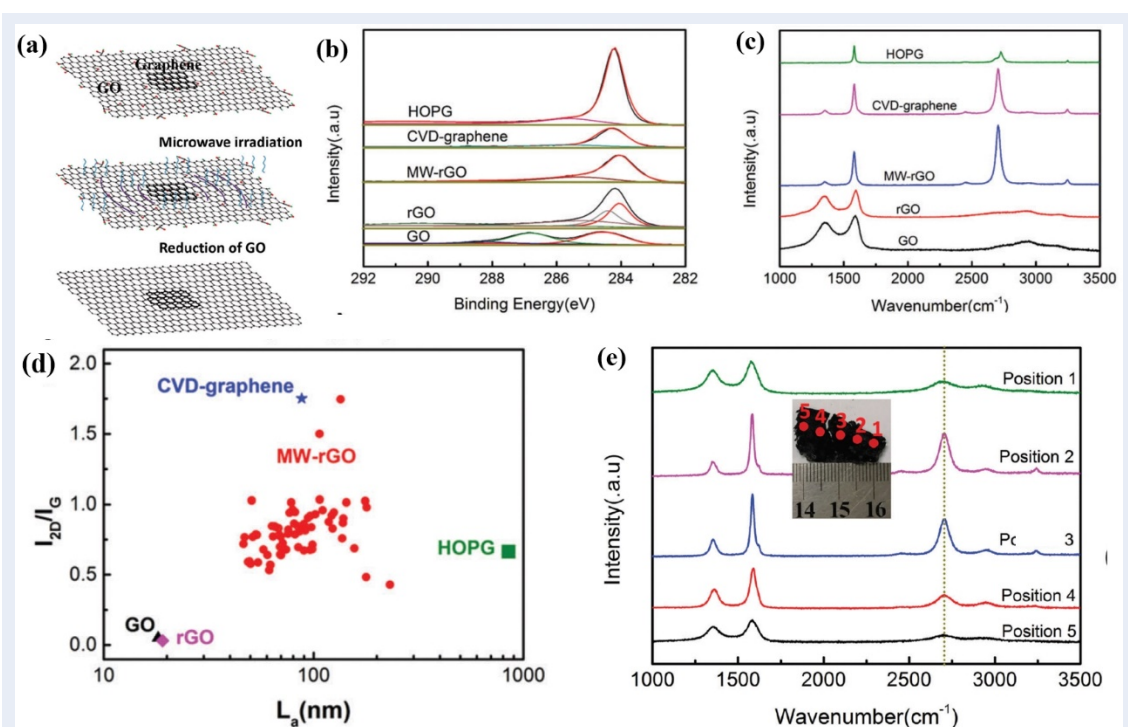


**Fig. 2-21.** (a) Schematic representation of rGO film on GO “paper” during microwave irradiation, (b-d) XPS spectra, Raman spectra, and the plotting of  $I_{2D}/I_G$  vs  $L_a$  for GO, rGO, HOPG, graphene prepared using CVD and microwave-assisted thermal reduction, (e) Raman spectra of graphene at different positions away from the secondary rGO susceptor [184].

From a survey of previous literature as shown in Table 2-3, it is found that numerous studies have been made to rationalise the microwave-assisted reduction of solid-state GO. Whilst many studies have been made to produce microwave-assisted rGO, most of the studies so far are focussed on the fixed power microwave synthesis. Moreover, the effects of different extents of inert atmosphere on graphene quality have not yet been systematically studied. Therefore, it is necessary to establish the correlation of various microwave powers/various extents of protective atmosphere on the quality evolutions of microwave-assisted reduced GO, which is one of the main objectives in this thesis.

**Table 2-3.** Overview of microwave-assisted reduction of solid-state GO at a fixed frequency of 2.45 GHz.

Atmosphere	Microwave power [W]	Microwave irradiation time	Secondary susceptor	References
Air	800	4-8 s	rGO	[184]
Air	700	1 min	N/A	[144]
Air or Argon or Ar/H <sub>2</sub>	1 600	40 s	Graphene nanosheet	[185]
Air	700	10 min	N/A	[189]
Vacuum or Argon	400-900	5 s	N/A	[187]
N <sub>2</sub>	1 000	1 min	N/A	[172]
Air	1 000	15 min	N/A	[137]
		5 s	Graphite	
Argon	1 000	1-2 s	N/A	[153]
Air	800	10 min	0.5%, 2.5% and 5.0% Graphene	[136]
Vacuum	900	Until explosion	N/A	[190]

#### 2.3.4. Microwave-induced arcing & hot-spots

The electrical conductivity of carbon materials is closely related to the mobility of  $\pi$  electrons in carbon conjugated framework and represents a very critical feature for microwave-induced Joule heating [167, 191]. With regard to a structurally “perfect” single-walled CNTs, they are typically ballistic conductors which have a defect-free carbon conjugated framework. The  $\pi$  electrons in such defect-free conjugated network are able to freely travel without generating any heating. However, if small amounts of structural defects are present, a Joule heating can be triggered by microwave irradiation. Notably, it does not necessarily mean that high-concentration structural defects in carbon conjugated framework are desired. A representative experiment concerning the effect of structural defects in GO on the microwave heatability was conducted by Hu *et al* [136]. They first synthesised GO with varying degrees of oxidation by adjusting the mass ratio of  $\text{KMnO}_4$  to graphite in the modified Hummer’s method. It was found in Fig. 2-22 (a) that the electrical conductivity and the C/O ratio of GO decreased with increasing the usage of  $\text{KMnO}_4$ . It can be readily understood because the presence of oxygen functional groups broke up the extended conjugated framework and reduced both the mobility and concentration of the  $\pi$  electrons. If GO was highly oxidised, such as GO-3.00, the graphitic structures were significantly broken down to polyaromatic islands with localised  $\pi$ - $\pi$  conjugated regions as shown in Fig. 2-22 (b). As such, the transport of the  $\pi$  electrons was impeded, especially over long-range scenario, thereby leading to a reduced electrical conductivity. Owing to the reduced mobility and concentration of the  $\pi$  electrons, the electric field of microwaves cannot drive the  $\pi$  electrons to generate sufficient Joule heating, which is clearly illustrated in Fig. 2-22 (c) [136].

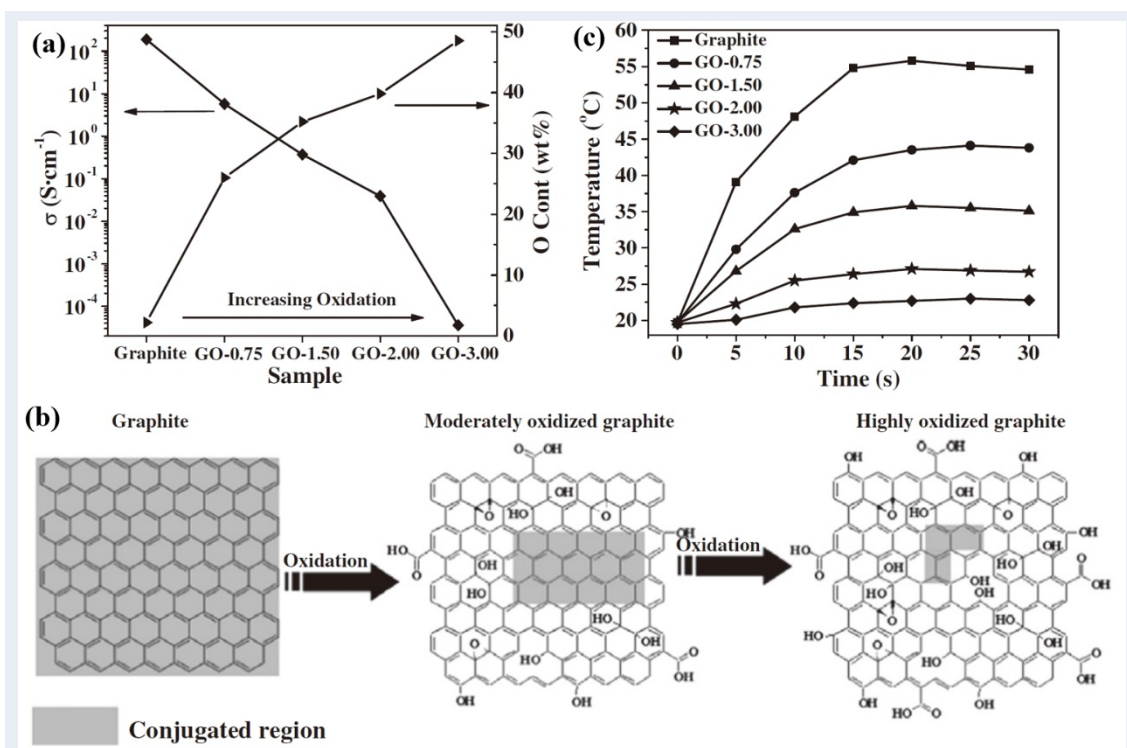


**Fig. 2-22.** (a) the changes of electrical conductivity and oxygen content with varying oxidation degrees of GO, (b) the microwave-induced heating of GO with different oxidation degrees, (c) schematic representation of the development of conjugate networks with oxidation treatment. (The  $x$  in GO- $x$  represents the mass ratio of  $\text{KMnO}_4$  to graphite) [136].

Another study regarding the effect of electrical conductivity on the microwave absorption of GO was performed by Tang *et al.* [172] who observed an interesting volume expansion and consecutive light emission phenomenon upon microwave irradiation, as shown in Fig. 2-23. When the high-power microwave (1,000 W) was irradiated on the GO, the remaining graphitic regions on basal planes interacted with microwave, leading to a pyrolytic process, the decomposition of oxygen functional groups and then exfoliation of GO. With further microwave irradiation, twinkling light emission started to occur in the GO and then it gradually developed across the GO to emit a homogenous light spectrum. The authors related this unique light emission during microwave irradiation to the electrical conductivity of GO. At the beginning, the electrical conductivity of GO was low, and the dielectric relaxation effect mainly contributed to the microwave-induced

heating which eliminated the oxygen moieties from the GO. The observed scintillation of the light of GO was associated to the restoration of carbon conjugated network. With ongoing microwave irradiation, higher crystallinity of graphitic backbones was achieved and thus the electrical conductivity of GO was drastically increased. In this case, the electron conduction started to dominate the microwave absorption process, thereby resulting in the full light emission across the GO [172].

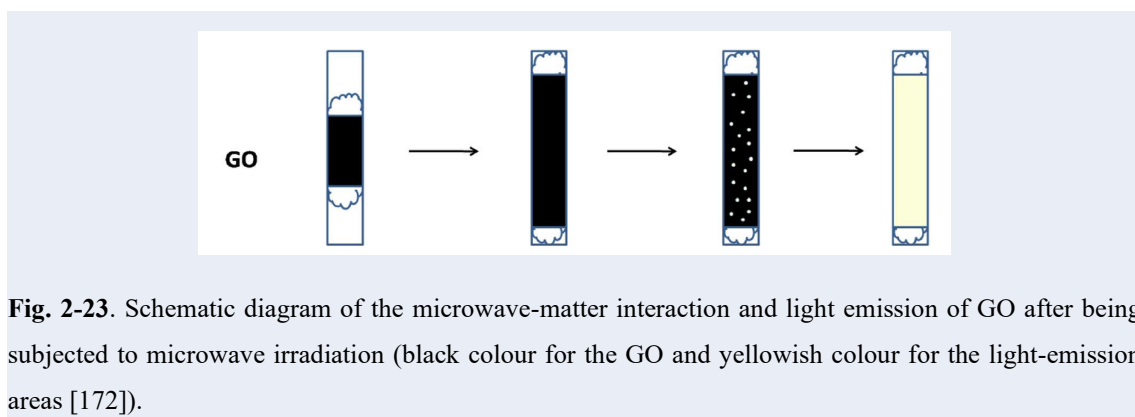


**Fig. 2-23.** Schematic diagram of the microwave-matter interaction and light emission of GO after being subjected to microwave irradiation (black colour for the GO and yellowish colour for the light-emission areas [172]).

The above two studies clearly indicate that the microwave absorption of GO is highly dependent on the electrical conductivity or, more specifically, the mobility of  $\pi$  electrons. The microwave-induced heating has been previously reported to increase linearly with the electrical conductivity [192, 193]. However, the presence of high-concentration oxygen functional groups and structural defects in GO induced by oxidation treatment significantly impairs the microwave-GO interaction. In order to restore the microwave absorptivity, GO can be subjected to a deoxygenation treatment at low temperature ( $\sim 200$  °C) to partially remove liable oxygen functional groups, such as hydroxyl and carboxyl groups on the plane edges, to partially restore the conjugated network. The thermal stability of oxygen functional groups and the decomposed gaseous species were simultaneously studied by combining TGA, DSC and FTIR, as shown in Fig. 2-24 (a-b) [146]. It can be seen that the GO was thermally unstable at 200 °C, as evidenced by a

sharp mass loss and an exothermic reaction. The decomposed gas was analysed using FTIR and was proven to be CO<sub>2</sub> and water vapour. In addition to CO<sub>2</sub> and water vapour, CO and SO<sub>2</sub> were also identified in the decomposed gas in another study using mass-spectrometer analysis, as given in Fig. 2-24 (c) [190]. The release of decomposed gas is always accompanied with a vigorous exfoliation of GO, which was believed to be caused by the rapid pressure build-up in the GO in which the decomposition rate of oxygen functional groups exceeds the diffusion rate of the decomposed gas. Hannes *et al.* provided a quantitative estimation of maximum pressure generated by CO<sub>2</sub> and water by using the interlayer spacing from diffraction measurement, the gas mass formed from TGA and assuming an isochoric heating process [146]. The pressures of CO<sub>2</sub> and water were calculated to 100 MPa and 60 MPa, which were greater than the van der Waals attraction (26 MPa) between the graphitic layers determined by a Lennard-Jones potential and pairwise summation [146]. Henceforth, GO can be effectively exfoliated due to the rapid thermal decomposition and sufficient pressure build-up.

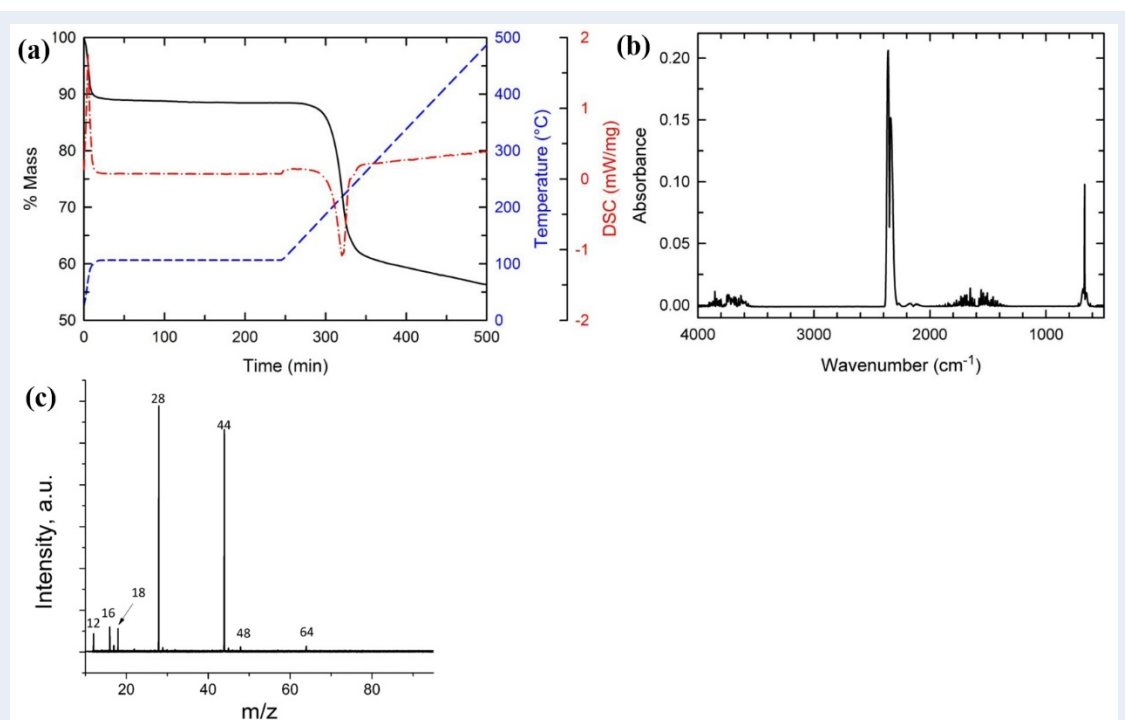


**Fig. 2-24.** (a) TGA/DSC scan of wet GO, (b) FTIR absorbance spectrum of the decomposed gas (the peaks at  $2350\text{ cm}^{-1}$  and  $670\text{ cm}^{-1}$  are assigned for  $\text{CO}_2$ , the regions from  $1400\text{--}1800\text{ cm}^{-1}$  and  $3500\text{--}3900\text{ cm}^{-1}$  are assigned for water vapour [146]), (c) mass-spectra of outlet gas produced at explosion of GO ( $\text{CO}$ :  $m/z=28$ ,  $\text{CO}_2$ :  $m/z=44$ , water:  $m/z=18$ ,  $[\text{SO}]^{+}$ :  $m/z=48$  and  $[\text{SO}_2]^{+}$ :  $m/z=64$ ) [190].

The partial restoration of graphitic structures induced by thermal treatment endows GO with improved absorption and dissipation of microwave energy, thus generating strong heating. Moreover, the microwave irradiation process may lead to intensive light emission which is perceived as microwave arcing or plasma. Multiple studies have been conducted to elucidate the intensive light emission, but there is still no consensus amongst researchers. The occurrence of microwave arcing or plasma is considered to be an additional source of the localised hot-spot, which can facilitate the reduction of GO.

A plasma collision mechanism was proposed for the reduction process of GO. The GO with preceding thermal treatment has gained a partially restored conjugated structure and an extended  $\pi$  system, which converted GO into a good microwave receptor. The GO effectively interacts with microwave and converts the energy to the surrounding gas



molecules [137]. As such, the gas molecules are activated to form a plasma which encloses large amounts of electrons and ions [194]. The electrons and ions possess high kinetic energies and are likely to bombard the polar chemical bonds in the oxygen functional groups, leading to the effective removal of remaining oxygen functional groups within nanoseconds, as schematically shown in Fig. 2-25 [194]. If this plasma collision process happens in argon atmosphere, Odedairo *at al.* demonstrated that graphene sheets with higher surface area and larger pore volume could be produced as compared to a vacuum atmosphere [187].

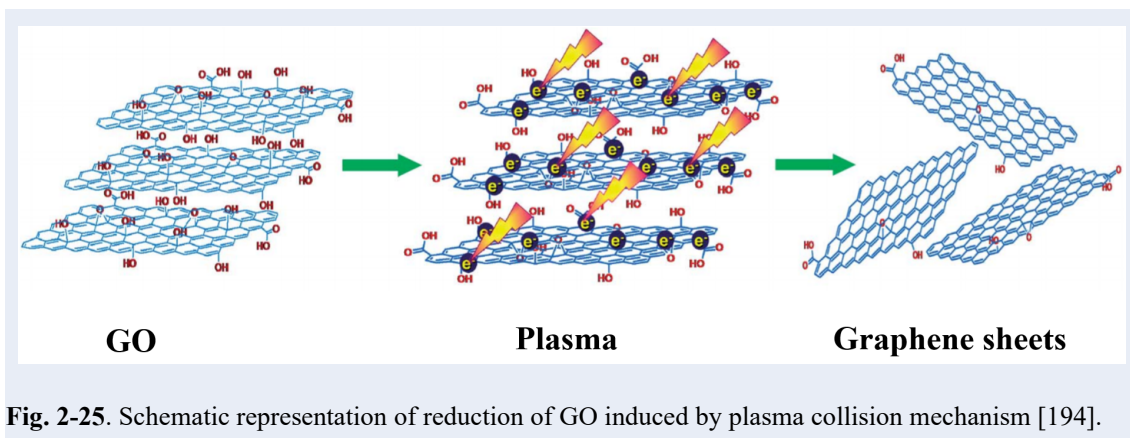


**Fig. 2-25.** Schematic representation of reduction of GO induced by plasma collision mechanism [194].

Another mechanism was also proposed for the formation of microwave arcing in the view of ionisation by high-energy  $\pi$  electrons [136, 167]. After the partial removal of liable functional groups by thermal treatment, the GO exhibited relatively broad regions in which the delocalised  $\pi$  electrons can freely move around. The strong microwave absorption provided the free  $\pi$  electrons with more kinetic energy, some of which may jump out of the materials and ionise the surrounding atmosphere [167]. The ionisation can be thought macroscopically as electric arcing and microscopically as hot-spots [167]. With regard to the  $\pi$  electrons moving in a delimited region of the GO, the microwave energy was converted to heat if the  $\pi$  electrons cannot couple to the changes in phase of the electric component of microwave. Therefore, remaining oxygen functional groups

were thermally decomposed.

No matter which mechanism is used to explain the decomposition of oxygen functional groups, the formation of hot-spots represents an important feature during microwave irradiation. However, the direct temperature measurement of the hot-spots have not been reported. The widely used temperature sensors, such as internal fibre optics or thermocouple or external infrared sensor, can only provide temperature averaged over a certain area rather than precise temperature on the nanoscale similar to hot-spots [170]. In addition to the type of temperature sensors, there are a variety of complexities to affect the temperature reading, including the distance between sample and sensor, the position of microwave susceptor [170], the bulk density of GO [195], and sample mass [136]. Druzhinina *et al.* demonstrated an indirect evidence of the formation of local hot-spots [196]. Iron nanoparticles were deposited on monolayer of *n*-octadecyltrichlorosilane, which functioned as a sensitive indicator of locally high temperature. By selectively microwave irradiation, the areas in close vicinity of the iron nanoparticles were decomposed, which was confirmed by the presence of defects observed in ex-situ atomic force microscopy (AFM), as shown in Fig. 2-26.

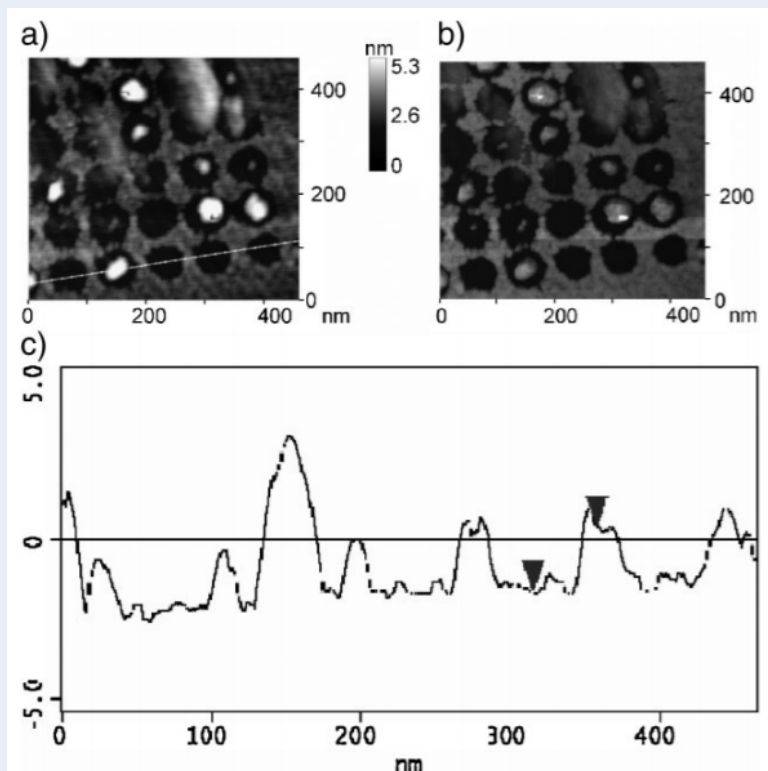


**Fig. 2-26.** Scanning force microscopy images of the array of iron nanoparticles. A significant degradation of the monolayer *n*-octadecyltrichlorosilane was detected after microwave irradiation. (a) height image, (b) phase image, and (c) line profile of the corresponding height image [196].

In addition to experimentally study the microwave reduction process of GO, Chaban *et al.* theoretically studied this sophisticated process using reactive molecular dynamics (RMD) and concluded that the oxygen-containing functional groups were deoxygenized at quite different temperature regimes, as shown in Fig. 2-27. Their work thus provided a fundamental understanding of electromagnetic interaction of GO with microwaves at a molecular-level [197]. It should be, however, note that the decomposition temperatures of oxygen functional groups calculated using RMD were far greater than the temperatures obtained in experiments (generally less than 1000 °C). The discrepancy in temperatures was due to the differences between average experimental temperature values and theoretically predicted values.

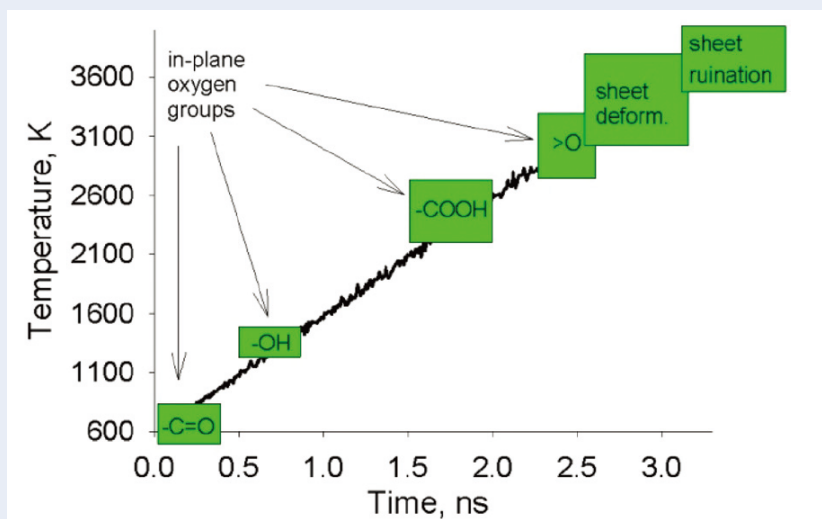


**Fig. 2-27.** The reduction temperatures of GO as a function of microwave irradiation time in a vacuum [197].

From the above literature review, it can be found that the microwave-assisted reduction of GO is a complex process involving not only microwave-induced thermal effect but also microwave-induced arcing/hot-spots. So far, much attentions have been paid to enhance the microwave reduction of GO by directly introducing a small amount of microwave susceptors. However, the effect of preceding thermal treatment on microwave absorptivity of GO has not been well studied, which leaves a research gap to be explored.

## 2.4. The use of CNTs and graphene in LIBs

The uses of CNTs and graphene as conductive fillers have been commonly found in energy storage devices, especially rechargeable Li ion battery due to the remarkable surface area, excellent electrical conductivity, tunable surface functionality, and robust structure. Many reviews have summarised recent progress on the enforcements of CNTs and graphene in LIBs and demonstrated their effectiveness in creating nanoscale circuitry throughout the electrode structure. One can refer to the outstanding reviews for detailed information [198-203]. It is not intended to give another research update in this section. Instead, it will only cover the influences of the incorporation of CNTs and graphene as conductive fillers in electrode and the percolation theory behind continuous conductive network established in electrode.

Indeed, when electrode is designed for LIBs, many electrode requirements have to be considered, such as electrical conductivity, architecture, energy density, cost, and safety-related issues. There is no doubt, among them, that electrical conductivity is one of the decisive properties. In electrode, the conductive filler primarily offers as much electrical conduction pathways as possible for charge carriers, *i.e.*, electron in this case, while it ideally does not compromise the Li diffusion in electrode at high loading. Under this protocol, the electrode for LIBs can be visualised, to some extent, as an intricate conductive phase connecting non-conductive phase, where both phases can be fully utilised. Therefore, it is of importance to assemble electroactive materials with a percolating electron- and ion- transport facilitator to obtain a high degree utilisation of electroactive materials, especially for those with poor conductivities, such as  $\text{LiCoO}_2$  ( $10^{-4} \text{ S cm}^{-1}$ ),  $\text{LiMn}_2\text{O}_4$  ( $10^{-6} \text{ S cm}^{-1}$ ), and  $\text{LiFePO}_4$  ( $10^{-9} \text{ S cm}^{-1}$ ) [84]. It is believed that when two phases with different electrical conductivities are thoroughly mixed and measured as

a function of the filler content, the overall electrical conductivity of the electrode behaves like a typical singular shape curve, as shown in Fig. 2-28. This process is termed as the critical percolation phenomenon and it follows percolation power law, which can be discussed in three regimes.

- (1) When the filler fraction ( $\phi$ ) < the critical percolation threshold ( $\phi_c$ ), the minor phase, *i.e.*, conductive filler in electrode, is isolated and a continuous conductive network cannot be established. In this scenario, the electrical conductivity of the electrode is predominantly determined by the intrinsic conductivity of the electroactive materials and the narrow gaps among the large clusters of the conductive filler. As  $\phi \rightarrow \phi_c$ , the conductive filler starts to develop percolative paths and the electrical conductivity ( $\sigma$ ) can be described as the following law [204]:

$$\sigma \propto \sigma_1(\phi_c - \phi)^{-s} \quad [\text{Equation 5}]$$

Where,  $\sigma_1$  represents intrinsic electrical conductivity of the major phase and  $s$  defines the critical exponent, which typically describes the divergence behaviour of conductivity of the mixture. The critical exponent  $s$  is dependent on the dimensionality ( $d$ ) in the bond and site percolation:  $s = 1.1 \sim 1.3$  for  $d = 2$  and  $s = 0.7 \sim 1.0$  for  $d = 3$  [204]. At this stage, the electrical conductivity of composite seems to be poor due to low incorporation of conductive filler and is likely affected by the occurrence of the quantum tunnelling effect in which electrons have the ability to hop through neighbouring fillers separated by a short distance. With more conductive filler introduced into the system, they start to form large clusters and the tunnelling resistance is reduced.

- (2) When the filler fraction  $\phi >$  the critical percolation threshold  $\phi_c$ , the conductive filler

in electrode has constructed a continuous conductive network. The electrical conductivity of the electrode is predominantly governed by conductive filler and follows the law [204]:

$$\sigma \propto \sigma_2 (\phi - \phi_c)^t \quad [\text{Equation 6}]$$

Where,  $\sigma_2$  represents intrinsic electrical conductivity of the conductive filler;  $t$  defines the critical exponent and is also dependent on the dimensionality ( $d$ ):  $t = 1.1 \sim 1.3$  for  $d = 2$  and  $t = 1.6 \sim 2.0$  for  $d = 3$  [204]. Based on the Skal-Shklovskii-de Gennes approximation [205, 206], the critical exponent  $t$  can be expressed as:

$$t = (d - 2)\phi + \xi \quad [\text{Equation 7}]$$

Where,  $\xi$  is the twistedness index for link bonds of the percolation clusters. It can be set as  $\xi = 1$  in the mean field approximation. In this regard,  $[(d - 2)\phi + 1]$  represents the lower bound for the critical exponent  $t$  in all dimensions. Therefore,  $(d - 2)\phi + 1 \leq t \leq (d - 2)\phi + \xi$  [204]. In this stage, with the further addition of conductive filler into the composite, the electrical conductivity increases slowly until levelling off at a constant value which is, for sure, lower than that of the conductive filler.

(3) As  $|\phi - \phi_c| \rightarrow 0$ , the electrical conductivity in narrow regime ( $\phi = \phi_c \pm \delta$ ) can be determined by combining Equation 5 and Equation 6:

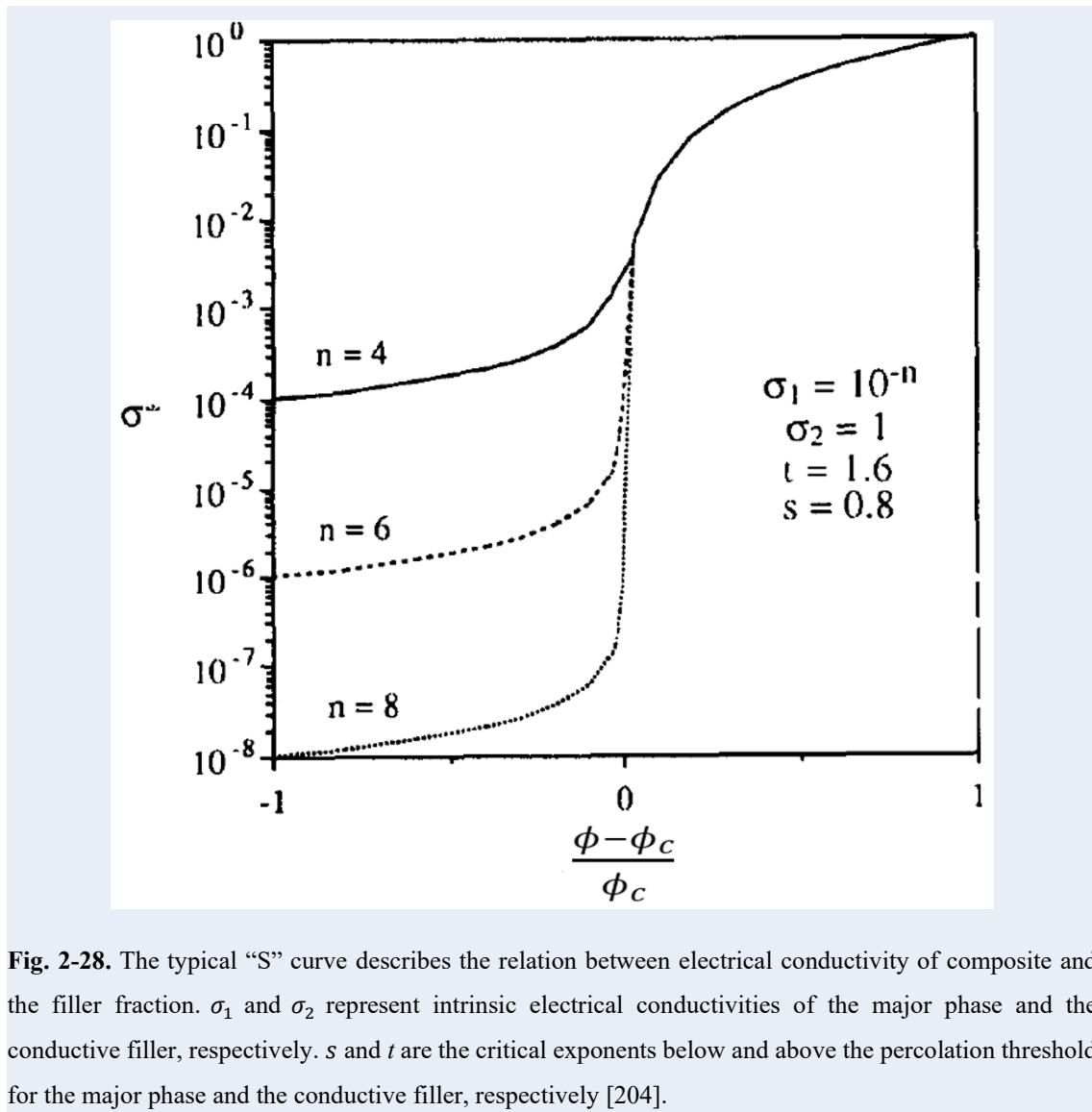
$$\sigma = \sigma_2 \delta^t = \sigma_1 \delta^{-s} \quad [\text{Equation 8}]$$

The crossover region which is generally termed percolation transition can be figured out:

$$|\phi - \phi_c| \leq \delta = (\sigma_1/\sigma_2)^{1/(t+s)} \quad [\text{Equation 9}]$$

The percolation transition is a direct result of the geometric phase transition in structure and the percolation power law can be depicted, as shown in Fig. 2-28. It should be

reminded that the percolation transition is valid only when  $\sigma_2/\sigma_1 \gg 1$ . Moreover, it has been claimed that the conductivity critical exponents  $s$  and  $t$  in real practice were considered belonging to the same universality system. However, there is still a debate on the non-universality of  $s$  and  $t$  observed from the large differences between some experimental and numerical results even after the percolation theory has been proposed for decades [207].



It can be easily seen in Fig. 2-28 that the larger the divergence between the physical properties, such as electrical conductivity, of the constituent phases, the sharper the



changes in the corresponding macroscopic physical properties of the electrode in the vicinity of the percolation threshold [204]. This fundamental sharp change over the narrow range is actually governed by a combination of several mechanisms with complex natures, *i.e.* intrinsic mobility of charge carriers, direct particle-particle contact, electron tunnelling [134]. In practical application, the physical properties can be readily measured experimentally, and thus the percolation threshold can be studied by the changes in the physical properties. For this sense, the relationship between electrode structure and electrode property can be established to guide the electrode design.

From the previously published data, it can be found that the electrical conductivity of electrode for LIBs in which carbon materials, such as graphite, CNTs and graphene, are employed as conductive fillers, can be predicted by the similar percolation theory. However, the onset of percolation in electrodes containing CNTs and graphene is influenced not only by the electrical conductivity, but also the morphology, aggregation, oxygen functional groups on the surface, electrode fabrication techniques as well as wrinkles and ripples distribution. Therefore, when an electrode with CNTs and graphene is designed, more attentions should be focussed on the filler aspect ratio, dispersibility, crystalline characteristics, and mixing techniques, rather than simply the electrical conductivity.

#### 2.4.1. CNTs as conductive filler

CNTs was first discovered by Japanese scientist, Sumio Iijima, in year 1991 and is typically characterised as 1D carbon allotrope that has the seamless form of cylindrical rolled-up graphene sheet, with nanometer-size diameter and micrometer-size length. Structurally speaking, CNTs can be envisioned as a central hollow core with hemisphere of fullerene structure as end caps. The aspect ratio (length-to-diameter ratio) is typically in excess of  $10^3$  [208]. It has been reported as a strong alternative to other carbonaceous allotropes, with varying successes, as conductive filler in advanced LIBs due to its remarkable electrical conductivity (usually  $10^2$  to  $10^6$  S cm<sup>-1</sup>), higher SSA, outstanding thermal conductivity and negligible thermal expansion coefficient. Furthermore, owing to the strong sp<sup>2</sup> graphitic bonds, CNTs are predicted to exhibit a Young's modulus as much as 1.2 TPa and a tensile strength as high as 50-200 GPa [208], which enables it to be a highly versatile platform for constructing LIBs. When CNTs is included as conductive filler in electrode, its electrical behaviour can be predicted by the above percolation power law. The critical exponent  $t$  for CNTs is highly dependent on the electrical conductivity ratio between CNT ( $\sigma_2$ ) and electroactive materials ( $\sigma_1$ ). Because the typical value of  $\sigma_2/\sigma_1$  could reach up to  $10^5$  [209], it may, based on theoretical prediction, lead to a value of 0.7~3.1 for critical exponent  $t$  [210-212]. However, it is not surprising that this value may also be changed by the CNT's 1D geometry, high aspect ratio, and dispersion in matrix.

CNTs is able to achieve a comparable electrical conductivity at considerably lower inclusion percentage as compared to the conventional carbon fillers, such as carbon black, acetylene black, and carbon nanofibers due to its high electrical conductivity. This could be seen for single-walled CNTs (SWCNTs) in composite prepared with only 0.1vol%

loading at which a continuous conductive network has been formed [210]. This pioneer work indicates that the use of CNTs presented a more effective strategy to reduce the dosage of conductive fillers more than an order of magnitude compared to conventional carbon fillers to obtain an appropriate electrical conduction. The lower usage of CNTs could bring in the immediate effect for relative increase in electroactive materials substitution, thereby increasing the energy density of electrode without compromising the rate performance. Recently, similar research works in which CNTs was used as conductive filler can be found for  $\text{LiCoO}_2$  [213],  $\text{LiFePO}_4$  [214-216] and  $\text{LiNi}_{0.5}\text{Mn}_{0.3}\text{Co}_{0.2}\text{O}_2$  [217] cathode materials, all of which demonstrated varying capacity improvements compared to carbon black counterparts.

In addition to lowering percolation threshold, the use of CNTs can provide other potential advantages when it is used in composite. Owing to the presence of p-orbital overlap in metallic CNT chiralities, CNTs can be ballistically conductive. This phenomenon manifests that the electrons transfer with mean free paths on the order of microns along the channel of CNTs without experiencing scattering due to impurities, local defects, or lattice vibrations [218]. This advantageous phenomenon is potentially useful to improve the rate capability of cathode active materials which generally have poor conductivity. Wang et al. studied the rate performance of LCO enhanced by the same loading of acetylene black, carbon fibres, and CNTs. And their results revealed that LCO cathode containing CNTs showed 10~15% improvement in reversible capacity than the other counterparts at 3C [209]. A similar study by Li et al. was also carried out in which  $\text{LiFeO}_4$  mixed with CNTs exhibited improved rate performance at 5C than acetylene black [219].

CNT's 1D geometry and extremely high aspect ratio can construct percolative paths in electrode at a considerably low percolation threshold. However, CNTs are prone to

agglomerate due to their strong intrinsic van der Waals attraction, the large surface area and the high aspect ratio [220, 221]. Moreover, the “clean” non-reactive CNTs surface restricted its dispersibility in organic solvents. Therefore, an intensive mixing step, such as ultrasonication, is generally required to de-entangle CNTs bundles and forms a homogeneous suspension. A typical example is given by Luo and co-workers’ research [222]. They employed ultrasonication and co-deposition method to fabricated binder-free electrodes in which LiCoO<sub>2</sub> particles were embedded in 3D structural network of super-aligned CNTs (SACNTs), as shown in Fig. 2-29. The binder-free electrode possessed the electrical conductivity as high as  $3.8 \times 10^2 \text{ S cm}^{-1}$  and  $2.0 \times 10^3 \text{ S cm}^{-1}$  for 1wt% and 5wt% of SACNTs, respectively. Due to the highly porous structure with favourable electrolyte intake and sufficient buffer volume for repetitious crystal change upon cycling, this LiCoO<sub>2</sub>-5wt%SACNT electrode attained the capacity of 151.4 mAh g<sup>-1</sup> at 0.1C and excellent rate capacity of 137.4 mAh g<sup>-1</sup> at 2C, which outperformed the Super P counterpart. Albeit that the electrode prepared in this work was binder-free and has demonstrated the promising gravimetric energy density, the actual physical density of LiCoO<sub>2</sub>-SACNT was low, *i.e.*, only 1.94 g cm<sup>-3</sup> for LiCoO<sub>2</sub>-SACNT. It, in other word, gave a poor volumetric energy density. Therefore, in order to simultaneously achieve high gravimetric and volumetric energy densities for LIBs, a novel fabrication technique is needed, such as abovementioned CSP.

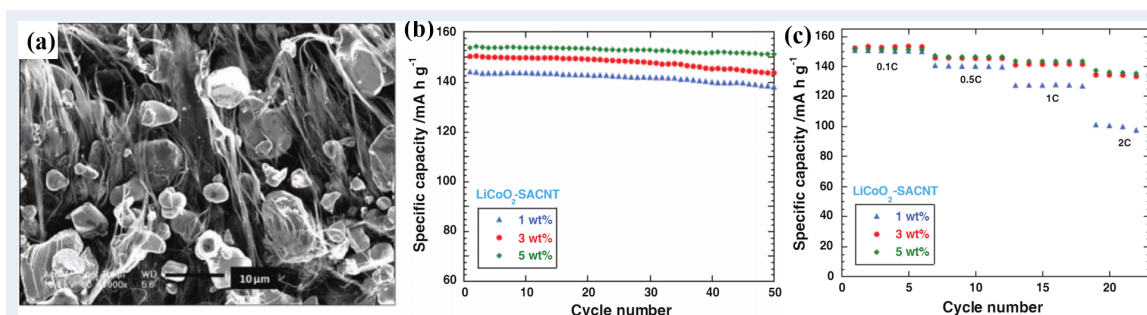


**Fig. 2-29.** (a) SEM image of cross-sectioned LiCoO<sub>2</sub>-SACNT. (b) life cycle of LiCoO<sub>2</sub>-SACNT at 0.1 C and (c) the rate capability of LiCoO<sub>2</sub>-SACNT at different C rate [222].

The effect of CNTs with different aspect ratio on the electrochemical performance of LCO was also studied. The LCO electrodes mixed with short-length CNTs (20-30  $\mu\text{m}$ ) and long-length CNTs (200-300  $\mu\text{m}$ ) showed comparable first-cycle capacity at 0.5C [223]. But the long-term cycle life and the rate capacity at super-high C rate of 25C and 30C pointed out the distinct benefits of large aspect ratio. The authors attributed the improved electrochemical behaviour of large aspect ratio CNTs to the building of continuous conductive network.

#### 2.4.2. Graphene as conductive filler

In contrast to the rolled shape of graphene sheet resembled for CNTs, graphene is shaped in a flat planar structure. Both of them can be envisaged as spheroidal with principal dimensions  $a_1 = a_2$  and  $a_3$ . Ideally, graphene sheet can be regarded as an oblate spheroid with  $a_3/a_1 = 0$ , whilst CNTs can be regarded as a prolate spheroid with  $a_3/a_1 = \infty$ . As discussed in Section 2.4, the percolation threshold of electrode is related to the aspect ratio of conductive fillers. Therefore, this markedly different geometry of graphene, along with the large specific surface area, can have an exceptional effect on the construction of electrical network in electrodes [224]. Xie et al. theoretically predicted that the graphene had lower percolation threshold in universal main matrix under a unified

theoretical framework and elaborated that the percolation threshold was very sensitive to shape aspect ratio [224].

Given that the graphene can provide (i) higher electrical conductivity, (ii) more efficient plane-to-point contact mechanism and (iii) more versatile microstructure than other carbonaceous conductive allotropes, it is expected to percolate active particles and gain the superior electrochemical performance with lower percolation threshold. However, the practical situation is more sophisticated for planar graphene. Kang et al. [34] studied the effect of graphene on 2 Ah LiFePO<sub>4</sub> commercial soft-pack aged battery pack and found that the cells containing 2 wt% graphene fillers delivered higher capacity than counterparts containing 7 wt% carbon black + 3 wt% conductive graphite (Fig. 2-30 a). This can be simply attributed to the establishment of the effective conductive network that span the entire electrode. However, the electrochemical curves of cells containing 2 wt% graphene fillers demonstrated apparent polarisation despite its higher capacity, as shown in Fig. 2-30 (b). The authors attributed this phenomenon to the obstruction of Li ions diffusion paths caused by the planar characteristics of graphene sheet which could result in a sluggish charge transfer kinetics. It can be seen, in this case, that even though the electrical conduction can be sufficiently guaranteed by the effective graphene scaffold, the suppressed Li ion diffusion from grain to grain resulted in higher polarisation. This finding leads to the hypothesis that over-size graphene sheets are not suitable for electroactive materials with nano-scale size, such as LiFePO<sub>4</sub> as it may lead to reduced power density and may be amplified in thick and dense electrodes at high C rate. Regardless of that, most publications still demonstrated improved rate performance for graphene-enhanced cathode [225-234].

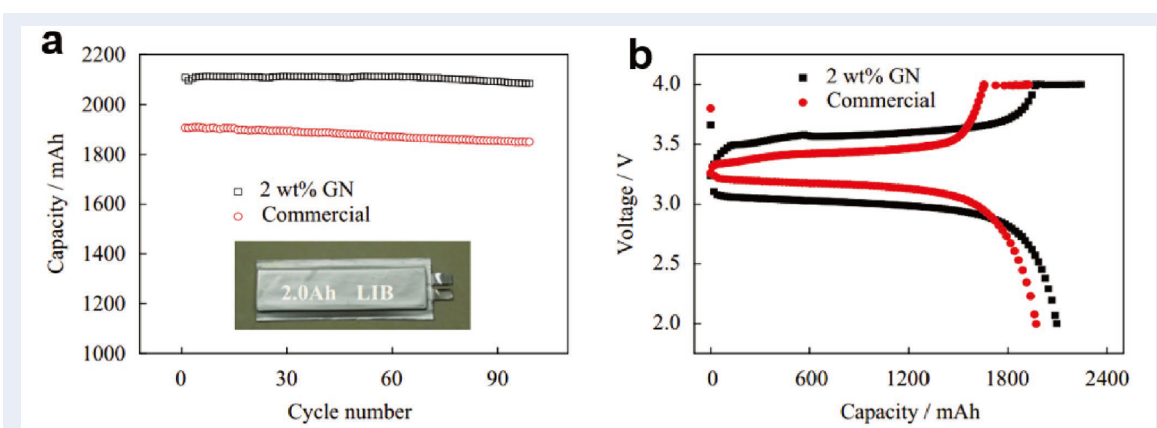


**Fig. 2-30. (a)** Life cycle and **(b)** galvanostatic curves of 2.0 Ah Li ion cells containing 2 wt% graphene, and 7 wt% carbon black + 3 wt% conductive graphite.

This abovementioned hindering effect of large graphene sheets can be negligible for micro-size electroactive materials, such as  $\text{LiCoO}_2$  which is generally larger than  $\text{LiFePO}_4$  by one order of magnitude, as schematically shown in Fig. 2-31. This is due to the fact that the lower specific surface area resulted from larger particle size requires less incorporation of graphene sheets to cover the surface of the LCO and create percolative paths. This negligible hindering effect has been confirmed in Yang's work [235]. Similar conclusions have been made in other  $\text{LiCoO}_2$  [236] and  $\text{LiFePO}_4$  [237]. Those works highlighted that the flake size of graphene should match with the particle size of the electroactive materials, rather than keep pursuing over-size flake.

The less addition of graphene conductive filler in electrode is the effective strategy to improve the volumetric energy density of batteries. The electrochemically inactive conductive filler cannot make any contribution to the capacity of cathode, but its low bulk density implies that it should occupy a large volume in electrode, which significantly reduces the overall volumetric energy density of batteries. Take graphene for example, it exhibits the bulk density as low as  $0.5 \text{ g cm}^{-3}$ , which is far lower than  $2.0\text{-}2.3 \text{ g cm}^{-3}$  of  $\text{LiFePO}_4$  and  $3.8\text{-}4.0 \text{ g cm}^{-3}$  of LCO. Therefore, if less graphene can be employed to build necessary conductive network in electrode, it is a great advantage of using graphene filler

to fabricate more compact electrode and 1 % reduction in use of graphene can lead to 4% and 8% increase in use for  $\text{LiFePO}_4$  and LCO, respectively, improving the gravimetric/volumetric energy density.

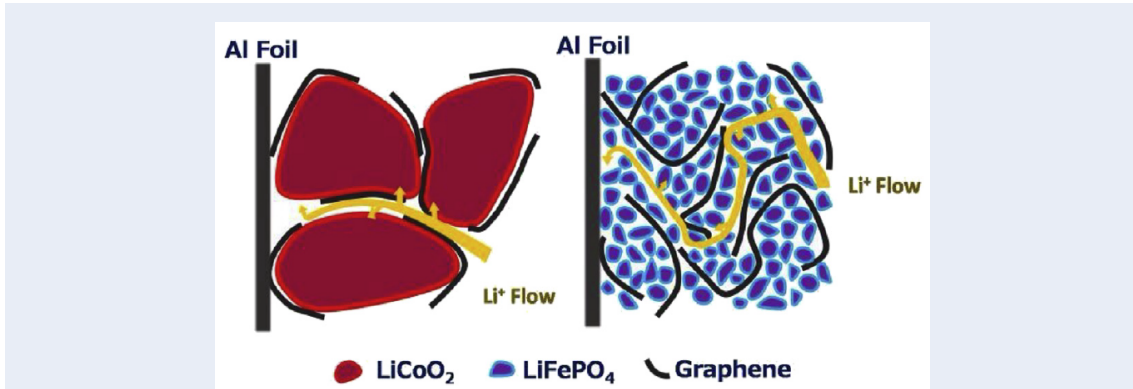


**Fig. 2-31.** Schematic illustration of the Li ion diffusion across electroactive materials with different particle sizes relative to same size graphene sheets. “plane-to-point” contact mode facilitates the electrical conduction, whilst the planar characteristic of graphene flake impedes the diffusion of Li ions when the particle sizes of graphene sheets are apparently larger than those of active materials [235].

The percolation phenomenon is not only affected by the intrinsic electrical conductivity and morphology of conductive fillers, but also the architectures which electroactive materials and graphene sheets construct. Unlike CNTs-enhanced electrode in which electroactive materials is only wired up by chain-like CNTs, graphene sheets with atomic or molecular thickness and infinite planar size can build with electroactive materials in varying forms. The diversity of architectures can be classified into six different models, as proposed by Raccichini et al. in Fig. 2-32 [201].



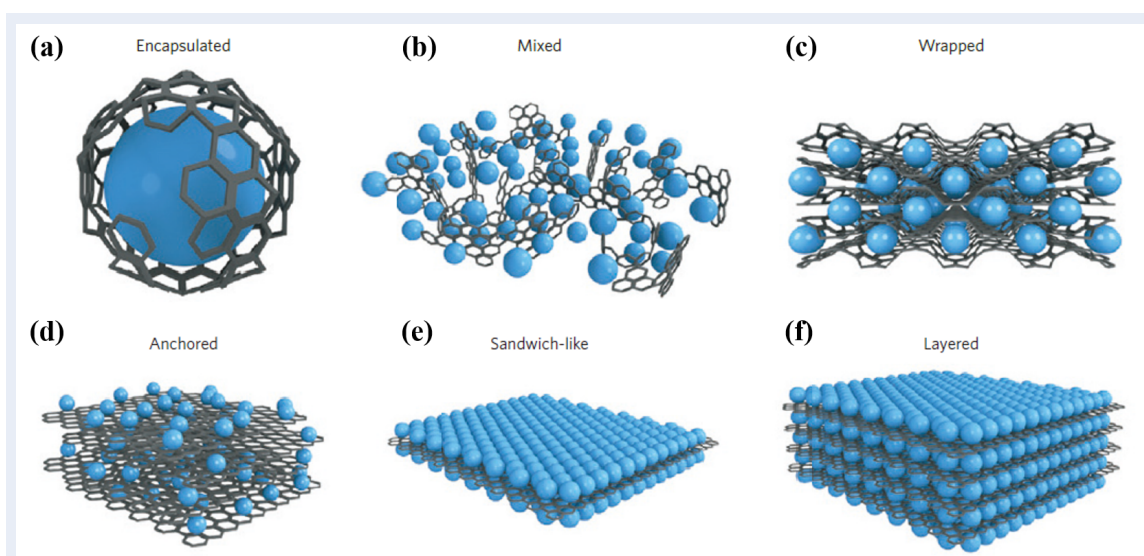


**Fig. 2-32.** Schematic representation of different electroactive materials/graphene sheets assembly models.

(a) Encapsulated: individual electroactive material particles are encapsulated by graphene.

(b) Mixed: the as-synthesised graphene and active materials are mixed mechanically forming a conductive networking across electrode.

(c) Wrapped: individual electroactive material particles are wrapped by graphene sheets.

(d) Anchored: individual electroactive material particles are anchored on graphene surfaces.

(e) Sandwich-like: electroactive material particles are squeezed between two graphene layers creating a sandwich-like structure.

(f) Layered: Active-material nanoparticles are alternated with graphene sheets to form a composite layered structure.

Rather than simply building a continuous conductive network, these active materials/graphene architectures can provide additional electrochemical benefits, such as rapid Li-ion transport. It is worth noting that most of the electroactive materials/graphene cathode composites may exhibit mixed architectural models, like encapsulated and anchored and layered models, in a single electrode.

### 2.4.3. Choice: CNT or graphene?

As discussed above, CNTs and graphene have demonstrated their distinct advantages when used as conductive fillers in high performance LIBs. The electrochemical differences between them are mainly caused by their morphology, contact mechanism, and the dispersion in electrode.

From the perspective of electrical conductivity, both of CNTs and graphene exhibit the similar values as high as  $10^6 \text{ S m}^{-1}$ . It is the morphology that greatly differentiates them from each other. In contrast to two-dimensional structure of graphene in which both sides can simultaneously provide contact points with electroactive materials, only the outer surfaces of CNTs are accessible to electroactive materials and contribute to the electrical conductivity of the material. In addition, graphene sheets can provide a remarkable electrical conduction in two dimensions whilst CNTs show electrical conduction in uniaxial direction [238]. The uniaxial electrical conduction of CNTs may make it develop anisotropic polarisation in nanohybrid electrodes, especially in the case where super-aligned CNTs is used, and thus affect the overall electrochemical performance of electrodes. Moreover, the large aspect ratio and the exclusive wrinkles and ripples formed on graphene flakes are able to wrap and/or anchor more particles, leading to an electrode with improved structural integrity and reduced interfacial resistance. This structural characteristic is extremely useful for binder-free electrode.

From the perspective of dispersion in organic solvent, typically NMP for electrode preparation, graphene is easier to spread than CNTs which have the long-standing issue of entangled bundles. Also, the residual oxygen functional groups on chemically prepared graphene can assist in the interaction with organic solvent and form stable suspension,

adding further merits for graphene in processing. Once graphene is well dispersed, all carbon atoms on the graphene sheets is capable to participate in the establishment of the conductive network, increasing the utilisation of carbon atoms. After the organic solvent is evaporated, graphene sheets are likely to create open pore system through which Li ions can diffuse easily and thus reduces the concentration polarisation, enabling graphene-containing electrode to gain improved power capability. Furthermore, due to the lower percolation threshold, the lower filler loading of graphene generally leads to cost-effectiveness and gives rise to the improved processability of the electrode.

Finally, compared to the large-scale but expensive methods to produce CNTs, such as CVD [239], arc-discharge [240, 241] and laser ablation [242], there are cheaper production methods for massive production of graphene, such as chemical exfoliation of GO or ultrasonication of liquid-based graphene suspension, which makes the graphene affordable for advanced LIBs. Moreover, it is worth noting that the residual metallic impurities from the use of metallic catalytic nanoparticles during CNTs production are hard to be completely removed even after purification and may impair the intrinsic properties and lead to undesired side reactions. However, this problem can be precluded in graphene and results in the construction of reliable LIBs [243, 244]. Therefore, not only the high production cost of CNTs but also the difficult-to-control amount of residual metallic impurities make graphene sheets an ideal alternative to CNTs.

In addition to the consideration for the abovementioned morphologies, dispersion, and cost, the choosing of CNTs or graphene for cold sintered composite electrode should be carefully made due to the high pressure applied during electrode fabrication. This is never encountered in conventional tape-cast electrodes in which the conductive filler is simply mixed/dispersed in main matrix and it should be investigated.

## 2.5. Aims and objectives of the project

Based on the above literature review, a few research gaps can be identified as follows:

- There has not yet been a comprehensive report on the fabrication of bulk  $\text{LiCoO}_2$ -based composite cathode via low-temperature CSP and the studies on its cathodic properties, especially volumetric energy density.
- It is essential to establish the correlation of various microwave powers/various extents of protective atmosphere with the structural evolutions of microwave-synthesised graphene.
- High-quality graphene has been obtained using microwave-assisted reduction of GO which was first subjected to thermal treatment. However, the effect of preceding thermal treatment on microwave absorptivity of GO should be clearly clarified.
- Graphene has been reported to exhibit superior electrical conductivity, large surface and distinct porous structure as compared to CNTs. However, whether the former (2D material) is able to outperform the latter (1D material) in bulk  $\text{LiCoO}_2$ -based composite cathode in terms of cycling stability and rate capability has not been studied in the relevant literature.

In efforts to study the abovementioned research gaps, the following strategies are adopted in this thesis:

- The effects of CSP conditions, namely temperature, pressure, and duration time, on the densification of monolithic LCO pellets are systematically investigated to figure out a standard CSP processing condition. Then, bulk  $\text{LiCoO}_2$ -based composite cathodes with CNTs as conductive filler are fabricated using the standard CSP

processing condition and electrochemically evaluated in half cell configuration.

- The microwave-synthesised graphene samples prepared in various microwave powers/various extents of protective atmosphere (*i.e.*, argon) are comprehensively characterised using Raman, XRD, TGA, FTIR, XPS, BET, FEGSEM, HR-TEM and four-probe conductivity measurement. Then the correlations amongst graphene properties, structural evolution and the microwave processing variable can be established and serve as a guide to tailor graphene to specific end use.
- GO samples with/without preceding thermal treatment are microwave irradiated at the identical condition. During microwave irradiation, the temperatures of both GO samples are monitored to study the differences in microwave-GO interactions. The resultant microwave products are then subjected to intensive characterisation to prove the role of the thermal treatment.
- A comparative study regarding the effects of the microwave-synthesised graphene (2D material) and CNTs (1D material) on the bulk  $\text{LiCoO}_2$ -based composite cathodes is performed in the same CSP processing condition.

## Chapter 3. Experimental details

This chapter details the experimental procedures to produce (i) LCO-based composite cathodes with high bulk density and high volumetric capacity using cold sintering process (CSP); and (ii) microwave reduced graphene oxide (MWrGO) using different microwave powers in different extents of argon atmosphere.

All the chemicals and agents used for the preparation of LCO-based composite cathodes, the synthesis of MWrGO, and the fabrication of Li-ion batteries are summarised in Section 3.1.

In Section 3.2, the synthesis of LCO powder was first involved in Section 3.2.1 and then the LCO powder was planetary ball milled and mixed with multi-walled carbon nanotubes (CNTs) to prepare LCO/ $x$ CNTs powder ( $x$  represents the weight percentage of CNTs relative to the as-milled LCO powder) in Section 3.2.2. Next, the as-milled LCO powder and the as-milled LCO/ $x$ CNTs powder were used to produce monolithic LCO pellets and LCO/ $x$ CNTs composite pellets using CSP, followed by post-CSP annealing treatment in Section 3.2.3. All the techniques related to the characterisation of the LCO-based pellets were given in Section 3.2.4. Finally, the optimised LCO/3%CNTs pellets were assembled in 2032 type coin cells, along with post-mortem analysis, which was detailed in Section 3.2.5.

In Section 3.3, the preparation of graphite oxide colloidal suspension via different reaction temperatures using the modified Hummer's method was first detailed in Section 3.3.1. Following that, the formation of graphene oxide (GO) beads in  $\text{CaCl}_2$  coagulation bath using graphite oxide colloidal suspension was given in Section 3.3.2. Then, the as-prepared GO was exfoliated and was microwave reduced against different microwave

powers in different inert extents of Ar atmosphere in Section 3.3.3. The comprehensive procedures to characterise the MWrGO samples were also included in Section 3.3.4, along with the electrochemical evaluation of MWrGO samples using 2032 type coin cell in Section 3.3.5.

In Section 3.4, the experimental procedures to produce LCO/xMWrGO composite pellets were similar to the procedures to prepared LCO/xCNTs composite pellets as detailed in Section 3.2. The LCO powder was first mixed with the MWrGO that was prepared in Section 3.3 using ultrasonication bath and planetary ball milling, as detailed in Section 3.4.1. Afterwards, the as-milled LCO/xMWrGO powder was used to produce LCO/xMWrGO pellets using CSP in Section 3.4.2. All the materials characterisation details were given in Section 3.4.3. Lastly, the LCO/1%MWrGO which has been annealed were electrochemically evaluated in a 2032 type coin cell, as detailed in Section 3.4.4.

### 3.1. Materials and reagents list

All the chemicals used in this project are alphabetically tabulated in Table 3-1, along with the chemical formula, the chemical grade as well as materials supplier. All the chemicals were used without further purification.

**Table 3-1.** The materials list of the chemical formula, the chemical name, the chemical grade, and the materials supplier used in this project.

Formula	Chemical name	Chemical grade	Supplier
AgNO <sub>3</sub>	Silver nitrate	≥ 99.0%, ACS reagent	Sigma Aldrich
Al	Aluminium foil	12 μm thick, purity > 99.9%	
Ar	Argon	99.9% purity	BOC Ltd. UK
C	Graphite	Briquetting grade, ~100 mesh	Alfa Aesar
CaCl <sub>2</sub>	Calcium chloride	≥ 99.0%, ACS reagent	Sigma Aldrich
(CH <sub>2</sub> O) <sub>2</sub> CO	Ethylene carbonate	≥ 99.0%	Fisher Scientific
C <sub>2</sub> H <sub>5</sub> OH	Ethanol	Analytical grade	Fisher Scientific
CNTs	Multi-walled carbon nanotubes	> 98.0%, 10 - 30 μm length, 10 - 20 nm outer diameter	Time Nano, China
Concentrated H <sub>2</sub> SO <sub>4</sub>	Concentrated sulfuric acid	97%, ACS reagent	Sigma Aldrich
Co <sub>3</sub> O <sub>4</sub>	Cobalt (II, III) oxide	≥ 99%	Sigma Aldrich
Cu	Copper foil	10 μm thick, purity > 99.9%	
HCl	Hydrogen chloride	10 wt%, Puriss	Sigma Aldrich
H <sub>2</sub> O <sub>2</sub>	Hydrogen peroxide	30%, Perhydrol <sup>®</sup> EMSURE	EMD Millipore
KMnO <sub>4</sub>	Potassium permanganate	> 99.0%, ACS reagent	Sigma Aldrich
KOH	Potassium hydroxide	≥ 99.9%, anhydrous	Sigma Aldrich
Li	Lithium metal	≥ 99.9% purity, 75 mm thick, 19 mm wide	Fisher Scientific
Li <sub>2</sub> CO <sub>3</sub>	Lithium carbonate	≥ 99%	Fisher Scientific
LiPF <sub>6</sub>	Lithium hexafluorophosphate	≥ 98.0% purity	Fisher Scientific
NaNO <sub>3</sub>	Sodium nitrate	> 99.0%, ReagentPlus	Sigma Aldrich
NMP	<i>N</i> -Methyl-2-pyrrolidone	> 99.0%, ACS reagent	Sigma Aldrich
OC(OCH <sub>3</sub> ) <sub>2</sub>	Dimethyl carbonate	≥ 99.9%, anhydrous	Sigma Aldrich
PVdF	Polyvinylidene fluoride	Mw=534 000 by GPC	Sigma Aldrich



### 3.2. Cold sintering process of $\text{LiCoO}_2$ and $\text{LiCoO}_2/\text{xCNTs}$ pellets

This section involves the experimental details to produce LCO pellets with CNTs being used as conductive fillers via CSP. As illustrated in Fig. 3-1, the flow chart starts from the synthesis of  $\text{LiCoO}_2$  powder to cold sintering process of  $\text{LCO}/\text{xCNTs}$  pellets, along with sample characterisation and the application of  $\text{LCO}/3\%\text{CNTs}$  pellet for LIBs.

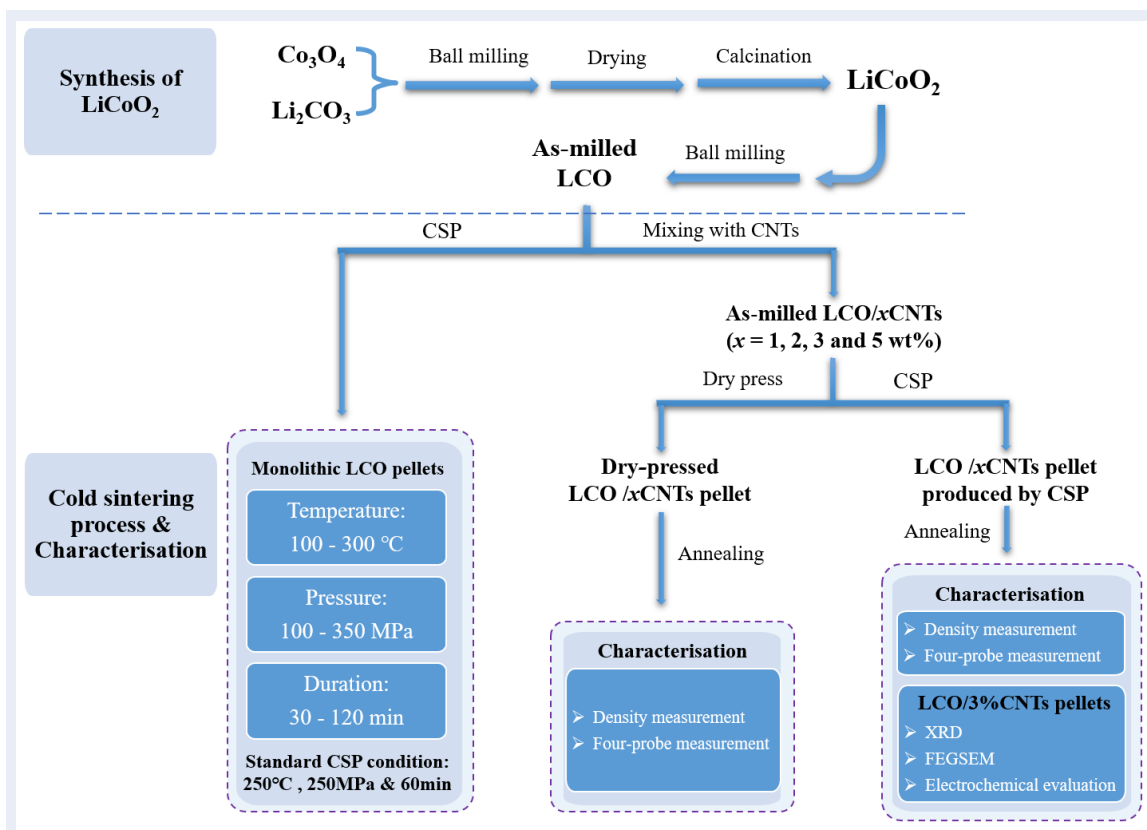


**Fig. 3-1.** The flow chart of the overall experimental works to make monolithic LCO pellets produced by CSP, dry-pressed  $\text{LCO}/\text{xCNTs}$  pellets and  $\text{LCO}/\text{xCNTs}$  pellets produced by CSP.

### 3.2.1. Synthesis of LCO powder

The LCO precursors were first planetary ball milled (Pulverisette-6, Fritsch, as shown in Fig. 3-2) using the stoichiometric amounts of  $\text{Co}_3\text{O}_4$  ( $\geq 99\%$ ) and  $\text{Li}_2\text{CO}_3$  ( $\geq 99\%$ ) in ethanol using 10 mm zirconia balls at the rotation speed of 200 rpm for 16 hours. An additional stoichiometry of lithium (5 mol%) was introduced to compensate for the evaporation of lithium during the subsequent high-temperature calcination process. The ball-to-powder weight ratio was fixed at 10:1. The as-milled precursors were then dried at 80 °C in air overnight. Afterwards, they were calcinated at 850 °C for 5 hours in air to synthesise LCO powder in a programmable tube furnace (Elite Thermal Systems Ltd., UK). In order to reduce the particle size of as-calcinated LCO powder to facilitate the subsequent cold sintering process, it was ball milled in ethanol using 2 mm zirconia balls (ball-to-powder weight ratio = 20:1) at the rotation speed of 300 rpm for 20 hours, followed by drying at 80 °C overnight in air. The as-milled LCO powder was then subjected to a screen process using 150-mesh sieve to break up large soft agglomerates, which was intended to retain the particles with good flowability and uniform size distribution.



**Fig. 3-2.** The photograph of Fritsch Pulverisette-6 planetary ball milling machine used in this project.

### 3.2.2. Preparation of LCO/xCNTs powder

Owing to the nature of high aspect ratio and the strong intermolecular interaction such as Van der Waals forces and dipole-dipole interactions, carbon nanotubes are prone to self-entangle [245, 246]. Therefore, the commercial multi-walled carbon nanotubes (CNTs, Time Nano, China) used in this project were first dispersed in ethanol by ultrasonic treatment (Grant XUBA1, with an output power of 35 W at the operating frequency of 44 kHz) for 30 min to obtain dispersed CNTs suspension. Then, the as-milled LCO powders which have been screened were homogenised with 1 wt%, 2 wt%, 3 wt%, and 5 wt% CNTs suspension (the weight percentage of CNTs is relative to the mass of as-milled LCO powder) by ultrasonic bath for 30 min. Thereafter, the mixtures were ball milled using 2 mm zirconia balls at the rotation speed of 300 rpm for 20 hours to obtain homogeneous mixtures of LCO powder and CNTs (denoted as as-milled LCO/xCNTs, where  $x$  represents the weight percentage of CNTs relative to the as-milled LCO powder). The ball-to-powder weight ratio is 20:1. The as-milled LCO/xCNTs mixtures were then dried at 80 °C overnight in air.

### 3.2.3. Cold sintering process and post-CSP annealing

First, the as-milled LCO powder which has been screened was used to produce monolithic LCO pellets by CSP which are used as reference samples. Typically, 0.5 g as-milled LCO powder was mixed thoroughly with 20 wt% 2 M LiOH solution using mortar and pestle for 10 min. Then, the mixture was loaded into a hardened steel mould (with the diameter of 10 mm) and pressed at the uniaxial pressures of 100 - 350 MPa at varying temperatures (100 - 300 °C) for different holding times (30 - 120 min). The prepared pellets were denoted as monolithic LCO pellets in this project. The experimental setup used for cold sintering process in this project is shown in Fig. 3-3. After comprehensive investigation as demonstrated in Section 4.1, it is found that the optimal CSP condition to prepare monolithic LCO pellets was the temperature of 250 °C with the pressure of 250 MPa for the duration time of 60 min. This optimal CSP condition was then selected as the standard cold sintering process condition for the subsequent experiments.

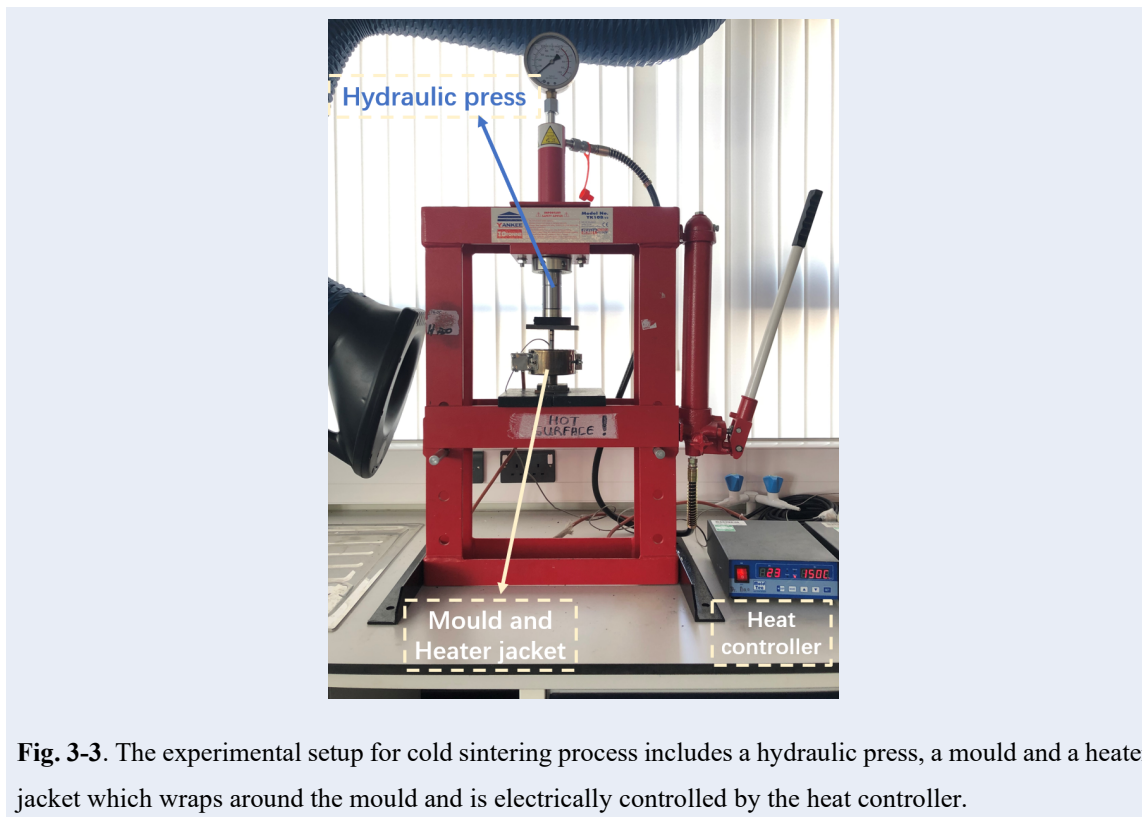
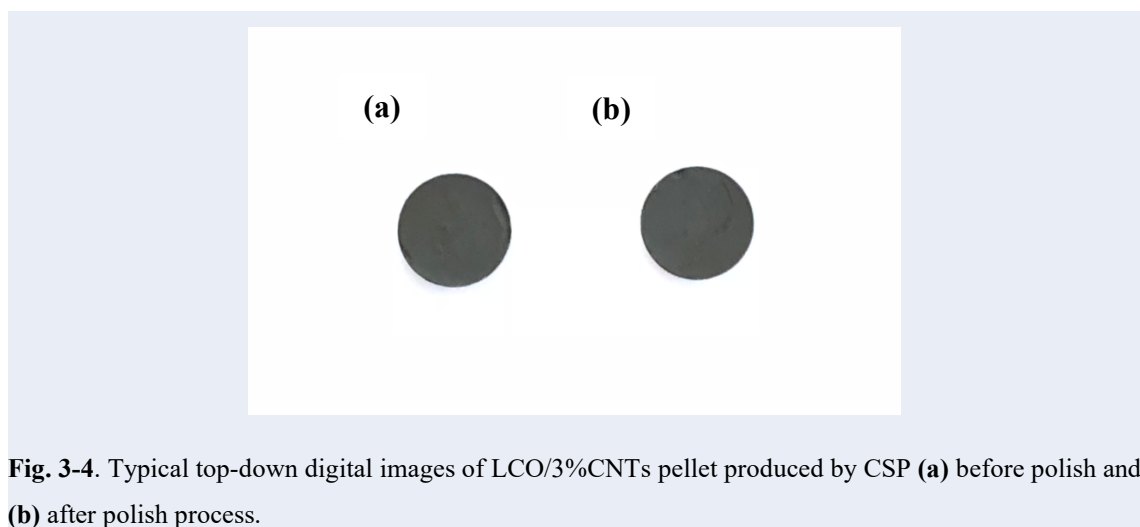


**Fig. 3-3.** The experimental setup for cold sintering process includes a hydraulic press, a mould and a heater jacket which wraps around the mould and is electrically controlled by the heat controller.

In the similar manner, the dried as-milled LCO/*x*CNTs (*x*=1 wt%, 2 wt%, 3 wt%, and 5 wt%) mixtures prepared above were used to produce LCO/*x*CNTs pellets at 250 °C and 250 MPa for 60 min. Typically, 0.5 g as-milled LCO/*x*CNTs mixture was mixed thoroughly with 20 wt% 2 *M* LiOH solution using mortar and pestle for 10 min. Afterwards, the well-mixed mixture was loaded into a 10 mm hardened steel die which was lubricated using PTFE spray to assist the ejection, and the mixture was pressed under the uniaxial pressures of 250 MPa at the temperatures of 250 °C for 60 min. Herein, the pellets produced by CSP were denoted as LCO/*x*CNTs pellets. A typical image of LCO/3%CNTs pellet was taken from the top-down view, as shown in Fig. 3-4 (a).



Subsequently, the LCO/*x*CNTs pellets produced by CSP were annealed at temperatures that ranged from 100 to 500 °C for 1 hour with a heating rate of 5 °C min<sup>-1</sup> in the tube furnace, followed by cooling to room temperature with a cooling rate of 5 °C min<sup>-1</sup>. For comparison, 0.5 g LCO/*x*CNTs mixture without the addition of LiOH solution was simply pressed at 250 MPa for 10 min at ambient temperature. The prepared pellets were denoted as dry-pressed LCO/*x*CNTs pellets and were used as control group. Afterwards, the dry-pressed LCO/*x*CNTs pellets were also annealed at the same temperatures (100 - 500 °C) for 1 hour with a heating rate of 5 °C min<sup>-1</sup> in the tube furnace.

### 3.2.4. Materials characterisation

The bulk densities of the pellets produced above, *i.e.*, monolithic LCO pellets and LCO/xCNTs pellets, were calculated by dividing the weight by the corresponding geometric dimensions. A digital micrometer (Mitutoyo 395, Kanagawa, Japan) was used to measure the dimensions of the pellets, including the thickness and the diameter of the pellets. Three pellets prepared at the same processing condition were measured and used to obtain arithmetic average density and standard deviation. The relative density was defined as the percentage of the bulk density over the theoretical density of the composite. The theoretical densities used for calculation are  $5.06 \text{ g cm}^{-3}$  for LCO [247] and  $1.80 \text{ g cm}^{-3}$  for CNTs [248].

X-ray diffraction (XRD) was used to characterise the phases of all the samples using a Bruker D2 Phaser X-ray diffractometer (Bruker AXS GmbH, Karlsruhe, Germany, 2000) which is controlled by Diffrac.suite software package. The diffraction data was collected in the scan range ( $2\theta$ ) of  $10^\circ - 80^\circ$  with a step size of  $0.05^\circ \text{ s}^{-1}$  (monochromatized Cu-K $\alpha$  radiation source operating at 30 kV and 10 mA,  $\lambda = 0.1542 \text{ nm}$ ). Field emission gun scanning electron microscope (FEGSEM) (JEOL JSM-7800F, JEOL Ltd. Japan) was used to study the morphologies of all the samples at an accelerating voltage of 5.0 kV in back scattering mode. Electrical conductivities of the pellets were measured at ambient temperature using a standard four-probe Van der Pauw method (Jandel RM3000 with DC current, UK). The direction of DC current was alternately changed to avoid generating a spurious appearance of accuracy caused by thermoelectric effect. Measurements were repeated 3 times to obtain mean electrical conductivity. The particle size distributions of the obtained as-calcined LCO powder and as-milled LCO powder were estimated using Horiba Partica LA-960V2 on the basis of laser diffraction. The specific surface areas of

the as-calcinated LCO powder and the as-milled LCO powder were measured using N<sub>2</sub> physisorption at the temperature of 77.35 K (Tristar<sup>TM</sup> 3000, Micromeritics Instrument Corporation, Norcross, USA) based on the Branauer-Emmett-Teller method (BET). Prior to the measurement, both samples were heated at 200 °C under vacuum condition (< 0.1 bar, Gallenkamp vacuum oven equipped with Edwards E8 rotary vacuum pump) overnight to remove all the adsorbed species.

### 3.2.5. Electrochemical measurements

#### 3.2.5.1. Coin cell assembly

The LCO/3%CNTs pellets produced by CSP were electrochemically evaluated by assembling into 2032 type coin cells. First, the LCO/3%CNTs pellets which has been subjected to annealing treatment at 400 °C for 1 hour were polished down to 100 ~ 200  $\mu\text{m}$  in thickness using abrasive-coated sandpapers with successively finer grit size of 220, 400, 600, and 1200 grit, followed by fabric cloth polishing. The typical top-down view and the fractured surface of the polished LCO/3%CNTs pellets are shown in Fig. 3-4 (b) and Fig. 3-5, respectively. Following that, the polished LCO/3%CNTs pellets were dried at 100 °C in vacuum oven for overnight to remove remaining moisture before transferring in Ar-gas filled glove box (LABstar, MBRAUN, Germany) with the  $\text{O}_2$  level of  $< 0.5$  ppm. Lithium metal discs with the diameter of 15 mm ( $\geq 99.9\%$  purity, 0.75 mm thick, Fisher Scientific) were polished with a stainless steel scalpel and used as counter electrode to build half cells. Microporous tri-layer membrane (Celgard<sup>®</sup> 2325 PP/PE/PP, 39% porosity, 25  $\mu\text{m}$ , as shown in Fig. 3-6) was used as separator and sandwiched between the working electrode and the lithium metal disc. The electrolyte was prepared by dissolving appropriate amount of  $\text{LiPF}_6$  salt in ethylene carbonate (EC)/dimethyl carbonate (DMC) (1:1 v/v for EC/DMC) to the concentration of 1.0 M, followed by storage over activated molecular sieves for 2 days because  $\text{LiPF}_6$  is likely to react with trace moisture and form HF. HF may attack oxidised  $\text{Co}^{4+}$  atoms upon cycling which results in a serious cycle to cycle capacity fading. 120  $\mu\text{L}$  of the electrolyte was equally added on both sides of the microporous separator using a micro-pipette. The top caps, springs, spaces, and bottom caps are made from 304 stainless steel. All the constituent parts used in the coin cell were stacked in the sequence as shown in Fig. 3-7. The



assembled cells were conditioned for 1 day before galvanostatic testing to ensure that the membranes and the working electrodes were fully impregnated in the electrolyte. The open-circuit voltages (OCV) of the as-fabricated coin cells were stabilised in the range of 2.0 – 3.2 V, which indicated that short-circuit did not occur between the working electrode and the lithium metal disc.

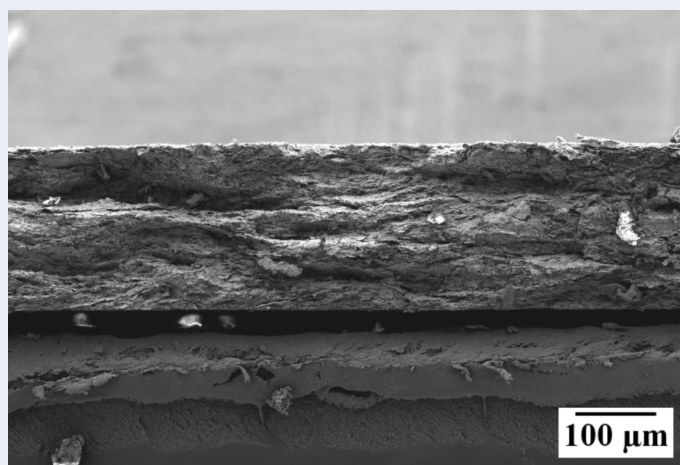


**Fig. 3-5.** FEGSEM image of the fractured LCO/3%CNTs pellet produced by CSP, revealing features such as the thickness and the surface flatness of the polished pellet.

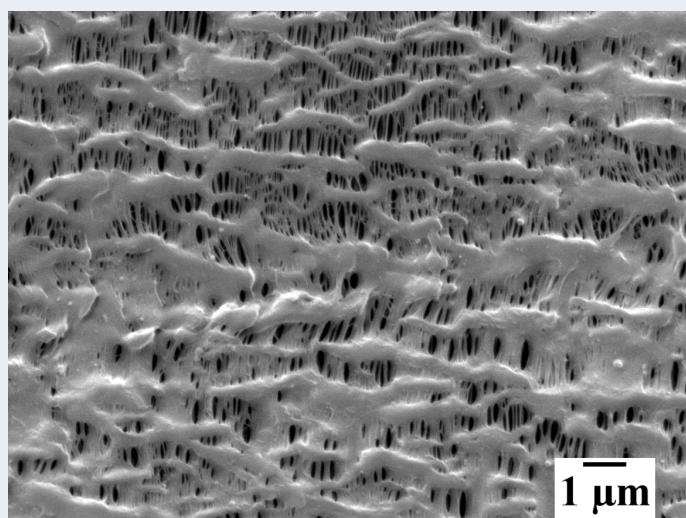


**Fig. 3-6.** FEGSEM image of Celgard® 2325 membrane used for all coin cell assembly, showing the pore size and pore distribution.

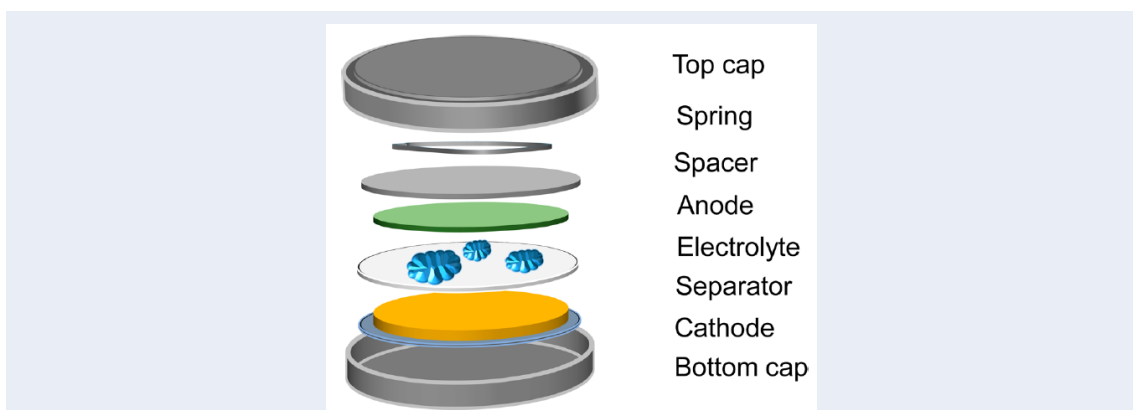


**Fig. 3-7.** Schematic illustration of all constituent parts used in 2032 type coin cell and the typical assembly configuration for LIBs (The anode is lithium metal disc in half cell configuration) [249].

### 3.2.5.2. Electrochemical evaluation

Galvanostatic charge/discharge measurements were carried out in the voltage window of 3.0 - 4.2 V (vs  $\text{Li}^+/\text{Li}$ ) at room temperature using Neware 8-channel battery test system (BTS-4008, China). The data acquisition was performed by BTSDA 6.0 Software package. For clarity, the current rate for the as-milled LCO was defined based on  $1\text{ C}=140\text{ mA g}^{-1}$  [82, 250]. Cyclability test was performed at the current rate of 0.1 C. Rate capability test was performed at the current rates of 0.1 C, 0.2 C, 0.5 C, and then 0.1 C. 5-min open-circuit-potential relaxation was programmed after each galvanostatic cycling step. For the calculation of the specific gravimetric capacity, the mass of the LCO was merely taken into consideration. For the calculation of the specific volumetric capacities, the total volume of the LCO and CNTs was taken into full consideration. Cycling voltammetry (CV) was carried out between 3.0 V and 4.2 V at the sweep rate of  $0.1\text{ mV s}^{-1}$  with two-electrode configuration using an electrochemistry workstation (Autolab PGSTAT204, Metrohm, Switzerland). All the key parameters to make coin cell using the LCO/3%CNTs pellets produced by CSP are summarised in Table 3-2.

### 3.2.5.3. Calculations for electrochemical data

- ✧ The specific gravimetric discharge capacity ( $C_g$ ) of a single cathode can be calculated from the galvanostatic charge-discharge curves using the formula:

$$C_g (\text{mAh g}^{-1}) = \frac{1}{m_{\text{LCO}}} \int_{t_1}^{t_2} I dt \quad [\text{Equation 10}]$$

Where,  $I$  is the constant current applied (unit: mA)

$t$  represents the discharge time (unit: hour)

$m_{\text{LCO}}$  is the net mass of  $\text{LiCoO}_2$  in a single cathode (unit: g)

- ✧ The specific volumetric discharge capacity ( $C_v$ ) of a single cathode is defined as the ratio of the total capacity to the total volume of a composite cathode. However, the conductive filler is electrochemically inactive and would not contribute for the total capacity. Henceforth, the total capacity of a composite cathode equals to the capacity of  $\text{LiCoO}_2$  in this case.

$$C_v (\text{mAh cm}^{-3}) = \frac{\text{Capacity}_{\text{composite}}}{\text{Volume}_{\text{composite}}} = \frac{\text{Capacity}_{\text{LiCoO}_2}}{\text{Volume}_{\text{composite}}} = \frac{m_{\text{LCO}} \times C_g}{\text{Volume}_{\text{composite}}} =$$

$$\frac{m_{\text{composite}} \times W_{\text{LCO}} \times C_g}{\text{Volume}_{\text{composite}}} = \text{Density}_{\text{composite}} \times W_{\text{LCO}} \times C_g \quad [\text{Equation 11}]$$

Where,  $m_{\text{LCO}}$  and  $m_{\text{composite}}$  are the total weights of  $\text{LiCoO}_2$  and composite cathode, respectively.

$W_{\text{LCO}}$  is the weight fraction of  $\text{LiCoO}_2$  in a single composite cathode

$\text{Volume}_{\text{composite}}$  is the measured volume of the composite cathode

$\text{Density}_{\text{composite}}$  is the overall density of a composite cathode. It can be determined if the relative density and theoretical density of the composite cathode are given.

The theoretical density of the composite cathode ( $\rho_{\text{composite}}$ ) can be defined as the ratio of the weight of the composite cathode ( $w_{\text{composite}}$ ) to the theoretical volume of the composite cathode ( $v_{\text{composite}}$ )

$$\rho_{composite} = \frac{m_{composite}}{v_{composite}}$$

According to the law of mixtures, the theoretical volume of the composite cathode is the sum of theoretical volumes of LCO ( $v_{LCO}$ ) and conductive filler ( $v_{CF}$ )

$$v_{composite} = v_{LCO} + v_{CF}$$

Therefore

$$\frac{m_{composite}}{\rho_{composite}} = \frac{m_{LCO}}{\rho_{LCO}} + \frac{m_{CF}}{\rho_{CF}}$$

$$\frac{1}{\rho_{composite}} = \frac{1}{\rho_{LCO}} \left( \frac{m_{LCO}}{m_{composite}} \right) + \frac{1}{\rho_{CF}} \left( \frac{m_{CF}}{m_{composite}} \right)$$

By expressing in terms of weight fractions

$$\frac{1}{\rho_{composite}} = \frac{W_{LCO}}{\rho_{LCO}} + \frac{W_{CF}}{\rho_{CF}}$$

$$\rho_{composite} = \frac{1}{\left( \frac{W_{LCO}}{\rho_{LCO}} + \frac{W_{CF}}{\rho_{CF}} \right)} \text{ [Equation 12]}$$

Where,  $\rho_{composite}$  is the theoretical composite density

$m_{LCO}$  and  $m_{CF}$  are the masses of LCO and conductive filler, respectively

$W_{LCO}$  and  $W_{CF}$  are the weight fractions of LCO and conductive filler, respectively

$\rho_{LCO}$  and  $\rho_{CF}$  are the theoretical densities of LCO and conductive filler, respectively

- ✧ If the operating voltage of LCO is given, one can easily calculate the specific volumetric energy density ( $E_v$ ) by the below equation:

$$E_v \text{ (Wh L}^{-1}\text{)} = C_v \times U \text{ [Equation 13]}$$

Where,  $C_v$  is the specific volumetric discharge capacity (unit: mAh cm<sup>-3</sup>)

$U$  is the operating voltage (unit: V)

#### 3.2.5.4. Post-mortem characterisation

In order to study the effect of electrochemical cycling on the electrode, the coin cells which have been galvanostatically charged/discharged for 40 cycles were carefully disassembled inside argon-filled glovebox and the electrodes were characterised using FEGSEM. Prior to the disassembly, the coin cells were fully discharged to 3.0 V until the discharge current was less than 0.01 C to ensure all the stored capacity was released. The disassembled electrodes were rinsed three times with DMC to clean off the lithium salts that had adsorbed on the surfaces, followed by immersion in DMC solvent overnight in glovebox. Afterwards, the treated electrodes were dried in a drying oven and fractured for FEGSEM observation. For comparison, an electrode without galvanostatic charge/discharge process was also fractured and characterised using FEGSEM.

**Table 3-2.** The formula, current collector, counter electrode, separator, electrolyte volume, and galvanostatic test conditions of LCO/3%CNTs pellets produced by CSP, LCO/1%MWrGO pellets produced by CSP, MWrGO anode, CNTs-containing cathode, and MWrGO-containing cathode.

Electrode	LCO/3%CNTs pellet	LCO/1%MWrGO pellet	MWrGO anode	CNTs-containing cathode	MWrGO-containing cathode
Formula	97 wt% LCO + 3 wt% CNTs	99 wt% LCO + 1 wt% MWrGO	60 wt% MWrGO + 40 wt% PVdF	89 wt% + 3 wt% CNTs + 8 wt% PVdF	91 wt% + 1 wt% MWrGO + 8 wt% PVdF
Current collector	N/A	N/A	Copper foil	Aluminium foil	Aluminium foil
Counter electrode	Lithium metal	Lithium metal	Lithium metal	Lithium metal	Lithium metal
Separator	Celgard <sup>®</sup> 2325	Celgard <sup>®</sup> 2325	Celgard <sup>®</sup> 2325	Celgard <sup>®</sup> 2325	Celgard <sup>®</sup> 2325
Electrolyte volume	120 $\mu$ L	120 $\mu$ L	500 $\mu$ L	120 $\mu$ L	120 $\mu$ L
Galvanostatic test condition [V vs Li <sup>+</sup> /Li]	3.0 - 4.2 V	3.0 - 4.2 V	0.01 - 2.5 V	3.0 - 4.2 V	3.0 - 4.2 V

### 3.3. Microwave-assisted reduction of graphene oxide

This section gives the details of the experimental procedures involved to synthesise microwave reduced graphene oxide (MWrGO) from graphene oxide (GO). The flow chart of the overall work undertaken on preparation of GO, coagulation bath, annealing treatment, microwave reduction, and characterisation techniques are given in Fig. 3-8.

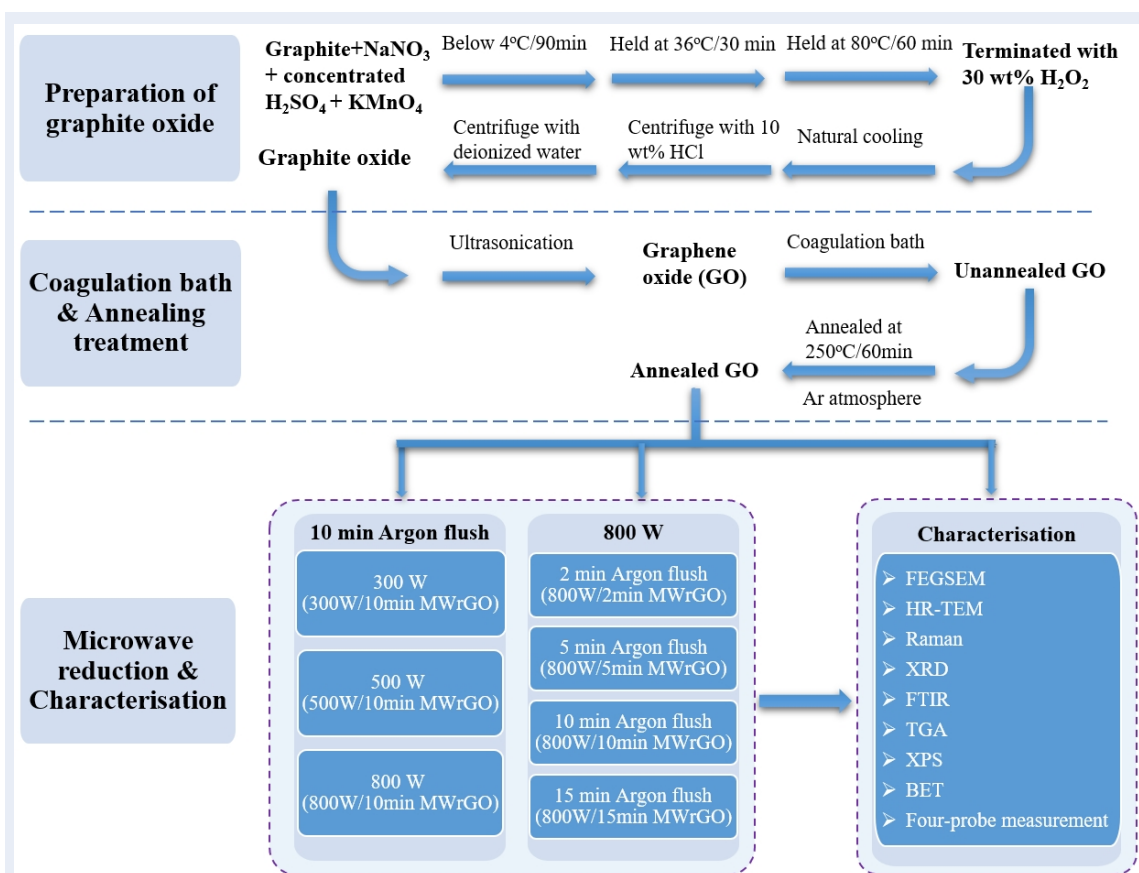


**Fig. 3-8.** The flow chart of the overall experimental work starting from raw materials to microwave reduction of graphene oxide, along with the materials characterisation techniques.

### 3.3.1. Synthesis of graphite oxide

The preparation of graphite oxide was adopted from a modified Hummer's method [158, 251]. The graphite oxide was synthesised through various temperature regimes (low temperature, medium temperature, and high temperature) to accelerate the reaction kinetics (within 4 hours) and precisely control the extent of the oxidation of pristine graphite, which was helpful to enhance the exfoliation of graphite oxide. All the chemical reagents used are in as-received condition without further purification.

Typically, 2.5 g graphite with particle size of ~100 mesh (briquetting grade, Alfa Aesar) and 1.2 g  $\text{NaNO}_3$  (> 99.0%, Sigma Aldrich) were slowly added in 55 ml concentrated  $\text{H}_2\text{SO}_4$  (97%, Sigma Aldrich) contained in a three-necked flask which was immersed in an ice bath (< 4 °C). The  $\text{NaNO}_3$  are able to intercalate between graphitic layers and expand its structures to promote the subsequent exfoliation. But it may generate toxic gaseous by-products, such as  $\text{NO}_2$  and  $\text{N}_2\text{O}_4$ , during the oxidation process [251]. Therefore, the reaction flask was required to be loosely capped and the synthesis of graphite oxide should be cautiously carried out in high-flowrate fume hood. After graphite and  $\text{NaNO}_3$  were thoroughly mixed with concentrated  $\text{H}_2\text{SO}_4$ , 7.5 g  $\text{KMnO}_4$  (> 99.0%, Sigma Aldrich) was slowly added over the course of 30 min so as to maintain the system temperature below 4 °C in the ice bath.

*Low temperature reaction:* The solution was magnetically stirred for 90 min and the temperature was carefully controlled below 4 °C.

*Medium temperature reaction:* The temperature of the solution was raised to 36 °C to accelerate oxidation reaction and hold for 30 mins. After the oxidation, the solution turned into a viscous brown suspension.



*High temperature reaction:* 110 ml deionised water (with a resistivity of  $> 1 \text{ M}\Omega\cdot\text{cm}$ ) was then added slowly in the suspension and the system temperature was found to rise up by  $\sim 20^\circ\text{C}$  because of dissipated heat. External heating was simultaneously applied to increase the suspension temperature at  $80^\circ\text{C}$  for 60 mins.

Afterwards, the oxidation reaction was terminated by adding 10 ml 30 wt%  $\text{H}_2\text{O}_2$  (Perhydrol<sup>®</sup> EMSURE), followed by a natural cooling to room temperature. The colour of the suspension turned into yellowish brown. In order to remove the residual metal ions, the suspension was re-dispersed and washed for three times with 10 wt% HCl solution (Sigma Aldrich) by centrifugation at 2000 rpm (Biofuge Primo centrifuge, Thermo Scientific). Finally, the resultant graphite oxide cake was copiously purified with deionised water for several times till no white precipitation of AgCl was observed in supernatant by adding  $\text{AgNO}_3$  solution. At this point, the pH value of the supernatant normally were in the range of 6-7 [178]. The last centrifugation was carried out at 3500 rpm for 30 min to remove un-exfoliated graphite oxide and/or un-oxidised pristine graphite.  $1.50 \pm 0.1$  g of graphite oxide was produced from 1 g pristine graphite through this step.

### 3.3.2. Coagulation bath of GO

The graphite oxide colloidal suspension was diluted to the concentration of  $15 \text{ mg ml}^{-1}$  and was ultrasonicated for 2 h to obtain homogeneous graphene oxide (GO) suspension. Then, the GO suspension was loaded in a plastic syringe equipped with a needle (BD Microlance<sup>®</sup>, inner diameter: 0.8 mm, length: 50 mm, and needle gauge: 21 G) and was extruded into 1 wt%  $\text{CaCl}_2$  ( $> 99.0\%$ , Sigma Aldrich) coagulation bath containing with 5 wt% ethanol (Analytical grade, Fisher Chemical) at the extrusion speed of  $2.0 \text{ ml min}^{-1}$  to form GO beads using a syringe pump (AL-1000, World Precision Instruments, UK). The freshly formed GO beads were too mechanically weak to be handled with. Hence, they were soaked in  $\text{CaCl}_2$  coagulation solution for 24 hours so as to achieve enough mechanical strength for handling. The formation of GO beads in  $\text{CaCl}_2$  coagulation bath is shown in [Video S1](#) and the images of bead-like spheroid GO are given in Fig. 3-9. The GO beads were then washed with deionised water for 3 times to remove the residual  $\text{CaCl}_2$  salt, followed by drying at  $50^\circ\text{C}$  overnight to obtain as-prepared GO. However, the spheroidal structure of GO beads collapsed after drying as a result of the loss of ethanol-containing water. The dried sample was then stored in a desiccator until use.

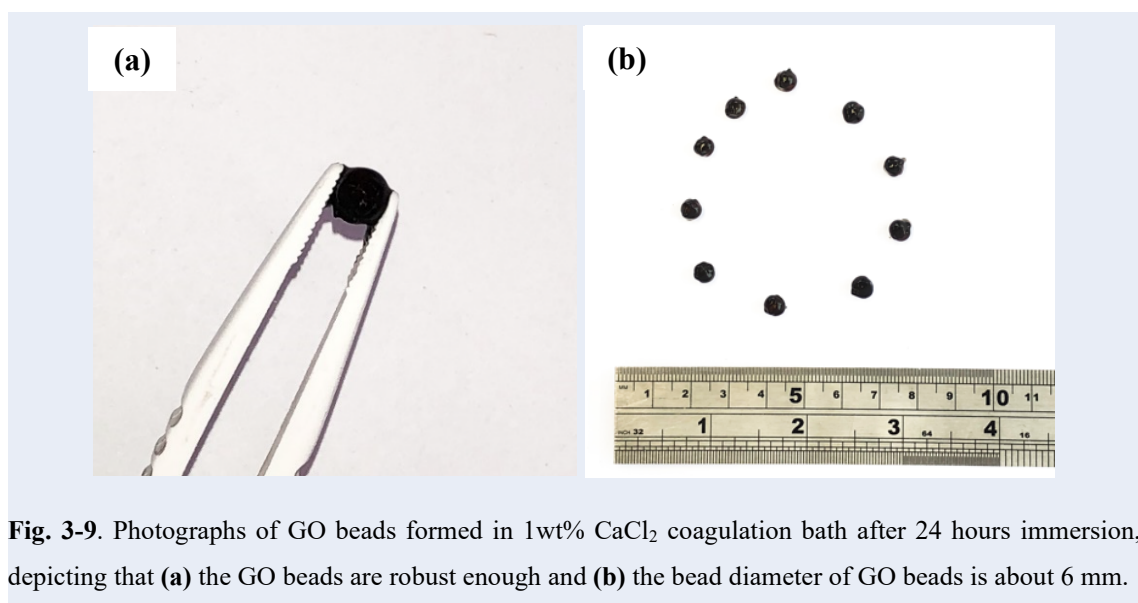


**Fig. 3-9.** Photographs of GO beads formed in 1wt%  $\text{CaCl}_2$  coagulation bath after 24 hours immersion, depicting that (a) the GO beads are robust enough and (b) the bead diameter of GO beads is about 6 mm.

### 3.3.3. Synthesis of MWrGO

The as-prepared GO were thermally annealed at 250 °C for 1 hour in argon atmosphere. The setup used for the microwave-assisted reduction of annealed GO was schematically shown in Fig. 3-10. The annealed GO was placed in an alumina crucible inside a microwave transparent quartz reactor which was filled with insulating quartz wool. Prior to microwave irradiation, the quartz reactor was evacuated and flushed with argon gas (99.9% purity) at the flow rate of 1.0 L min<sup>-1</sup> for different times (2 mins, 5 mins, 10 mins, and 15 mins) to create inert gas atmospheres for the subsequent microwave-assisted reduction of GO. Microwave irradiation was then carried out at different powers of 300 W, 500 W, and 800 W operating at the frequency of 2.45 GHz using a customised variable power microwave oven (WaveDOM 7020, LG Milton Keynes, UK). During microwave irradiation, the microwave oven was properly sealed to the detectable microwave leakage less than 5 mW cm<sup>-2</sup> using a microwave detector (Apollo Microwaves, Ltd., Canada), which ensured most the microwave energy was absorbed by the samples. The final products are denoted as microwave power/argon flushing time + MWrGO, as given in Table 3-3. Upon microwave irradiation, the real-time temperature field across all the samples was monitored using a high-resolution thermal imaging camera (FLIR Thermovision® A655sc, FLIR Systems AB, Sweden) through a top hole of the microwave oven. The frame rate of the camera can achieve up to 50 Hz. Interestingly, during microwave irradiation, strong microwave arcing was initiated from annealed GO samples. A typical video and photographs of microwave arcing were given in [Video S2](#) and Fig. 3-11, respectively. The microwave irradiation process was ceased immediately after the arcing happened. For comparison, an as-prepared GO sample without the annealing treatment (unannealed GO) was exposed to 800 W microwave irradiation after 10 min

Argon flow atmosphere but no arcing was observed on the unannealed GO samples.

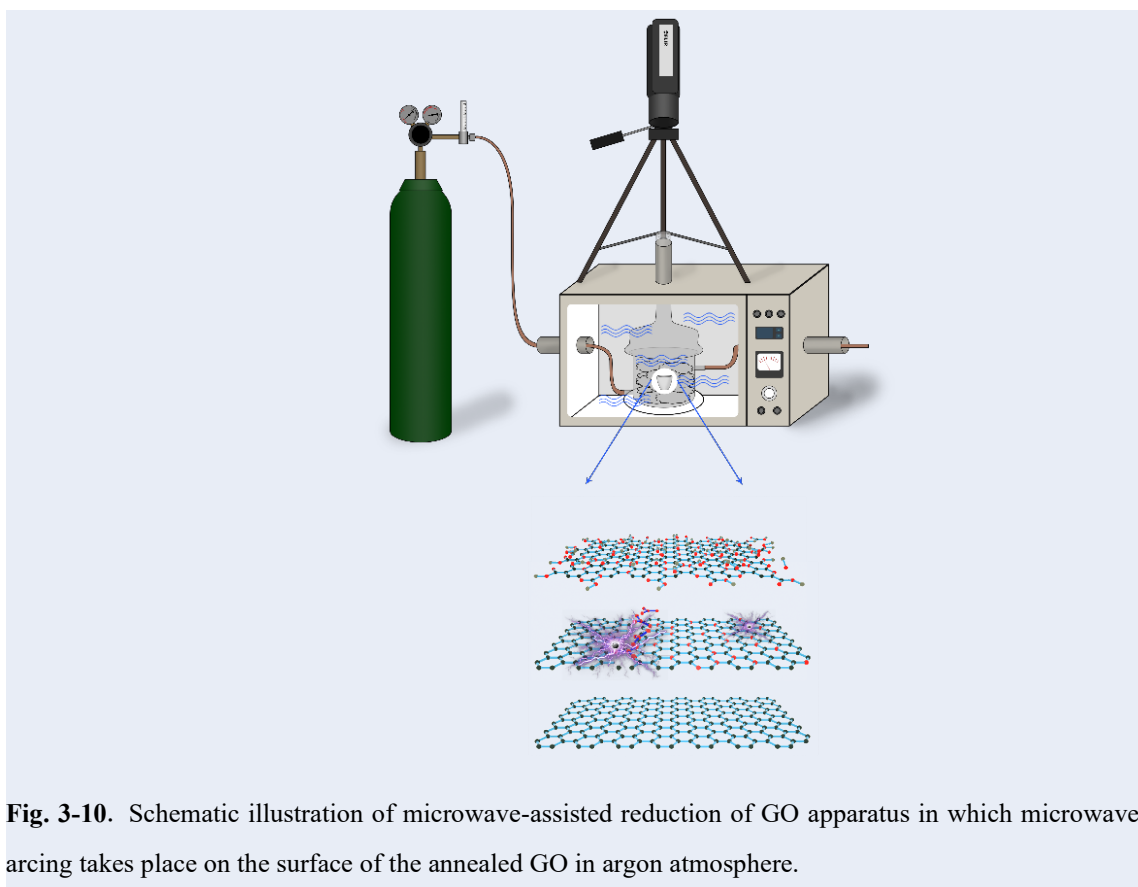


**Fig. 3-10.** Schematic illustration of microwave-assisted reduction of GO apparatus in which microwave arcing takes place on the surface of the annealed GO in argon atmosphere.

**Table 3-3.** The sample denotation of all the MWrGO synthesised with various microwave powers and argon flushing times.

Microwave power [W]	Argon flushing time [min]	Denotation
300	10	300W/10min MWrGO
500	10	500W/10min MWrGO
800	10	800W/10min MWrGO
800	2	800W/2min MWrGO
800	5	800W/5min MWrGO
800	15	800W/15min MWrGO

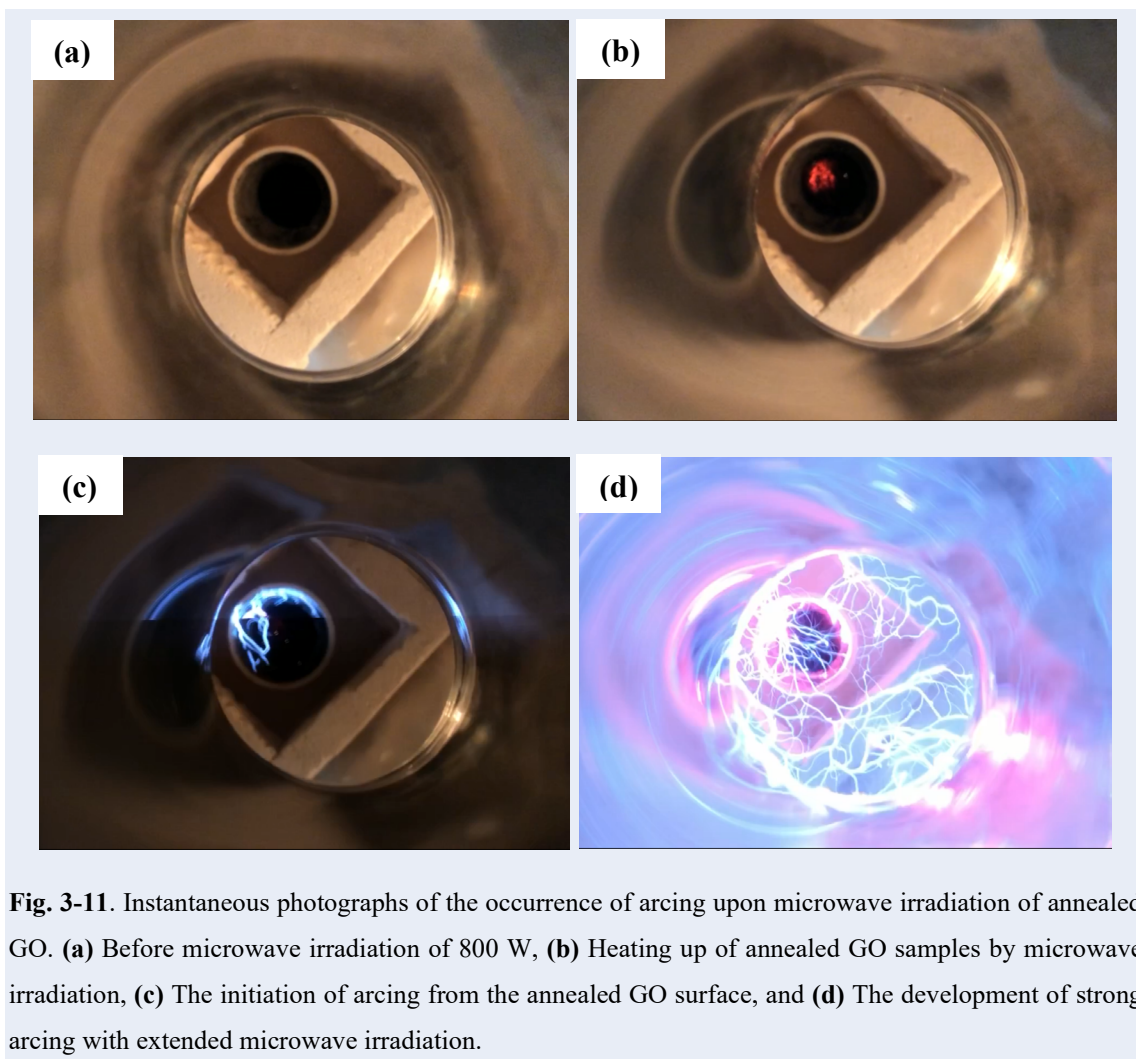


**Fig. 3-11.** Instantaneous photographs of the occurrence of arcing upon microwave irradiation of annealed GO. **(a)** Before microwave irradiation of 800 W, **(b)** Heating up of annealed GO samples by microwave irradiation, **(c)** The initiation of arcing from the annealed GO surface, and **(d)** The development of strong arcing with extended microwave irradiation.

### 3.3.4. Materials characterisations of MWrGO

Field emission gun scanning electron microscope (FEGSEM) (JEOL JSM-7800F, JEOL Ltd. Japan) equipped with an energy dispersive X-ray spectrometer (Oxford Instrument, UK) was used to study the morphologies and the compositions of MWrGO at a low accelerating voltage of 3.0 kV in gentle-beam mode. High-resolution transmission electron microscopy (HR-TEM) (FEI Tecnai™ F20 S-twin, Thermo Scientific, UK) equipped with Supertwin symmetric lenses and spherical aberration corrector, was employed to characterise the MWrGO dispensed on 300-mesh TEM grids covered with thin amorphous Lacey carbon. The accelerating voltage of 100 kV was applied on the

susceptible MWrGO samples to minimize electron beam induced structural damages whilst achieving sufficient image contrast. Micron-Raman spectroscopic analysis was obtained from the powder samples with glass slides as substrates in the back-scattering configuration on a Horiba Jobin-Yvon LabRam HR Spectrometer equipped with a N<sub>2</sub> cooled charge coupled device detector. The argon-air laser excitation of 514.5 nm (2.41 eV, 80 mW at the microscope objective) was used with a 50× objective lens mounted on an optical microscope (Olympus) and the spot size of the laser was ~1 μm<sup>2</sup>. Raman spectra were recorded over the range of 1000 - 3500 cm<sup>-1</sup>. A standard silicon wafer sample was used to factory calibrate the equipment till the peak position was at 520 cm<sup>-1</sup> with a resolution less than 1 cm<sup>-1</sup>. The X-ray diffraction (XRD) patterns were collected in the scan range (2θ) of 10° - 80° with a step size of 0.05° s<sup>-1</sup> (monochromatized Cu-Kα radiation source operating at 30 kV and 10 mA, λ = 0.1542 nm) using a Bruker D2 Phaser X-ray diffractometer (Bruker AXS GmbH, Karlsruhe, Germany, 2000). Attenuated total reflectance-Fourier transform infrared spectroscopy (FTIR) (Shimadzu FTIR-8400S, Japan, maximum wavelength resolution of 0.85 cm<sup>-1</sup>) was conducted to evaluate the presence of functional groups on the samples. The FTIR spectra were recorded against an air background. Thermogravimetric analysis (TGA) was performed on a TA Instruments Q5000IR thermobalance. The samples were loaded in a tared 100 μL alumina crucible and the mass was monitored over the temperature range of 20 - 800 °C under constant nitrogen flow (100 mL min<sup>-1</sup>). The TGA heating rate was 1 °C min<sup>-1</sup> for as-prepared GO and 5 °C min<sup>-1</sup> for other samples. The heating rate of as-prepared GO had to be kept at or below 1 °C min<sup>-1</sup> to avoid exfoliating the material during the scan. Faster heating rates produce deflagration sufficiently powerful to remove the pan lid and most of the sample from the pan, resulting in inaccurate scans. X-ray photoelectron spectroscopy (XPS) was recorded using a monochromatic Al-Kα anode X-ray source ( $h\nu=1486.6$  eV, 400 μm spot

size) with a K-Alpha Spectrometer (Thermo Scientific, UK). The chamber pressure was maintained at  $\sim 10^{-8}$  Torr. Prior to XPS characterisation, all the samples were dried at 100 °C overnight to remove trapped water and oxygen due to the hygroscopic nature of GO and the large surface area of MWrGO, which may increase the oxygen detection [159]. The surface charge was calibrated by the binding energy of C1s hydrocarbon peak at 284.8 eV and was neutralised with an electron flood gun. The XPS data was interpreted using the Thermo Scientific Advantage software. For each sample, a survey scan was first performed, followed by high-resolution scans on the spectral regions of interest. C1s peaks were fitted using a Shirley background subtraction and 75% Gaussian/25% Lorentzian line shapes. The isotherms of N<sub>2</sub> physisorption were recorded at the temperature of 77.35 K using a Micromeritics equipment (Tristar™ 3000, Micromeritics Instrument Corporation, Norcross, USA). Prior to measurement, the test samples were degassed at 100 °C in a vacuum line ( $< 0.1$  bar) overnight to remove all the adsorbed species. The specific surface area ( $S_{\text{BET}}$ ) and the pore size distribution were calculated based on the Branauer-Emmett-Teller method (BET) and Barrer-Joyner-Halenda method (BJH), respectively. Electrical conductivity was measured on pelletized powders (diameter: 10 mm and pressing force: 5 tons) at ambient temperature using a standard four-probe Van der Pauw method (Keithley Micro-ohmmeter 580 with DC source). Measurements were repeated 3 times to obtain mean values for each sample.

### 3.3.5. Electrochemical measurements

Due to the low  $\text{Li}^+$  intercalation/deintercalation potential ( $< 1 \text{ V vs Li}^+/\text{Li}$ ) and the robust graphitic structure of carbonaceous materials, 800W/10min MWrGO is believed to be a promising electroactive material used in anode for LIBs. In addition, owing to the high electrical conductivity and the large surface area, 800W/10min MWrGO can also be used as conductive additive in cathode for LIBs. Therefore, in this project, the selected 800W/10min MWrGO was used as electroactive material in anode and was used as conductive additive in  $\text{LiCoO}_2$  cathode. Moreover, in efforts to demonstrate the advantages of the synthesised 800W/10min MWrGO as conductive additive in cathode,  $\text{LiCoO}_2$  cathode containing 800W/10min MWrGO is electrochemically compared with the counterpart containing commercial multi-walled carbon nanotubes (CNTs) by assembling 2032 type half cells.

#### 3.3.5.1. MWrGO anode preparation

Electrochemical evaluation of the 800W/10min MWrGO used as electroactive material in anode was carried out by assembling 2032 type coin cells. The slurry of 60 wt% 800W/10min MWrGO and 40 wt% polyvinylidene difluoride (PVdF) was made at  $60^\circ\text{C}$  using *N*-methyl pyrrolidinone (NMP,  $> 99.0\%$ , Sigma Aldrich) as solvent and was continuously stirred using PTFE-coated magnetic stirrers for overnight. The homogenous slurry was then cast to form a uniform coating onto battery-grade copper foil ( $10 \mu\text{m}$  thick, purity  $> 99.9\%$ ) using doctor blade technique, followed by drying at  $100^\circ\text{C}$  for 10 h in a vacuum oven ( $< 0.1 \text{ bar}$ ). Afterwards, the dried electrode being free of visible defects was mechanically compacted with a roller compressor to achieve improved adherence of the graphene sheets to the copper substrate and electrode wettability. After the drying and



roll-pressing processes, the dried coating was reduced to  $\sim 25\ \mu\text{m}$  in thickness. A typical cross section of roll-pressed MWrGO anode is shown in Fig. 3-12. MWrGO anode discs with the diameter of 8 mm were then punched out for cell assembly. The mass loading on each MWrGO anode disc amounted to  $\sim 0.2\ \text{mg cm}^{-2}$ .

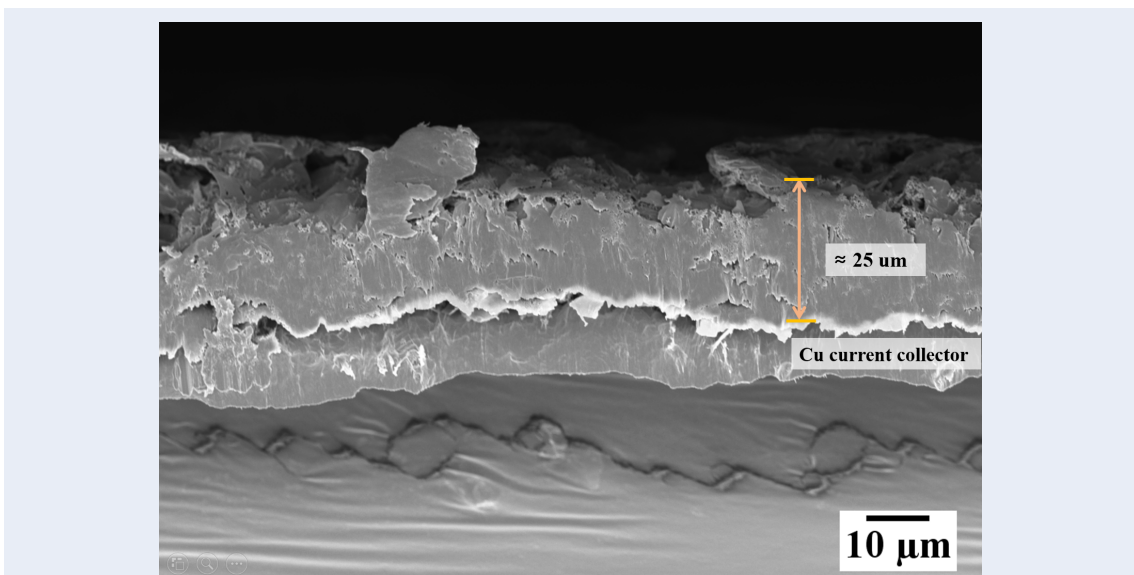


**Fig. 3-12.** Typical FEGSEM image of cross-sectioned MWrGO anode which has been dried and roll pressed, along with the copper current collector.

### 3.3.5.2. Cathode preparation

The  $\text{LiCoO}_2$  used in this section was the as-calcinated LCO powder prepared in Section 3.2.1. The slurry of 91 wt% LCO, 1 wt% 800W/10min MWrGO and 8 wt% PVdF was made for MWrGO-containing LCO cathode (LCO-MWrGO) and the slurry of 89 wt% LCO, 3 wt% CNTs and 8 wt% PVdF was made for CNTs-containing LCO cathode (LCO-CNTs) using appropriate amount of NMP. The slurries were thoroughly stirred at  $60\ ^\circ\text{C}$  using PTFE-coated magnetic stirrer for overnight. The homogenous slurries were then cast to form a coating with the thickness of  $100\ \mu\text{m}$  on freshly etched aluminium foils ( $12\ \mu\text{m}$  thick, purity  $> 99.9\%$ , etched with 5 wt% KOH solution [252]) using doctor blade technique, followed by drying at  $100\ ^\circ\text{C}$  for 10 h in a vacuum oven ( $< 0.1\ \text{bar}$ ). Afterwards,

the dried electrode being free of visible cracks was mechanically compacted with a roll compressor to improve the inter-particle contact and enhance the adhesion to the aluminium substrate [253]. After the drying and the roll-pressing processes, the dried coating was reduced to  $\sim 50\ \mu\text{m}$  in thickness. A quintessential example of roll-pressed LCO-MW<sub>r</sub>GO cathode is shown in Fig. 3-13. Notably, the cross-sectional FEGSEM image reveals the intimate contact between the electroactive LCO powder and the current collector. Cathode discs with the diameter of 8 mm were then punched out for cell assembly. Cathode mass was measured using a laboratory analytical balance (Fisher Scientific). The mass loading on the electrodes amounted to  $\sim 3.1\ \text{mg cm}^{-2}$  for LCO-MW<sub>r</sub>GO cathode discs and to  $\sim 3.0\ \text{mg cm}^{-2}$  for LCO-CNTs cathode discs. In order to compare the electrical conductivities of the conductive additives, the 800W/10min MW<sub>r</sub>GO powder and the CNTs powder were pelletized with the diameter of 10 mm at the same pressing force of 5 tons and were measured to be  $761.4\ \text{S m}^{-1}$  and  $528.2\ \text{S m}^{-1}$ , respectively, at ambient temperature using a four-probe Van der Pauw method (Jandel RM3000 with DC source with DC current, UK).

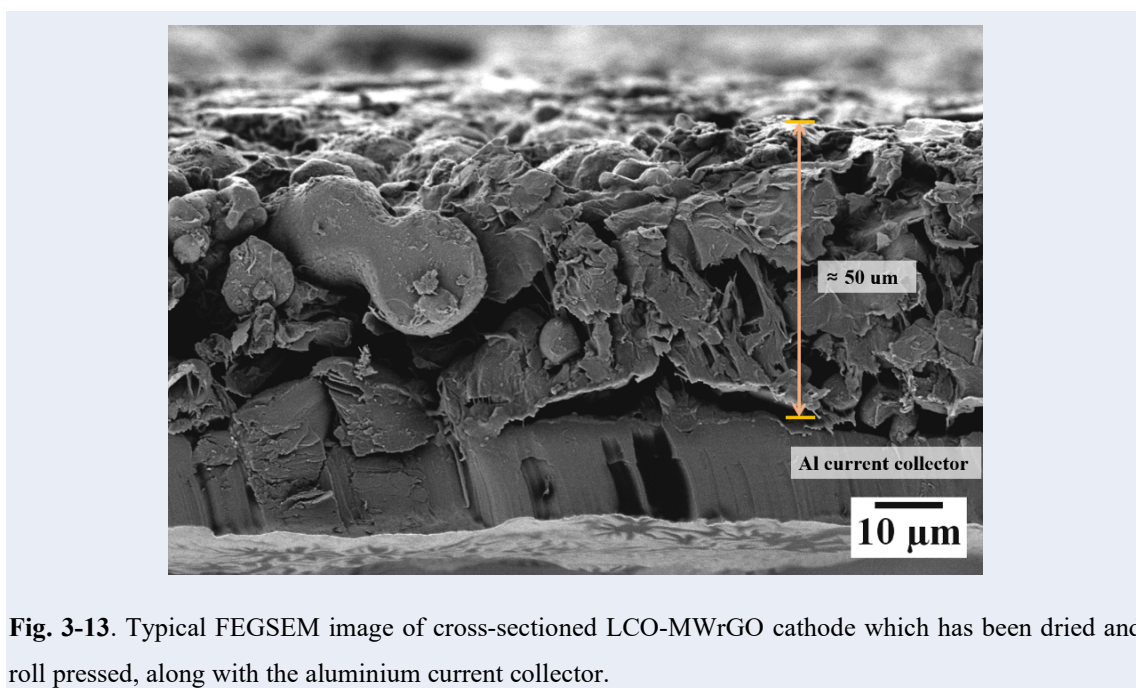


**Fig. 3-13.** Typical FEGSEM image of cross-sectioned LCO-MW<sub>r</sub>GO cathode which has been dried and roll pressed, along with the aluminium current collector.

### 3.3.5.3. Coin cell assembly

The coin cell assembly follows the same working procedures as explained in Section 3.2.5.1. All the working electrodes prepared above, *i.e.*, MWrGO anode, LCO-MWrGO cathode and LCO-CNTs cathode, were dried in vacuum oven ( $< 0.1$  bar) at  $100\text{ }^{\circ}\text{C}$  for overnight to remove remaining moisture before transferring in Ar-gas filled glove box which was maintained at  $< 0.5$  ppm of  $\text{O}_2$  level. Polished lithium metal discs with the diameter of  $15\text{ mm}$  ( $\geq 99.9\%$  purity,  $0.75\text{ mm}$  thick, Fisher Scientific) were punched out and used as counter electrode to build half cells. Microporous tri-layer membrane (PP/PE/PP) (39% porosity,  $25\text{ }\mu\text{m}$ , Celgard<sup>®</sup> 2325) was used as separator and sandwiched between the working electrodes and lithium metal disc. The electrolyte was prepared by dissolving appropriate amount of  $\text{LiPF}_6$  salt in ethylene carbonate (EC)/dimethyl carbonate (DMC) (1:1 v/v for EC/DMC) to the concentration of  $1.0\text{ M}$ , followed by storage over activated molecular sieves for 2 days. In consideration of the porous nature of MWrGO, the electrolyte dosage was  $500\text{ }\mu\text{L}$  for MWrGO anode and  $120\text{ }\mu\text{L}$  for cathodes. All the constituent parts used in the coin cell were stacked in the sequence as shown in Fig. 3-7. All of the assembled cells were conditioned for 1 day before galvanostatic testing to ensure that the membranes and the working electrodes were fully impregnated in the electrolyte.

### 3.3.5.4. Electrochemical evaluation

Galvanostatic charge/discharge measurements were carried out in the voltage window of  $0.01 - 2.5\text{ V}$  (*vs*  $\text{Li}^+/\text{Li}$ ) for the MWrGO anode and  $3.0 - 4.2\text{ V}$  (*vs*  $\text{Li}^+/\text{Li}$ ) for the LCO cathodes at room temperature using Neware 8-channel battery test system. The data acquisition was performed by BTSDA 6.0 Software package (Neware<sup>®</sup>, China). For the

calculation of the specific gravimetric capacities, the mass of the electroactive materials on each electrode disc was merely taken into consideration.

MWrGO anode: Given that the theoretical capacity of 800W/10min MWrGO is unknown, current density ( $\text{A g}^{-1}$ ) is used for galvanostatic charge/discharge measurement and is determined based on the mass of the 800W/10min MWrGO. Cyclability test was performed at the current density of  $0.2 \text{ A g}^{-1}$  for 100 cycles. Rate capability test was performed at the current densities of  $0.1 \text{ A g}^{-1}$ ,  $0.2 \text{ A g}^{-1}$ ,  $0.5 \text{ A g}^{-1}$ ,  $1.0 \text{ A g}^{-1}$ ,  $2.0 \text{ A g}^{-1}$ ,  $5.0 \text{ A g}^{-1}$ ,  $10.0 \text{ A g}^{-1}$ , and then  $0.1 \text{ A g}^{-1}$  with 10 cycles for each current density. 5-min open-circuit-potential relaxation was programmed after each galvanostatic cycling step. Cycling voltammetry (CV) was performed between 0.01 V and 2.5 V at the sweep rate of  $0.1 \text{ mV s}^{-1}$  using an electrochemistry workstation (Bio-Logic Science Instruments VSP, France).

Cathodes: The C-rate for the as-milled LCO powder in this project was defined based on  $1 \text{ C} = 140 \text{ mA g}^{-1}$  [82, 250]. Cyclability test was performed at the current rate of 0.2 C for 100 cycles. Rate capability test was performed at the current rates of 0.1 C, 0.2 C, 0.5 C, 1 C, 2 C, 5 C, 10 C, and then 0.1 C with 5 cycles for each current rate. 5-min open-circuit-potential relaxation was programmed after each galvanostatic cycling step.

All the key parameters to make coin cells using aforementioned MWrGO anode, MWrGO-containing LCO cathode, and CNTs-containing LCO cathode are summarised in Table 3-2.

### 3.4. Cold sintering process of LiCoO<sub>2</sub>/MWrGO

The cold sintering process to produce LCO/MWrGO pellets is similar to the procedures to produce LCO/CNTs pellets in Section 3.2 except that the conductive filler in LCO/CNTs pellets, *i.e.*, CNTs, was substituted by 800W/10min MWrGO which was prepared in Section 3.3. Following that, the LCO/MWrGO pellets produced by CSP were assembled in 2032 type coin cells and were electrochemically evaluated. The overall experimental flow chart is given in Fig. 3-14.

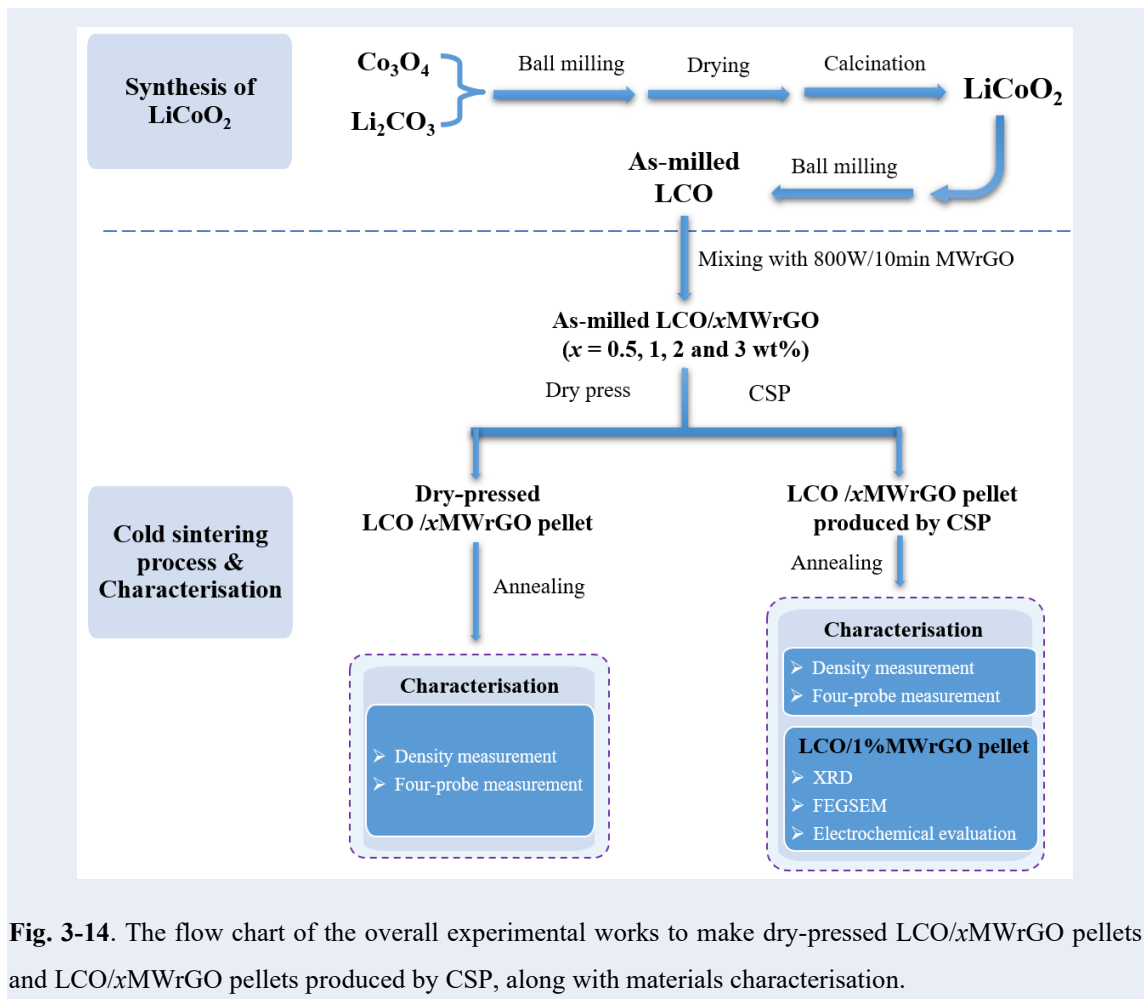


**Fig. 3-14.** The flow chart of the overall experimental works to make dry-pressed LCO/xMWrGO pellets and LCO/xMWrGO pellets produced by CSP, along with materials characterisation.

### 3.4.1. Preparation of LCO/xMWrGO powder

In order to improve the dispersity of 800W/10min MWrGO, ultrasonic bath (Grant XUBA1) was used to assist the dispersion of 800W/10min MWrGO in ethanol for 30 min. Thereafter, the as-milled LCO powders prepared in Section 3.2.1 were homogenised with 0.5 wt%, 1 wt%, 2 wt%, and 3 wt% 800W/10min MWrGO by ultrasonic bath for 30 min. The application of ultrasonication is believed to lead to the formation of cavitation bubbles in ethanol, which can implode during bubble propagation and thereby create localised high pressure and powerful shock waves to effectively break up large agglomerates of LCO particles and separate the restacked graphene sheets [254-256]. Therefore, the ultrasonication aided the uniform dispersion of small LCO particles on the graphene sheets to enhance the intimate contact between them. The mixtures were mixed using 2 mm zirconia balls at the rotation speed of 300 rpm for 20 hours to obtain homogeneous mixtures of LCO powder and 800W/10min MWrGO (denoted as as-milled LCO/xMWrGO, where  $x$  represents the weight percentage of MWrGO relative to the as-milled LCO powder). The as-milled LCO/xMWrGO mixtures were then dried at 80 °C overnight in air.

### 3.4.2. Cold sintering process and post-CSP annealing

Similar to the CSP procedures to produce LCO/*x*CNTs pellets in Section 3.2.3, the dried as-milled LCO/*x*MW<sub>r</sub>GO (*x*=0.5 wt%, 1 wt%, 2 wt%, and 3 wt%) mixtures prepared above were used to produce LCO/*x*MW<sub>r</sub>GO pellets at 250 °C and 250 MPa for 60 min. Typically, 0.5 g as-milled LCO/*x*MW<sub>r</sub>GO powder was mixed thoroughly with 20 wt% 2 *M* LiOH solution using mortar and pestle for 10 min. Afterwards, the well-mixed mixture was loaded into a 10 mm hardened steel die which was lubricated using PTFE spray to assist ejection, and the mixture was pressed under the uniaxial pressures of 250 MPa at the temperatures of 250 °C for 60 min. Herein, the prepared pellets produced by CSP were denoted as LCO/*x*MW<sub>r</sub>GO pellets.

Subsequently, the LCO/*x*MW<sub>r</sub>GO pellets produced by CSP were annealed at temperatures that ranged from 100 to 500 °C for 1 hour with a heating rate of 5 °C min<sup>-1</sup> in the tube furnace. For comparison, a control group was made using dry-pressed LCO/*x*MW<sub>r</sub>GO without the addition of LiOH solution at 250 MPa for 10 min at room temperature. The prepared pellets were denoted as dry-pressed LCO/*x*MW<sub>r</sub>GO pellets. Afterwards, the dry-pressed LCO/*x*MW<sub>r</sub>GO pellets were annealed at the same temperatures (100 - 500 °C) for 1 hour with a heating rate of 5 °C min<sup>-1</sup> in the tube furnace, followed by cooling to room temperature with a cooling rate of 5 °C min<sup>-1</sup>.

### 3.4.3. Materials Characterisation

The bulk densities of the LCO/xMWrGO pellets were calculated by dividing the weight by the corresponding geometric dimensions. Three pellets prepared at the same processing condition were measured and used to obtain arithmetic average density and standard deviation. The relative density was defined as the percentage of the bulk density over the theoretical density of the composite. The theoretical densities used for calculation are  $5.06 \text{ g cm}^{-3}$  for LCO [247] and  $2.10 \text{ g cm}^{-3}$  for 800W/10min MWrGO [257].

XRD was used to characterise the phases of all the samples using a Bruker D2 Phaser X-ray diffractometer (Bruker AXS GmbH, Karlsruhe, Germany, 2000) which is controlled by Diffrac.suite software package. The XRD diffraction data was collected in the scan range ( $2\theta$ ) of  $10^\circ - 80^\circ$  with a step size of  $0.05^\circ \text{ s}^{-1}$  (monochromatized Cu-K $\alpha$  radiation source operating at 30 kV and 10 mA,  $\lambda = 0.1542 \text{ nm}$ ). FEGSEM (JEOL JSM-7800F, JEOL Ltd. Japan) was used to study the morphologies of all the samples at an accelerating voltage of 5.0 kV in back scattering mode. Electrical conductivities of the pellets were measured at ambient temperature using a standard four-probe Van der Pauw method (Jandel RM3000 with DC current, UK). The direction of DC current was alternately changed to avoid measurement errors caused by thermoelectric effect. Measurements were repeated 3 times to obtain mean electrical conductivity. The specific surface areas of 800W/10min MWrGO and CNTs were also measured using N<sub>2</sub> physisorption at the temperature of 77.35 K (Tristar<sup>TM</sup> 3000, Micromeritics Instrument Corporation, Norcross, USA) based on the Branauer-Emmett-Teller method (BET). The carbonaceous samples were heated to 100 °C under vacuum ( $< 0.1 \text{ bar}$ ) overnight to remove all the adsorbed species.



#### 3.4.4. Electrochemical measurements

The LCO/1%MWrGO pellets produced by CSP were electrochemically evaluated by assembling into 2032 type coin cells. The LCO/1%MWrGO pellets were first annealed at 400 °C for 1 hour. Following the same polishing process using abrasive-coated sandpapers, the LCO/1%MWrGO pellets with the thickness of 100 ~ 200  $\mu\text{m}$  were assembled in 2032 type coin cells using the same procedures outlined in Section 3.2.5 with the same electrolyte, the lithium counter electrode, and the microporous tri-layer membrane. Subsequently, the assembled coin cells were rest for 1 day and the OCV of the as-fabricated coin cells were normally stabilised to be 1.9 – 3.0 V, which indicated that short-circuit did not occur between the working electrode and the lithium metal disc. Then, the as-fabricated cells were galvanostatically charged/discharged in the voltage window of 3.0 - 4.2 V (*vs*  $\text{Li}^+/\text{Li}$ ) at room temperature using Neware 8-channel battery test system. The C-rate for the ball-milled LCO in this project was defined based on 1 C = 140 mA  $\text{g}^{-1}$  [82, 250]. Cyclability test was performed at the current rate of 0.1 C. Rate capability test was performed at the current rates of 0.1 C, 0.2 C, 0.5 C, 1 C, 2 C, 5 C, and then 0.1 C. 5-min open-circuit-potential relaxation was programmed after each galvanostatic cycling step. For the calculation of the specific gravimetric capacities, the mass of the LCO was merely taken into consideration. For the calculation of the specific volumetric capacities, the total volume of the LCO and 800W/10min MWrGO was taken into full consideration. Cycling voltammetry (CV) was performed with a PGSTAT204 Autolab potentiostat (Metrohm, Switzerland) with a cut-off voltage of 3.0 V and 4.2 V for discharge and charge in a two-electrode configuration at different sweep rates (0.1, 0.2, and 0.5  $\text{mV s}^{-1}$ ). The lithium ion diffusion coefficients ( $D_{\text{Li}}$ ) of the LCO/1%MWrGO cathode produced by CSP were calculated according to the linear relationship between

peak currents and the linear sweep rates using Randles-Sevcik equation [258]. Electrochemical impedance spectroscopy (EIS) was conducted on LCO-based cathodes in the frequency range 10 kHz–0.01 Hz with a potential perturbation of 5 mV using a multi-Potentiostat/Galvanostat VSP from Bio-Logic Science Instruments (France). The measurements were carried out in automatic sweep mode from high to low frequency after prolonged potentiostatic equilibration. And the impedance spectrum obtained were fitted with equivalent circuit model using Zview<sup>®</sup> software (Scribner Company). Direct current internal resistance (DCIR) testing was performed by applying a constant current discharge pulse ( $I_{app}$ ) of 5 C on 10-s intervals at 25%SOC, 50% SOC and 75%SOC. The cell was charged at a slow current rate of 0.1 C to 4.2 V, such that the overpotential bias incurred by other factors has been reduced to minimum and can be neglected. The DCIR was calculated by dividing the change in voltage by the change in applied current using the below equation:

$$R_{DCIR} = \frac{V_t(t=0) - V_t(t=10)}{I_t(t=0) - I_t(t=10)} \quad [\text{Equation 14}]$$

All the key parameters to make coin cell using the LCO/1%MWrGO cathode are summarised in Table 3-2.

## **Chapter 4. Cold sintering process and electrochemical evaluation of $\text{LiCoO}_2/\text{CNTs}$ composite electrode with high volumetric capacity**

In this chapter, bulk  $\text{LiCoO}_2$  (LCO) cathode without the addition of polymeric binder was fabricated by cold sintering process (CSP) and electrochemically characterised. First of all, the effects of CSP processing conditions, *i.e.*, temperature, pressure and holding time, on the relative densities of monolithic LCO pellets were assessed in Section 4.1. Considering the intrinsically low electrical conductivity nature of LCO, it is necessary to introduce conductive additive, *i.e.*, multi-walled carbon nanotubes (CNTs) in this work, in the monolithic LCO pellets to build an electrically conductive network. Therefore, the effect of CNTs inclusion on the electrical conductivity of  $\text{LCO}/x\text{CNTs}$  pellets produced by CSP was explored in Section 4.2. Amorphous phase of oxides has been known to occur on the grain boundaries during CSP due to the non-equilibrium precipitation, which deteriorate the properties of oxides and thus it requires to be eliminated via post-CSP annealing treatment. In Section 4.3, the effects of post-CSP annealing treatment on the relative density and electrical conductivity of  $\text{LCO}/\text{CNTs}$  pellets were studied. Ultimately, the optimised  $\text{LCO}/\text{CNTs}$  composite electrode was electrochemically evaluated in a 2032-type configuration cell (-)  $\text{Li} \mid 1 \text{ mol L}^{-1} \text{ LiPF}_6\text{-EC+DMC} \mid \text{Cathode (+)}$  and the electrochemical results were present in Section 4.4.

#### 4.1. The CSP of monolithic LCO pellets

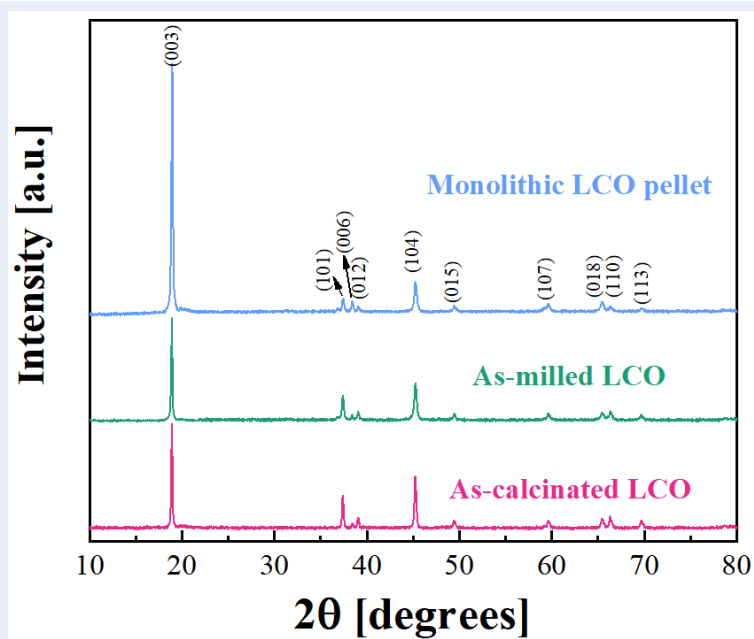


**Fig. 4-1.** XRD patterns of as-calcinated LCO, as-milled LCO, and monolithic LCO pellet produced by CSP.

XRD was carried out to characterise the crystal structures of as-calcinated LCO powder, as-milled LCO powder and monolithic LCO pellets produced by CSP, as interpreted in Fig. 4-1. The XRD result for the as-calcinated LCO powder synthesised at 850 °C was consistent with the regular hexagonal structure observed in pure polycrystalline LCO ( $\alpha$ -NaFeO<sub>2</sub> structure [259]) and it matched with the Joint Committee for Powder Diffraction Studies (JCPDS) reference card no. 70-2685 [260, 261]. The sharp XRD diffraction peaks along with the well-resolved splitting of doublet peaks (006)/(012) and (018)/(110) are indicative of the well-ordered hexagonal layered structure of LCO formed during calcination [262]. In addition, no remnant phase and impurity phase were present in the XRD pattern of as-calcinated LCO powder. The solid-state synthesis of LCO was typically achieved at elevated calcination temperature (up to 1000 °C) for extended periods (up to 24 hours) [72, 263-265], which may result in the excess volatilisation of lithium species and thus deteriorate electrochemical performance of LCO [69]. But much

shorter calcination time (5 hours) at lower calcination temperature (850 °C) was used in this work. It was mainly attributed to (i) the significant reduction in the particle sizes of the precursors, *i.e.*, Co<sub>3</sub>O<sub>4</sub> and Li<sub>2</sub>CO<sub>3</sub>, induced by planetary ball milling, and (ii) the resultant shorter inter-diffusion distance during calcination. Moreover, the as-milled LCO powder in Fig. 4-1 exhibited an identical diffraction pattern to the as-calcinated LCO powder, indicating the planetary ball milling process did not artificially alter the crystal structure of as-calcinated LCO.

The FEGSEM images in Fig. 4-2 shows that the particle size of LCO powder was significantly reduced from > 1 µm to < 0.2 µm after planetary ball milling process. Notably, the morphology of the LCO powder changed from granular shape to platelet shape. With the particle size analyser, it has been shown in Fig. 4-3 that the D<sub>50</sub> particle size was reduced from 1.92 µm for as-calcinated LCO powder to 0.15 µm for as-milled LCO powder, which agreed with the above FEGSEM results. The reduced particle size of LCO powder led to a dramatic increase in surface area from 0.65 m<sup>2</sup> g<sup>-1</sup> for as-calcinated LCO powder to 6.24 m<sup>2</sup> g<sup>-1</sup> for ball-milled LCO powder, as shown in Fig. 4-4, which is believed to bring about three advantageous features for the subsequent cold sintering process:

(i) the increased solubility of solid-phase particles, which can be described by Ostwald-Freundlich equation [266]:

$$\ln \frac{S_r}{S_\infty} = \frac{2 \Omega \gamma_{sl}}{k T r} \quad [\text{Equation 15}]$$

Where,  $S_r$  and  $S_\infty$  is the solubility of powder with radius  $r$  and with infinite radius, respectively.  $\gamma_{sl}$  represents the interfacial tension between solid phase and liquid phase,  $\Omega$  represents the atomic volume, and  $k$  is the Boltzmann constant, and  $T$  is absolute

temperature. It can be clearly seen that the reduction in LCO powder size can significantly lead to increase in powder solubility in liquid phase due to the Gibbs-Thomson effect. And this effect become more significant for very small powder size.

(ii) The increased contact area with LiOH solution provided larger number of lattice sites for dissolution during dissolving process and nucleation during precipitation process.

(iii) In comparison with as-calcinated LCO powder, the as-milled LCO powder had smaller particle size and platelets morphological feature, so as to re-orientate themselves to minimise the vacancies among the particles and achieve more compact pellets under the application of external CSP pressure.

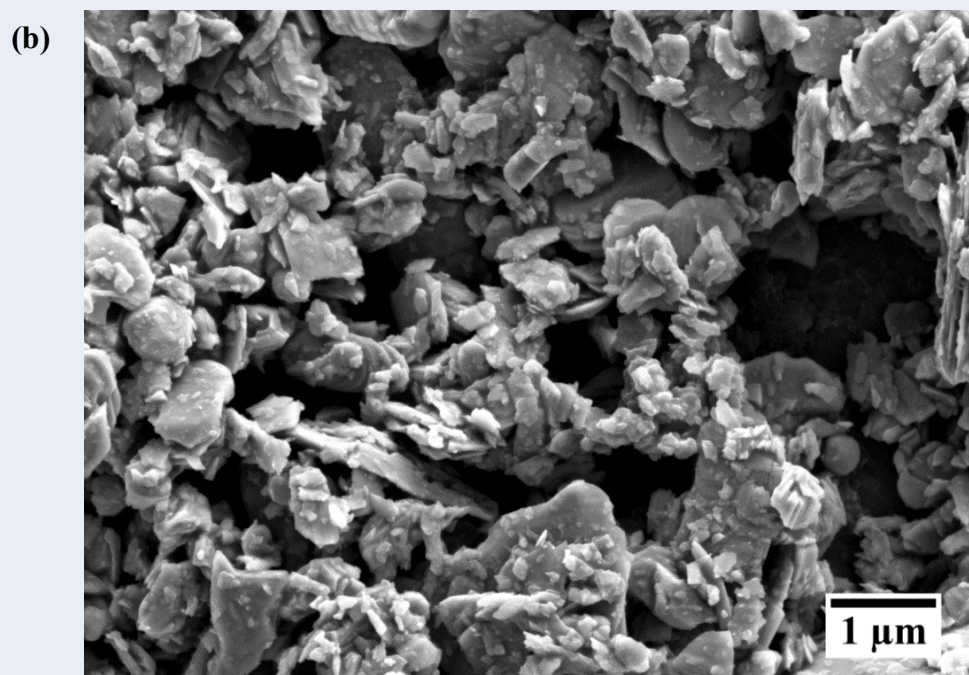
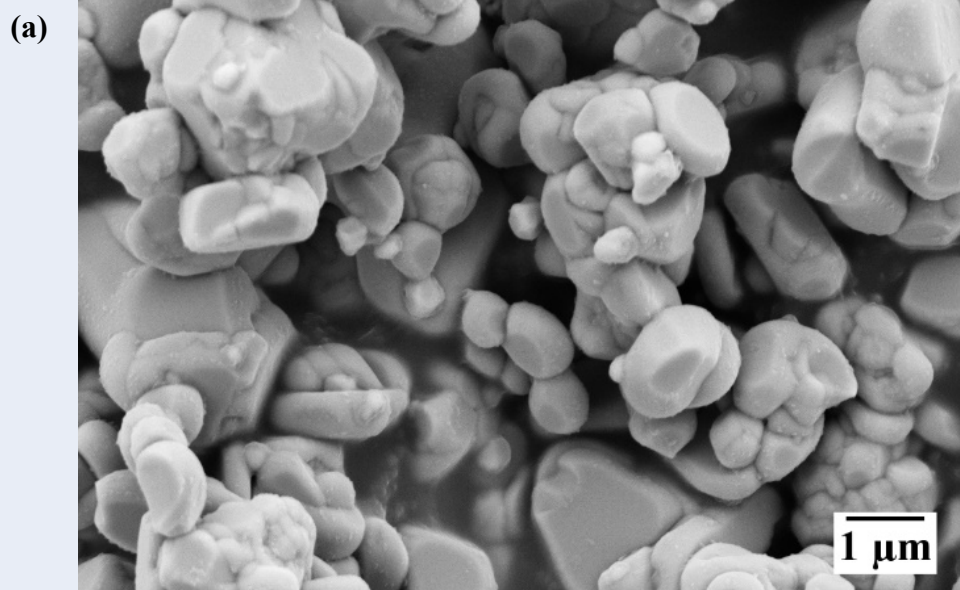


**Fig. 4-2.** FEGSEM images of (a) as-calcinated LCO powder and (b) as-milled LCO powder.

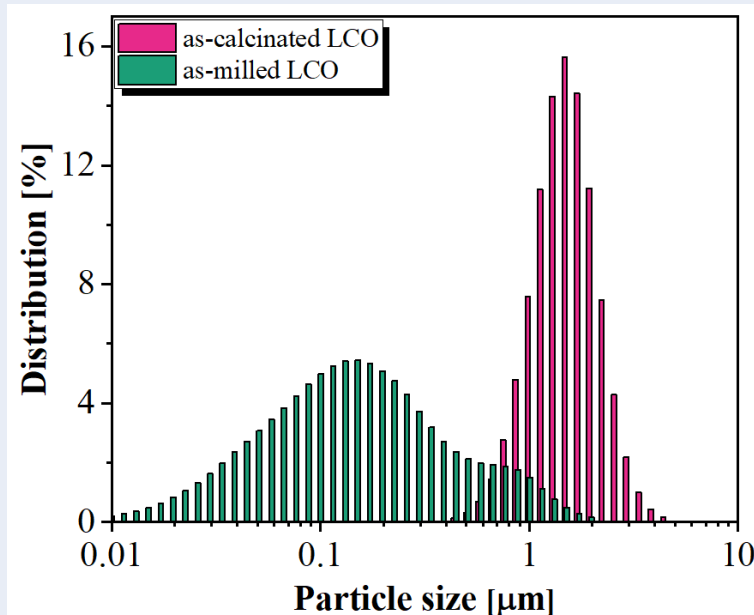


**Fig. 4-3.** The particle size comparison of as-calcined LCO powder and as-milled LCO powder.

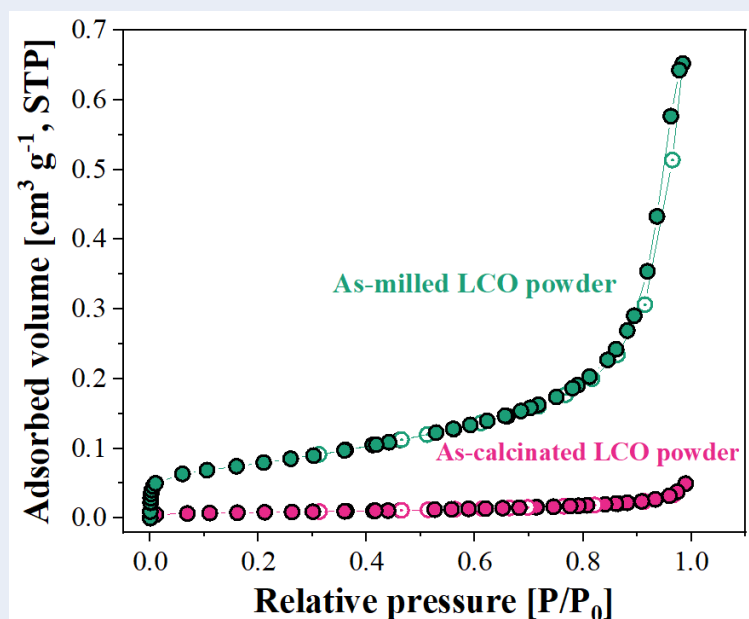


**Fig. 4-4.** Nitrogen adsorption/desorption hysteresis loops of as-calcined LCO powder and as-milled LCO powder, revealing the specific surface areas based on Branauer-Emmett-Teller (BET) method.

Fig. 4-5 shows the effects of CSP pressure, temperature, and duration on the densification of monolithic LCO pellets. Fig. 4-5 (a) depicts the relative densities of the monolithic LCO pellets with increasing CSP pressures at the CSP temperature of 250 °C for 60 min. The relative densities of the monolithic LCO pellets were greatly improved from 61.5%



at 100 MPa to 71.4% at 200 MPa and further to 77.7% at 250 MPa, indicating the critical role of external applied pressure in improving the density of LCO pellets. The density improvement by external applied pressure during CSP can be explained by (i) the compaction/sliding, (ii) the solubility characteristics, and (iii) diffusive mass transport of pure LCO particles.

(i) In the early stage of sintering, the surfaces of LCO particles ensembles were homogenously moisturized with LiOH solution which was intentionally introduced at the particle-particle contacts. This liquid film could effectively lubricate the LCO particle surfaces and assisted in the re-orientation, sliding, and compaction of LCO particles under pressure [99]. And these physical effects become more significant with increasing the external applied pressure because LiOH solution could readily redistributes itself and fill into the pores among the LCO particles. The presence of LiOH solution in the particle interstitials could facilitate the subsequent mass transport, as discuss below, because the mass transport in liquid phase is much higher than in solid phase which is generally observed in conventional thermal sintering.

(ii) The application of external pressure ( $P_{ext}$ ) is also believed to improve the solubility ( $S_p$ ) of ceramic particles at the particle-particle contacts due to a stress difference and this effect can be described by [267]:

$$S_p = S_0 \exp \left[ P_{ext} \frac{(\Omega_s - \Omega_l)}{RT} \right] \quad [\text{Equation 16}]$$

Where,  $S_0$  is the solubility of ceramic particles in the absence of external applied pressure.  $R$  is the gas constant and  $T$  represents the absolute temperature.  $\Omega_s$  and  $\Omega_l$  represent the solid molar volume and liquid molar volume, respectively. The component  $\Omega_s - \Omega_l$  is generally greater than 0 as the apparent molar volume of the atoms in the liquid is smaller

than in the solid phase [267]. This can be attributed to the chemical interactions between solute atoms and solvent, which result in a re-arrangement of the liquid molecules and a reduction in volume. Because LCO particle was cold sintered using LiOH solution as liquid phase, this can lead to an increased solubility of LCO because the particle-particle contacts becomes more prevalent at higher applied pressure. This implied more LCO species were dissolved in LiOH solution and promoted the formation of supersaturation phase.

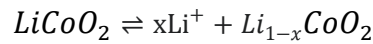
(iii) In fact, sintering is densification process that requires mass transport controlled by thermodynamic factor (driving force) and by a kinetic factor (mass transport). The driving force is a gradient in the chemical potential of atoms caused by pressure difference at the microstructural perspective and it tends to reach an equilibrium status between the solid and liquid phases in CSP. With the influence of external applied pressure, the contact points between LCO particles had an increased chemical potential so that the dissolved species diffused along the liquid film and precipitated on the particles at sites away from the stressed contact areas. This diffusivity process minimised the excess surface free energy of the LCO system and reduced the porosity as the LCO formed a dense body [101]. From the perspective of system's kinetics, the re-distribution of LiOH solution in the LCO particle interstitials caused by external applied pressure contributed to the transportation of dissolved species because the transportation in liquid phase was more efficient. The dissolved species can travel faster to the pore spaces, which resulted in dense body. Therefore, the application of an external pressure during CSP showed the identical effect of increasing the driving force and increasing diffusion rate.

Nevertheless, the improvement in density became less influential at higher pressures (> 250 MPa) and thus the relative densities of monolithic LCO pellets started to level off at

250 MPa. It is worth mentioning that an increased wear level was observed on the stainless-steel dies used in our works when the external pressure was higher than 250 MPa and thus the lifetime of stainless-steel dies was apparently reduced. Henceforth, according to our experience, the CSP pressure of 250 MPa was suggested and will be employed in the following CSP experiments.

Fig. 4-5 (b) presents that the relation between the relative densities of monolithic LCO pellets and the CSP temperatures at the CSP pressure of 250 MPa for 60 min. The monolithic LCO pellets produced by CSP experienced a substantial increase in relative densities from 59.4% at 100 °C to 73.1% at 200 °C but a slow increase in relative densities at higher temperature (> 250 °C). The increases in relative densities of the monolithic LCO pellets were largely due to (i) the enhanced dissolution at higher processing temperature and (ii) the enhanced diffusion rate of dissolved LCO species.

(i) Dissolution of LCO plays an important role in densification during CSP because it is the precondition of mass transport in LiOH solution, and it can be described by dissolution product constant ( $K_{sp}$ ). LCO is the only constituent that dissolute in LiOH solution in this case. An equilibrium can be established for LCO and  $K_{sp}$  can be represented as:



$$K_{sp} = [Li^+]^x [Li_{1-x}CoO_2]^1$$

Since  $K_{sp}$  is greatly influenced by temperature and it becomes greater with increasing temperature, the LiOH solution dissolved more LCO species at higher temperature, which was beneficial to the formation of supersaturated liquid phase. The positive correlation

between solubility of LCO and temperature can also be achieved using Equation 15, provided that the external pressure is constant.

(ii) The high processing temperature was also beneficial to lower the viscosity of LiOH solution and thus improved the diffusivity of dissolved LCO species that would precipitate on particle sites with lower chemical potential.

In Fig. 4-5 (b), the relative densities between 250 °C and 300 °C were very close (77.7% vs 78.7%, respectively), which indicated that the solvent has been completely dried at 250 °C after 1-h processing. The temperature increase cannot further improve the relative density. Therefore, the subsequent densification of monolithic LCO pellets was performed at the CSP temperature of 250 °C with the intention of lowering power consumption.

Fig. 4-5 (c) depicts the relative densities of monolithic LCO pellets with the increasing CSP duration at the CSP temperature of 250 °C and the CSP pressure of 250MPa. The relative density of 66.9% was obtained at the duration time of 30 min and was risen to 77.7% at the duration time of 60 min. Thereafter, it fluctuated at ~78% relative density with prolonged duration time. The variation of densification rate with the CSP duration time is determined by the evaporation of LiOH solution at 250 °C. With short duration of 30 min, the presence of residual water may leave an amorphous phase on grain boundary that has not been crystallised. In such , the relative density of monolithic LCO pellets was relatively low. With the CSP duration time more than 60 min, Leng *at al.* [102] has explained that the liquid phase has been completed dried in the first hour and no diffusion/densification occurred after that period. Therefore, the fixed duration of 60 min was sufficient to obtain highest relative density of monolithic LCO pellets in this work.

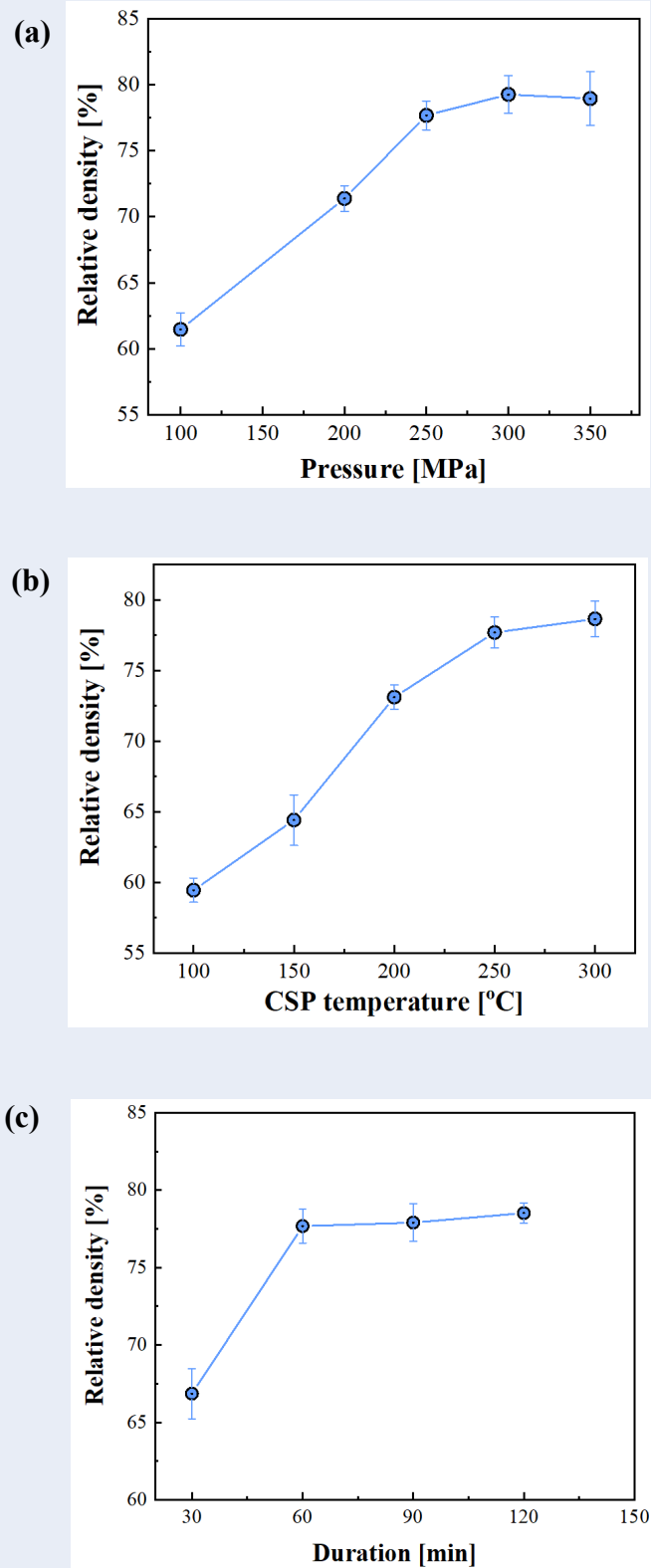


**Fig. 4-5.** The effects of CSP processing conditions on the relative densities of monolithic LCO pellets: **(a)** Relative density as a function of CSP pressures at the temperature of 250 °C for 60 min; **(b)** Relative density as a function of CSP temperatures at the pressure of 250 MPa for 60 min; **(c)** Relative density as a function of CSP duration times at 250 °C and at 250 MPa. 20 wt% LiOH solution was used in all cases.

To sum up, the monolithic LCO pellets with the relative density of 77.7% was successfully produced via CSP at 250 °C and 250 MPa for 60 min. The microstructures of a monolithic LCO pellet cold-sintered with this set of processing conditions and a benchmark LCO pellet dry-pressed at 250 MPa are shown in Fig. 4-6 for comparison. In sharp contrast with what is seen for the loosely packed microstructure in dry-pressed LCO pellet, the sintering morphologies, including particle packing and the sintering necks, were evident in the monolithic LCO pellet prepared by CSP. The XRD pattern of monolithic LCO pellet was similar to those of as-calcinated LCO powder and as-milled LCO powder, excepted that increased peak intensity was observed for (003) peak of monolithic LCO pellet, as shown in Fig. 4-1. It is found that no impurity phases were formed during CSP. This optimised CSP parameters were selected as the standard processing conditions for the subsequent experiments to densify LCO/carbon composite electrode, considering that

(i) the “dissolution-precipitation” process of LCO/carbon composites during CSP is primarily determined by LCO because of the insolubility of carbon additives in aqueous solution

(ii) the minor addition of carbon additives in ceramic matrix, *i.e.*, generally <5wt%.

Therefore, the effects of CSP processing variables on densification behaviour of LCO/carbon composites is identical to that of monolithic LCO pellets.

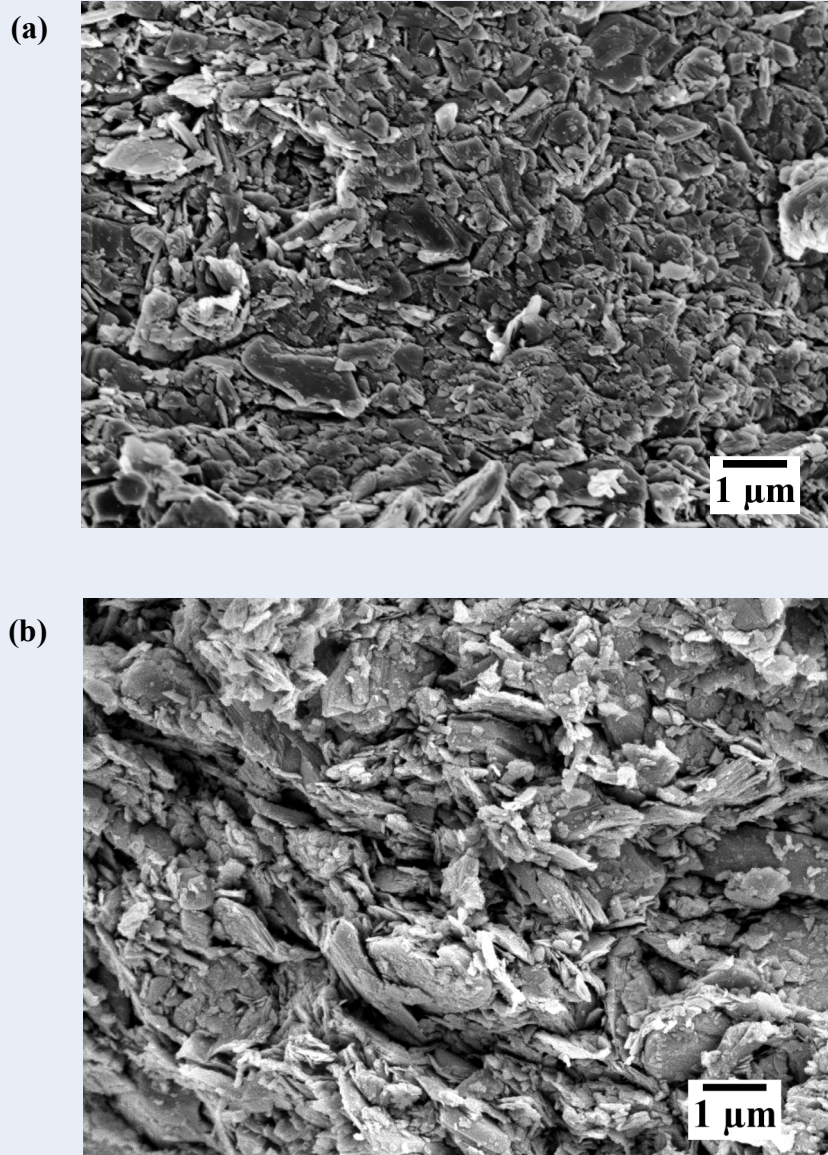


**Fig. 4-6.** FEGSEM images of (a) monolithic LCO pellet cold-sintered at 250 °C and 250 MPa for 60 min and (b) LCO pellets dry-pressed at 250 MPa.

## 4.2. Effect of CNTs content on electrical conductivity of composite cathode

Albeit that monolithic LCO pellets with promising relative density, *i.e.*, 77.7%, can be produced at the optimised CSP condition as discussed in Section 4.1, the electrical conductivity of monolithic LCO pellets was measured to be only  $\sim 1.66 \times 10^{-4} \text{ S cm}^{-1}$  using four-probe method as shown in Fig. 4-7. This electrical conductivity is comparable to that of LCO pellets which were pressed and sintered at high temperature ( $> 800 \text{ }^{\circ}\text{C}$ ), as showed in Table 4-1. It implied that the LCO particles were sintered at a relatively low temperature of  $250 \text{ }^{\circ}\text{C}$ . The low electrical conductivity, therefore, is sure to be a barrier towards the application of monolithic LCO pellets for LIBs. In this sense, the incorporation of electrically reinforced CNTs into LCO matrix, in this work, became increasingly essential. Fig. 4-7 depicts the electrical conductivities of LCO/*x*CNTs pellets produced by CSP as a function of conductive CNTs inclusion. It is discovered that the electrical conductivities of LCO/*x*CNTs pellets experienced a significant improvement in electrical conductivity with the inclusion of CNTs increased. Specifically, the electrical conductivities of LCO/*x*CNTs pellets increased from  $\sim 3.73 \times 10^{-4} \text{ S cm}^{-1}$  at 1 wt% CNTs inclusion to  $\sim 2.84 \text{ S cm}^{-1}$  at 3 wt% CNTs inclusion, which is an exceptional improvement in an approximate magnitude order of 4. This is principally due to the formation of conductive CNTs network in LCO/*x*CNTs pellets. However, with further inclusion of CNTs to 5 wt%, the electrical conductivity enhancement showed little variation, which can be inferred that the percolation threshold of CNTs to form a 3D conductive network in LCO matrix was 3 wt%. Therefore, the LCO/3%CNTs pellets were selected for subsequent microstructure and electrochemical property characterisation.



**Table 4-1.** Literature survey of the electrical conductivities of LCO pellets produced by conventional sintering.

Processing conditions	Electrical conductivity [ $\text{S cm}^{-1}$ ]	References
LCO pellets pressed and sintered at 800 °C	$1 \times 10^{-3}$	[268]
LCO pellets pressed and sintered at 900 °C	$1 \times 10^{-4} \sim 1 \times 10^{-3}$	[269]
LCO pellets pressed and sintered at 900 °C	$1 \times 10^{-4} \sim 1 \times 10^{-3}$	[75]
LCO pellets pressed and sintered at 850 °C	$\sim 1 \times 10^{-4}$	[270]

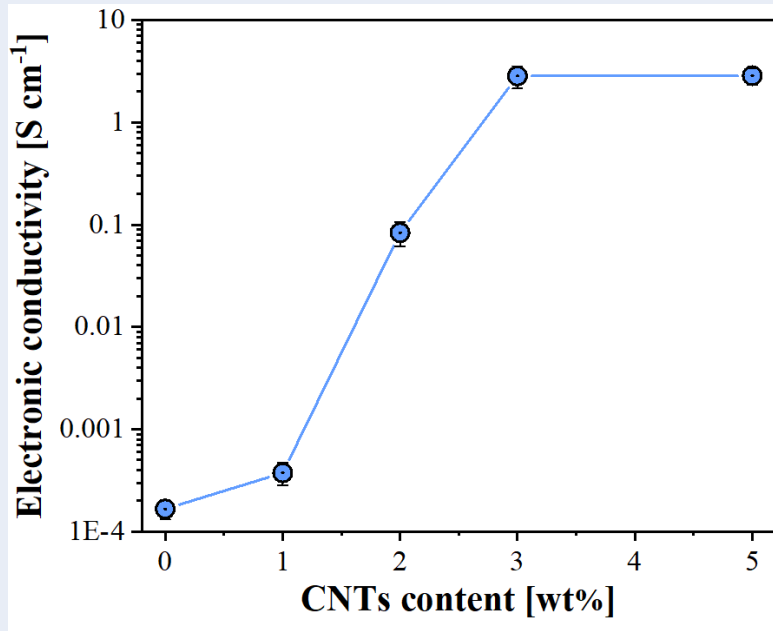


**Fig. 4-7.** The dependency of the electrical conductivities on the conductive CNTs content for LCO/xCNTs pellets prepared at the CSP condition of 250 °C and 250 MPa for 60 min.

As shown in Fig. 4-8, the XRD pattern of LCO/3%CNTs pellet was identical to those of as-calcinated LCO powder, as-milled LCO powder and monolithic LCO pellet. In comparison with the randomly oriented nature of as-calcinated LCO powder and as-milled LCO powder, the more intense characteristic (003) peaks of monolithic LCO pellet

and LCO/3%CNTs pellet implied the preferential *c*-axis orientation of LCO platelets as a result of the applied external pressure, which was similarly reported for platelet-shape LCO [271]. Moreover, the  $I_{(003)}/I_{(104)}$  factor is widely used as a measure of the high degree of crystallinity and less degree of cation-mixing in layered materials if it is greater than 1.2 [272]. The  $I_{(003)}/I_{(104)}$  factor of LCO/3%CNTs pellet was calculated to be more than 1.5 in this case, which is indicative of the excellent layered structure of LCO. In addition, it is found that no additional diffraction peak could be indexed to CNTs due to the presence of small amount CNTs. The microstructure of LCO/3%CNTs pellet produced by CSP is also given in Fig. 4-9. It shows a compact matrix with the CNTs embedded inside, which indicated the successful densification of LCO/3%CNTs pellets with the assist of LiOH transient liquid phase. Although CNTs were entangled in some regions, an electrically conductive network can still be established, yielding a value of 2.84 S cm<sup>-1</sup>.

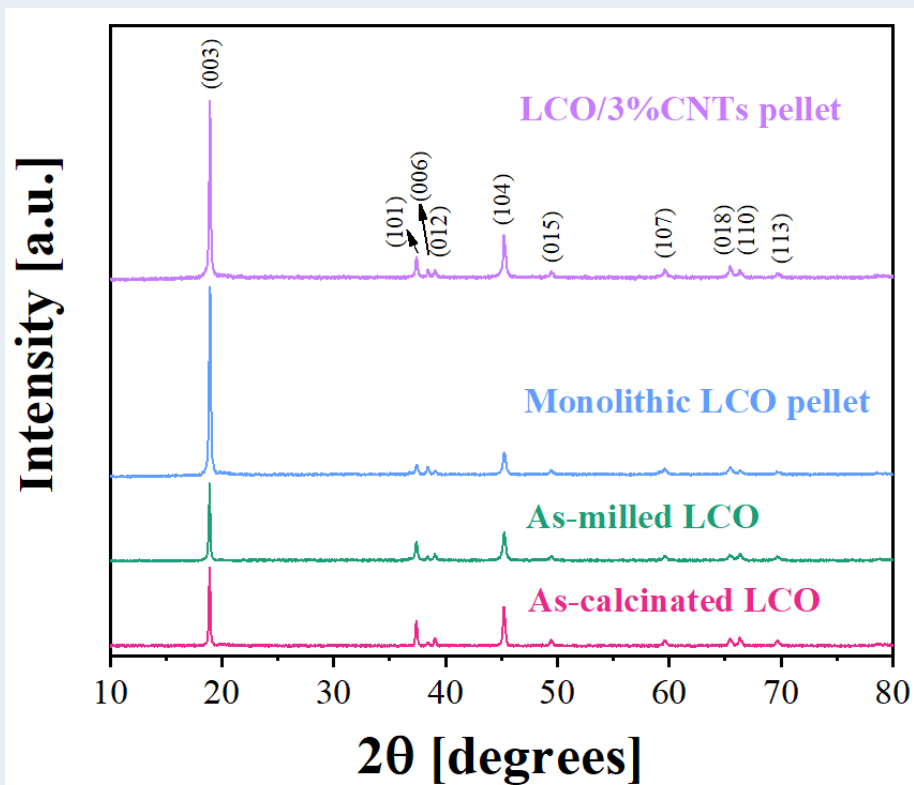


**Fig. 4-8.** X-ray diffractograms of LCO/3%CNTs pellet produced by CSP, together to those related to as-calcinated LCO, as-milled LCO and monolithic LCO pellet.

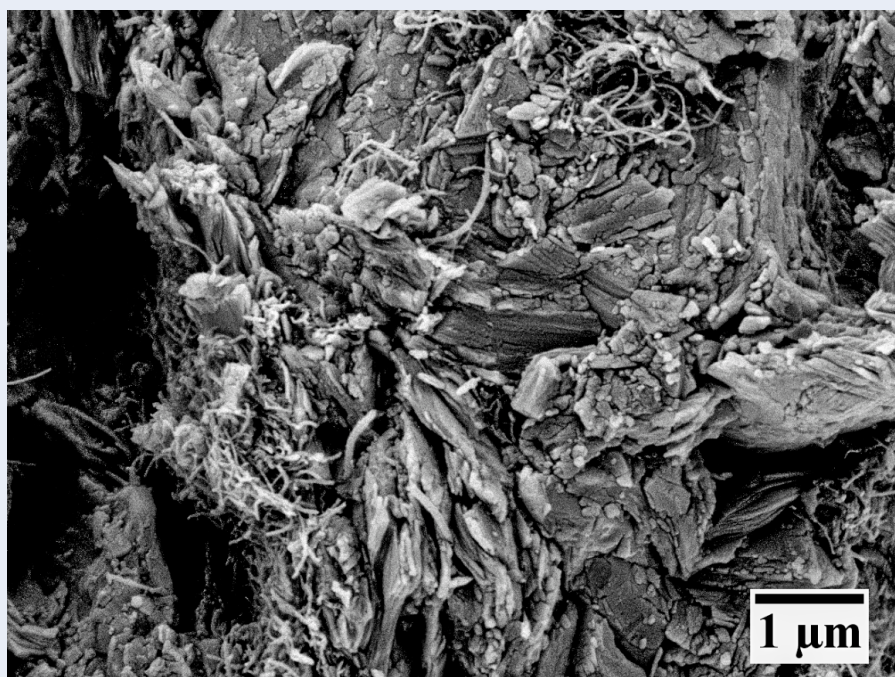


**Fig. 4-9.** FEGSEM image of the fractured surface of LCO/3%CNTs pellets produced by CSP.

### 4.3. The effect of post-CSP annealing treatment

From above investigation, the LCO/3%CNTs pellets with the electrical conductivity of  $\sim 2.84 \text{ S cm}^{-1}$  can be produced by means of CSP at 250 °C and 250 MPa for 60 min. It has been reported that amorphous phase was usually formed at the grain boundaries in oxides material system during CSP due to the non-equilibrium precipitation process [16, 97, 102, 104-108]. But the amorphous phase can be crystallised by post-CSP annealing at temperatures lower than conventional sintering temperatures. Therefore, the impacts of post-CSP annealing treatment (temperature range of 100 - 500 °C) on improving the relative density and the electrical conductivity of LCO/3%CNTs pellets produced by CSP were studied, as shown in Fig. 4-10. In comparison, the control group, dry-pressed LCO/3%CNTs pellets, was also annealed at the same temperatures range from 100 °C to 500 °C.

As clearly shown in Fig. 4-10 (a), the relative densities of LCO/3%CNTs pellets were found little increases in the annealing temperature range from 100 °C to 500 °C, leading to a slightly improved relative density from 76.7% at 100 °C to 79.5% at 400 °C and further to 79.8% at 500 °C. The highest relative density (79.8%) at the annealing temperature of 500 °C was only slightly greater than as-CSPed LCO/3%CNTs pellets (76.3%). On the contrary, the dry-pressed LCO/3%CNTs pellets underwent a significant increase in the relative densities upon the identical annealing treatment. Specifically, the relative density of dry-pressed LCO/3%CNTs pellet increased from 51.4% at room temperature to 68.5% at 500 °C. It is worth noting that the relative density of dry-pressed LCO/3%CNTs pellets annealed at 500 °C was still inferior than those of as-CSPed LCO/3%CNTs pellet (76.3%), which indicated that CSP was capable to produce ceramics with much higher density through a remarkable dissolution-precipitation process that is

not attainable in traditional sintering technique.

Fig. 4-10 (b) depicts the electrical conductivities of both LCO/3%CNTs pellets produced by CSP and dry-pressed LCO/3%CNTs pellets after being subjected to the same annealing temperatures (100 - 500 °C). The electrical conductivities of LCO/3%CNTs pellets considerably rose from 2.84 S cm<sup>-1</sup> at room temperature to 3.48 S cm<sup>-1</sup> at 400 °C, and then stayed stable on higher annealing temperature (500 °C). Interestingly, the electrical conductivities of LCO/3%CNTs pellets produced by CSP experienced a significant improvement in the annealing temperature range of 100 - 500 °C whereas the relative densities only showed minor improvement. This could be attributed to the annealing-induced crystallisation of amorphous LCO phase precipitated on the grain boundaries.

Typically, it is reported that crystalline LCO phase has higher density and higher diffusive motion of Li<sup>+</sup> ion than its amorphous counterpart [110, 273]. The presences of interfacial amorphous phase formed during CSP in other material systems have been studied by researchers using transmission electron microscopy and FEGSEM [14, 18, 102, 105]. In comparison, the electrical conductivities of dry-pressed LCO/3%CNTs pellets were also increased with increasing annealing temperatures, resulting in the highest value of only 1.80 S cm<sup>-1</sup> at 500 °C. This value was still far lower than that of as-CSPed LCO/3%CNTs pellets (2.84 S cm<sup>-1</sup>) and was only half of LCO/3%CNTs pellets annealed at 500 °C (3.49 S cm<sup>-1</sup>). The increase in electrical conductivities of dry-pressed LCO/3%CNTs pellets was believed to be solely associated with the densification of pellets, which facilitated the contacting area among adjacent LCO particles via sintering. Based on the above analysis, the annealing treatment at as low as 400 °C for 1 hour is proven to effectively enhance the electrical conductivity by eliminating the adverse amorphous LCO phase

precipitated on the grain boundary and will be used to treat LCO/3%CNTs pellets for cathode application.

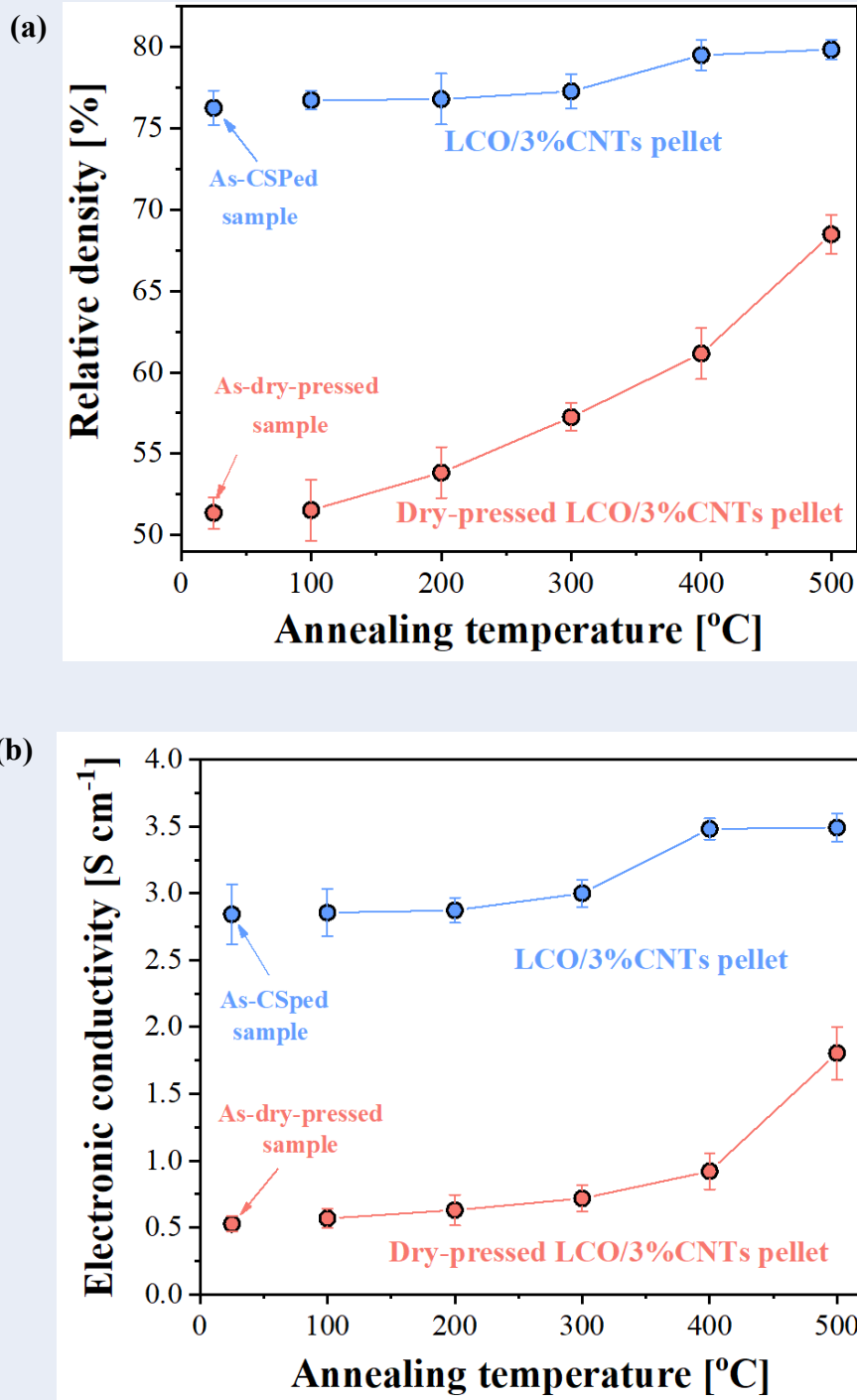


**Fig. 4-10.** The plots of (a) relative density and (b) electrical conductivity of LCO/3%CNTs pellets produced by CSP and dry-pressed LCO/3%CNTs pellets as a function of annealing temperatures in comparison with as-CSPed LCO/3%CNTs pellets and as-dry-pressed LCO/3%CNTs pellets.

#### 4.4. Electrochemical characterisation

In summary, the LCO/3%CNTs pellets with the relative density of 79.5% and the electrical conductivity of  $3.48 \text{ S cm}^{-1}$  were produced at the CSP condition of  $250^\circ\text{C}$ , 250 MPa and 1-hour duration time with 20 wt% LiOH solution, followed by post-CSP annealing treatment at  $400^\circ\text{C}$ . The LCO/3%CNTs pellets were then polished to low-aspect-ratio cathodes ( $< 200 \mu\text{m}$  in thickness). Finally, the LCO/3%CNTs cathodes were assembled into 2032 type coin cells for electrochemical evaluation, as outlined in the Experimental Section 3.2.5.

CV test has established itself as a powerful tool to analyse cathodic kinetics and various phase transformation during lithiation/delithiation process of  $\text{LiCoO}_2$ . Fig. 4-11 gives the initial-cycle cyclic voltammetry curve for LCO/3%CNTs cathode in the electrolyte of 1 M  $\text{LiPF}_6/(\text{EC}+\text{DMC})$  at the sweep rate of  $0.1 \text{ mV s}^{-1}$ . The CV curve is represented by three sets of reversible redox peaks, which indicates the lithium ions insert/de-insert the host lattice via a three-step mechanism. The two redox peaks appearing at 3.97 V and 3.86 V indicated the typical deintercalation/intercalation process of Li ions from/in LCO layered crystal structure, respectively, which corresponded to the first-order phase transition from  $\text{LiCoO}_2$  (hexagonal I) to  $\text{Li}_{0.75}\text{CoO}_2$  (hexagonal II) [274, 275]. By means of *in-situ* XRD studies of  $\text{Li}_{1-x}\text{CoO}_2$ , Reimers and Dahn proposed that  $\text{Li}_{1-x}\text{CoO}_2$  was a single hexagonal I phase when  $x < 0.07$  but it started to transform to hexagonal II phase when  $x > 0.07$  [71]. The hexagonal I phase and the hexagonal II phase had the similar  $a$  lattice, but they differed in the  $c$  lattice with  $c_{\text{H(I)}} = 14.089 \text{ \AA}$  and  $c_{\text{H(II)}} = 14.370 \text{ \AA}$ , respectively [276]. The first-order phase transition was completed when  $x = 0.25$  and was reversible during discharge process [71]. The hysteresis divergence between the cathodic/anodic redox peaks was about 0.11 V, which indicated the low ohmic resistance

and high electrochemical reversibility of LCO/3%CNTs cathode [274].

It is worth noting that there existed two minor peaks between 4.07 V and 4.19 V, which has been generally pertained to the order-disorder transition from the hexagonal structure ( $R\bar{3}m$ ) to the monoclinic structure ( $C2/m$ ) as a result of the shearing of the rhombohedral oxygen lattice [69, 71, 274]. Moreover, the close cathodic /anodic currents revealed the high electrochemical reversibility of the LCO/3%CNTs cathodes prepared by CSP.

The first three CV curves of LCO/3%CNTs cathode are shown in Fig. 4-12. Notably, a small shoulder-like anodic peak (marked in violet circle) was found to appear at a broad voltage window of 3.82 -3.88 V in the first cycle but disappear in the successive cycles. It can be attributed to the decomposition of the electrolyte which led to the formation of solid electrode interface (SEI) on the lithium counter electrode and this process was completed in the initial galvanostatic charge cycle [259, 277, 278]. The structure of the CV curves maintained its integrity throughout the first three cycles and the redox peaks were highly repeatable, which indicated the excellent structural stability of LCO/3%CNTs cathodes at room temperature [279].



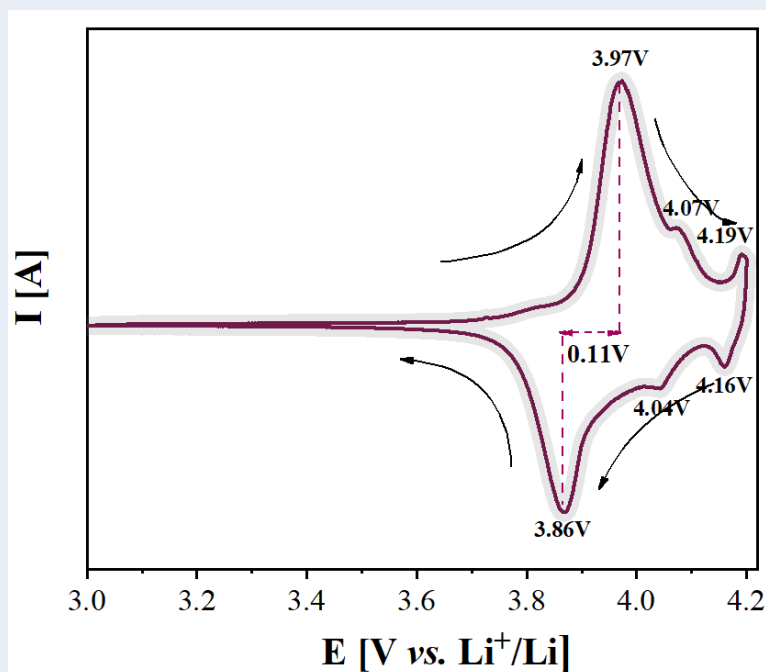


**Fig. 4-11.** The cyclic voltammogram of LCO/3%CNTs pellet for the initial cycle recorded at the sweep rate of  $0.1 \text{ mV s}^{-1}$ .

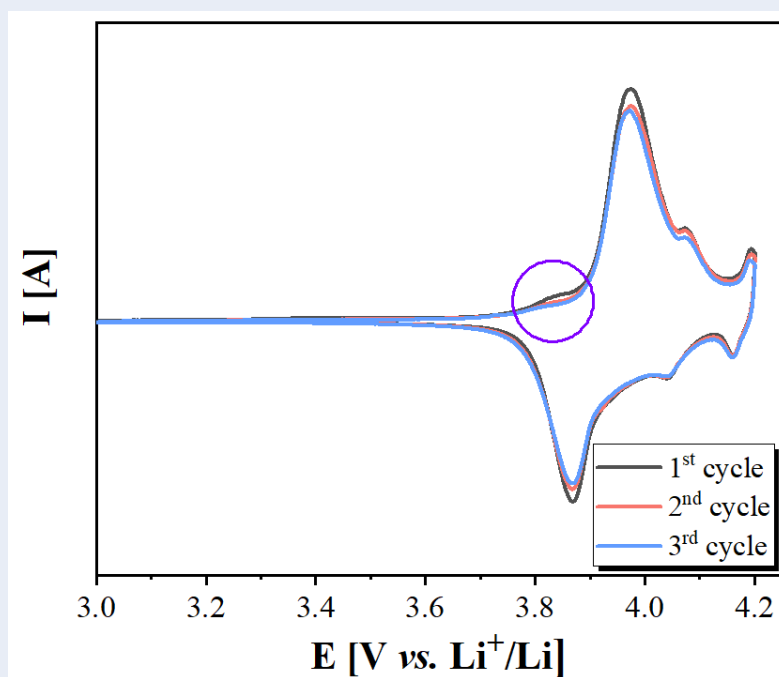


**Fig. 4-12.** The cyclic voltammetry curves of LCO/3%CNTs pellet for the first three cycles at the sweep rate of  $0.1 \text{ mV s}^{-1}$ .

The galvanostatic charge/discharge curves of LCO/3%CNTs cathode produced by CSP are shown in Fig. 4-13, along with their corresponding gravimetric/volumetric capacities

at the current rate of 0.1 C. The charge/discharge curves represented typical lithium storage behaviour of  $\text{LiCoO}_2$  in layered O3 structure. The LCO/3%CNTs cathode delivered a gravimetric charge capacity of  $160 \text{ mAh g}^{-1}$  and a gravimetric discharge capacity of  $124 \text{ mAh g}^{-1}$  in the initial cycle, yielding a relatively low coulombic efficiency of 77.5%. This low coulombic efficiency of LCO/3%CNTs cathode was attributed to the formation of stable SEI which consumed partial  $\text{Li}^+$  ions. The density of LCO/3%CNTs composite cathode was calculated to be  $3.82 \text{ g cm}^{-3}$ , which was much greater than that of electrodes prepared by conventional tape-casting technique ( $\sim 0.55 \text{ g cm}^{-3}$ ) due to the densification achieved by CSP and the remove of inactive components, *viz.* polymeric binders. In the perspective of volumetric capacity, the LCO/3%CNTs cathode delivered a volumetric discharge capacity of  $\sim 459 \text{ mAh cm}^{-3}$  in the initial cycle which is generally not accessible in conventional tape-casting electrodes ( $\sim 75 \text{ mAh cm}^{-3}$ ). Considering that the discharge voltage was 3.86 V in CV results, the volumetric energy densities of LCO/3%CNTs cathode can be calculated to be as high as  $\sim 1764 \text{ Wh L}^{-1}$ .

Notably, a polarisation spike was observed over the initial-cycle capacity range of 5-10  $\text{mAh g}^{-1}$  which corresponded to  $x=0.02\text{-}0.04$  for  $\text{Li}_{1-x}\text{CoO}_2$ . The occurrence of this polarisation spike at low-voltage region was intimately related to the semiconductor-metal structural transition but it completely disappeared in the successive cycles [280]. At the very beginning of charge process, a tiny amount of  $\text{Li}^+$  ions were deintercalated from the host and it triggered the irreversible semiconductor-metal structural transition. The irreversibility of semiconductor-metal structural transition was ascribed to the difficulty of re-intercalating this tiny amount of  $\text{Li}^+$  ions to restore the original host state in the following discharge process [73]. This explains the disappearance of polarisation spike from the 2<sup>nd</sup> cycle onwards.

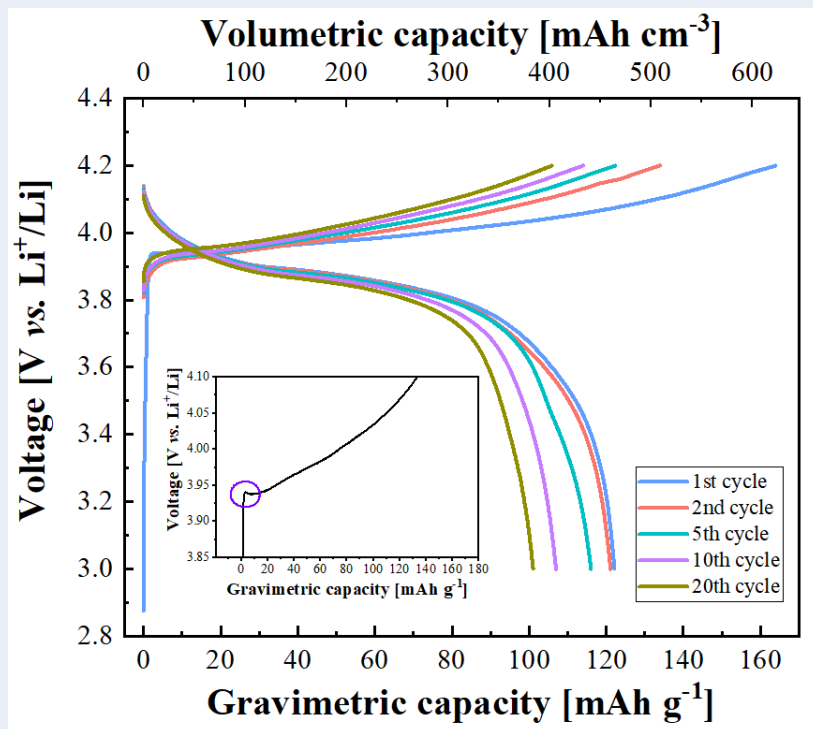


**Fig. 4-13.** Galvanostatic charge/discharge curves of LCO/3%CNTs pellet for 1<sup>st</sup>, 2<sup>nd</sup>, 5<sup>th</sup>, 10<sup>th</sup>, and 20<sup>th</sup> cycles at the current rate of 0.1 C (inset: the magnified region of polarisation spike appearing in the first charge cycle).

Fig. 4-14 depicts the cycling behaviour of LCO/3%CNTs cathode at the current rate of 0.1 C. After 40 cycles, the gravimetric discharge capacity monotonically diminished from  $\sim 120 \text{ mAh g}^{-1}$  to  $\sim 75 \text{ mAh g}^{-1}$  with a capacity retention of only 62%. A post-mortem FEGSEM characterisation was performed on the LCO/3%CNTs cathode after 40 cycles. As shown in Fig. 4-15, the surface morphologies of LCO particles represent a few apparent changes before and after galvanostatic (dis)charge process. The LCO/3%CNTs particles exhibited smooth and intact surfaces before galvanostatic process whilst a number of micro-cracks were found on the LCO/3%CNTs particles after long-term galvanostatic process. This could be one of the culprits behind the significant cycle to cycle capacity degradation of the LCO/3%CNTs cathode.

The low capacity retention over long-term cycling and the morphological changes of

LCO/3%CNTs particles could be due to two reasons: (i) The brittle intercalation transition-metal oxides are known to possess high elastic moduli (70 GPa) but low fracture toughness ( $K_{IC} < 5 \text{ MPa m}^{1/2}$ ). It is reported that  $\text{LiCoO}_2$  structure underwent 0.2% shrinkage along the  $a$  direction and 2.4% expansion along the  $c$  direction with a total volumetric change of 1.9% upon the deintercalation of Li ions, which induces large strains on the LCO particles [11]. Consequently, the repetitious intercalation/deintercalation process of LCO/3%CNTs cathode may induce nucleation and propagation of microstructural cracks within the structure and even destroy the mechanically weak sinter-necks of adjacent LCO particles, leading to electrode deformation, fragmentation, and electrochemical pulverisation [281]; (ii) Owing to the absence of polymeric binder which can function as a flexible cushion to sufficiently buffer the volumetric change of LCO, the LCO/3%CNTs matrix became rigid and the disintegration of electroactive materials became worse, which resulted in the declining capacity.

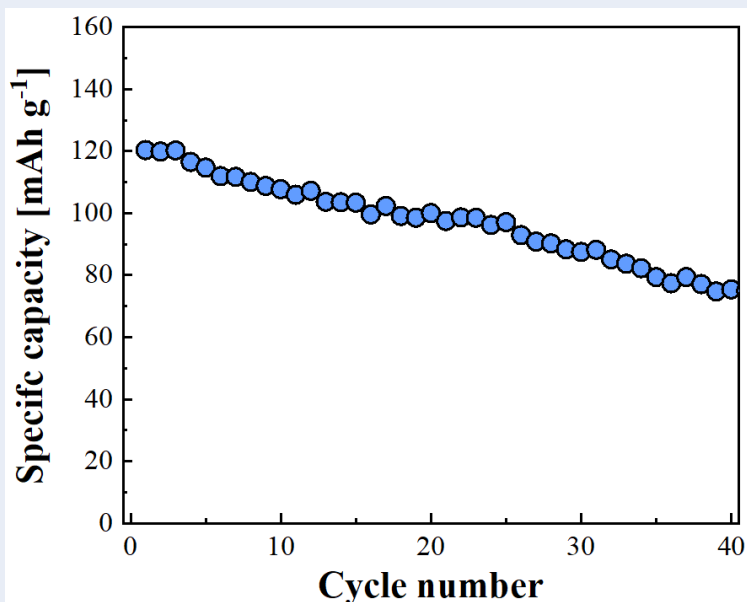


**Fig. 4-14.** The cycling performance of LCO/3%CNTs pellet between 3.0 V and 4.2 V at the constant rate of 0.1 C.

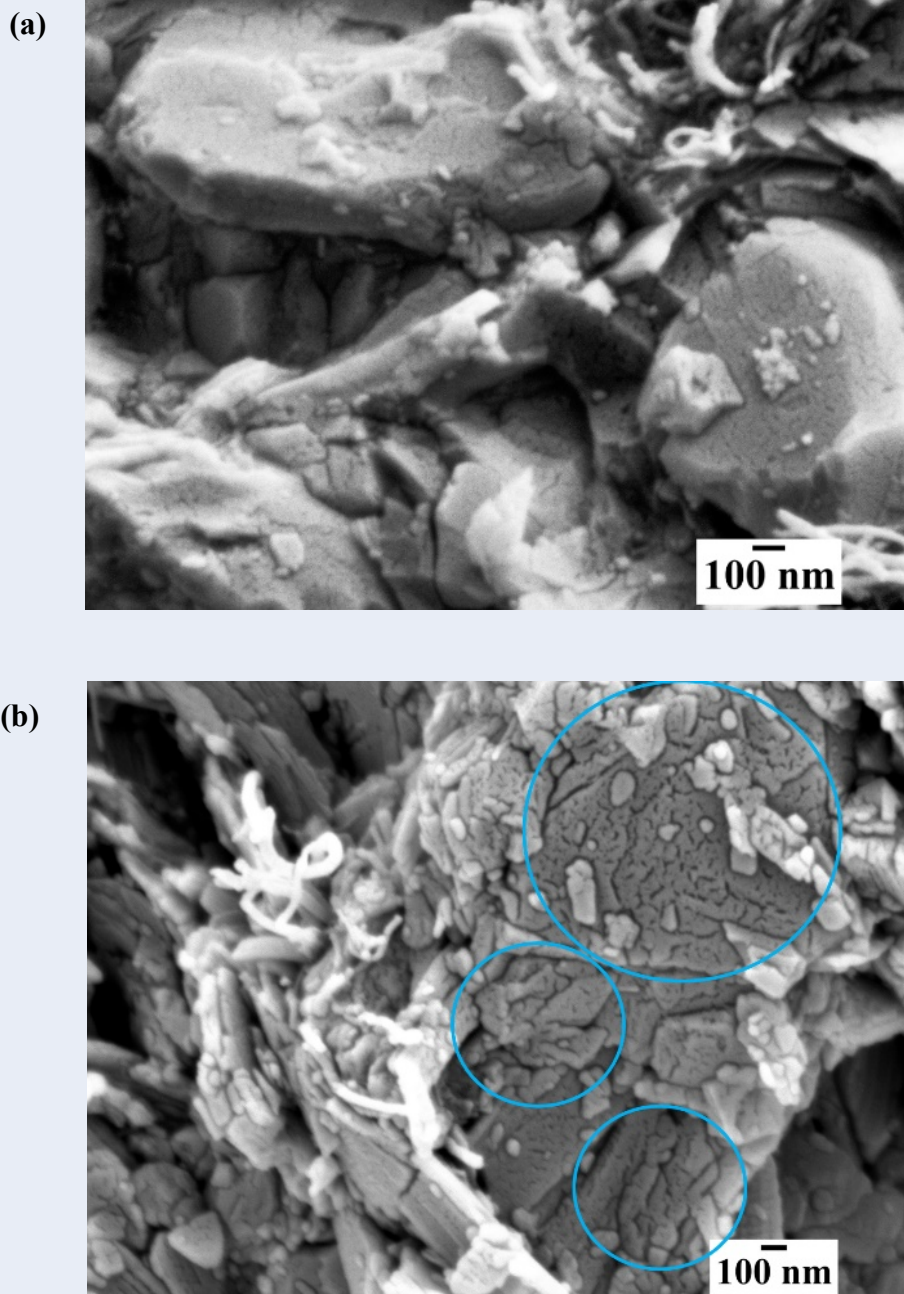


**Fig. 4-15.** FEGSEM images of LCO/3%CNTs pellet (a) before and (b) after 40 galvanostatic cycles (the micro-cracks were marked in cyan circles).

Fig. 4-16 shows the discharge rate capabilities of the half-cell made by LCO/3%CNTs cathode at various current rates. At low current rates, the LCO/CNTs cathode delivered gravimetric capacities of  $\sim 120 \text{ mAh g}^{-1}$  and  $\sim 80 \text{ mAh g}^{-1}$  at 0.1 C and 0.2 C, respectively, which corresponded to the volumetric capacities of  $\sim 440 \text{ mAh cm}^{-3}$  and  $\sim 295 \text{ mAh cm}^{-3}$ , respectively. The corresponding volumetric energy densities were  $\sim 1700 \text{ Wh L}^{-1}$  at 0.1 C

and  $\sim 1138.7 \text{ Wh L}^{-1}$  at 0.2 C. The gravimetric capacities of LCO/3%CNTs cathode were promising at low current rates and are comparable to bulk  $\text{LiCoO}_2$  cathodes densified by different methods at the identical current rates, which are tabulated in Table 4-2. Nevertheless, the gravimetric capacity of LCO/3%CNTs cathode significantly reduced to merely  $\sim 20 \text{ mAh g}^{-1}$  at 0.5 C, which can be ascribed to the slow diffusion rate of lithium ions in the compact  $\text{LiCoO}_2$  matrix. Notably, when the current rate returned to 0.1 C immediately after 0.5 C, a remarkable reversible discharge gravimetric capacity of  $\sim 110 \text{ mAh g}^{-1}$  could be retained, indicating the robust crystalline microstructure of LCO/3%CNTs cathode.

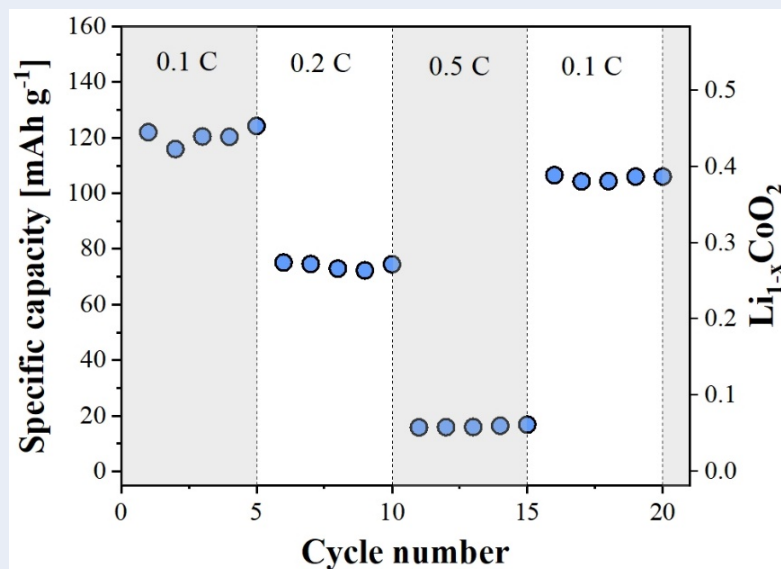


**Fig. 4-16.** The discharge rate capabilities of LCO/3%CNTs pellet every five cycles at various current rates.

**Table 4-2.** Electrochemical performance of densified LiCoO<sub>2</sub> cathodes prepared by different methods.

Electrode composition	Processing technique	Thickness [μm]	Current rate	Gravimetric capacity [mAh g <sup>-1</sup> ]	Volumetric capacity [mAh cm <sup>-3</sup> ]	Current rate	Gravimetric capacity [mAh g <sup>-1</sup> ]	Volumetric capacity [mAh cm <sup>-3</sup> ]	References
LiCoO <sub>2</sub>	Co-extrusion	300	C/10	144.6	~455	C/5	118.9	~375	[12]
LiCoO <sub>2</sub>	Cold sintering	230	C/10	~131	~443	C/5	~116.8	~390	[96]
LiCoO <sub>2</sub>	Conventional sintering	260	C/10	~140	~524	C/5	~135	~505	[11]
LiCoO <sub>2</sub>	Rotating magnetic field	130	C/30	~142	N/A	C/3	102.3	N/A	[13]
32LCO/65LLTO/ 3MWCNT*	Spark plasma sintering	170	C/20	81.9	N/A	N/A	N/A	N/A	[87]
90LCO/7LBO/ 3MWCNT**	Spark plasma sintering	200	C/2	99	N/A	N/A	N/A	N/A	[282]
LiCoO <sub>2</sub> + 3wt%MWCNTs	CSP	100-200	C/10	~120	~440	C/5	~115	~295	This work

\*LLTO—Li<sub>5</sub>La<sub>3</sub>Ta<sub>2</sub>O<sub>12</sub>\*\*LBO—Li<sub>3</sub>BO<sub>3</sub>

## 4.5. Chapter conclusions

In this chapter, a novel densification strategy, i.e., cold sintering process (CSP), with aqueous-based solution has been successfully employed to fabricate binder-free LCO-based composite cathode at ultra-low temperature for the first time.

- The effects of uniaxial pressure, CSP processing temperature, duration time and post-CSP annealing treatment on the relative densities of monolithic LCO pellets and LCO/*x*CNTs pellets were also studied. The addition of transient liquid is a requirement for cold sintering process because it assists the particle re-arrangement and dissolution-reprecipitation process for the densification. Uniaxial pressure provides additional driving force and facilitates the (i) the redistribution of transient liquid, (ii) the solubility of LCO, and (iii) diffusive mass transport of dissolved LCO species during CSP. Increasing CSP temperature has an equivalent impact of increasing CSP pressure on densification [99, 101]. CSP is time dependant and requires at least 60 min of duration time for the densification to accomplish. Generally speaking, higher pressure, higher temperature and longer duration is beneficial to improving densification but the selection of CSP is highly dependent on the materials characteristics and experimental apparatus/conditions [98]. In this work, the optimum density of monolithic LCO pellets was obtained at 77.7% with 20 wt% LiOH solution, 250 °C, 250 MPa and 1-hour duration time. It provides the evidence that the density of ceramic pellets can be tuned in CSP, which is incredibly challenging to achieve in conventional sintering techniques.
- The fabrication of LCO/CNTs composites, in which their melting points exhibit large difference, was successfully achieved for the first time at the temperature as low as



250 °C, demonstrating CSP could be a game changing technology in ceramics processing and component manufacturing.

- The experimental work found that the percolation threshold of CNTs in LCO/*x*CNTs pellets was 3 wt% which yielded a decent electrical conductivity of  $\sim 2.84 \text{ S cm}^{-1}$ . After elimination of sluggish amorphous phase on grain boundary at 400 °C, the binder-free LCO/3%CNTs cathode possessed a commendable electrical conductivity of  $3.48 \text{ S cm}^{-1}$  and delivered a high volumetric capacity of  $\sim 459 \text{ mAh cm}^{-3}$  and the corresponding volumetric energy densities of  $\sim 1764 \text{ Wh L}^{-1}$ , which were much higher than those values obtained in conventional tape-cast electrodes. The high volumetric capacity/energy densities of CSP-ed LCO/3%CNTs cathode indicates that it can find itself for applications where the space to accommodate LIBs is limited.
- Nevertheless, this CSP strategy was compromised by the apparent capacity degradation at 0.1 C and the low specific gravimetric capacity of  $\sim 20 \text{ mAh g}^{-1}$  at 0.5 C, largely due to the rigid network formed by CNTs and the intrinsically low electrical conductivity. Henceforth, it is proposed that the electrochemical properties of LCO pellets produced by CSP can be improved if the conductive CNTs is replaced with an alternative that has porous structure and higher electrical conductivity. The former property is beneficial for providing flexible structure to buffer conceivable volumetric change of LCO particles, while the latter is believed to reduce the intrinsic ohmic resistance of LCO matrix by facilitating the flow of electrons on higher conductive network.
- Graphene, a typically 2D hexagonal structure of carbon atoms, is renowned to exhibit high electrical conductivity, high surface area and advantageous porous structure,

which predestines it a strong candidate to replace CNTs as the conductive filler of choice in this scenario. Therefore, the following chapter will mainly discuss the synthesis of graphene using microwave-assisted method and demonstrate its potential use in LCO pellets produced by CSP.

## **Chapter 5. Rapid microwave-assisted bulk production and characterisation of reduced graphene oxide synthesised under tuneable microwave powers for Li-ion battery application**

In this chapter, the MWrGO synthesised using various microwave powers and Ar flushing times was comprehensively characterised, together with the influence of preliminary annealing treatment on microwave absorption capability of GO. The effect of the coagulation bath variables on the preparation of the GO beads and the formation mechanism of GO beads was discussed in Section 5.1. Prior to microwave irradiation, GO beads were subject to annealing treatment at 250 °C to partially restore the conjugated graphitic structures and eliminate the inter-boundaries of defective regions formed by oxygen functional groups. Moreover, the enhanced microwave absorption of as-prepared GO by annealing treatment was demonstrated in Section 5.2 and was rationalised in Section 5.3 using a combination of technical techniques, including Raman, XRD, TGA, FTIR, XPS, BET, SEM, HR-TEM and four-probe conductivity measurement. A modified Raman metric was also proposed to investigate the structural evolutions of MWrGO samples by deducting the intensity contribution of D' peak from the apparent G peak in Raman spectrum, giving a more reliable evaluation metric. The last part of this chapter, Section 5.4, presented the electrochemical evaluations of the selected MWrGO as an electroactive material in anode and as a conductive additive in cathode of Li-ion batteries (LIBs), respectively.

## 5.1. Coagulation bath of GO

Coagulation bath method has been widely used to produce GO beads because of its ease of preparation, low cost, and scale-up capability. In this project, spherical-like GO beads were made in 1 wt%  $\text{CaCl}_2$  coagulation bath mixed with 5 wt% ethanol. In general, the coagulation bath of GO involves three stages: (i) the extrusion of GO suspension; (ii) the formation of core-shell GO beads; and (iii) the soaking of GO beads. It has been reported that the concentration of GO suspension needs to be carefully tailored to give decent viscosity prior to the extrusion stage [283]. If the viscosity of GO suspension is too high, the GO suspension is extruded continuously, which leads to the formation of GO fibres/filaments, depending on the nozzle size. If the viscosity is too low, GO suspension behaves like liquid and cannot hold the bead shape once being hit by the coagulation bath [283]. From our research experience, the GO concentration of  $15 \text{ mg ml}^{-1}$  was used by taking into the account of both lateral size and the oxidation extent of the GO flakes.

In the first stage of coagulation bath of GO, many factors have been identified to affect the formation of GO beads and ultimately the properties of GO beads. The most paramount factor is believed to be the concentration of coagulating agent, *i.e.*,  $\text{CaCl}_2$ , used in the bath. To figure out the optimum  $\text{CaCl}_2$  concentration, three different concentrations of  $\text{CaCl}_2$  coagulation bath, *i.e.*, 0 wt%  $\text{CaCl}_2$  (deionised water without coagulating agent), 1 wt%  $\text{CaCl}_2$ , and 3 wt%  $\text{CaCl}_2$ , were prepared. Then, the  $15 \text{ mg ml}^{-1}$  GO suspension was extruded through a needle with the inner diameter of 0.8 mm at the distance of  $\sim 6 \text{ cm}$  above the coagulation bath surface to produce spherical-like GO. Thereafter, the GO beads were soaked and observed in the coagulation baths for 60 min. It was intriguing to find that the GO beads soaked in the 0 wt%  $\text{CaCl}_2$  solution started to collapse after 30 min and completely collapsed after 60 min, as shown in Fig. 5-1. The

collapse of GO beads is attributed to the diffusion of GO flakes which cannot self-assembly at the absence of  $\text{CaCl}_2$ . On the contrary, the GO beads soaked in 1 wt% and 3 wt%  $\text{CaCl}_2$  solutions were able to maintain the sphere-like shapes after even 24 hours, as shown in Fig. 5-2, indicating the excellent structural stability of GO beads in  $\text{CaCl}_2$ -containing coagulation bath.

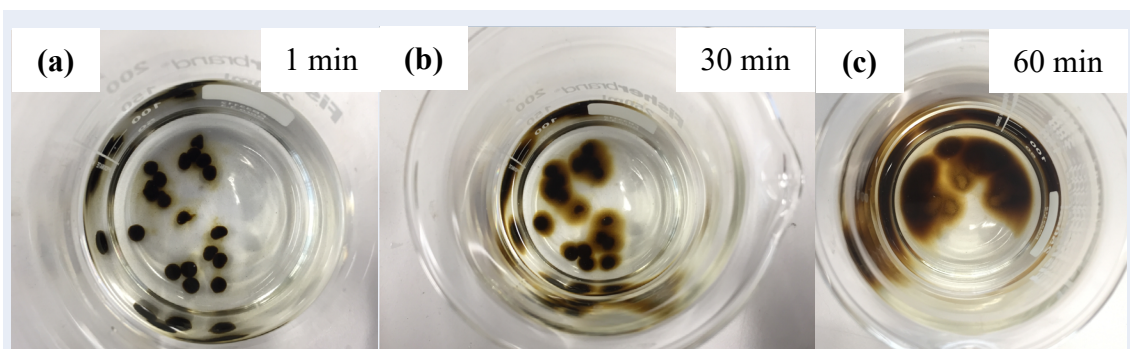


**Fig. 5-1.** The evolutions of the GO beads soaking in 0 wt%  $\text{CaCl}_2$  solution (de-ionised water) after (a) 1 min, (b) 30 min, and (c) 60 min.

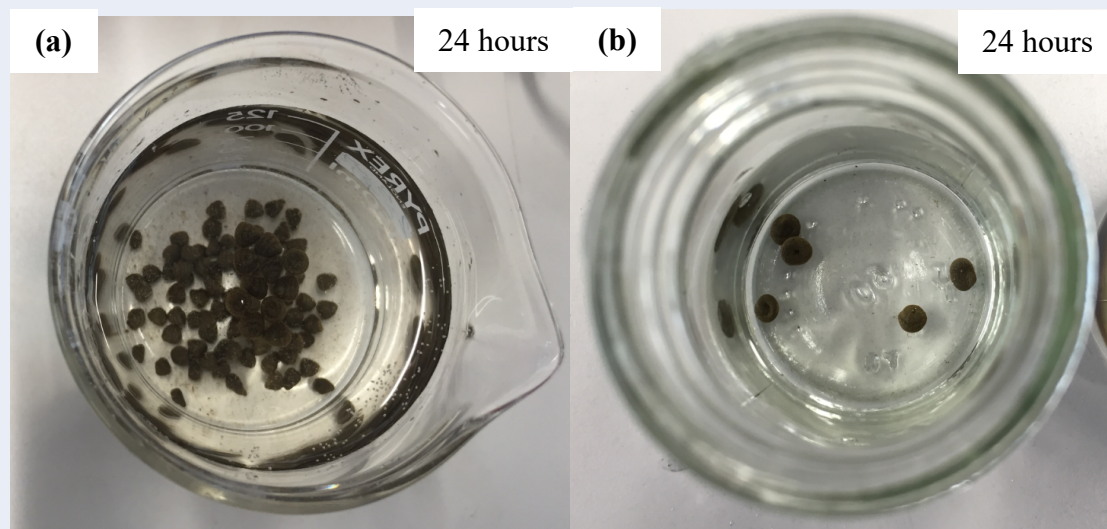


**Fig. 5-2.** The photographs of the GO beads which have been soaked in (a) 1 wt%  $\text{CaCl}_2$  and (b) 3 wt%  $\text{CaCl}_2$  after 24 hours.

Higher concentration of  $\text{CaCl}_2$  coagulation bath was reported to bring about higher mechanical property and better integrity of the GO beads within shorter soaking time [283]. However, the increase in the concentration of  $\text{CaCl}_2$  coagulation bath implies stronger adsorption of cationic ions on the surfaces of the GO beads. Moreover, the

presence of the residual  $\text{Ca}^{2+}$  ions can adversely affect the electrical conductivity of rGO after reduction [284]. Fig. 5-3 compares the XRD spectra of GO beads soaked in 1 wt% and 3 wt%  $\text{CaCl}_2$  solutions after 24 hours. It is recognised that the XRD spectrum of GO beads soaked in 3 wt%  $\text{CaCl}_2$  solution presents strong diffraction peaks related to  $\text{CaCl}_2$ , indicating the high content of  $\text{CaCl}_2$  on the surfaces of GO. The amount of  $\text{CaCl}_2$  presented on the GO beads soaked in 3 wt%  $\text{CaCl}_2$  solution was also confirmed using energy dispersive X-ray spectroscopy (EDS), as shown in Fig. 5-4. And it is found that  $\text{Ca}^{2+}$  and  $\text{Cl}^-$  ions fully covered the surfaces of GO beads soaked in 3 wt%  $\text{CaCl}_2$  solution. In this regard, the concentration of 3 wt%  $\text{CaCl}_2$  in coagulation bath was too high and 1 wt%  $\text{CaCl}_2$  solution is selected to produce GO beads in this project.

The addition of ethanol into coagulation bath solution is alternative way to hold the shape of GO beads. The surface tension of the aqueous coagulation bath is large and can be an obstacle for GO beads to break through. Increasing the dripping distance from the nozzle tip to the coagulation solution can increase the potential energy of GO beads but adversely leads to shape deformation. Alternatively, this problem can be tackled by mixing 5 wt% ethanol with aqueous coagulation solution because ethanol is beneficial to diminishing the surface tension and lower the density of coagulation solution [283].

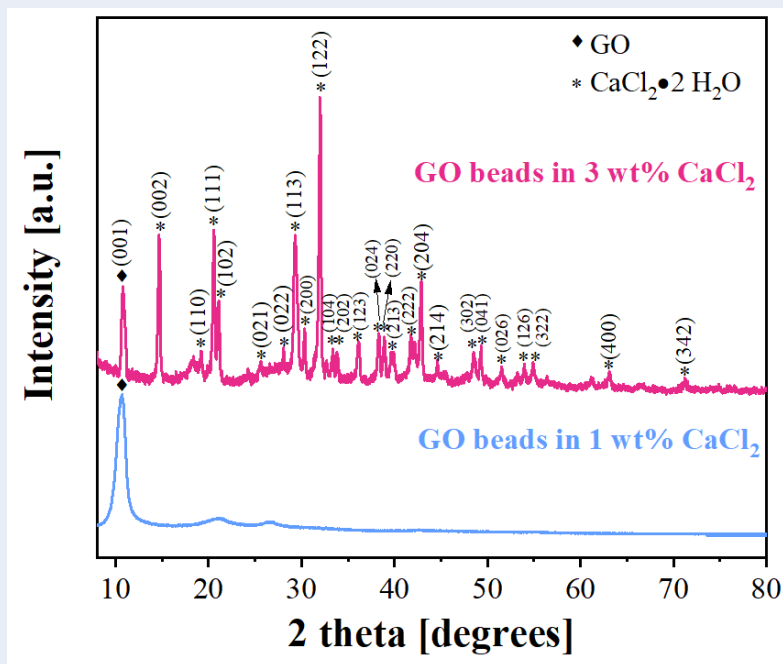


**Fig. 5-3.** XRD spectra of the GO beads which have been soaked in 1 wt% and 3 wt%  $\text{CaCl}_2$  solutions after 24 hours.

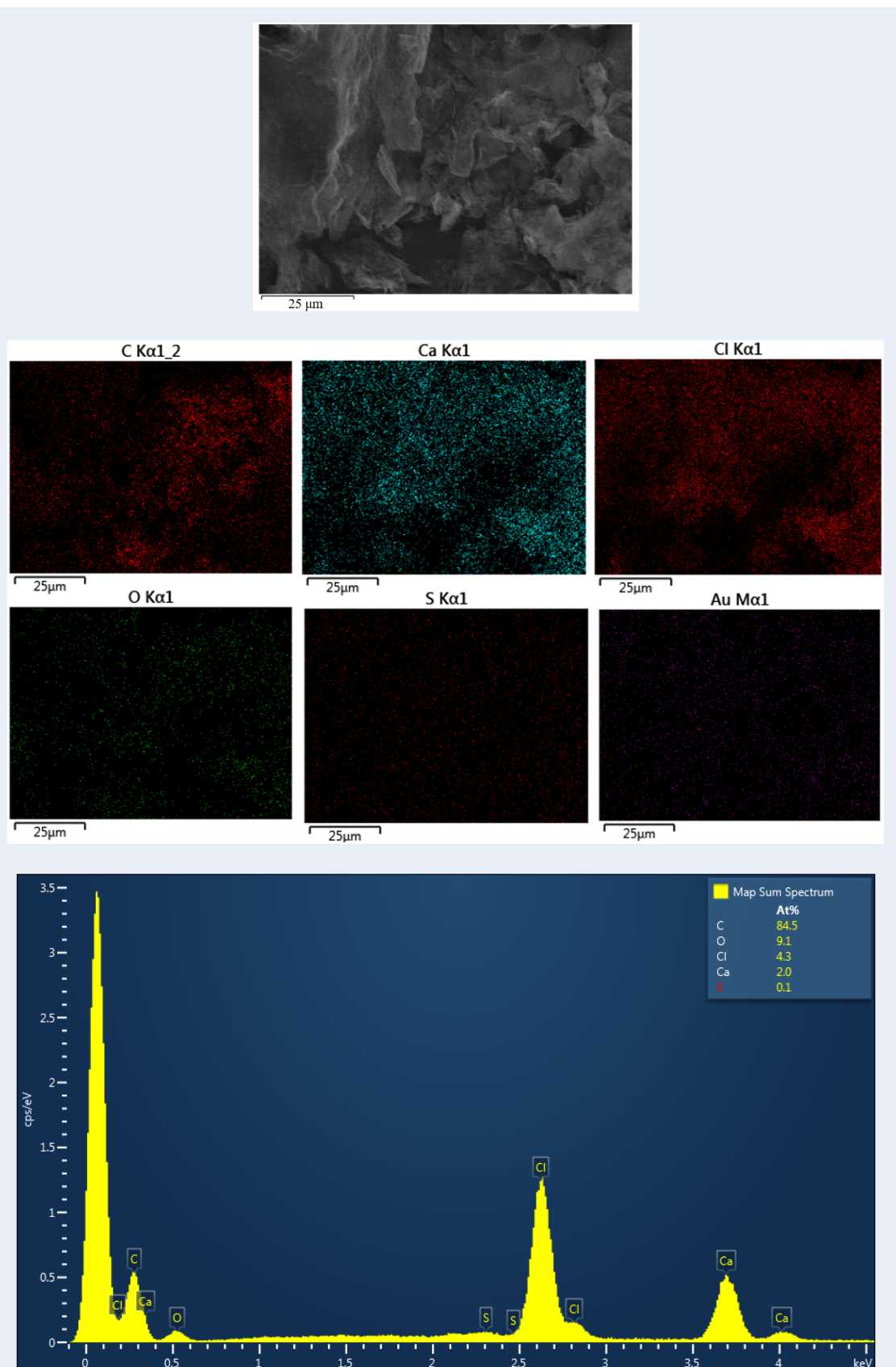


**Fig. 5-4.** EDS compositional mapping of the GO beads which have been soaked in 3 wt%  $\text{CaCl}_2$  solution after 24 hours (Au elemental mapping was caused by the conductive coating on sample surface).



After the extrusion stage, the formation of core-shell structure occurred on the GO beads once they come in contact with  $\text{CaCl}_2$  containing coagulation solution. The formation of core structure mainly involves the self-assembly process in which GO flakes align themselves to take up the densest configuration. The oxygen functional groups endow the GO flakes with negative charges which can repulse the GO flakes in a steady state [285]. However, once the GO beads are immersed in the coagulation solution, the positively charged cationic ions, such as  $\text{Ca}^{2+}$ , are likely to react with negatively charged GO flakes, which leads to the aggregation and segregation of GO on the surfaces. In this scenario, a robust outer GO shell is formed while the inner part of the GO beads is still in the liquid state, as shown in Fig. 5-5 (a). The freshly formed GO beads are physically weak owing to the thin GO shell. Therefore, it is indispensable to soak the GO beads in the bath to further coagulate the GO beads. In the final stage, the water molecules diffuse out from the inner part of GO beads to the high-concentration bath and the  $\text{Ca}^{2+}$  ions diffuse in the opposite direction due to the presence of concentration gradient across the shell, as shown in Fig. 5-5 (b) [283]. Meanwhile, the inner GO flakes align themselves to self-assembly, which results in the growth of GO shell and the increase in structural stability. After soaking in coagulation bath for 24 hours, the resultant GO beads were washed and dried to produce as-prepared GO. This GO coagulation procedure is believed to benefit the subsequent annealing treatment because the more compact GO configuration would conduce to the rapid pressure build-up and lead to more violent exfoliation, which will be discussed later.

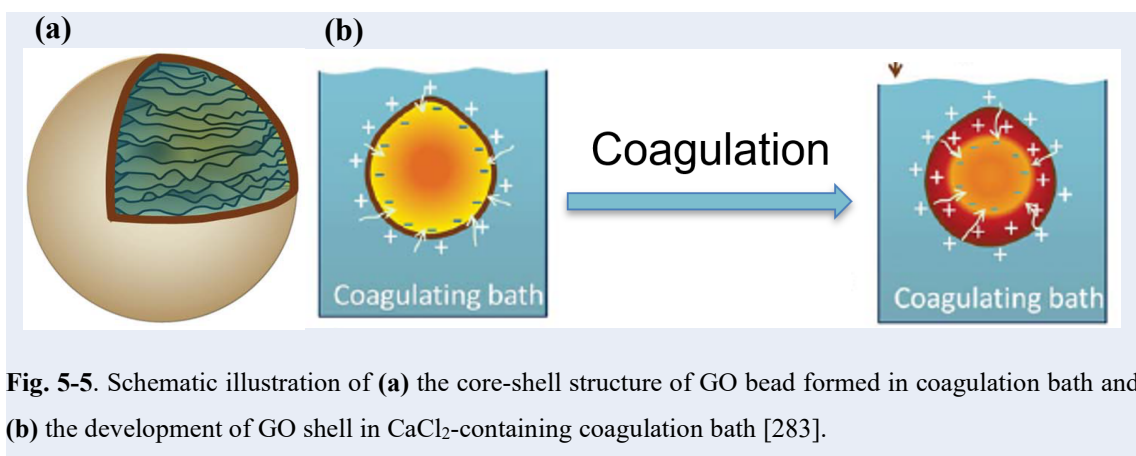
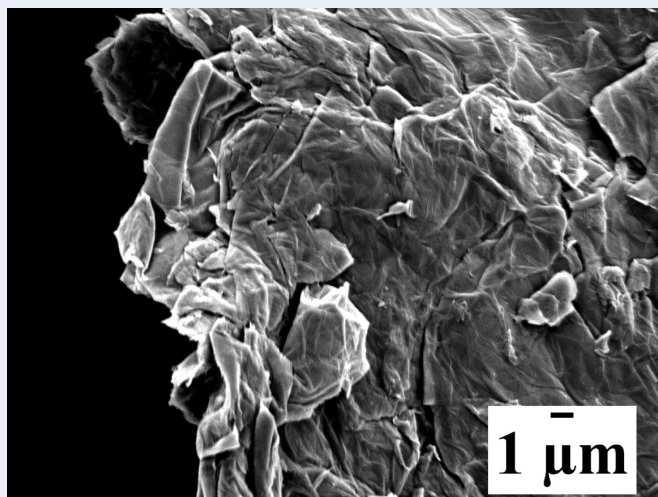


**Fig. 5-5.** Schematic illustration of **(a)** the core-shell structure of GO bead formed in coagulation bath and **(b)** the development of GO shell in  $\text{CaCl}_2$ -containing coagulation bath [283].

## 5.2. The enhanced microwave absorption of GO by annealing treatment

The as-prepared GO beads produced using coagulation bath were then subjected to annealing treatment at 250 °C prior to microwave irradiation in order to boost its microwave coupling capability. It has been believed that the oxidation reaction of pristine graphite introduces a number of oxygen functional groups on the basal planes of GO, which cleave the defect-free conjugated network down to tiny polyaromatic islands [136]. Those polyaromatic islands create inter-boundaries along the vicinity of the oxygen functional groups and thus confine the transportation of free  $\pi$  electrons within delimited regions. Consequently, the  $\pi$  electrons on the GO are unlikely to be driven by the electric field component of electromagnetic microwaves to transport over a long range to generate sufficient Joule heating to effectively reduce GO. Fortunately, GO is thermodynamically unstable due to the incorporated -OH and -C=O groups [136, 178]. Therefore, upon annealing at 250 °C in inert Ar atmosphere, the thermal pyrolysis of -OH and -C=O groups occurred and led to a vigorous gas release of CO, CO<sub>2</sub>, H<sub>2</sub>O, and trace amount of volatile acetone [178, 185, 197, 286]. Since the microstructure of as-prepared GO was quite compact as shown in Fig. 5-6 (a), the majority of decomposed gases were easily trapped in the GO, which incurred a rapid pressure building-up. That was because the decomposition rate of oxygen functional groups exceeded the diffusion rate of the gas. Once the internal pressure reached the threshold of van der Waals binding forces, the graphitic layers were violently exfoliated and it concurrently resulted in the formation of mesopores (Fig. 5-6 (b)), which will be proved further with BET results in Section 5.3. This is also evidenced by a remarkable volume change, as shown in Fig. 5-7, which implied the as-prepared GO were efficiently exfoliated to a very large extent.

(a)



(b)

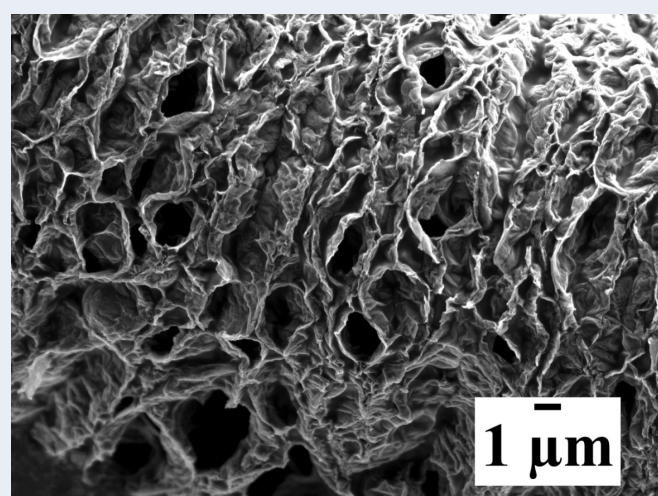


**Fig. 5-6.** Typical FEGSEM micrographs of (a) as-prepared GO and (b) annealed GO which has been subjected to annealing at 250 °C.



**Fig. 5-7.** Photos of 100 mg of (left) as-prepared GO and (right) fluffy annealed GO, showing the large volume expansion (almost doubles the apparent volume) upon annealing treatment at 250 °C in argon atmosphere.

Chaban *et al.* simulated the decomposition of labile oxygen functional groups during annealing process using reactive molecular dynamics (RMD) simulation and claimed that only in-plane -C=O groups could be decomposed [197]. Note that their conclusion was drawn on the computer simulation model where only -C=O groups were present on graphitic layers. Nevertheless, we speculated that not only -C=O but also -OH could be decomposed during the annealing process, which will be clarified in the following FTIR and XPS results. The throughput exfoliation of annealed GO provided two advantageous features for the subsequent microwave reduction process: (i) more GO surfaces are accessible for microwave irradiation; (ii) the presence of residual polar functional groups, such as -OH, -C=O and -COOH, can realign in tandem with oscillating microwaves filed.

The annealing treatment of as-prepared GO partially restore the conjugated graphitic structures and partially eliminate the inter-boundaries of defective regions through removing -OH and -C=O, which is beneficial for improving the interaction with microwave radiation. Fig. 5-8 depicts the temperature profiles of annealed GO and unannealed GO as a function of time when exposed to microwave irradiation of 800 W in 10 min argon flushing atmosphere. When the microwave oven was switched on, there was a count-down of 10 seconds for the microwaves to be directed on the samples. The obtained temperature profiles exhibited a common trajectory of microwave-induced heating where an initial linear increase in temperature was achieved, followed by a levelling off when the thermal dissipation equalled to the thermal generation in the reaction system, and a dynamic equilibrium was established. In sharp contrast with the highest temperature of  $\sim 160$  °C achieved on the unannealed GO, the annealed GO could be heated up to  $\sim 670$  °C by microwave irradiation within few milliseconds, yielding a remarkable heating rate of  $\sim 30\,000$  °C min<sup>-1</sup>. This superfast heating rate of annealed GO

is the direct results of both intense microwave absorption and efficient conversion from microwave energy to thermal energy. Additionally, the elevated temperature ( $\sim 670\text{ }^{\circ}\text{C}$ ) of annealed GO is in good agreement with the observation by Hu *et al.* in which the improved microwave heatability was positively related to the lower structural defect level [136]. Furthermore, the elevated temperature ( $\sim 670\text{ }^{\circ}\text{C}$ ) of annealed GO is believed to lead to a localised thermal decomposition of oxygen functional groups. Meanwhile, the rearrangement of carbon lattices on annealed GO occurred, yielding a more crystalline carbon hexagonal structure [184]. This superfast heating rate by microwave irradiation is far greater than the heating rate of  $2000\text{ }^{\circ}\text{C min}^{-1}$  obtained in conventional heating method [146]. The superfast heating rate is generally desired to rapidly generate pressure to overcome the van der Waals binding force between adjacent graphitic layers [128, 146]. Henceforth, the intense microwave absorption of annealed GO signifies the distinct advantage of microwave synthesis over conventional heating methods to produce graphene. A typical FEGSEM image of MWrGO synthesised from annealed GO with the microwave power of 800 W and the argon flushing time of 10 min was shown in Fig. 5-9, which displayed nanoscale thickness.

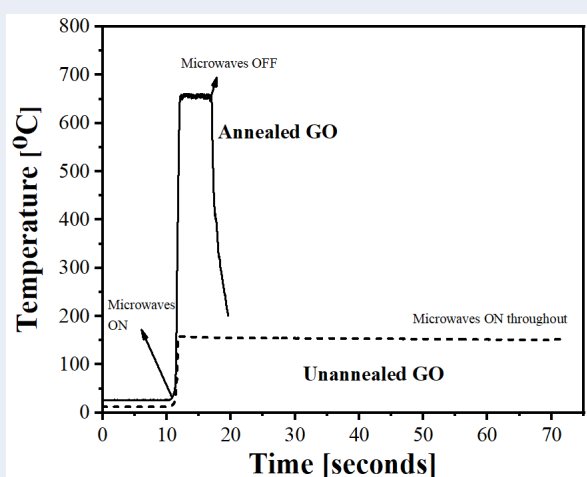


**Fig. 5-8.** A comparison of time-temperature profiles of annealed GO and unannealed GO upon irradiation by 800 W microwaves with the argon flushing time of 10 min. The heating rate is  $\sim 30\,000\text{ }^{\circ}\text{C min}^{-1}$  for annealed GO and  $\sim 150\text{ }^{\circ}\text{C s}^{-1}$  for unannealed GO. The temperature records were extracted from [Video S2](#).

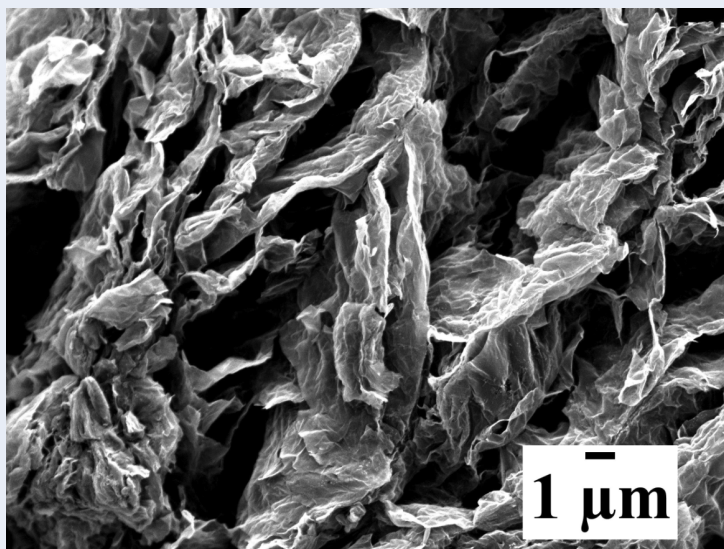


**Fig. 5-9.** Typical FEGSEM image of 800W/10min MWrGO. The graphene sheets were efficiently exfoliated and showed a wrinkled surface morphology.

In addition to the microwave reaction rate enhancement, a strong arcing was observed on annealed GO after only 1 - 3 s duration of microwave irradiation whereas no arcing was observed on unannealed GO after even 60 s. The occurrence of microwave-induced arcing may be ascribed to the congregation of free electrons at the sharp sites on graphene, which led to the ionisation of the surrounding gas [287]. During microwave irradiation of annealed GO, the restoration of graphitic structure occurred in the way that the isolated polyaromatic islands were merged to a larger graphitic structure, which enabled the transportation of the  $\pi$  electrons over a longer distance. In this scenario, there was a higher concentration of  $\pi$  electrons at sharp sites, such as plane edges or defective points, of the annealed GO sheets, resulting in the formation of intense electrostatic field [167, 287]. The induced electrostatic field was likely to ionise the surrounding gas through electron excitation, which was perceived as a form of electric-arcing from the macroscopic point of view. This is the plausible reason why the arcing started from hot-spot sites on annealed GO as shown in Fig. 3-11 (C) and, thereafter, propagated to fill the entire microwave reaction chamber as shown in Fig. 3-11 (D). A schematic illustration of microwave-



induced hotspots and arcing on graphene flake is provided in Fig. 5-10. We also believe that the microwave reduction of GO is a self-accelerating deoxygenation process because the freshly formed MWrGO themselves became the additional microwave absorption regions and in turn converted more microwave energy to thermal energy to remove the residual oxygen functional groups.

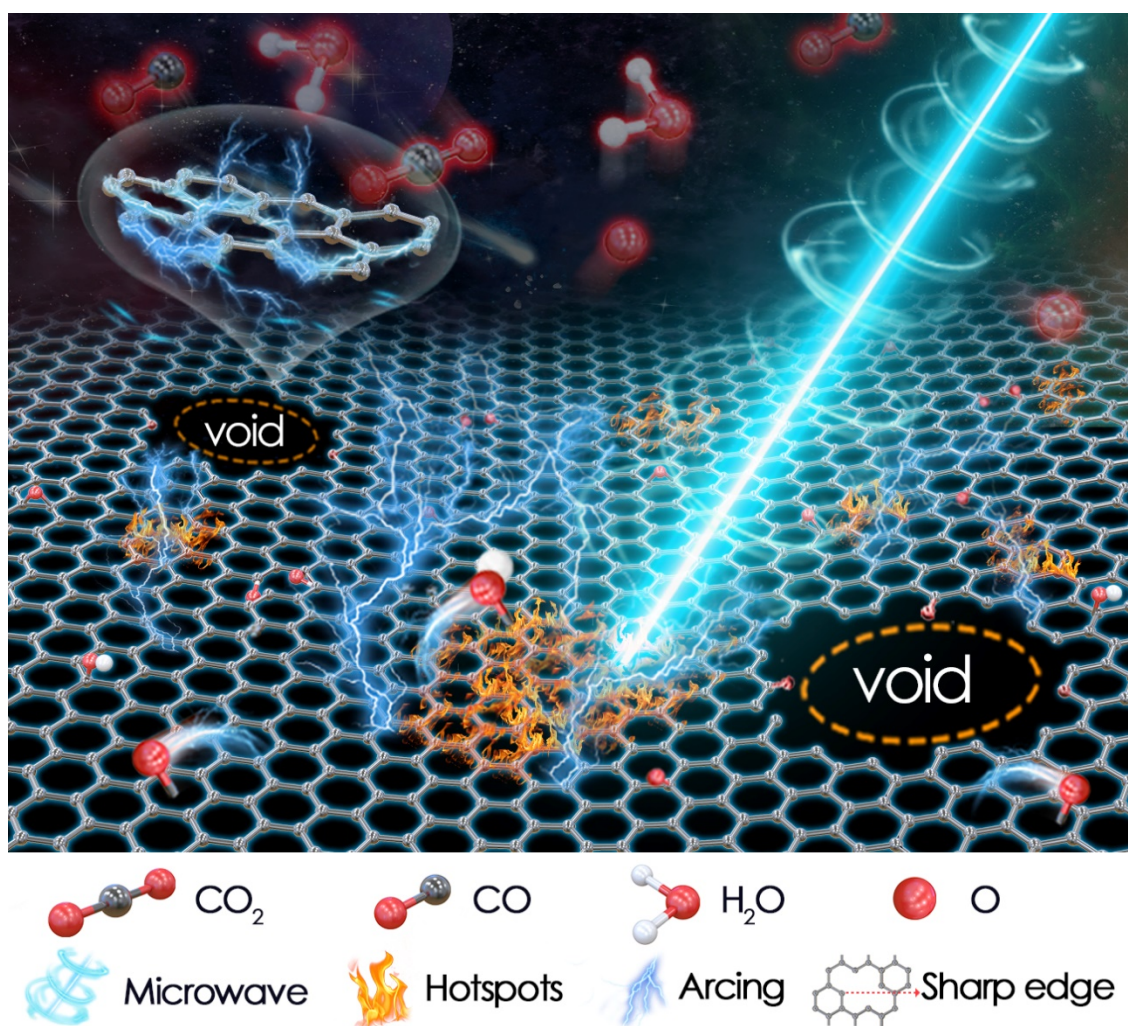


**Fig. 5-10.** A schematic illustration of microwave-induced hotspots and arcing on graphene flake.



### 5.3. MWrGO characterisation

After as-prepared GO was annealed at 250 °C, various microwave power outputs (300 W, 500 W, and 800 W) were used to reduce the annealed GO to obtain MWrGO samples in a reaction system flushed with high-purity argon gas for different periods of time (2 min, 5 min, 10 min, and 15 min). Thereafter, the synthesised MWrGO samples were extensively characterised in perspective of structural evolutions by Raman and XRD, chemistry analysis by FTIR, TGA and XPS, physical properties by BET and four-probe electrical conductivity, as well as morphological observation by FEGSEM and HR-TEM. The Raman and XRD results revealed that the highest-quality MWrGO can be synthesised at the microwave power of 800 W with the argon flushing time of 10 min. Chemistry analysis provided insight into the changes in oxygen functional groups during annealing treatment and microwave reduction process. Combined with BET and four-probe electrical conductivity, the 800W/10min MWrGO was measured to exhibit the high C/O of 14.29, the thermal stability up to 750 °C, the specific surface area of 310.24 m<sup>2</sup> g<sup>-1</sup> and the electrical conductivity of 761.4 S m<sup>-1</sup>. Moreover, FEGSEM and HR-TEM characterisation showed the efficient exfoliation/reduction of GO and the porous structure of 800W/10min MWrGO.

Raman spectroscopy has been the method of choice to study carbon derived materials and provides insights into structural evolution relating to lattice defects due to its unique phonon interaction with carbon hexagonal structure [288]. All Raman spectra of MWrGO samples synthesised at various microwave powers and various argon flushing times are shown in Fig. 5-11 (a) and Fig. 5-11 (b), respectively. It is recognised that all the Raman spectra exhibit four characteristic peaks: D peak at ~1350 cm<sup>-1</sup>, G peak at ~1580 cm<sup>-1</sup>, 2D peak at ~2680 - 2700 cm<sup>-1</sup>, and 2D' at ~3240 cm<sup>-1</sup>. Among them, D peak and G peak

have been most intensively studied to quantify disorder density in carbonaceous materials. The former is the  $A_{1g}$  breathing mode of  $sp^3$ -induced disorders in graphitic structure that break the symmetry and selection rules while the latter is the characteristic first-order phonon scattering  $E_{2g}$  mode related to in-plane stretching of ordered  $sp^2$ -hybridised carbon domains [288, 289].

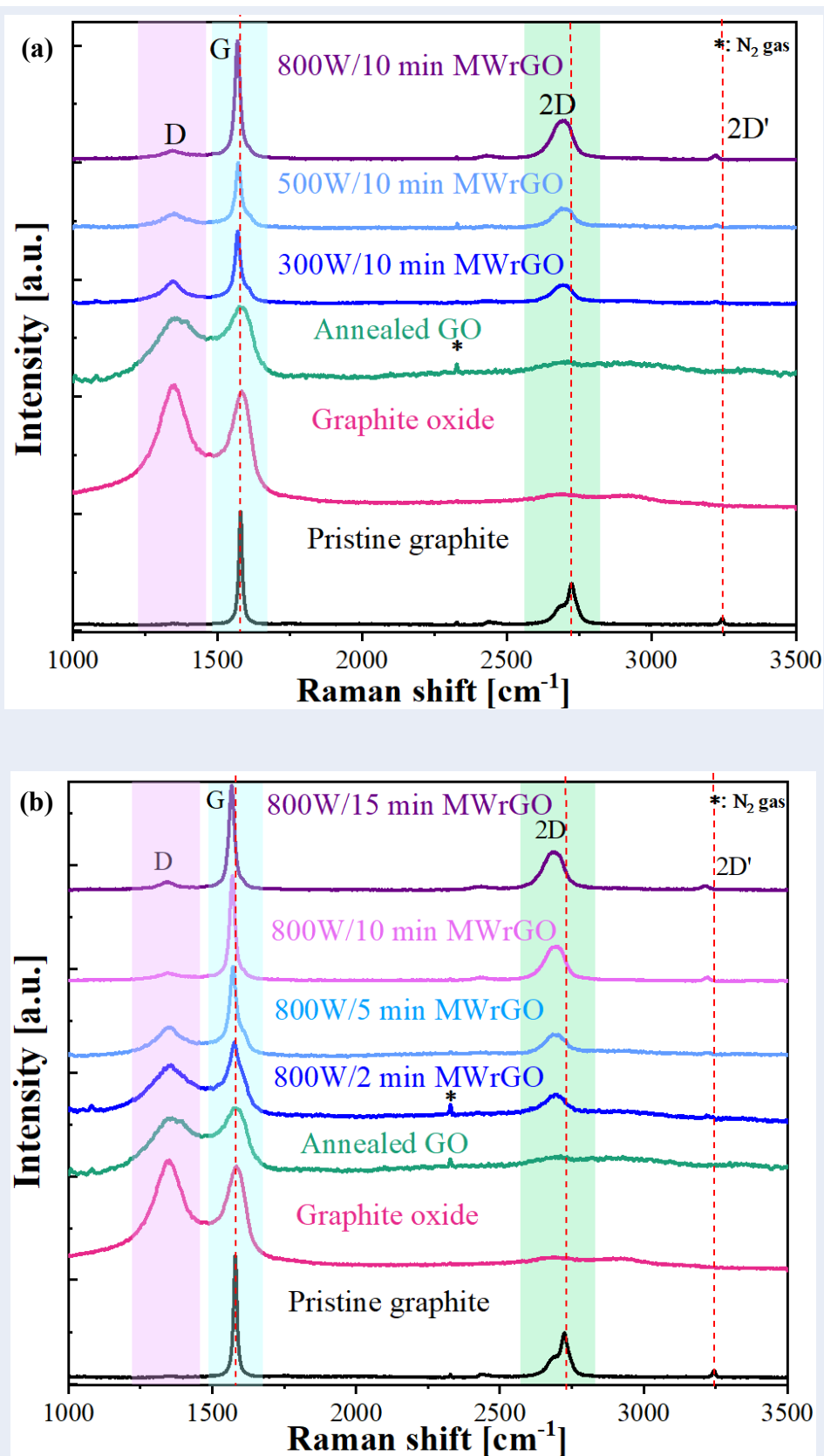


**Fig. 5-11.** Raman spectra of MWrGO synthesised (a) at various microwave powers after 10 min of constant argon flushing and (b) under various argon flushing times at the microwave power of 800 W in comparison with pristine graphite, graphite oxide, and annealed GO.

The intensity ratio between D peak and G peak, *i.e.*,  $I_D/I_G$ , in carbon derived materials has been commonly utilised as a measure of defect density presented in hexagonal networks of graphene and as a direct indicator for the extent of recovery of crystalline aromaticity. A reduced  $I_D/I_G$  ratio correlates to a graphitic structure with less disorder. However, this empirical measuring tool, *i.e.*,  $I_D/I_G$ , may give contradictory results on reduced GO (rGO) synthesised by various reduction methods, such as chemically/thermally rGO, because an increased  $I_D/I_G$  may be observed when the rGO is reduced from its GO precursors [159, 290-292]. As suggested by King *et al.*, the unreliability of the empirical  $I_D/I_G$  is attributed to the superposition of G peak and D' peak, the latter of which is generally present at the high-Raman-shift shoulder of G peak. D' peak may overlap with G peak position at *ca.* 1580  $\text{cm}^{-1}$ , depending on the defect concentrations on GO and rGO [291]. Due to the additional intensity contribution of D' peak to the observed apparent G peak (labelled as  $G_{\text{App}}$ ), the empirical  $I_D/I_G$  ratio is actually the intensity ratio between the D peak and  $G_{\text{App}}$  peak ( $I_D/I_{G-\text{App}}$ ).  $I_D/I_{G-\text{App}}$  may vary from sample to sample and thus gives inconsistent comparisons over graphene-based materials. Therefore, we proposed a modified measuring ratio ( $I_D/I_{G-\text{in}}$ ) to study the structural evolutions of MWrGO during microwave irradiation by subtracting the intensity contribution of D' peak from the intensity of  $G_{\text{App}}$  (*i.e.*, the intensity of intrinsic G peak,  $I_{G-\text{in}}$ , equals to  $I_{G-\text{App}} - I_{D'}$ ). As claimed in King's work, the 2D' peak is the overtone mode of D' peak and is distinctly far away from other Raman peaks. Therefore, the position of D' peak is able to be calculated by halving the energy of the 2D' peak [291]. Once the position of D' peak is determined, the intensity contribution of D' peak can be separated from the intensity of  $G_{\text{App}}$  peak by peak fitting of  $G_{\text{App}}$  peak which is a superposition of  $G_{\text{in}}$  peak and D' peak, as demonstrated in Fig. 5-12.

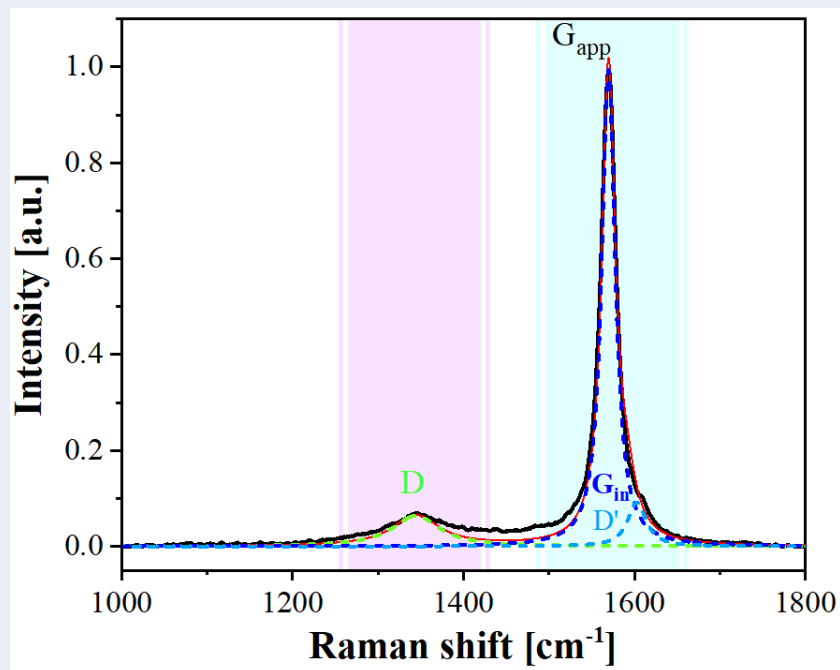


**Fig. 5-12.** A quintessential example of peak fitting of  $G_{\text{app}}$  peak in the Raman spectrum of 800W/10min MWrGO (The peak fitting analysis was carried out using PeakFit V4.12 software. The peak fitting was analysed using Voigt deconvolution function till Chi-square is not less than 0.98).

The  $I_D/I_{G-\text{in}}$  ratios of all the MWrGO in this work were calculated and listed in Table 5-1. It is observed that the  $I_D/I_{G-\text{in}}$  ratio increased from  $\sim 0$  to 1.258 in the pristine graphite and graphite oxide, respectively, which indicated that the acid treatment of pristine graphite incorporated a high concentration of defects in the graphitic structure and transformed  $sp^2$  graphitic domains into  $sp^3$  amorphous domains. After annealing treatment at 250 °C, the  $I_D/I_{G-\text{in}}$  ratio was significantly reduced to 0.906, representing the partial recovery of conjugated graphitic structure. After microwave irradiation at various powers with the argon flushing time of 10 min, the  $I_D/I_{G-\text{in}}$  ratio of MWrGO decreased from 0.392 at 300 W to 0.251 at 500 W and then to 0.062 at 800 W, as shown in Fig. 5-11 (a). To this end, it can be concluded that the effective removal of defects and oxygen functional groups can be accomplished at higher microwave power (800 W).

The argon flushing times also had a similarly profound effect on the structural evolutions

of MWrGO at the constant microwave power of 800 W. In Fig. 5-11 (b), the changes in  $I_D/I_{G-in}$  ratios of pristine graphite, graphite oxide and annealed GO were essentially the same as that in Fig. 5-11 (a). With the increase in argon flushing time as shown in Fig. 5-11 (b) and Table 5-1, the  $I_D/I_{G-in}$  ratio was reduced from 0.758 at 2 min argon flushing time to only 0.062 at 10 min argon flushing time, which is an exceptional reduction in an approximate magnitude order of 1. Even with further increasing of argon flushing time to 15 min, the  $I_D/I_{G-in}$  ratio showed a negligible variation, indicating that 10 min argon flushing was long enough to create a protective atmosphere to hinder freshly formed dangling bonds from being oxidised by oxygens.

Additionally, the spectral difference between D' peak and  $G_{App}$  peak has been proposed by King *et al.* to define the boundary between rGO and graphene, as given below [291].

$$\text{Graphene} = D' - G_{App} > 25 \text{ [Equation 17]}$$

As detailed in Table 5-1, the values of  $D' - G_{App}$  of all MWrGO are much higher than 25 and reach its height for the 800W/10min MWrGO and 800W/15min MWrGO samples, indicating the effective reduction of annealed GO triggered by microwave irradiation. The distance between defects ( $L_D^2$ ) is another indicator of the quality of MWrGO and they are also summarised in Table 5-1. Herein, the defects are specifically referred to the zero-dimensional point-like defects which are commonly induced by aggressive chemical oxidation reaction and are observed in  $sp^2$  carbon lattices [293, 294]. It is easy to understand that a larger value of  $L_D^2$  represents larger coverage of prefect graphitic structure and a largest value was observed for 800W/10min MWrGO. So far, the aforementioned Raman-based analysis revealed that the highest-quality MWrGO could be obtained with the microwave of 800 W and the argon flushing time of 10 min. The

most attractive 800W/10min MWrGO was then characterised using other techniques, together with pristine graphite, graphite oxide, and annealed GO.

**Table 5-1.** Calculated Raman spectral features of pristine graphite, graphite oxide, annealed GO, and MWrGO synthesised at different conditions (based on the data extracted from Fig. 5-11)

	$I_D/I_{G-in}$	2D' [cm <sup>-1</sup> ]	D' [cm <sup>-1</sup> ]	G <sub>App</sub> [cm <sup>-1</sup> ]	D'- G <sub>App</sub> [cm <sup>-1</sup> ]	$L_D^2$ [nm <sup>2</sup> ]*
<b>Pristine graphite</b>	~0	3244.49	1622.245	1580.19	42.055	N/A
<b>Graphite oxide</b>	1.258	N/A	N/A	1580.19	N/A	9.924
<b>Annealed GO</b>	0.906	N/A	N/A	1580.19	N/A	11.699
<b>300W/10min MWrGO</b>	0.392	3225.18	1612.59	1578.74	33.85	17.795
<b>500W/10min MWrGO</b>	0.251	3223.68	1611.84	1572.56	39.28	22.207
<b>800W/10min MWrGO</b>	0.062	3221.93	1610.965	1570.77	40.195	44.471
<b>800W/2min MWrGO</b>	0.758	3231.14	1615.57	1578.42	37.15	12.786
<b>800W/5min MWrGO</b>	0.387	3224.96	1612.48	1576.12	36.36	17.901
<b>800W/15min MWrGO</b>	0.077	3216.41	1608.205	1567.51	40.695	39.934

\*The distance between defects ( $L_D^2$ ) are calculated from the intensities of D peak and G peak, as given [293]

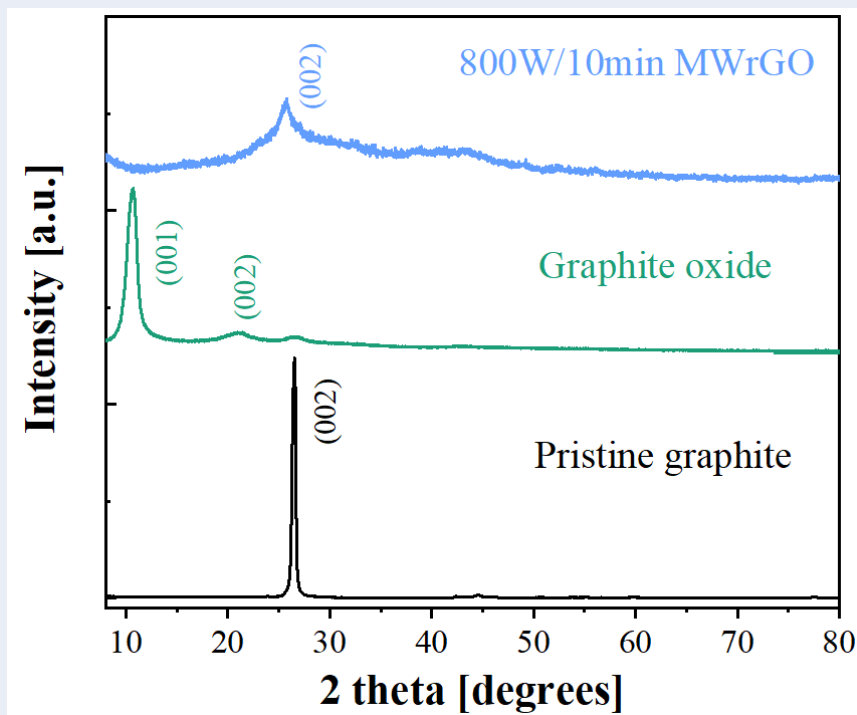
$$L_D^2 (\text{nm}^2) = (1.8 \pm 5) \times 10^{-9} \times \lambda^4 \times \left(\frac{I_D}{I_G}\right)^{-1} \quad [\text{Equation 18}]$$

In which  $\lambda$  is the wavelength of the Raman excitation laser (in nm).

$I_D$  and  $I_G$  represent the intensities of the D peak and G peak, respectively.

XRD is a complementary tool to Raman spectroscopy to interrogate the structural fine-detail of MWrGO in the perspective of interlayer spacing. As shown in Fig. 5-13, the ‘fingerprint’ peak of pristine graphite shifted from  $26^\circ$  (corresponding to 0.34 nm intersheet distance, JCPDS card 41-1487) to  $10.5^\circ$  (corresponding to 0.84 nm intersheet distance) after the strong oxidation process by  $\text{KMnO}_4$  and  $\text{H}_2\text{O}_2$ , implying the successful intercalation of oxygen functional groups between adjacent graphitic sheets [295-297]. The structural expansion along the *c* axis caused by the intercalation of oxygen functional groups has been theoretically confirmed using first-principle atomistic model in which the presence of functional epoxy groups and the underlying hybridised carbon atom induced additional height variations with respect to the carbon basal plane [146]. The prominent (001) peak of graphite oxide at  $10.5^\circ$  indicates a high oxidation extent of *ca.* 50 wt%, as ascertained in Morimoto’s study in which the (001) peak position was correlated to the oxidation extent of GO [298]. After being subjected to annealing treatment and microwave irradiation, the (001) peak of graphite oxide completely vanished and a broad (002) peak appeared at  $\sim 26^\circ$  for 800W/10min MWrGO, which was suggestive of the efficient removal of covalently bond oxygen functional groups by microwave irradiation. The broad (002) peak on 800W/10min MWrGO is attributed to the statistical distribution of re-aggregated graphene nanosheets with varying interlayer distances (in the range of 0.31 nm to 0.38 nm).

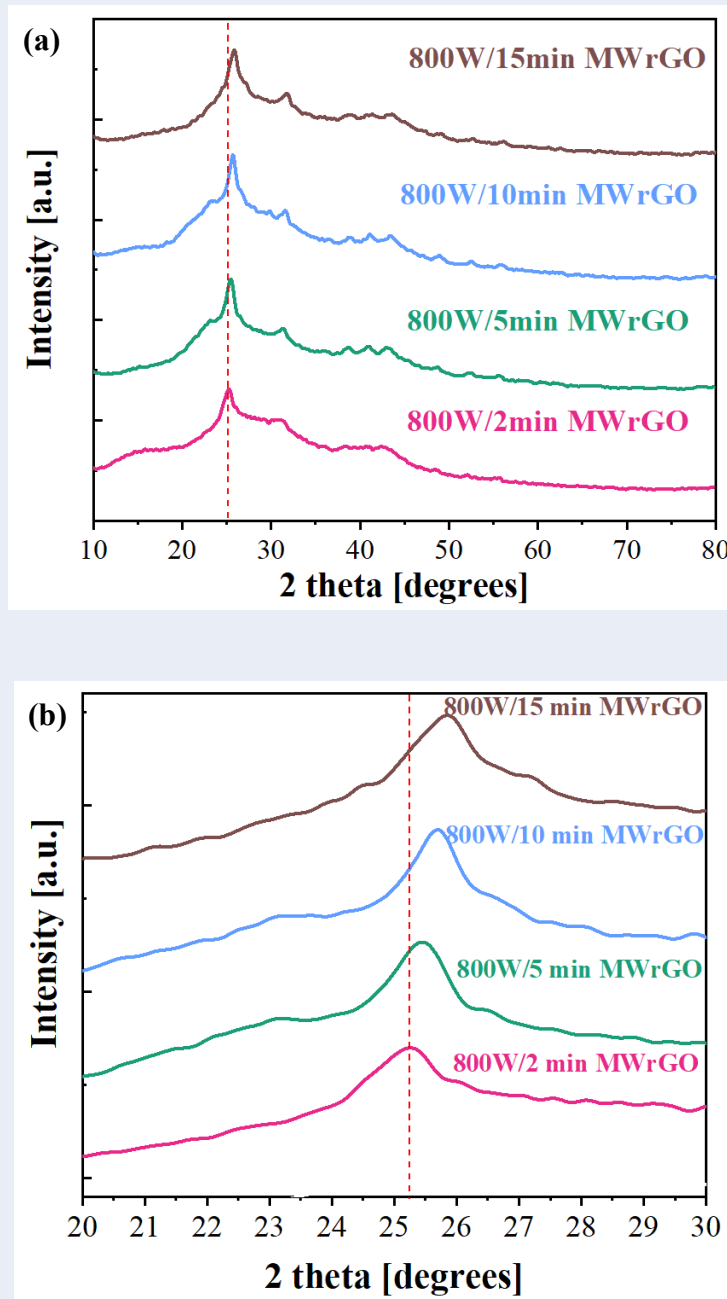




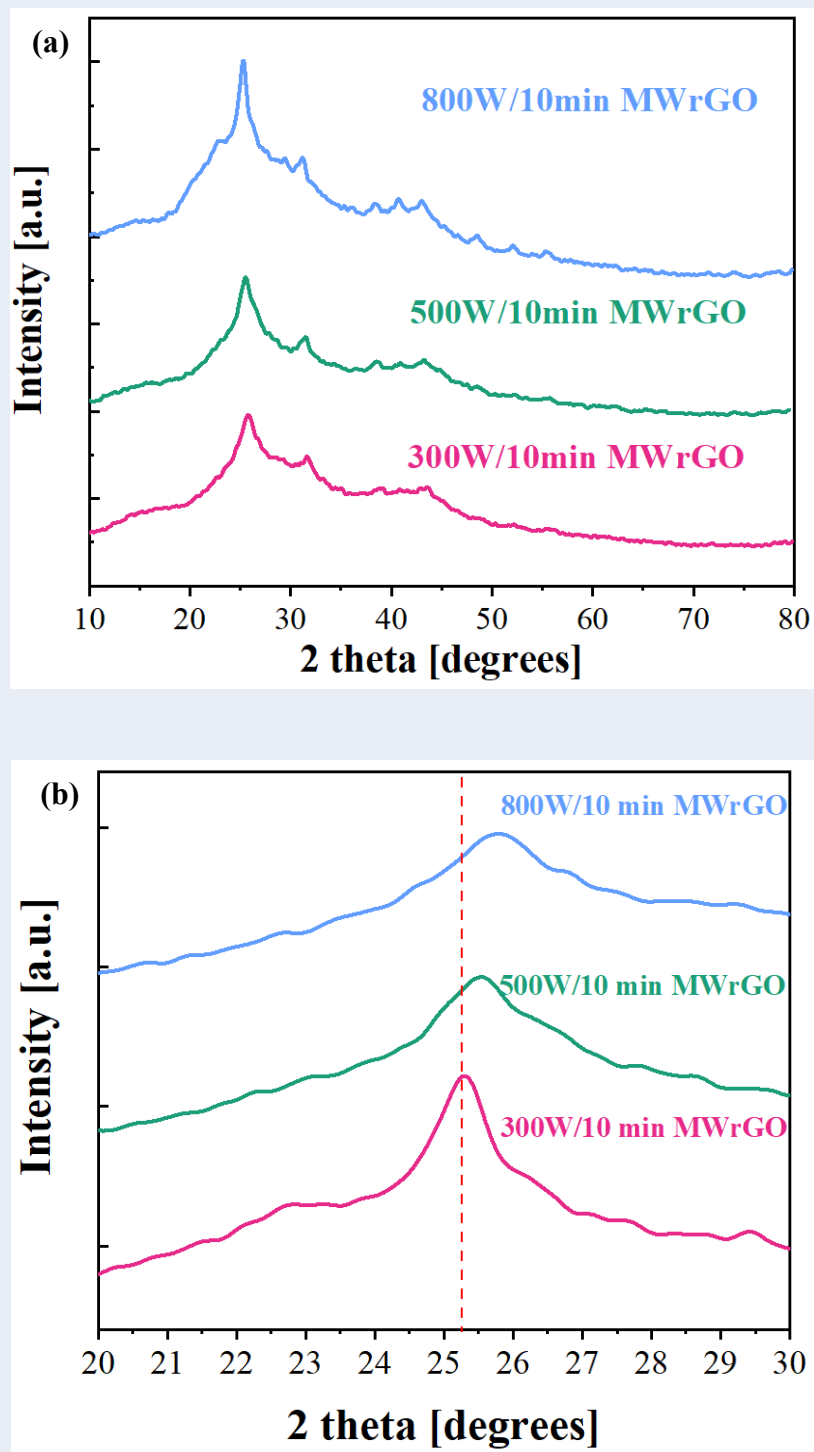
**Fig. 5-13.** XRD patterns of pristine graphite, graphite oxide, and 800W/10min MWrGO.

Fig. 5-14 (a) shows the evolution of XRD spectra of the MWrGO synthesised with the argon flushing times of 2 min, 5 min, 10 mins and 15 mins using the constant microwave power of 800 W. The (002) peaks of all the synthesised MWrGO were present at  $\sim 26^\circ$  but it is worth mentioning that the (002) peak for 800W/2min MWrGO at  $25.2^\circ$  slightly shifted to  $25.4^\circ$  for 800W/5min MWrGO, to  $25.7^\circ$  for 800W/10min MWrGO and to  $25.8^\circ$  for 800W/15min MWrGO, as shown in the enlarged XRD plot in the range of  $20^\circ - 30^\circ$  in Fig. 5-14 (b). The subtle increase in peak positions of all the synthesised MWrGO confirms the higher reduction extent of annealed GO by microwave irradiation because of the improve inert gas atmosphere. Similar results were also observed for MWrGO synthesised with the different microwave powers of 300 W, 500 W, and 800 W after 10 min of argon flushing, as shown in Fig. 5-15 (a). The (002) peak for 300W/10min MWrGO at  $25.3^\circ$  shifted to  $25.5^\circ$  for 500W/10min MWrGO and to  $25.8^\circ$  for 800W/10min MWrGO, as shown in Fig. 5-15 (b). Moreover, a prolonged microwave

irradiation time was needed for microwave arcing to happen at lower microwave power. Therefore, the XRD results of the synthesised MWrGO are in good agreement with the aforementioned Raman analysis, demonstrating 800 W of microwave power and 10 min of argon flushing is the optimal processing condition to synthesise MWrGO.



**Fig. 5-14. (a)** XRD patterns of MWrGO synthesised with various argon flushing times at the constant microwave power of 800 W and **(b)** The enlarged XRD plot of 20° - 30° showing the changes in position of (002) peak.



**Fig. 5-15.** (a) XRD patterns of MWrGO synthesised with various microwave powers after 10 min of constant argon flushing and (b) The enlarged XRD plot of 20° - 30° showing the changes in position of (002) peak.

The oxygenation and deoxygenation of oxygen functional groups during chemical oxidation and microwave reduction were examined using FTIR, as shown in Fig. 5-16.

The pristine graphite only exhibits four main bands: (i) A broad band centered at  $\sim 3435.74\text{ cm}^{-1}$  which can be assigned to the stretching vibration mode of O-H, *i.e.*  $\nu(\text{OH})$ , from the trapped moisture in graphite powder; (ii) Two distinct stretching vibration modes of C-H; symmetric band,  $\nu_s(\text{C-H})$ , at  $2920.85\text{ cm}^{-1}$  and asymmetric band,  $\nu_{as}(\text{C-H})$ , at  $2850.21\text{ cm}^{-1}$ ; and (iii) An in-plane vibration mode of C=C, *i.e.*  $\delta(\text{C=C})$  at  $1620.70\text{ cm}^{-1}$ , which originates from the C=C component of aromatic structures [189, 299-301].

After oxidised by  $\text{KMnO}_4$  and  $\text{H}_2\text{O}_2$ , numerous oxygen-derived bands were present in the infrared spectra: (i) a stretching vibration mode of C=O, *i.e.*  $\nu(\text{C=O})$  at  $1724.20\text{ cm}^{-1}$ , which was attributed to carbonyl and carboxyl groups on the basal planes of GO; (ii) a stretching vibration mode of C-O-C, *i.e.*  $\nu(\text{C-O-C})$  at  $1218.12\text{ cm}^{-1}$ , which represented the formation of epoxy functional groups within basal planes; (iii) a stretching vibration mode of C-OH, *i.e.*  $\nu(\text{C-OH})$  at  $1383.56\text{ cm}^{-1}$ , which is related to hydroxyl groups, and (iv) a  $\nu(\text{C-O})$  stretching vibration mode in the low IR wavenumber region ranging from  $1044\text{ cm}^{-1}$  to  $1100\text{ cm}^{-1}$  [300, 302]. For easy interpretation, the assignments of each FTIR peak are shown in Table 5-2. After annealing treatment, it is unambiguously observed that peak intensities related to the oxygen functional groups other than the thermally stable C-O groups were significantly reduced, which confirmed the restoration of conjugated network and the aforementioned thermally annealing mechanism on GO. Notably, all the oxygen-rich groups, particularly C-O groups, were virtually removed after microwave reduction, indicating the feasibility of microwave-assisted reduction of annealed GO. Moreover, the increases in peak intensities of symmetric and asymmetric C-H bands further proved the well-exfoliation of GO since they only appear at the edges of graphene nanosheets [300].

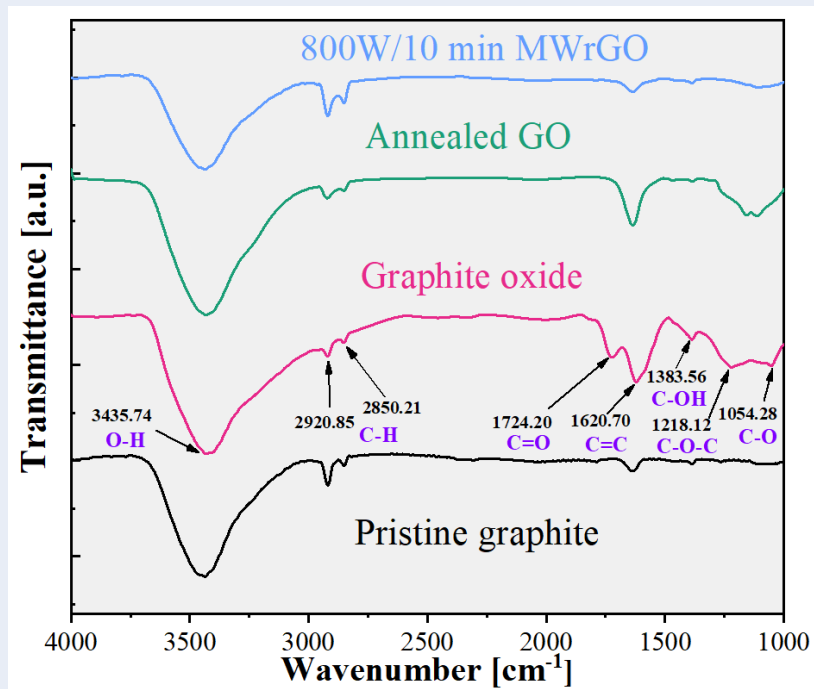


**Fig. 5-16.** FTIR spectra of pristine graphite, graphite oxide, annealed GO, and 800W/10min MWrGO.

**Table 5-2.** The assignment of FTIR peaks for pristine graphite, graphite oxide, annealed GO, and 800W/10min MWrGO.

Wavenumber [cm <sup>-1</sup> ]	Vibration mode	Assignment
~3435.74	Stretching vibration of O-H	$\nu$ (OH) from moisture
2920.85	Symmetric stretching vibration of C-H	$\nu_s$ (C-H) from CH <sub>2</sub> group
2850.21	Asymmetric stretching vibration of C-H	$\nu_{as}$ (C-H) from CH <sub>2</sub> group
1724.20	Stretching vibration of C=O	Carbonyl and carboxyl functional groups
1620.70	In-plane vibration of C=C	$\delta$ (C=C) component of aromatic structure
1383.56	Stretching vibration of C-OH	Hydroxyl functional groups
1218.12	Stretching vibration of C-O-C	Epoxy functional groups
1044 ~ 1100	Stretching vibration of C-O	Carboxyl functional groups

TGA measurement illuminates and provides an insight into the thermal stabilities of all the oxygen-containing functional groups formed on the GO. It was recognised that the graphite oxide was thermally unstable and three-stage weight loss was observed against increasing temperature, as shown in Fig. 5-17 (a). The initial weight loss was *ca.* 10 wt% up to 100 °C, which was ascribed to the evaporation of the interlamellar water [303]. The second-stage weight loss was consisted of one sharp slope (100 °C to 200 °C) and one slow slope (200 °C to 600 °C), and the weight loss reached at 50 wt% at 600 °C, which was indicative of *ca.* 50 wt% oxidation degree of pristine graphite. The result was in a good agreement with the previous XRD analysis in which the (001) peak of graphite oxide at 10.5° was closely related to the high oxidation degree of *ca.* 50 wt%. The sharp slope was attributed to the decomposition of the labile oxygen-containing functional groups, such as hydroxyl groups and carboxyl groups. It led to the vigorous release of CO, CO<sub>2</sub>, vapour, and trace acetone as well as the violent thermal expansion/exfoliation of as-prepared GO basal planes [159, 189, 303]. The slow slope was principally due to the decomposition of double bond-containing functional groups, *i.e.*, carbonyl and epoxy functional groups, as a result of strong dipole moment between oxygen and carbon atoms [189, 304]. The third stage weight loss happening above 600 °C resulted in a char residue of *ca.* 30 wt% and was related to the pyrolysis of carbon skeleton [303]. The three-stage weight loss were distinctly represented by three main peaks in the DTG plot of graphite oxide as shown in Fig. 5-17 (b).

After annealing treatment, annealed GO only experienced first-stage decomposition (moisture removal), partial second-stage decomposition (decomposition of carbonyl and carboxyl groups), and third-stage decomposition (pyrolysis of carbon skeleton) upon heating to 800 °C. It clearly indicated that the decomposition of labile hydroxyl and epoxy

groups was completed after being subjected to annealing at 250 °C, which is evidenced by the absence of the peak at about 190 °C in Fig. 5-17 (b). The TGA result of 800W/10min MWrGO showed an excellent thermal stability up to 750 °C with a small weight loss of only 10 wt%, indicating the effective elimination of various functional groups on GO structure by microwave irradiation. Pyrolysis of carbon skeleton of 800W/10min MWrGO started at the identical decomposition temperature (~600 °C) as the graphite oxide and the annealed GO. It led to a similar char residue of 30 wt% at 800 °C. The DTG of 800W/10min MWrGO merely featured a prominent peak above 600 °C related to the pyrolysis of carbon skeleton. The disappearance of moisture-induced peak showed the hydrophobic nature of 800W/10min MWrGO because most of the hydrophilic functional groups were removed by microwave irradiation. In addition, the DTG result of 800W/10min MWrGO revealed that 800W/10min MWrGO was thermally stable up to 750 °C, which is higher than the graphene sheets produced by conventional thermal reduction (507 °C), argon arc discharge (525 °C), and hydrogen arc discharge (601 °C) [148]. The higher thermal stability of 800W/10min MWrGO can be ascribed to the self-healing effect of defects by microwave irradiation and the low content of vacancies and topological defects on the basal plane, which can avoid the premature break-down of carbon skeleton [148].

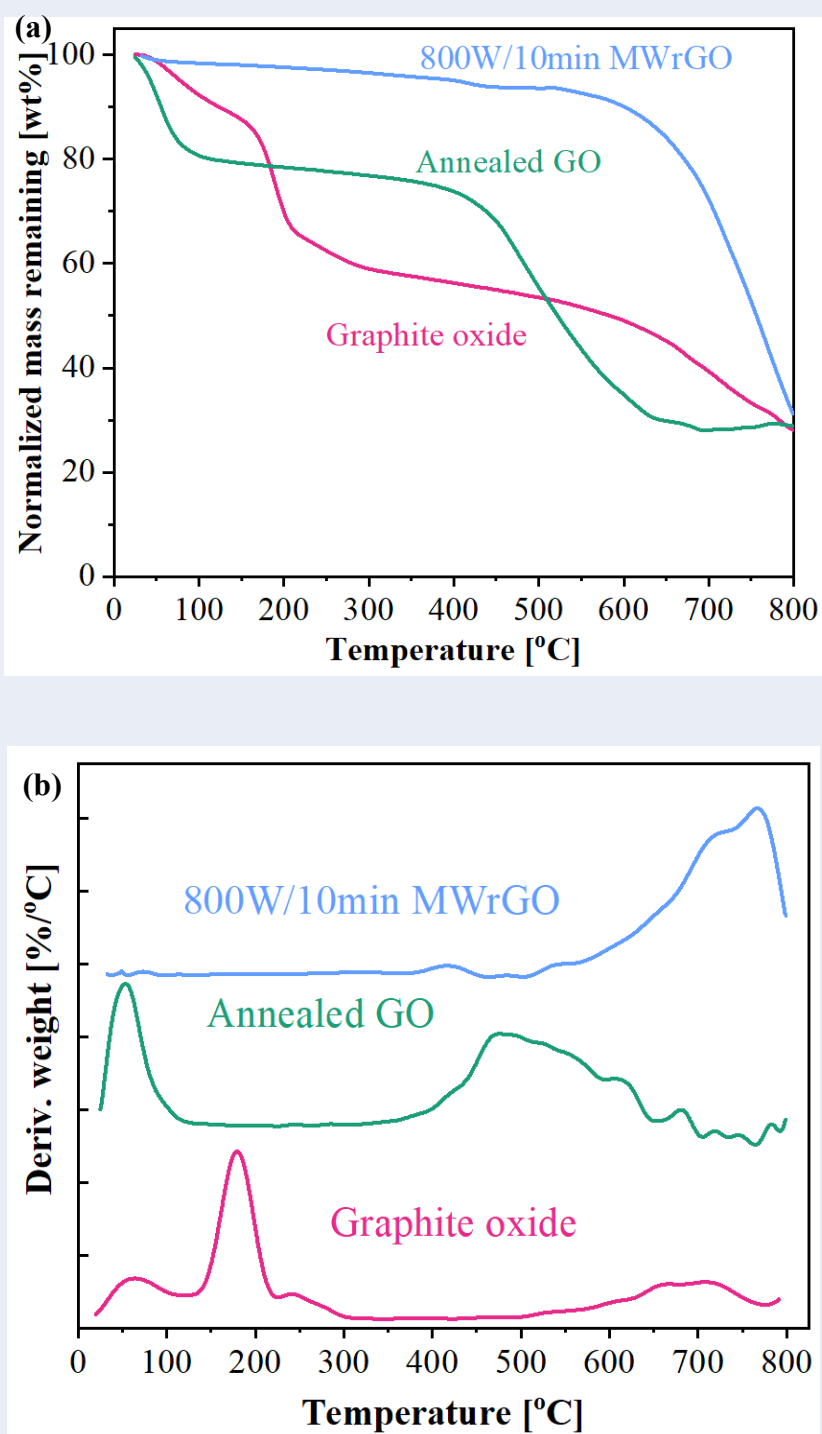


**Fig. 5-17.** (a) Normalised TGA plots and (b) DTG plots for graphite oxide, annealed GO, and 800W/10min MWrGO over the temperature range from 25 °C to 800 °C at the heating rate of 5 °C min<sup>-1</sup>.

The amounts of oxygen functional groups on the pristine graphite, graphite oxide, annealed GO and 800W/10min MWrGO were quantitatively determined using XPS and are summarised in Table 5-3, along with the C/O molar ratios. The detailed evolution of



C1s spectra are shown in Fig. 5-18. The XPS C1s spectra featured the following bands: non-oxygenated ring C-C at 284.48 eV, C-O at 285.98 eV, C=O at 287.48 eV, O-C=O at 288.98 eV, as well as  $\pi$ - $\pi^*$  shake-up satellite peak at 291.28 eV. The intensities in peaks of the oxygen-containing functional groups (C=O, O-C=O and C-O) on the graphite oxide became significant after modified Hummer's process and were then effectively reduced after the annealing process and the microwave irradiation. The re-appearance of  $\pi$ - $\pi^*$  shake-up satellite peak (that is characteristic of aromatic systems [146]) and the increase in the C-C band intensity for the annealed GO and the 800W/10min MWrGO samples experimentally confirmed: (i) the effective reduction of the oxygenated graphene layers during annealing treatment at 250 °C; and (ii) the self-healing of damaged conjugated network upon microwave irradiation in inert gas atmosphere [305, 306]. The intensity ratio of C peak and O peak, *i.e.*, C/O, is a supportive evidence of the effectiveness of the microwave-assisted irradiation in the removal of oxygen functional groups from GO. The increase of C/O specifically indicates a large extent of reduction of GO. The C/O ratios were 2.05, 5.04 and 14.29 for graphite oxide, annealed GO and 800W/10min MWrGO, respectively. The highest C/O ratio (14.29) of 800W/10min MWrGO is in good agreement with the above FTIR analysis and is comparable to the reported values of rGO which was also reduced from GO using microwave irradiation [178, 185, 187].

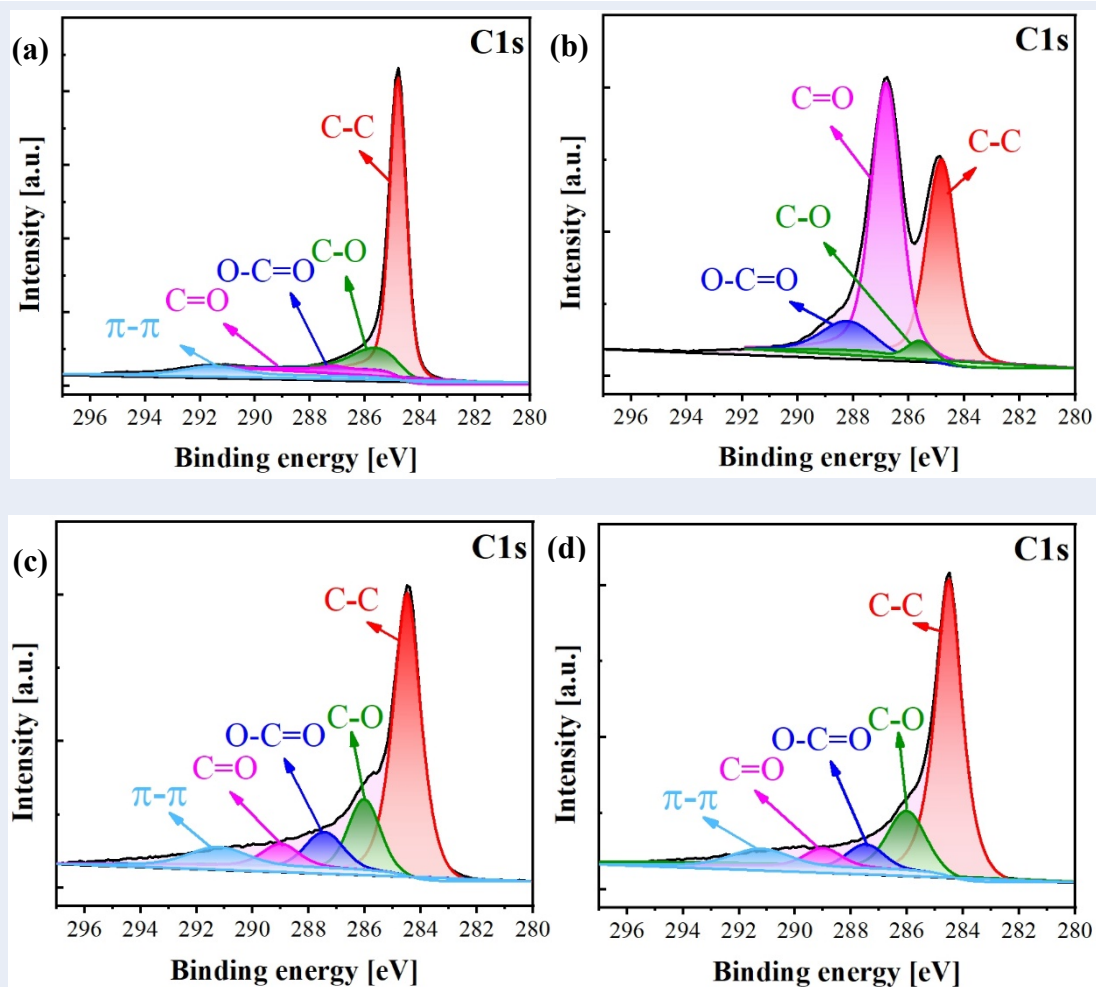


**Fig. 5-18.** The dynamic evolution of high-resolution XPS C1s photoemission spectra of (a) pristine graphite, (b) graphite oxide, (c) annealed GO, and (d) 800W/10min MWrGO.

**Table 5-3.** Quantative analysis of oxygen functional groups on pristine graphite, graphite oxide, annealed GO and 800W/10min MWrGO.

	Pristine graphite	Graphite oxide	Annealed GO	800W/10min MWrGO
C/O	75.9	2.05	5.04	14.29
C1s C-C [at%]	76.29	24.59	50.56	61.39
C1s C-O [at%]	13.68	2.31	13.65	13.52
C1s C=O [at%]	1.38	33.13	8.07	6.01
C1s O-C=O [at%]	0.52	6.42	5.21	5.03
C1s $\pi$ - $\pi^*$ [at%]	7.22	-	6.49	6.97
O1s [at%]	0.91	33.55	16.02	7.08

Table 5-4 shows the evolution of XPS C1s spectra of the MWrGO synthesised with the argon flushing times of 2 min, 5 min, 10 mins and 15 mins using the constant microwave power of 800 W. The peak intensities of the oxygen functional groups on the synthesised MWrGO decreased with the increasing argon flushing time. Furthermore, the C/O ratio increased with the increasing argon flushing time. It is clearly confirmed that prolonged Argon flushing time is beneficial to hindering freshly formed MWrGO from being oxidised. Similar results were also observed for MWrGO synthesised with the different microwave powers of 300 W, 500 W and 800 W after 10 min of constant argon flushing, as shown in Table 5-5. With the microwave powers increasing, the intensities of the oxygen functional groups on the synthesised MWrGO decreased and the C/O ratio increased. Combined with the aforementioned Raman and XRD analysis, the XPS results confirmed that MWrGO with higher extent of reduction can be obtained at the selected microwave power of 800 W and the argon flushing time of 10 min.

**Table 5-4.** The evolution of XPS C1s spectra of MWrGO synthesised with various argon flushing times at the microwave power of 800 W.

	800W/2min MWrGO	800W/5min MWrGO	800W/10min MWrGO	800W/15min MWrGO
<b>C/O</b>	6.03	7.96	14.29	13.08
<b>C1s C-C [at%]</b>	51.02	54.79	61.39	61.53
<b>C1s C-O [at%]</b>	16.00	15.48	13.52	13.81
<b>C1s C=O [at%]</b>	7.08	6.81	6.01	5.82
<b>C1s O-C=O [at%]</b>	5.11	5.08	5.03	4.93
<b>C1s <math>\pi</math>-<math>\pi^*</math> [at%]</b>	6.33	6.75	6.97	7.11
<b>O1s [at%]</b>	14.46	11.09	7.08	6.80

**Table 5-5.** The evolution of XPS C1s spectra of MWrGO synthesised with various microwave powers with the argon flushing time of 10 min.

	300W/10min MWrGO	500W/10min MWrGO	800W/10min MWrGO
<b>C/O</b>	4.47	11.48	14.29
<b>C1s C-C [at%]</b>	52.50	57.95	61.39
<b>C1s C-O [at%]</b>	11.90	14.98	13.52
<b>C1s C=O [at%]</b>	5.00	7.67	6.01
<b>C1s O-C=O [at%]</b>	3.73	4.95	5.03
<b>C1s <math>\pi</math>-<math>\pi^*</math> [at%]</b>	8.42	7.03	6.97
<b>O1s [at%]</b>	18.45	7.42	7.08

The high electrical conductivity of graphene generally arises from the perfection of carbon hexagonal structures. In this sense, it can be envisaged as an indicator of the extent of reduction by microwave irradiation. GO is electrically insulated because the extended  $\pi$ - $\pi^*$  electronic conjugated network of pristine graphite was damaged by the presence of oxygen containing hydroxide, epoxide, carbonyl, and carboxyl functional groups by the treatment of strong oxidants. Henceforth, the decrease in  $sp^3$  carbon backbones is beneficial for improving the electrical conductivity. The electrical conductivity ( $\sigma$ ) is determined from sheet resistance ( $R_s$ ) using the below equations:

$$R_s = \frac{\pi}{\ln 2} \frac{\Delta V}{I} = 4.5324 \frac{\Delta V}{I} \quad [\text{Equation 19}]$$

$$\rho = R_s d = 4.5324 d \frac{\Delta V}{I} \quad [\text{Equation 20}]$$

$$\sigma = \frac{1}{\rho} \quad [\text{Equation 21}]$$

Where,  $\Delta V$  is the voltage drop between the inner two probes (Unit: V),  $I$  is the applied current between the outer two probes (Unit: Amperes),  $d$  is the sample thickness,  $\rho$  represents the bulk resistance. As shown in Fig. 5-19, the electrical conductivity of the as-prepared GO ( $1.83 \times 10^{-2} \text{ S m}^{-1}$ ) was much inferior than that of the pristine graphite ( $851.2 \text{ S m}^{-1}$ ), implying that the pathways of  $\pi$  electrons were blocked by oxygen functional groups on as-prepared GO. After annealing treatment and microwave-assisted reduction, the electrical conductivities of annealed GO and 800W/10min MWrGO yielded values of  $268.9 \text{ S m}^{-1}$  and  $761.4 \text{ S m}^{-1}$ , respectively, which compare favourably with the literature values [136, 144, 185, 187]. There is direct relation between electrical conductivity and C/O ratios of all the samples as shown in Fig. 5-20, indicating the removal of oxygen functional groups can enhance the transportation of the  $\pi$  electrons on graphene nanosheets. The electrical conductivity of 800W/10min MWrGO ( $761.4 \text{ S m}^{-1}$ ) was much higher than the reported values of rGO synthesised by chemical reduction method, as shown in Table 5-6.

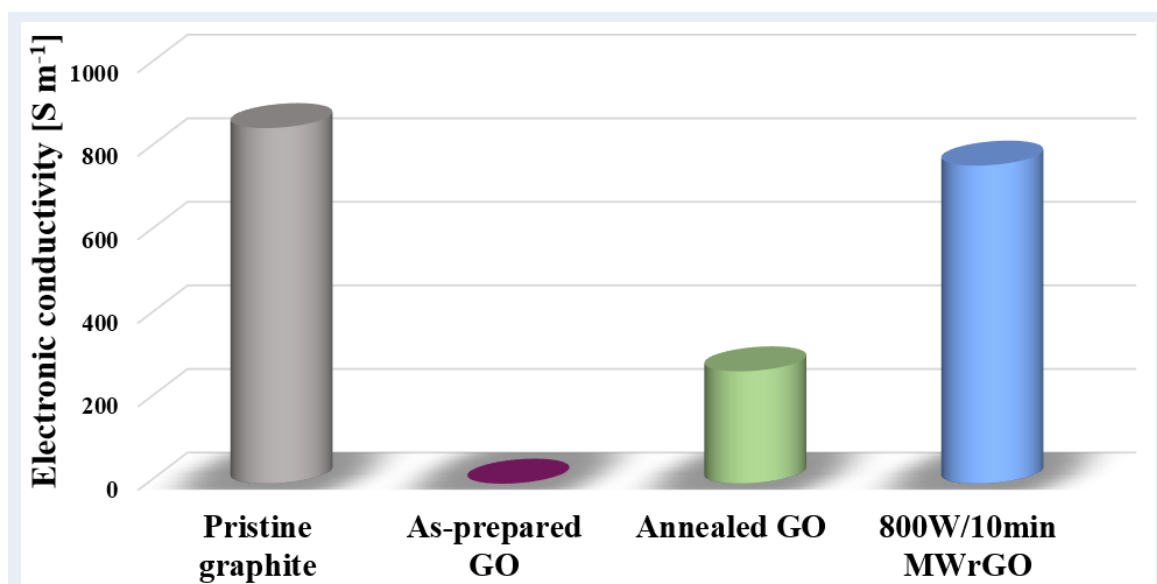


**Fig. 5-19.** The bar chart of the electrical conductivities of pristine graphite, as-prepared GO, annealed GO, and 800W/10min MWrGO measured by four-probe method.

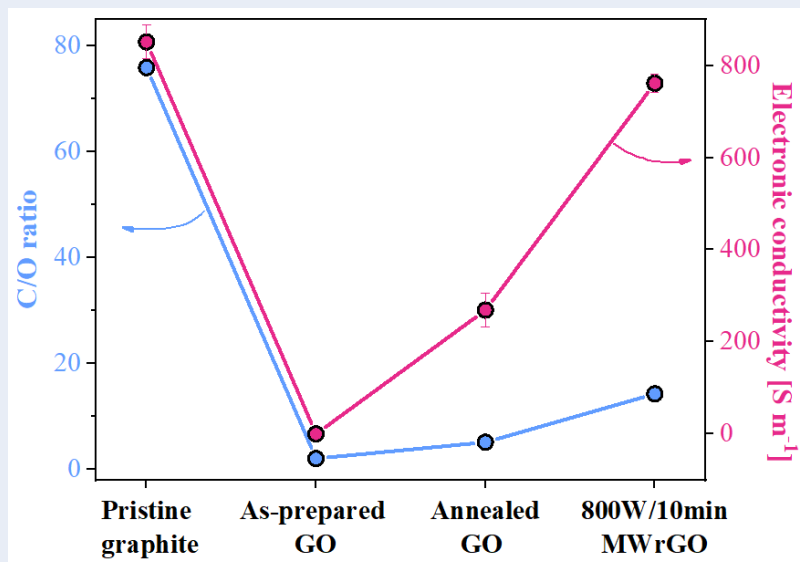


**Fig. 5-20.** The plot of C/O ratios and electrical conductivities of pristine graphite, as-prepared GO, annealed GO and 800W/10min MWrGO, showing the strong relationship among them.

**Table 5-6.** Summary of electrical conductivities of rGO reduced by various chemical agents.

Preparation method	Electrical conductivity [ $\text{S m}^{-1}$ ]	References
rGO by hydrazine	$2.0 \times 10^2$	[307]
rGO by 15 mM $\text{NaBH}_4$	$1.5 \times 10^{-4}$	[162]
rGO by 50 mM $\text{NaBH}_4$	$1.7 \times 10^1$	
rGO by 150 mM $\text{NaBH}_4$	$4.5 \times 10^1$	
rGO by hydrazine	$2.0 \times 10^2$	[308]
rGO by $\text{NaPO}_2\text{H}_2$	$3.8 \times 10^2$	[309]
rGO by hydrazine	$2.0 \times 10^2$	[159]
rGO by urea	$4.3 \times 10^1$	[310]
rGO by urea hydrolysable tannin	$4.2 \times 10^2$	[311]
rGO by $\text{N}_2\text{H}_4$	$1.5 \times 10^2$	[312]
rGO by <i>L</i> -ascorbic acid	$8.0 \times 10^2$	[313]
rGO by hydrazine	$1.0 \times 10^2$	[143]
rGO by microwave-assisted reduction in this project	$7.6 \times 10^2$	This work

The significant microstructure evolutions of as-prepared GO, annealed GO and 800W/10min MWrGO was also analysed using nitrogen adsorption-desorption isotherms, as given in Fig. 5-21 (a). In strong contrast with annealed GO and 800W/10min MWrGO, as-prepared GO possessed an extremely low  $S_{\text{BET}}$  of  $\sim 33.55 \text{ m}^2 \text{ g}^{-1}$  which indicated a tightly packed microstructure as shown in Fig. 5-6 (a). The annealed GO and 800W/10min MWrGO possessed an increased  $S_{\text{BET}}$  values of  $\sim 219.85$  and  $\sim 310.24 \text{ m}^2 \text{ g}^{-1}$ , respectively. They exhibited typical type IV isotherm curves with a rapid nitrogen adsorption at a high relative pressure region of 0.85 - 0.99, which are characteristic evidences of the presence of mesopore geometry after the annealing treatment and microwave irradiation. Fig. 5-21 (b) also displays the pore size distributions calculated on the basis of the desorption data branch of adsorption-desorption isotherm. A narrow pore size range centering at 3.52 nm and 3.69 nm for annealed GO and 800W/10min MWrGO, respectively, was found, which demonstrated the uniformity of mesopore sizes. According to the International Union of Pure and Applied Chemistry (IUPAC) classification, pores with size less than 2 nm are named micropores; pores with size between 2 nm and 50 nm are named mesopores and pores with size exceeding 50 nm are named macropores [314]. The formation of the uniform mesopores in 800W/10min MWrGO is considered as a result of the benefit of microwave absorption process. All the evolutions of the BET results are in good agreement with the pressure-induced exfoliation analysis during annealing treatment as clarified in Section 5.2. The increase in  $S_{\text{BET}}$  of 800W/10min MWrGO ( $310.24 \text{ m}^2 \text{ g}^{-1}$ ) implied that the removed oxygen functional groups endowed more accessible nitrogen adsorption/desorption sites. However, the obtained  $S_{\text{BET}}$  of 800W/10min MWrGO ( $310.24 \text{ m}^2 \text{ g}^{-1}$ ) is much lower than the theoretical surface area of graphene ( $\sim 2630 \text{ m}^2 \text{ g}^{-1}$ ) because the theoretical surface area of graphene would only be observed in an ideal case where no agglomeration, stacking and oxygen

functional groups exist on single graphene flake. This is not practically possible to achieve, especially for dry-state graphene powder in this project.

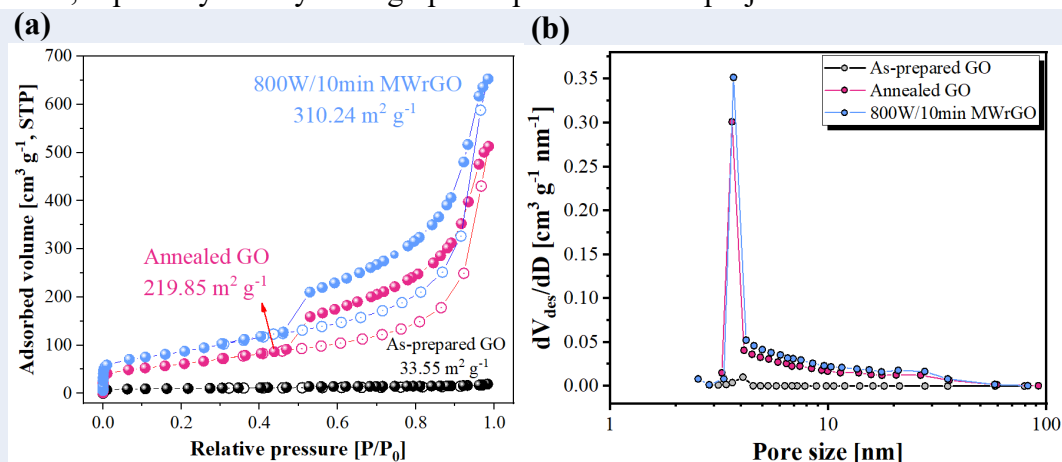


**Fig. 5-21.** Nitrogen adsorption/desorption hysteresis loops of as-prepared GO, annealed GO and 800W/10min MWrGO, revealing (a) the specific surface area and (b) the pore size distribution based on Branauer-Emmett-Teller method (BET) and Barrer-Joyner-Halenda (BJH) methods, respectively.

The morphological feature and microstructure of 800W/10min MWrGO flakes were characterised using HR-TEM, as depicted in Fig. 5-22 (a) and (b) at low magnification and high magnification, respectively. Microscopic overview on 800W/10min MWrGO flakes in Fig. 5-22 (a) revealed that the microwave-synthesised graphene sheet featured distinctively transparent and wrinkled surface with some stacking regions at the edges. Furthermore, the close microscopic examination in Fig. 5-22 (b) shows a flat graphene edge with a well-resolved lattice fringes, suggesting the thorough exfoliation of annealed GO sheets by annealing-induced gas expansion. It has been reported that the occurrence of wrinkled structures was ascribed to the weak lattice distortions developed on the graphene structure [146]. The inset shows sharp selected area electron diffraction (SAED) pattern with two sets of symmetric hexagonal patterns obtained from the edge-on region, further indicating the well-crystallised carbon hexagonal structure. More importantly, the higher intensity of the first-order spots over the second-order spots is an indicator of the presence of single layer free-standing graphene in this region.



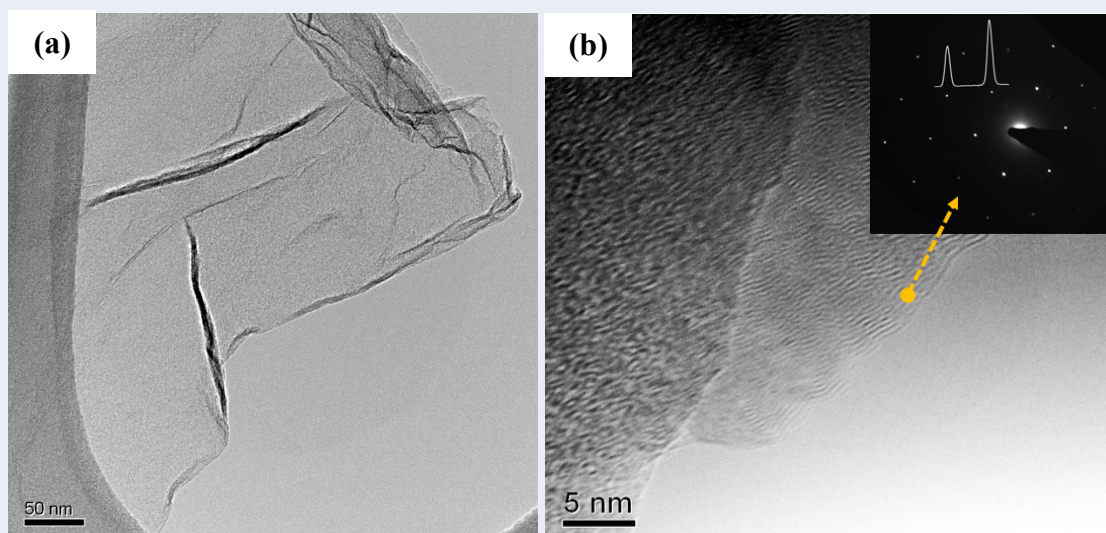


**Fig. 5-22.** Typical aberration-corrected HR-TEM micrographs of 800W/10min MWrGO prepared by solid-state microwave irradiation method at **(a)** low magnification and **(b)** high magnification, and the electron diffraction pattern of 800W/10min MWrGO is given in the inset, along with the diffraction intensity profiles of  $(11\bar{2}0)$  and  $(1\bar{1}00)$ .

## 5.4. The application of MWrGO in lithium-ion batteries

As discussed above, the high  $S_{\text{BET}}$  ( $310.24 \text{ m}^2 \text{ g}^{-1}$ ) and the high electrical conductivity ( $761.4 \text{ S m}^{-1}$ ) attained in this project enable 800W/10min MWrGO to be a promising electroactive material in anode and a conductive additive in cathode for LIBs by virtue to (i) the sufficient uptake sites for Li ions on the robust graphitic structure; (ii) the formation of elastic and highly conductive 3-dimensional interconnected framework; (iii) the provision of abundant contacting points between electroactive materials and graphene; as well as (iv) the enhanced lithium ion mobility through large-size pores. Therefore, the selected 800W/10min MWrGO was investigated as electroactive materials in the low voltage range of 0.01 - 2.5 V (*vs*  $\text{Li}^+/\text{Li}$ ), as discussed in Section 5.4.1, and investigated as conductive filler in the voltage window of 3.0 - 4.2 V (*vs*  $\text{Li}^+/\text{Li}$ ), as discussed in Section 5.4.2. A reference sample processed with multi-walled carbon nanotube (CNTs) was also elaborated to compare with MWrGO.

#### 5.4.1. 800W/10min MWrGO in anode for LIBs

The MWrGO anode was typically prepared by casting the slurry of 60 wt% 800W/10min MWrGO and 40 wt% PVdF on copper foil. The amount of binding agent, *i.e.* PVdF, used to bind the 800W/10min MWrGO to copper current collector in this project was much higher than those values reported in relevant literature [315-317] due to the large surface area of 800W/10min MWrGO. Based on the experimental experience, it was found that lower PVdF usage could result in serious detachment of 800W/10min MWrGO coating from the copper current collector during the subsequent drying process, whereas higher PVdF usage reduced the loading of electroactive material and thus deteriorated the electrical conductivity.

Fig. 5-23 illustrates the galvanostatic charge/discharge profiles of 800W/10min MWrGO half cell for 1<sup>st</sup>, 5<sup>th</sup>, 20<sup>th</sup>, 50<sup>th</sup> and 100<sup>th</sup> at the current density of 0.2 A g<sup>-1</sup> between 0.01 V and 2.5 V. It is recognised that the structure of the galvanostatic curves maintained its integrity throughout cycling, and the slopes and voltage plateaus were highly repeatable. 800W/10min MWrGO exhibited a discharge capacity of 1523.9 mAh g<sup>-1</sup> and a charge capacity of 755.1 mAh g<sup>-1</sup> in the initial galvanostatic cycle, yielding low coulombic efficiency of 49.55%. The large discharge capacity in the initial cycle was chiefly contributed by two processes: (i) the reversible intercalation process of lithium ions in the subsurface layers of the multi-layered graphene; and (ii) the irreversible side reactions leading to the formation of a passivating solid electrolyte interphase (SEI) on the graphene flakes which trapped Li<sup>+</sup> ions [315]. This SEI formation can be related to the plateaus located in the voltage range of 0.6 – 0.7 V in the initial discharge profile, but it completely disappeared in the successive cycles, implying that the irreversible side reaction merely occurred in the initial cycle. Moreover, it is claimed that larger surface

area of graphene flake resulted in larger irreversible capacity loss [315].

A close observation of the successive voltage profiles shows that the Li-storage in nanostructured carbons in the voltage window of 0.01 - 2.5 V can be considered as two main contributors with one locating at below 0.5 V (*vs* Li<sup>+</sup>/Li) and the other above 0.5 V (*vs* Li<sup>+</sup>/Li). The former is simply due to the electrochemical lithiation/delithiation process whilst the latter is related to Faradic capacitance between electrolyte species and sp<sup>3</sup> carbon sites, such as the surfaces or edge sites, on the graphene flakes [137, 318]. Notably, the low working potential of 800W/10min MWrGO resembles that of graphite anode which is widely implemented in commercial LIBs, indicating that 800W/10min MWrGO can be the main contender to replace graphite as the electroactive material of choice.

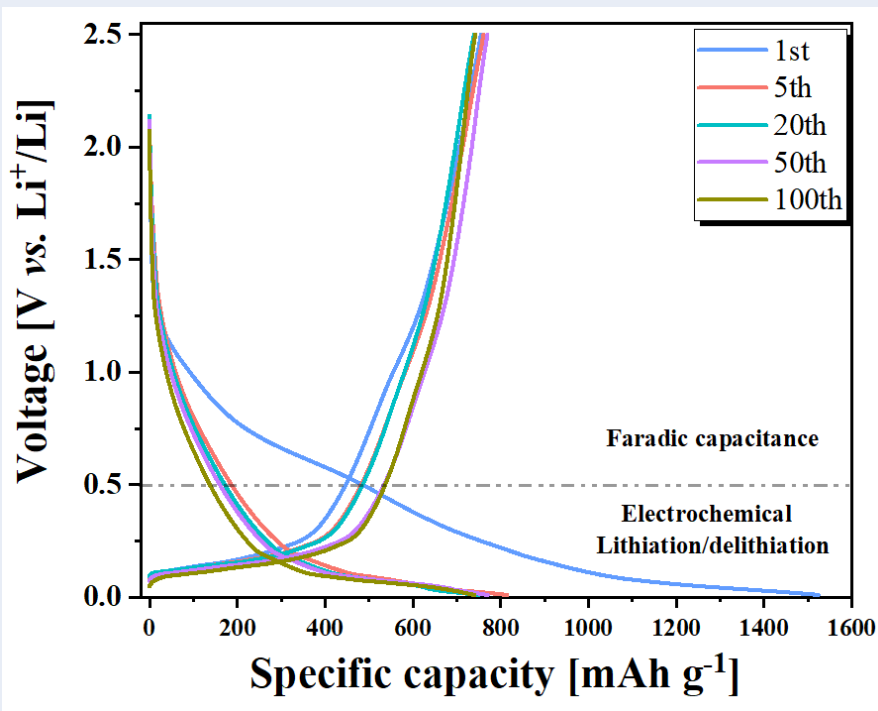


**Fig. 5-23.** The galvanostatic charge/discharge curves of MWrGO anode for 1<sup>st</sup>, 5<sup>th</sup>, 20<sup>th</sup>, 50<sup>th</sup> and 100<sup>th</sup> at the current density of 0.2 A g<sup>-1</sup>. The regions of the electrochemical cycling data that are attributed for the electrochemical lithiation/delithiation and Faradic capacitance are separated by a dash line.

The Li-ion storage behaviour of MWrGO-800W was further studied using CV technique between 0.01–2.5 V, as interpreted in Fig. 5-24. In the first cathodic scan, a signature reduction peak was observed at 0.66 V, which was attributed to the formation of SEI layer. However, this reduction peak disappeared in the subsequent cathodic scans, which was indicative of the high SEI stability. In the initial five scans, MWrGO-800W electrode featured a reduction peak at 0.02 V and an oxidation peak at 0.19 V, which exhibited an excellent consistency in shape/intensity and were assigned to the intercalation/deintercalation of Li ions in a manner reflecting  $\text{Li}_x\text{C}_6$  bulk storage. Overall, the CV curves exhibited high reproducibility and consistency, indicating the good reversibility of the MWrGO-800W anode.

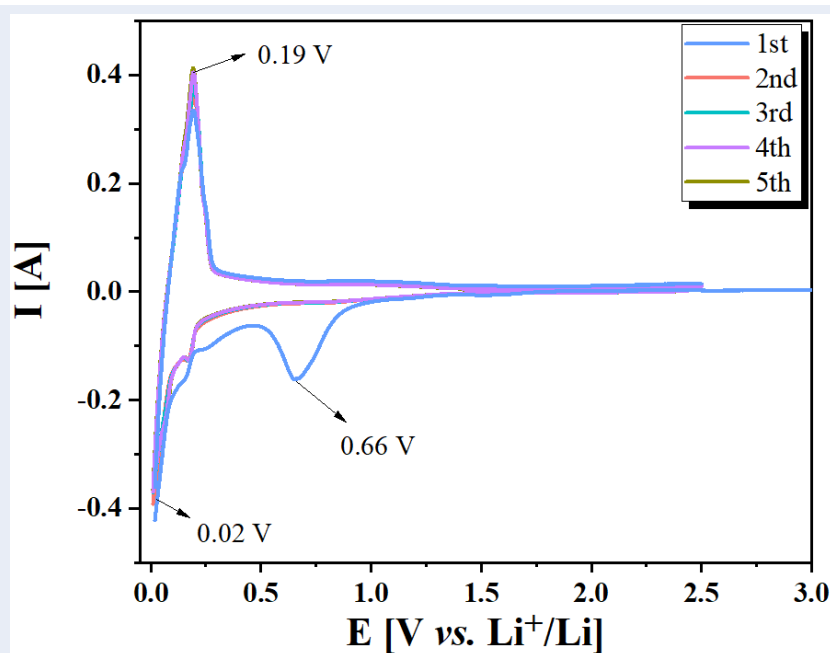


**Fig. 5-24.** The cyclic voltammogram of 800W/10min MWrGO anode for the first 5 cycles taken at the sweep rate of  $0.1 \text{ mV s}^{-1}$ .

Fig. 5-25 shows the cyclic performance of MWrGO anode at the current density of  $0.2 \text{ A g}^{-1}$  for 100 cycles, along with the corresponding coulombic efficiency. It is found that the specific discharge capacity of 800W/10min MWrGO remained steady *ca.*  $750.0 \text{ mAh g}^{-1}$  with near-zero capacity loss over the long-term test, which corresponded to a high

stoichiometric graphitic intercalation compound  $\text{Li}_x\text{C}_6$  ( $x \approx 2.0$ ). In contrast with the crystalline graphite in which each graphitic flake is believed only to accommodate a single layer of Li ions, well-exfoliated MWrGO flake is able to uptake two layers of lithium ions with each layer on each sides of graphene flake, making the specific capacity of 800W/10min MWrGO much higher than that of crystalline graphite ( $372 \text{ mAh g}^{-1}$  [319]). Furthermore, the structural defects, such as voids and micro-pores, on the 800W/10min MWrGO flakes can function as additional storage sites for lithium ions and further increased the specific capacity of 800W/10min MWrGO. It is also noting that the low coulombic efficiency of 49.5% in the initial cycle progressively increased to 90.0% at 2<sup>nd</sup> cycle and 96.9% at 5<sup>th</sup> cycle, indicating more Li ions uptake sites were activated and the stable SEI was formed on graphene flakes in the initial 5 cycles. After the activation charge/discharge cycles, the coulombic efficiencies fluctuated around 100%, implying the excellent reversibility of intercalation/deintercalation reactions of Li ions through SEI.

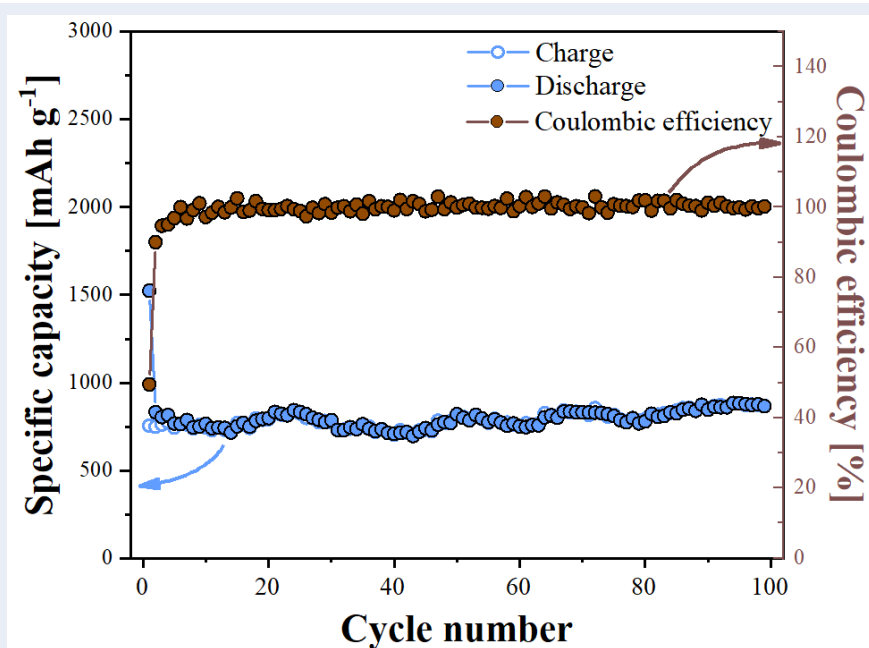


**Fig. 5-25.** The galvanostatic cycling performance and the coulombic efficiency of 800W/10min MWrGO half cell at the current density of  $0.2 \text{ A g}^{-1}$  between 0.01 V and 2.5 V for 100 electrochemical cycles.

The rate capability of MWrGO anode at the varying current densities between 0.01 V and 2.5 V is shown in Fig. 5-26. It can be noticed that 800W/10min MWrGO exhibited identical specific reversible capacity of  $\sim 750 \text{ mAh g}^{-1}$  at the low current densities of 0.1 and  $0.2 \text{ A g}^{-1}$ . However, with stepwise increasing the current densities, the specific reversible capacities of 800W/10min MWrGO were declined to  $\sim 610 \text{ mAh g}^{-1}$  at  $0.5 \text{ A g}^{-1}$ ,  $\sim 450 \text{ mAh g}^{-1}$  at  $1 \text{ A g}^{-1}$ ,  $\sim 330 \text{ mAh g}^{-1}$  at  $2 \text{ A g}^{-1}$ ,  $\sim 195 \text{ mAh g}^{-1}$  at  $5 \text{ A g}^{-1}$  and  $\sim 120 \text{ mAh g}^{-1}$  at  $10 \text{ A g}^{-1}$ . The diminishing reversible capacities of 800W/10min MWrGO at high current densities can be attributed to (i) the increased polarisation at high current density; and (ii) the steric hindrance effect of planar graphene flakes in which wrinkled graphene flakes with large lateral size are prone to impede the transportation of lithium ions, especially at a high current density [34, 201, 320]. More notably, the exceptional specific reversible capacity of  $\sim 120 \text{ mAh g}^{-1}$  at  $10 \text{ A g}^{-1}$  is a direct evidence of the thorough exfoliation of graphitic layers and the existence of mesopores, which provided commodious channels for fast diffusive motion of lithium ion. A remarkable specific reversible capacity of  $\sim 750 \text{ mAh g}^{-1}$  can be retained at the current density of  $0.1 \text{ A g}^{-1}$  immediately after being charge/discharged at  $10 \text{ A g}^{-1}$ , indicating the robust microstructure of 800W/10min MWrGO and the stable SEI formed in the initial cycles.

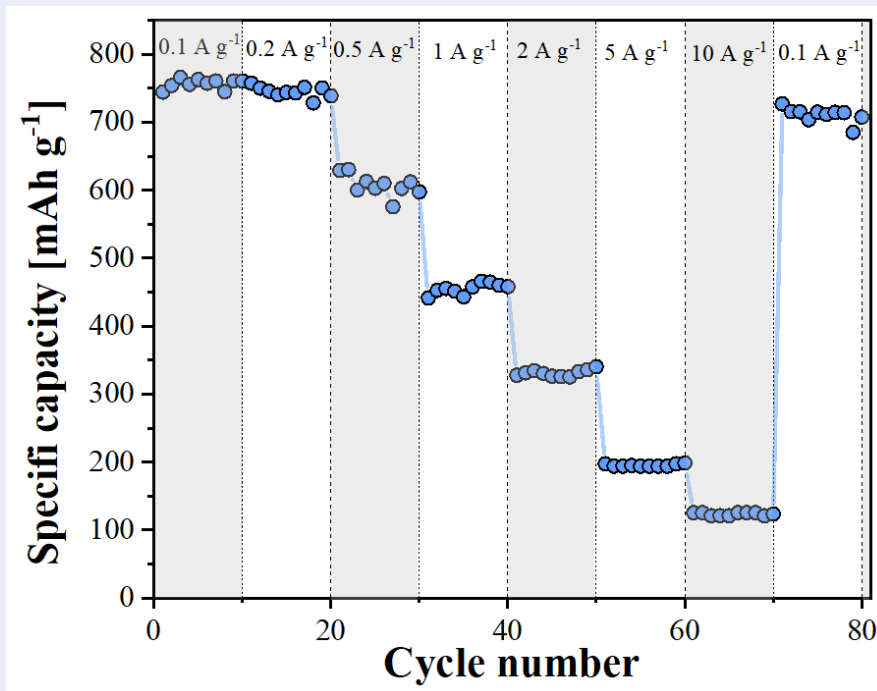


**Fig. 5-26.** Rate capability of MWrGO anode every ten cycles at the various current densities between 0.01 V and 2.5 V.



#### 5.4.2. 800W/10min MWrGO in cathode for LIBs

800W/10min MWrGO has great potentials to be employed as conductive additive in cathode owing to its distinct 2-dimensional structure, high electrical conductivity, and large surface area. As an exemplary demonstration, the electrochemical enhancement of 800W/10min MWrGO on LCO cathode was electrochemically compared with the counterpart of CNTs. It is worth pointing out that the content of 800W/10min MWrGO, as outlined in Section 3.3.5.2, was only 1 wt% of the total mass of the LCO-MWrGO composite, which is less than that of the CNTs used (3 wt%) in LCO-CNTs composite. This is because the higher electrical conductivity of 800W/10min MWrGO allowed lower amount of conductive additive to effectively minimize the internal ohmic resistance of cathode. The lower usage of conductive additive indicates that higher volumetric capacity can be realised for LCO-MWrGO cathode system.

The electrochemical evaluations of the LCO cathodes containing 1 wt% MWrGO and 3 wt% CNTs are shown in Fig. 5-27. The initial specific discharges of LCO-MWrGO and LCO-CNTs were  $142.8 \text{ mAh g}^{-1}$  and  $140.4 \text{ mAh g}^{-1}$ , respectively. Compared with LCO-MWrGO which experienced a smooth capacity decay over 100 cycles, LCO-CNTs suffered from a rapid capacity decay in the first 20 cycles, followed by a smooth capacity decay in the subsequent cycles. After being subjected to long-term cycles, the capacity retentions were 87.7% for LCO-MWrGO (0.123% decay per cycle) and 74.6% for LCO-CNTs (0.254% decay per cycle) relative to their initial capacities. The higher capacity retention attained in LCO-MWrGO was ascribed to the large planar character which was inferred to fully wrap the LCO particles. This structural model of graphene-wrapping-LCO is clearly demonstrated in Fig. 5-28 and Fig. 5-29. In this scenario, more LCO particles were able to firmly anchor in the elastic composite matrix with a sponge-like

architecture and continually contribute to the overall capacity. In addition, the planar character is believed to prevent the LCO particles from agglomeration and give a uniform dispersion of LCO particles on graphene surfaces. In contrast, the tube-shape CNTs were not able to provide additional anchor sites for LCO particles during electrochemical lithiation/delithiation process in which the LCO particles were expanded and contracted along *c* axis [281, 321], thereby leading to electrode disintegration and capacity fading upon long-term cycling.

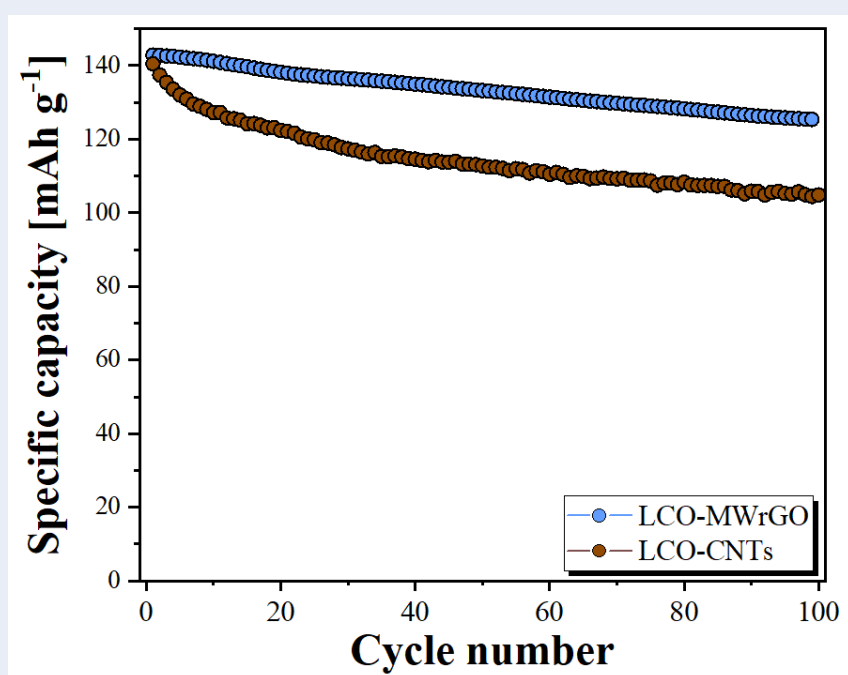


**Fig. 5-27.** The cycling performances of LCO-MWGrGO and LCO-CNTs cathode over 100 electrochemical cycles between 3.0 V and 4.2 V at the current rate of 0.2 C.

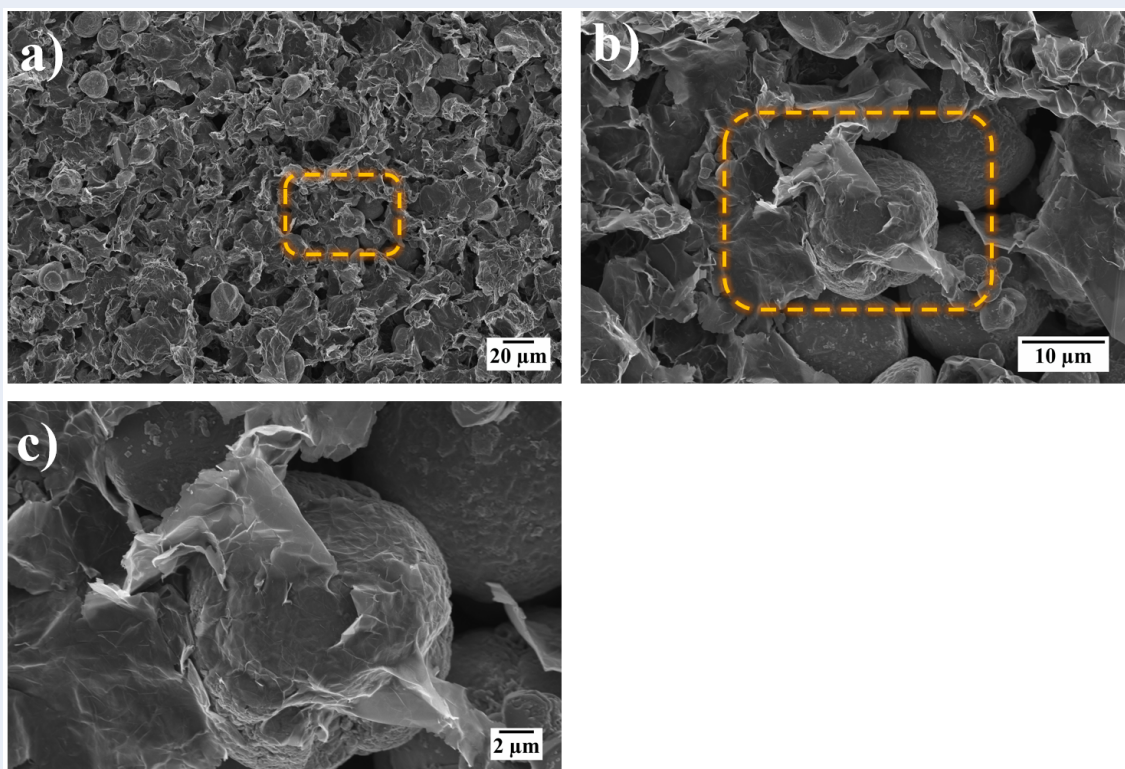


**Fig. 5-28.** FEGSEM images of LCO-MWrGO cathode at (a) lower magnification, (b) medium magnification, and (c) higher magnification, depicting the graphene-wrapping-LCO structural model in which the LCO particles were fully wrapped by a thin layer of graphene.

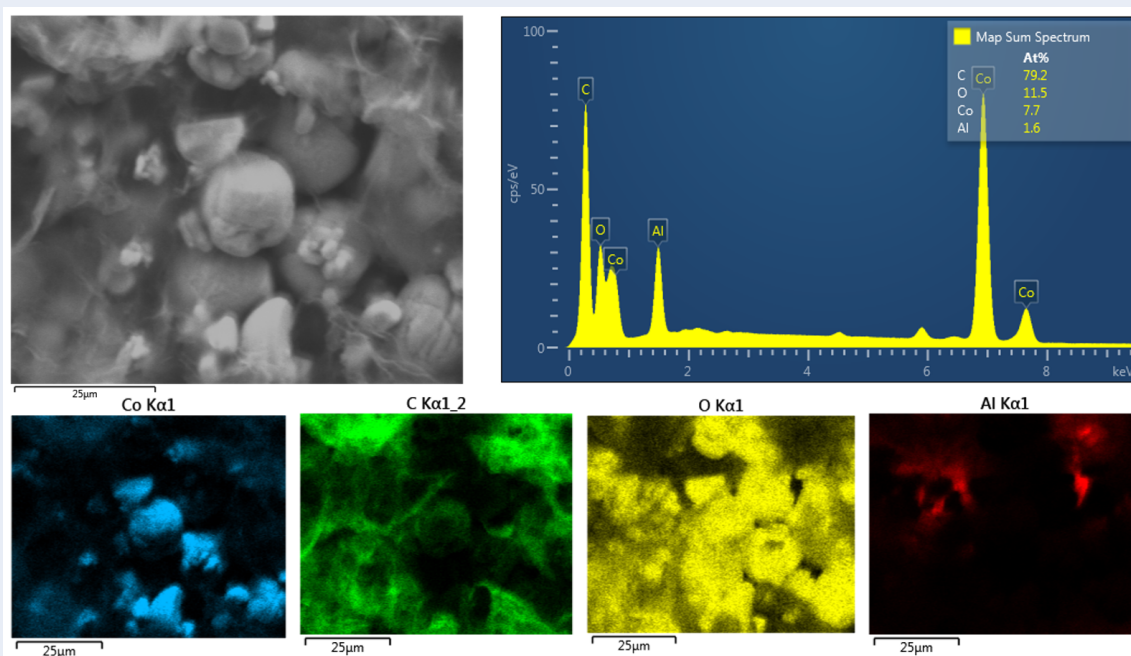


**Fig. 5-29.** EDS compositional mapping of the LCO-MWrGO cathode along with EDS spectrum of the whole area. The Al signal in the spectrum is a result of the Al substrate used for current collector.

Fig. 5-30 compares the rate capabilities of LCO-MWrGO and LCO-CNTs at varying current rates. When the current rates were increased stepwise to 0.2 C, 0.5 C, 1 C, 2 C, 5 C and 10 C, the LCO-MWrGO cathode showed reversible capacities of  $\sim 132 \text{ mAh g}^{-1}$ ,  $\sim 127 \text{ mAh g}^{-1}$ ,  $\sim 122 \text{ mAh g}^{-1}$ ,  $\sim 116 \text{ mAh g}^{-1}$ ,  $\sim 104 \text{ mAh g}^{-1}$ , and  $\sim 85 \text{ mAh g}^{-1}$ , respectively. However, the LCO-CNTs could just deliver reversible capacities of  $\sim 131 \text{ mAh g}^{-1}$ ,  $\sim 127 \text{ mAh g}^{-1}$ ,  $\sim 122 \text{ mAh g}^{-1}$ ,  $\sim 111 \text{ mAh g}^{-1}$ ,  $\sim 32 \text{ mAh g}^{-1}$ , and  $\sim 0 \text{ mAh g}^{-1}$ , respectively, at the identical current rates. The highly achieved reversible capacity of LCO-MWrGO can be attributed to (i) the effective plane-to-point conductive model in which the spherical-shape LCO particles come in close contact with planar graphene flakes, giving a long-range conductive network [34]; (ii) the higher utilisation efficacy of the  $\text{sp}^2$  carbon atoms on the planar graphene flakes [34]; and (iii) the porous structure of MWrGO which can facilitate the absorption and storage of excess electrolyte solution, providing an intimate contact between electroactive material and electrolyte [236, 253]. When the current rate was returned to 0.1 C, a slightly higher reversible capacity of LCO-MWrGO, *i.e.*,  $\sim 130 \text{ mAh g}^{-1}$ , was achieved in comparison to the reversible capacity of  $\sim 125 \text{ mAh g}^{-1}$  in LCO-CNTs. It is also worth noting that the amount of MWrGO used in LCO-MWrGO is less than that in LCO-CNTs, indicating the higher volumetric capacity can be realised in LCO-MWrGO cathode.

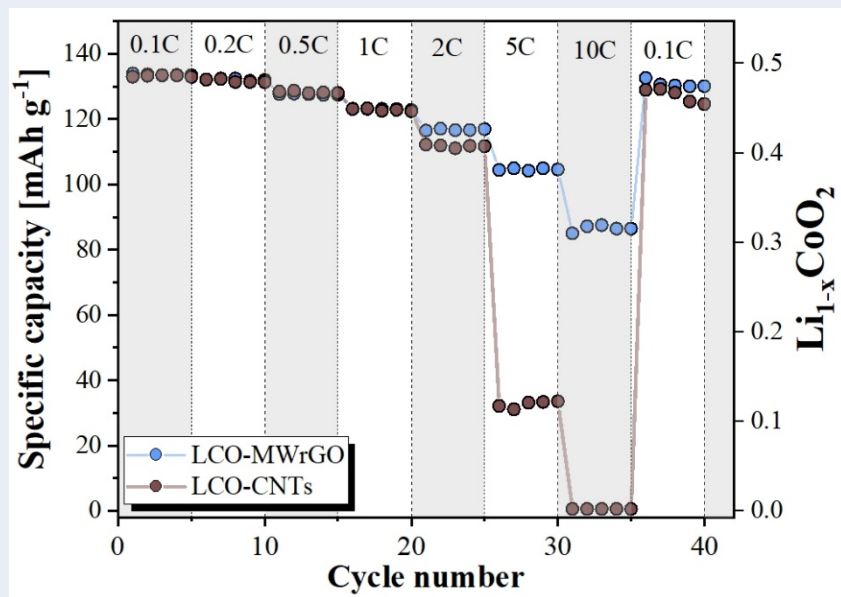


**Fig. 5-30.** The rate capability comparison of LCO-MWtGO and LCO-CNTs cathodes every five cycles at charge/discharge current rates from 0.1 C to 10 C between 3.0 V and 4.2 V.

## 5.5. Chapter conclusions

This chapter demonstrates the successful preparation of nanoporous MWrGO synthesised using microwave irradiation of solid-state GO within a matter of few seconds and the application of 800W/10min MWrGO in cathodes and anode for LIBs. The quality of MWrGO was found to be strongly affected by the oxidation of pristine graphite, preliminary annealing treatment, the microwave power, and the inert gas atmosphere. In addition, the electrochemical evaluation showed the great potential of microwave synthesised graphene as electroactive materials or conductive filler for LIBs.

- The robust GO beads can be obtained in 1 wt%  $\text{CaCl}_2$  solution after 24 hours soaking by forming a hard GO shell through the aggregation and the segregation of GO flakes on the bead surfaces. The concentration of  $\text{CaCl}_2$  solution was found to play a decisive role in the formation and development of GO beads. In pure water (0 wt%  $\text{CaCl}_2$  solution), the aggregation and the segregation of GO cannot occur due to the lack of positively charged cationic ions, *i.e.*,  $\text{Ca}^{2+}$ , whilst high concentration of  $\text{CaCl}_2$  solution (3 wt%  $\text{CaCl}_2$  solution) gave rise to a strong absorption of  $\text{CaCl}_2$  salt on the surfaces of GO beads, as confirmed by XRD and EDS compositional mapping.
- With comparative studies of microwave-assisted reduction of annealed and unannealed GO, the microwave-coupling behaviour of GO was confirmed to be enhanced via annealing treatment of GO at 250 °C in argon atmosphere, which allows for the partial recovery of  $\pi$ - $\pi$  conjugated networks of carbon hexagonal structure. The partially recovered GO can effectively interact with electromagnetic microwaves, leading to a high localised reaction temperature and a significant decomposition of oxygen functional groups [153]. The phenomenon of strong arcing against

microwave irradiation was attributed to the induced intense electrostatic field by high-concentration congregation of the  $\pi$  electrons at sharp edges of the graphene nanosheets [287]. This strategy can inspire other works to purify carbonaceous materials at a rapid and efficient manner.

- The properties and structures of MWrGO can be precisely tailored by tuning the microwave powers and can be improved in protective Argon atmosphere. The microwave-assisted reduction of annealed GO approach represents a facile method to produce high-quality graphene within the matter of seconds. Due to its simplicity, ease of preparation and controllable quality, this approach possesses the potential for mass production of graphene at an affordable cost and at bulk scale.
- A modified  $I_D/I_{G-in}$  ratio was proposed to investigate the structural evolutions of MWrGO by deducting the intensity contribution of D' peak from the apparent G peak, giving a more reliable evaluation. This modified  $I_D/I_{G-in}$  ratio could be applicable to other graphene-based materials prepared using other methods, such as thermal/chemical reduction, liquid/gas exfoliation or CVD.
- The 800W/10min MWrGO was used as electroactive materials in anode for LIBs and afforded a remarkable practical capacity of 750.0 mAh g<sup>-1</sup> at 0.2 A g<sup>-1</sup> with near-zero capacity loss after 100 cycles and a high reversible capacity of 120.0 mAh g<sup>-1</sup> up to 10 A g<sup>-1</sup>. Through comparative studies with CNTs as conductive additive in LCO cathode, 800W/10min MWrGO showed an excellent cycling stability and a commendable rate capability of LCO cathode, especially at or above the current rate of 2 C owing to the high electrical conductivity and the robust graphene-encapsulated structure. This preliminary work demonstrated that MWrGO was a promising

candidate to replace CNT as conductive filler in LCO-based electrode.



## **Chapter 6. Cold sintering process and electrochemical evaluation of high-performance LiCoO<sub>2</sub>-matrix cathode with MWrGO as conductive filler**

Following the discussion in Chapter 4, the concept of CSP has been successfully applied to produce LCO-matrix composite cathodes without the addition of polymeric binder. However, even with 3 wt% of CNTs inclusion, the LCO/3%CNTs cathodes produced by CSP experienced an apparent capacity loss of 38% after 40 cycles at 0.1 C and delivered a low reversible capacity at high current rates, which plagued its wide application. Through extensive characterisation of 800W/10min MWrGO prepared using solid-state microwave absorption method in Chapter 5, the highly conductive 800W/10min MWrGO with flexibility and porous structure has been proved to improve the overall electrochemical properties of LCO-MWrGO half cell in comparison with CNTs as conductive filler in the same battery configuration. Therefore, there is no doubt to propose to substitute CNTs with MWrGO (referred to 800W/10min MWrGO in this chapter, unless otherwise noted) in LCO composite cathodes to improve the electrochemical performances.

This chapter started with the microstructural characterisation and the investigation of electrical conductivities of LCO pellets as a function of varied contents of MWrGO in Section 6.1 and Section 6.2, respectively. In the same vein, the annealing effect on the selected LCO/1%MWrGO pellets produced by CSP was studied in terms of relative density and electrical conductivity in Section 6.3. Lastly, the LCO/1%MWrGO cathode with annealing treatment is electrochemically compared with its counterpart, *i.e.*, LCO/3%CNTs cathode, using cyclic voltammetry (CV) and galvanostatic cycling test in

Section 6.4. More specifically, CV test is applied at different sweep rates to gain further insight into the lithium-ion chemical diffusion coefficient of LCO/1%MWrGO composite cathode.

## 6.1. Microstructural characterisation of LCO/xMWrGO composites

Fig. 6-1 interprets the XRD patterns of as-milled LCO powder, MWrGO, and LCO/xMWrGO pellets ( $x=0.5$  wt%, 1 wt%, 2 wt% and 3 wt%) produced by CSP. All the XRD results of LCO/xMWrGO pellets have diffraction peaks at the same locations within instrument error and are in close agreement with the JCPDS crystallography entry database No.: 70-2685 [260, 261], which can be correlated to the layered hexagonal structure ( $\alpha$ -NaFeO<sub>2</sub> structure [259]). No amorphous background noise is presented, and all the major peaks are sharp and intense. Moreover, no minor peak can be identified to the characteristic (002) peak of MWrGO in the  $2\theta$  range of  $20^\circ - 30^\circ$ , as shown in Fig. 6-2. This is not a surprise because the minor amount of MWrGO inclusions in the LCO matrix was difficult to discern in the XRD patterns.

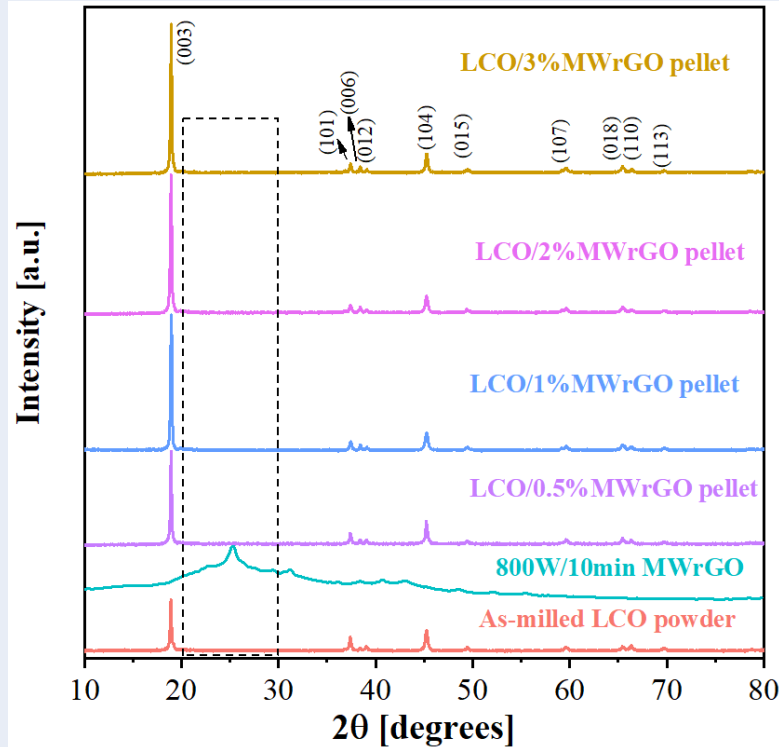


**Fig. 6-1.** XRD patterns of as-milled LCO powder, MWrGO, and LCO/xMWrGO ( $x=0.5$  wt%, 1 wt%, 2 wt%, and 3 wt%) pellets produced by CSP.

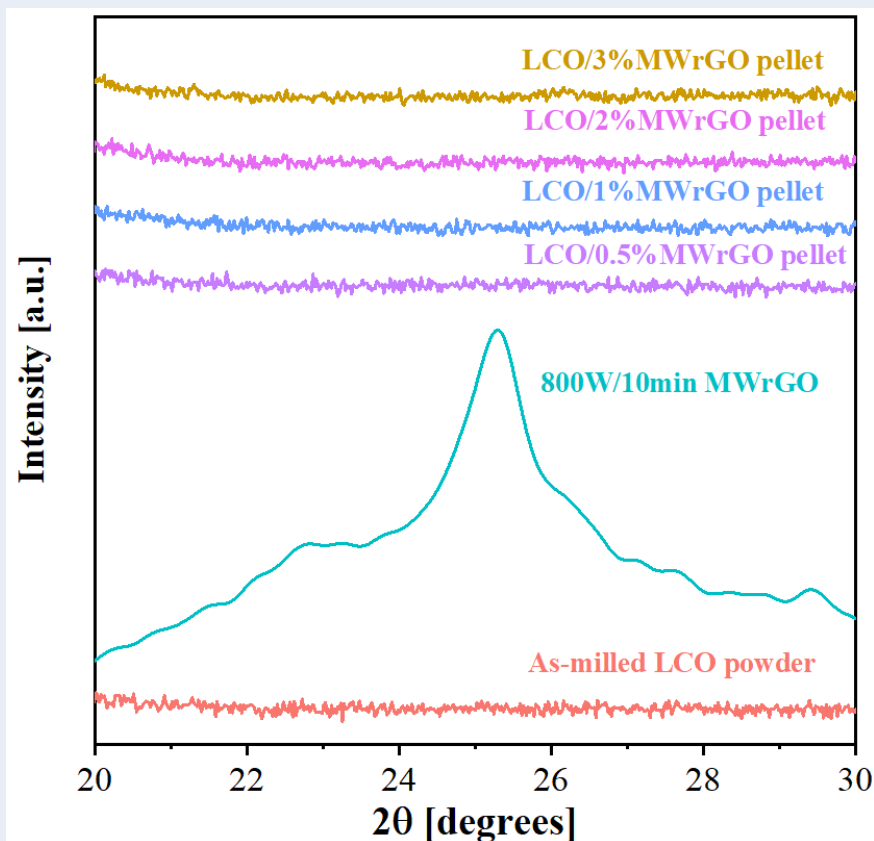


**Fig. 6-2.** The enlarged XRD plots of 20° - 30° range as indicated in Fig. 6-1.

It is worth mentioning that in comparison with LCO/3%CNTs pellet, a more intensive *c*-axis (003) peak can be observed for the LCO/1%MWrGO pellet in Fig. 6-3, which can be attributed to the preferential rearrangement and improved compaction of as-milled LCO powders under external pressure. As shown in Fig. 4-2 (b), the as-milled LCO powders presented itself as platelet with sharp edges which was believed to increase the difficulty in powder rearrangement and compaction under external pressure. Through a combination of ultrasonication bath and ball-milling process, the platelet-shape LCO particles were believed to be thoroughly mixed with planar graphene sheets. Compared to CNTs, graphene sheets were able to provide more contact sites with LCO particles. In this scenario, the graphene sheets can help reduce the friction during re-orientation and rearrangement of LCO particles at high uniaxial pressure, thereby increasing the alignment degree and yielding a more pronounced (003) texturing orientation, as shown

in Fig. 6-4. A typical FEGSEM image of fractured surface of LCO/1%MWrGO pellet is given in Fig. 6-5 and it is worth noting that the graphene sheets were uniformly distributed across the dense LCO/1%MWrGO pellet without presence of any cracks. The intrinsic wrinkles and ripples on the graphene flakes also lays a foundation for intact contact between planar graphene sheets and LCO.

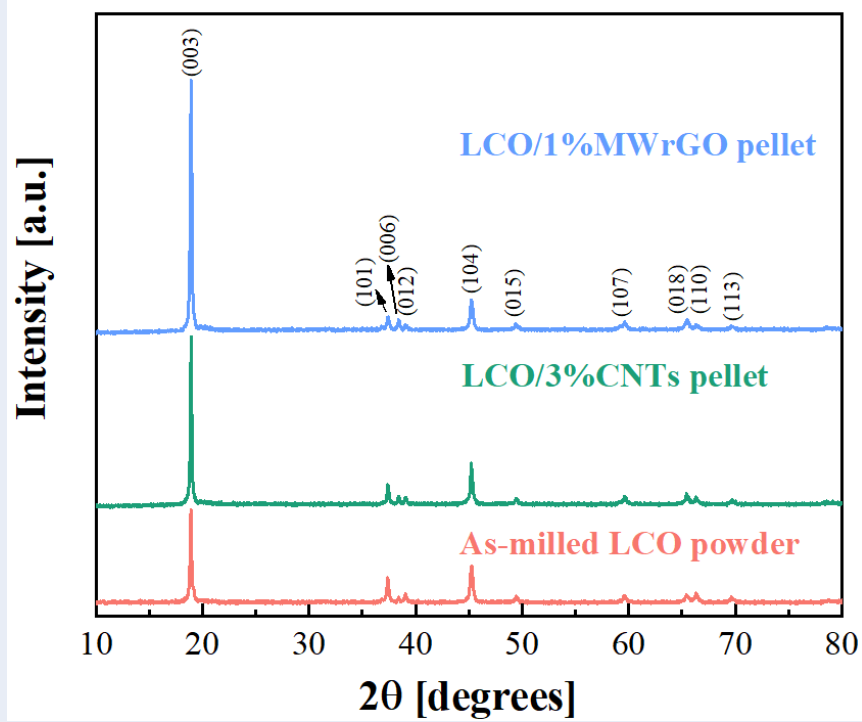


**Fig. 6-3.** X-ray diffractograms of as-milled LCO powder, LCO/3%CNTs pellet produced by CSP, and LCO/1%MWrGO pellet produced by CSP.

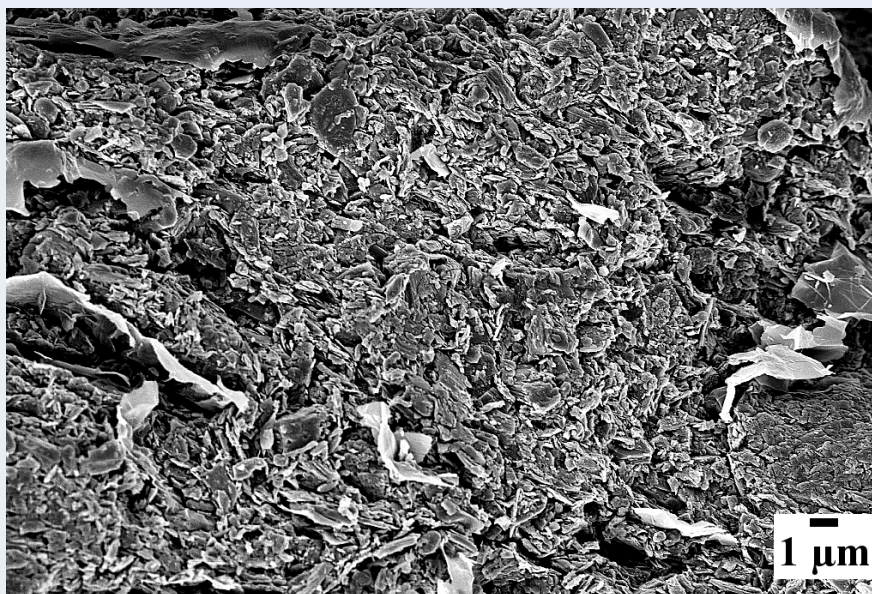


**Fig. 6-4.** FEGSEM images of fractured surface of LCO/1%MWrGO pellet produced by CSP.

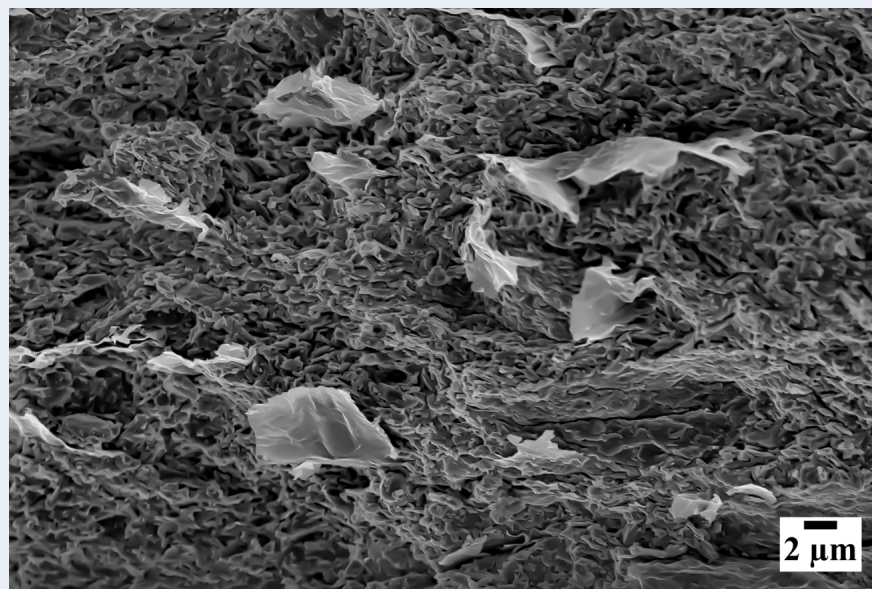


**Fig. 6-5.** FEGSEM image of the fractured surface of LCO/1%MWrGO pellet produced by CSP.

## 6.2. The effect of graphene content on electrical conductivity of composite cathode

As discussed in Section 4.2, the electrical conductivities of LCO/ $x$ CNTs pellets were significantly increased from  $\sim 1.66 \times 10^{-4} \text{ S cm}^{-1}$  at  $x=0 \text{ wt}\%$  to  $\sim 2.84 \text{ S cm}^{-1}$  at  $x=3 \text{ wt}\%$  and then levelled off with further increasing  $x$  values, indicating that the percolation threshold of CNTs to form a 3D conductive network in LCO/ $x$ CNTs pellets was 3 wt%. Highly conductive MWrGO with porous structure was applied as conductive filler alternative to CNTs to reduce the usage of conductive filler in LCO composite. The effect of MWrGO inclusion on the electrical conductivities of LCO/ $x$ MWrGO pellets was first investigated in Fig. 6-6. It is similarly observed that the electrical conductivities of LCO/ $x$ MWrGO pellets underwent an incremental improvement with increasing MWrGO inclusion. The electrical conductivity of LCO/ $x$ MWrGO pellets at  $x=0.5 \text{ wt}\%$  was only  $4.15 \times 10^{-3} \text{ S cm}^{-1}$  which means that the long-range 3D conductive network has not yet established, but it significantly increased to  $2.81 \text{ S cm}^{-1}$  at 1 wt% which was comparable to  $\sim 2.84 \text{ S cm}^{-1}$  that was achieved for LCO/3%CNTs pellets produced by CSP. With further increasing MWrGO inclusions, the electrical conductivities of LCO/ $x$ MWrGO pellets was raised to  $\sim 3.21 \text{ S cm}^{-1}$  at  $x=2 \text{ wt}\%$  and  $\sim 6.49 \text{ S cm}^{-1}$  at  $x=3 \text{ wt}\%$ .

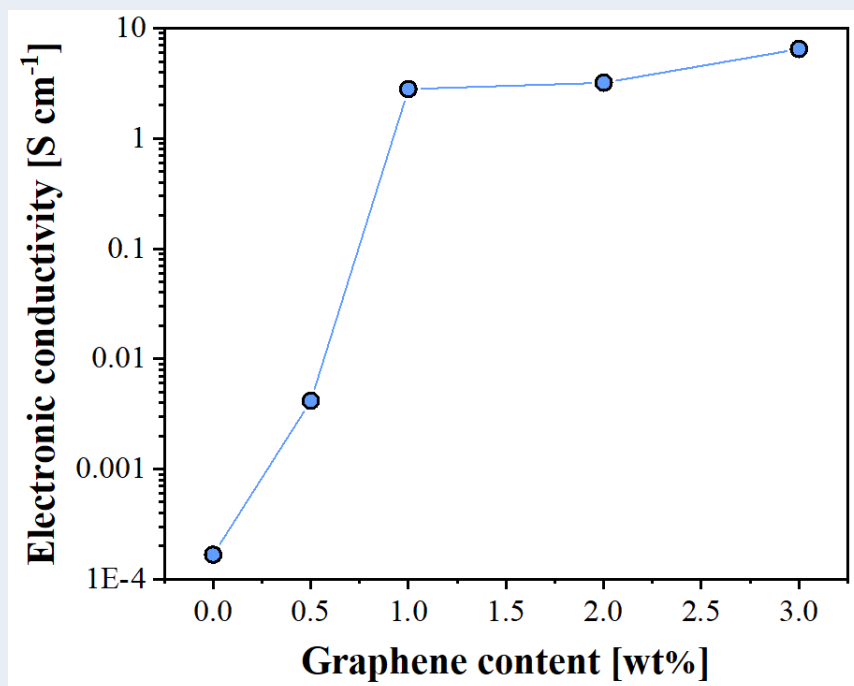


**Fig. 6-6.** The effect of MWrGO content on the electrical conductivities of LCO/xMWrGO pellets prepared at CSP conditions of 250 °C, 250 MPa, and 60 min.

The electrical conductivities of LCO/xMWrGO pellets and LCO/xCNTs pellets with respect to the various contents of 800W/10min MWrGO and CNTs, respectively, are compared and plotted in the same scale in Fig. 6-7. It is easily found that 1 wt% MWrGO inclusion endowed LCO/MWrGO pellets with the competitive electrical conductivity to that of LCO/3%CNTs pellets. The lower conductive filler content of MWrGO can be largely related to the larger surface areas and porous structure of MWrGO which was prepared using rapid microwave absorption method. Fig. 6-8 shows the comparison between MWrGO and CNTs in terms of the surface areas and porous structure. From the perspective of surface area, MWrGO exhibited much higher surface area ( $310.24 \text{ m}^2 \text{ g}^{-1}$ ) than CNTs ( $125.01 \text{ m}^2 \text{ g}^{-1}$ ). The larger surface area can provide more contact sites with LCO particles at the same content of conductive filler. On the other hand, the  $\text{N}_2$  adsorption/desorption hysteresis loops of MWrGO was larger than that of CNTs in the relative pressure range of  $> 0.4$ , indicating impediment in the release of  $\text{N}_2$  gas during



desorption process by the presence of porous structure in MWrGO. The porous structure of MWrGO is believed to effectively establish an interconnecting 3D electrically conductive network. Moreover, the porous structure can enhance the absorption and retention of excess electrolyte solution, providing more lithium ion source to smoothly complete intercalation/deintercalation process in LIBs, which will be discussed below.

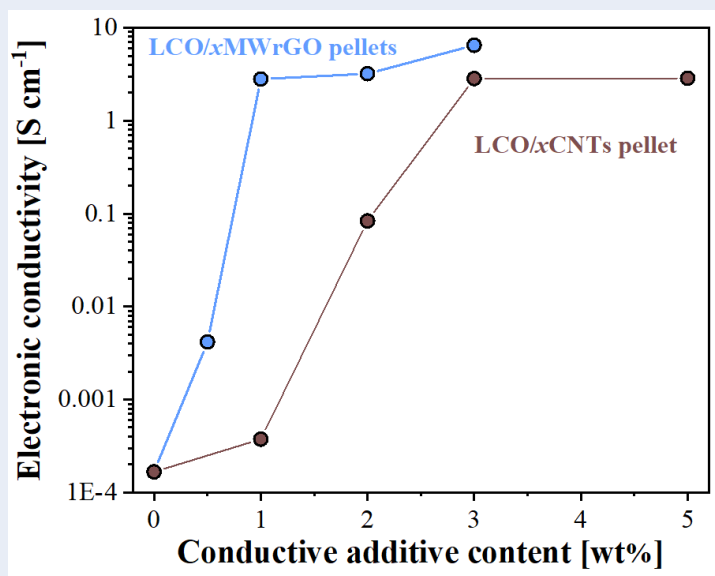


**Fig. 6-7.** The comparison of electrical conductivities of LCO/xMWrGO pellets produced by CSP and LCO/xCNTs pellets produced by CSP with respect to the varied contents of 800W/10min MWrGO and CNTs, respectively.

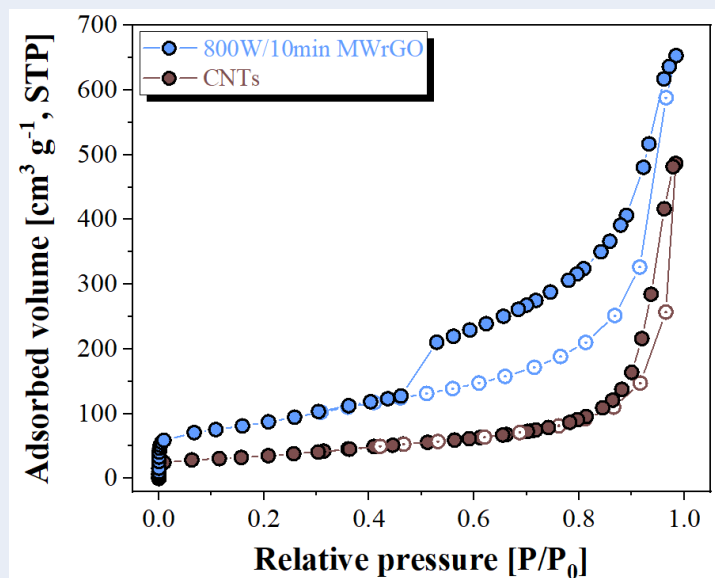


**Fig. 6-8.** Nitrogen adsorption/desorption hysteresis loops of MWrGO and CNTs.

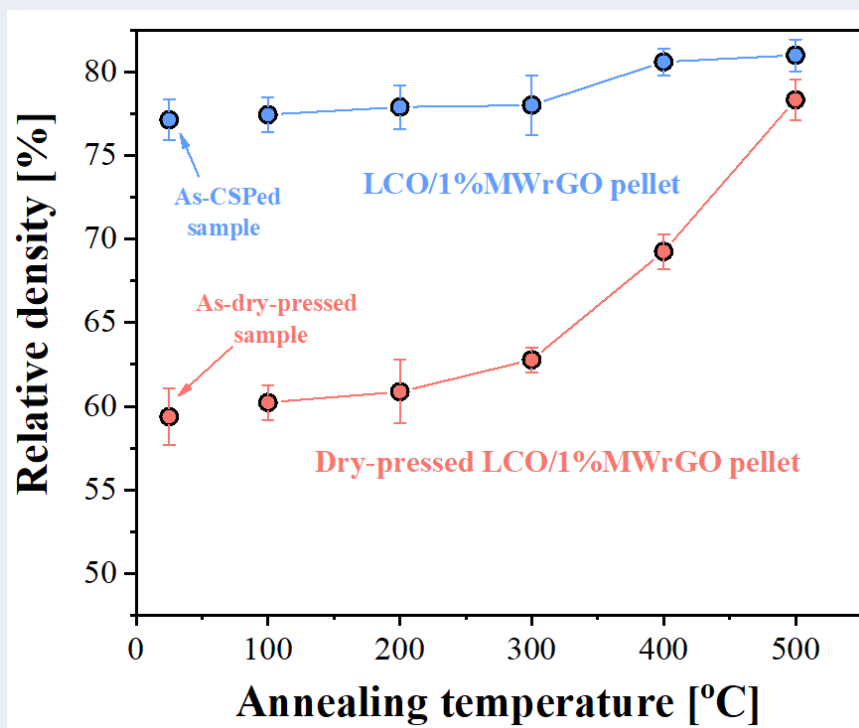
Albeit that LCO/3%MWrGO pellets showed the highest electrical conductivity in Fig. 6-7, our experimental work found that they had difficulty of being polished down to the thickness of less than 200  $\mu\text{m}$  for the subsequent battery testing, which was presumably due to the significant “pull-out” effect of planar graphene sheets by sand paper. Note that the electrical conductivity ( $2.81 \text{ S cm}^{-1}$ ) of LCO/1%MWrGO pellets was very close to that ( $2.84 \text{ S cm}^{-1}$ ) of LCO/3%CNTs pellets. In order to make a meaningful comparison with LCO/3%CNTs pellets, LCO/1%MWrGO pellet was used for the subsequent experimental process.

### **6.3. The effect of post-CSP annealing treatment**

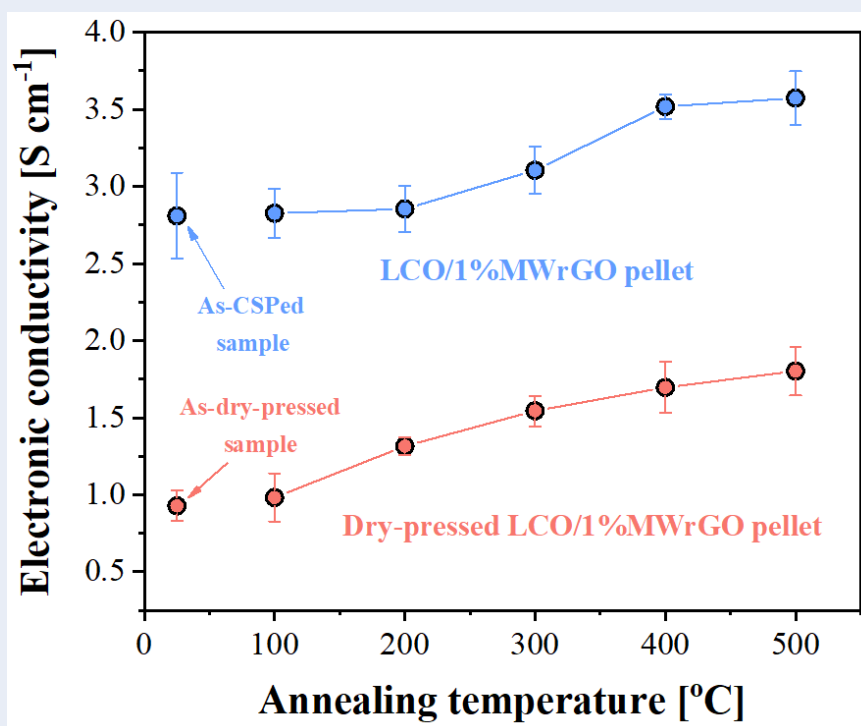
In the same vein, the effects of post-CSP annealing treatment (temperature range of 100 - 500  $^{\circ}\text{C}$ ) on the relative densities and electrical conductivities of LCO/1%MWrGO pellets produced by CSP were studied, as shown in Fig. 6-9. In comparison, the control group, dry-pressed LCO/1%MWrGO pellets, was also annealed at the temperatures range from 100 to 500  $^{\circ}\text{C}$ . After being subjected to annealing treatment up to 500  $^{\circ}\text{C}$ , the relative densities of LCO/1%MWrGO pellets were slightly increased from 77.1% at room temperature to 80.6% at 400  $^{\circ}\text{C}$  and to 81.0% at 500  $^{\circ}\text{C}$ , as shown in Fig. 6-9. In contrast, an appreciable effect on densification was observed in dry-pressed LCO/1%MWrGO pellets. Specifically, the relative density of dry-pressed LCO/1%MWrGO pellets increased from 59.4% at room temperature to 78.4% at 500  $^{\circ}\text{C}$ .

Fig. 6-10 shows the impact of post-CSP annealing treatment (100 - 500  $^{\circ}\text{C}$ ) on the electrical conductivities of both LCO/1%MWrGO pellets produced by CSP and dry-pressed LCO/1%MWrGO pellets. It can be found that the electrical conductivities of LCO/1%MWrGO pellets increased slightly from  $2.81 \text{ S cm}^{-1}$  at room temperature to  $2.85$

S cm<sup>-1</sup> at 200 °C and then significantly to 3.51 S cm<sup>-1</sup> at 400 °C before levelling off at 500 °C. Despite that little improvement was observed for the relative densities of LCO/1%MWrGO pellets after being annealed at 100 - 500 °C, the electrical conductivities of LCO/1%MWrGO pellets can be effectively improved, which is presumably associated with the crystallisation of amorphous LCO phase precipitated on the grain boundaries of LCO/1%MWrGO pellets produced by CSP. On the contrary, the annealing treatment increased the electrical conductivities of dry-pressed LCO/1%MWrGO pellets from 0.93 S cm<sup>-1</sup> at room temperature to 1.80 S cm<sup>-1</sup> at 500 °C. It can be concluded that the annealing treatment at 400 °C is beneficial to crystallising the amorphous LCO phase formed during non-equilibrium precipitation process induced by CSP. As such, higher relative density and electrical conductivity of LCO/1%MWrGO pellets can be obtained after annealing treatment at 400 °C. Henceforth, all the LCO/1%MWrGO pellets produced by CSP were first annealed at 400 °C for 1 hour prior to being polished to thin pellets (< 200 µm in thickness).



**Fig. 6-9.** The plot of relative densities of LCO/1%MWrGO pellets produced by CSP and dry-pressed LCO/1%MWrGO pellets as a function of annealing temperatures in comparison with as-CSPed LCO/1%MWrGO pellets and as-dry-pressed LCO/1%MWrGO pellets.



**Fig. 6-10.** The plot of electrical conductivities of LCO/1%MWrGO pellets produced by CSP and dry-pressed LCO/1%MWrGO pellets as a function of annealing temperatures in comparison with as-CSPed LCO/1%MWrGO pellets and as-dry-pressed LCO/1%MWrGO pellets.

In summary, the LCO/1%MWtGO pellets (80.6% relative density, 3.51 S cm<sup>-1</sup>) were successfully prepared at the CSP condition of 250 °C, 250 MPa and 1-hour duration time with 20 wt% LiOH solution, followed by post-CSP annealing treatment at 400 °C.

## 6.4. Electrochemical characterisation

The LCO/1%MWrGO pellets prepared above were then electrochemically probed using cyclic voltammetry (CV), galvanostatically charge/discharge techniques and electrochemical impedance spectroscopy (EIS). All the obtained data are compared with the data of LCO/3%CNTs pellets produced by CSP to study the viable substitution of CNTs with MWrGO in LCO composite cathodes.

The CV test is a complementary technique to provide insights regarding the electrochemical reactions happening in cathode, such as redox potentials, reaction kinetics, and reaction reversibility. Fig. 6-11 shows the first-cycle CV curve of LCO/1%MWrGO cathode at a slow-scan rate of  $0.1 \text{ mV s}^{-1}$  in the potential window of 3.0 - 4.2 V. The CV behaviour of LCO/1%MWrGO cathode was also characterised by three sets of well-defined redox peaks, which resembled very much LCO/3%CNTs cathode as shown in Fig. 6-12. More notably, the current peaks of LCO/1%MWrGO cathode were sharper and more distinguished in comparison with the counterpart. The main redox peaks represented the typical oxidation and reduction reaction of  $\text{Co}^{3+}/\text{Co}^{4+}$ , which was associated with the first-order phase transition between hexagonal I and hexagonal II in which lithium ions were inserted into/extracted from  $\text{LiCoO}_2$  hexagonal host matrix [247, 274, 275]. The two successive redox peaks at 4.06 V/4.05 V and 4.18 V/4.16 V have been ascribed to the second-order hexagonal/monoclinic phase transition due to the lithium ion ordering in the  $\text{CoO}_2$  framework [71]. In short summary, when the LCO/1%MWrGO cathode was galvanostatically charged from 3.0 V to 4.2 V, a sequence of multiple phase transitions occurred by the variation in the value of  $x = 0.5 \sim 1$  in  $\text{Li}_x\text{CoO}_2$ : (i) hexagonal I to hexagonal II; and (ii) hexagonal structure to monoclinic structure, which agrees well with the *in situ* XRD analysis by Reimers and Dahn [71]. Furthermore, the

nearly symmetrical area under redox peaks in the CV curve of LCO/1%MWrGO was indicative of the excellent coulombic efficiency without too much capacity loss upon cycling.

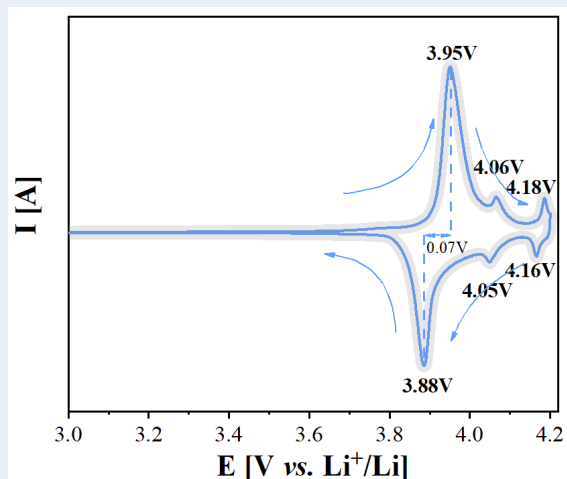


**Fig. 6-11.** The cyclic voltammogram of a half-cell consisted of LCO/1%MWrGO pellet for the initial cycle recorded at the sweep rate of  $0.1 \text{ mV s}^{-1}$

In closer inspection of first-cycle CV curve of LCO/1%MWrGO cathode in Fig. 6-12, the anodic peak (3.95 V) and the cathodic peak (3.88 V) were separated by 0.07 V, which is smaller than 0.11 V for LCO/3%CNTs cathode. The reduced peak separation manifested the lower ohmic resistance in LCO/1%MWrGO cathode owing to the higher electrical conductivity of MWrGO over CNTs. The divergence in electrical conductivity between MWrGO over CNTs can also be studied by direct current internal resistance (DCIR). Despite that DCIR measures the overall ohmic resistance of testing cells which includes all the resistivity of the components of the cells, such as cell casing, active material itself, electrolyte, and conductive fillers, it can still be used to give an indication of electrical conductivity of MWrGO over CNTs because all the cell components used were the same except the conductive fillers. The DCIR of LCO/1%MWrGO pellet and LCO/3%CNTs pellet is compared at the 25%SOC, 50%SOC and 75%SOC in Fig. 6-13. This range of SOC was chosen because any associated error can be minimised within this range and it

can give a more reliable evaluation. Their results were calculated in Table 6-1. It can be readily seen that the DCIR for LCO/1%MWrGO pellet was lower than those for LCO/3%CNTs pellet regardless of SOC, which is simply attributed to the divergence in electrical conductivity of conductive fillers. It is worth noting that the DCIR for both LCO/1%MWrGO and LCO/3%CNTs decreased with increasing SOC. This decreasing trend is line with the reduce in electrical conductivity of LCO when the lithium ion are extracted from the host structure [322, 323].

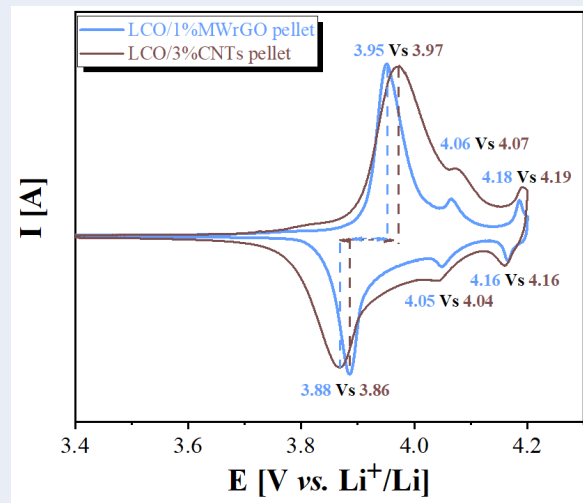


**Fig. 6-12.** The comparison for initial-cycle CV plots of LCO/1%MWrGO pellet and LCO/3%CNTs pellet at the sweep rate of  $0.1 \text{ mV s}^{-1}$

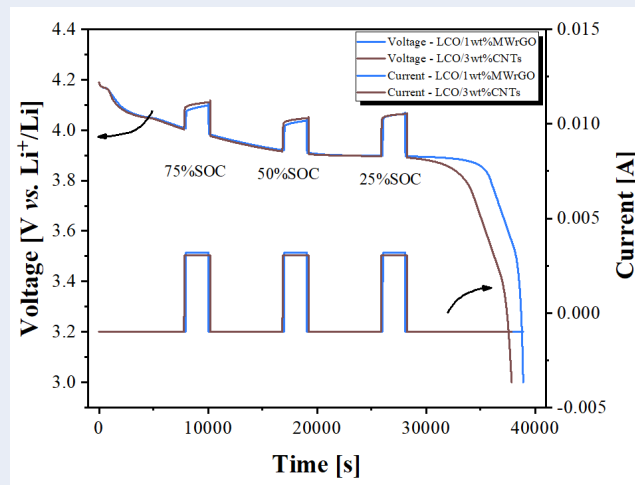


**Fig. 6-13.** The DCIR profiles of LCO/1%MWrGO pellet and LCO/3%CNTs pellet performed at the same state of charge (SOC).



**Table 6-1.** The calculated DCIR values for LCO/1%MWrGO pellet and LCO/3%CNTs at different SOC.

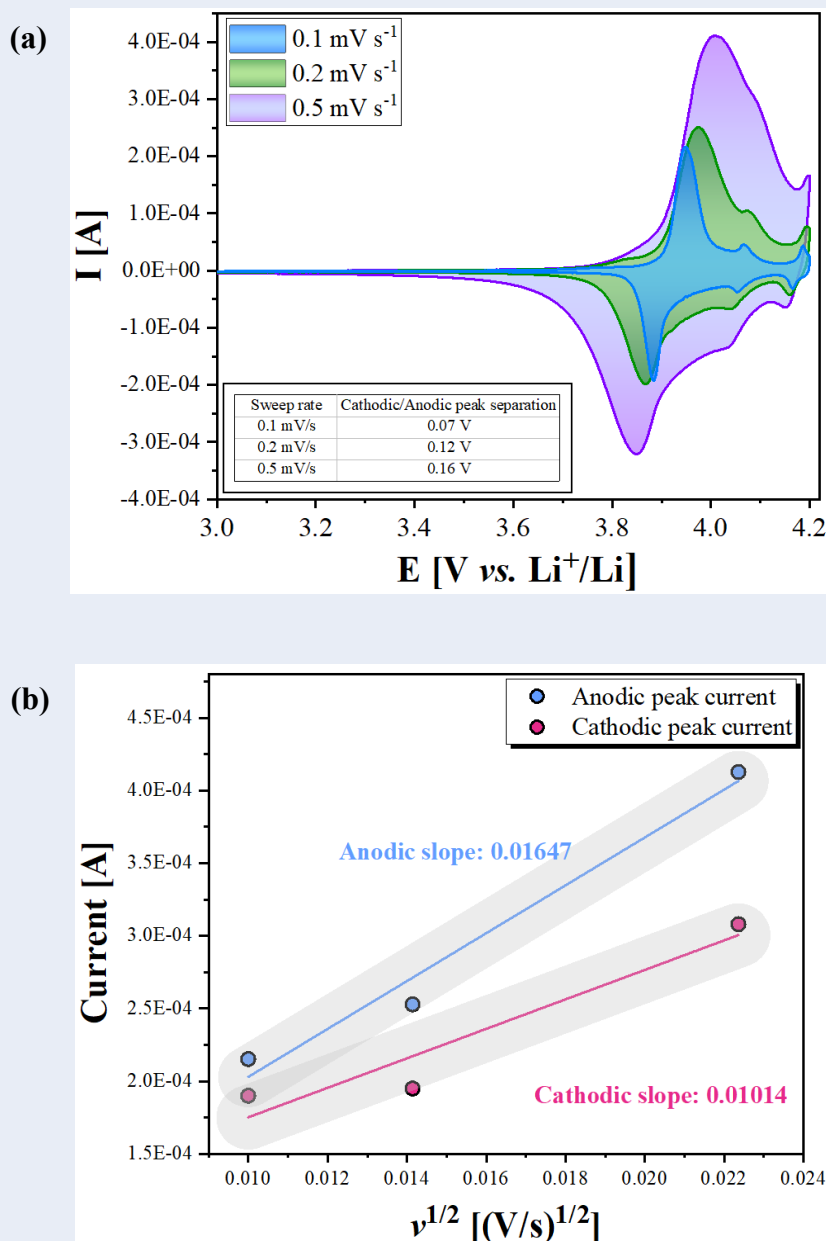
	LCO/1%MWrGO	LCO/3%CNTs
<b>25%SOC [<math>\Omega</math>]</b>	23.31	46.97
<b>50%SOC [<math>\Omega</math>]</b>	20.33	37.35
<b>75%SOC [<math>\Omega</math>]</b>	18.41	31.49

Fig. 6-14 (a) shows the CV curves of LCO/1%MWrGO composite cathode at various sweep rates in the potential window of 3.0 - 4.2 V. Three sets of well-defined current peaks were clearly observed at low sweep rate of 0.1 mV s<sup>-1</sup>. However, with increasing sweep rates, the anodic peaks shifted to higher potential while the cathodic peaks shifted to lower potential, as shown in the inset of Fig. 6-14 (a). Also, both anodic and cathodic peaks were less identified at high sweep rates. Since the insertion of Li ions in the bulk of the electrode material is a diffusion-based process, the kinetic reaction can be assumed to be in a condition of semi-infinite diffusion. It is worth noting that the peak currents ( $I_p$ ) of the main peak ( $E_p=3.95$  V) was found to be positively proportional to the square root of the sweep rates, which is shown in Fig. 6-14 (b) and can be described as Randles-Sevcik equation [258]:

$$I_p = (2.69 \times 10^5) n^{\frac{3}{2}} A D_{Li}^{\frac{1}{2}} C_{Li} v^{\frac{1}{2}} \quad [\text{Equation 22}]$$

Where,  $I_p$  is peak current (unit: A),  $n$  is the number of electrons per molecule during Li ion insertion ( $n=1$  for LiCoO<sub>2</sub>),  $A$  is the surface area of the electrode (unit: cm<sup>2</sup>),  $D_{Li}$  is the Li-ion chemical diffusion coefficient (unit: cm<sup>2</sup> s<sup>-1</sup>),  $C_{Li}$  is the Li-ion concentration (unit: mol cm<sup>-3</sup>), and  $v$  is the sweep rate (unit: V s<sup>-1</sup>). The anodic and cathodic chemical diffusion coefficients in the solid phase at room temperature were determined using the Randles-Sevcik equation to be  $2.276 \times 10^{-12}$  cm<sup>2</sup> s<sup>-1</sup> and  $0.863 \times 10^{-12}$  cm<sup>2</sup> s<sup>-1</sup>,

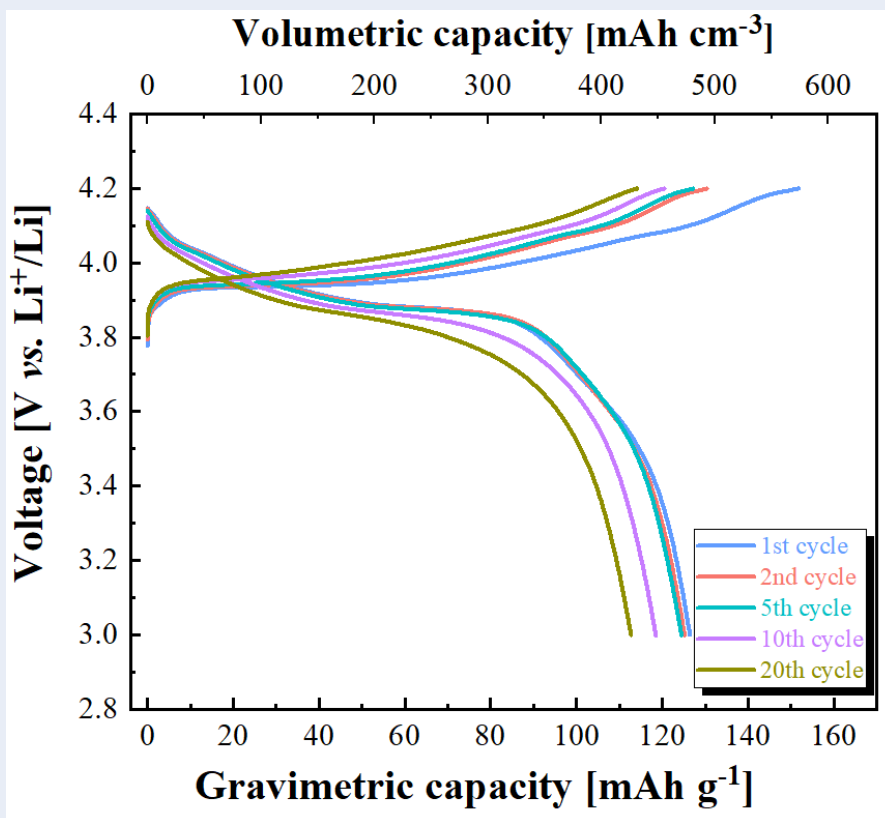
respectively, which are comparable with the reported values for thin-film  $\text{LiCoO}_2$  electrodes ( $7.7 \times 10^{-12} \text{ cm}^2 \text{ s}^{-1}$  in reference [247] and  $0.3\sim 9.9 \times 10^{-13} \text{ cm}^2 \text{ s}^{-1}$  in reference [324]). The small divergence in the anodic and cathodic chemical diffusion coefficients was indicative of the excellent reaction reversibility, which is governed by Li-ion diffusion process.



**Fig. 6-14.** (a) Sweep rate dependence of cyclic voltammogram for LCO/1%MWrGO pellet produced by CSP, (b) The relationship between the square root of the sweep rates for the LCO/1%MWrGO pellet and anodic/cathodic peak currents.

Fig. 6-15 shows the galvanostatic charge/discharge response of LCO/1%MWrGO cathode produced by CSP, along with their corresponding gravimetric/volumetric capacities at the constant current rate of 0.1 C in the potential scan range of 3.0 - 4.2 V. Due to the tiny inclusion of MWrGO, the LCO/1%MWrGO composite cathode exhibited a remarkably high density of  $4.02 \text{ g cm}^{-3}$  (corresponding to 80.6% relative density), which was even larger than that ( $3.82 \text{ g cm}^{-3}$  corresponding to 79.5% relative density) of LCO/3%CNTs composite cathode prepared in Section 4.4. Indeed, it is overwhelmingly higher than that of conventional electrodes prepared by tape-cast method ( $\sim 0.55 \text{ g cm}^{-3}$ ), showing the merits of CSP to obtain dense cathode.

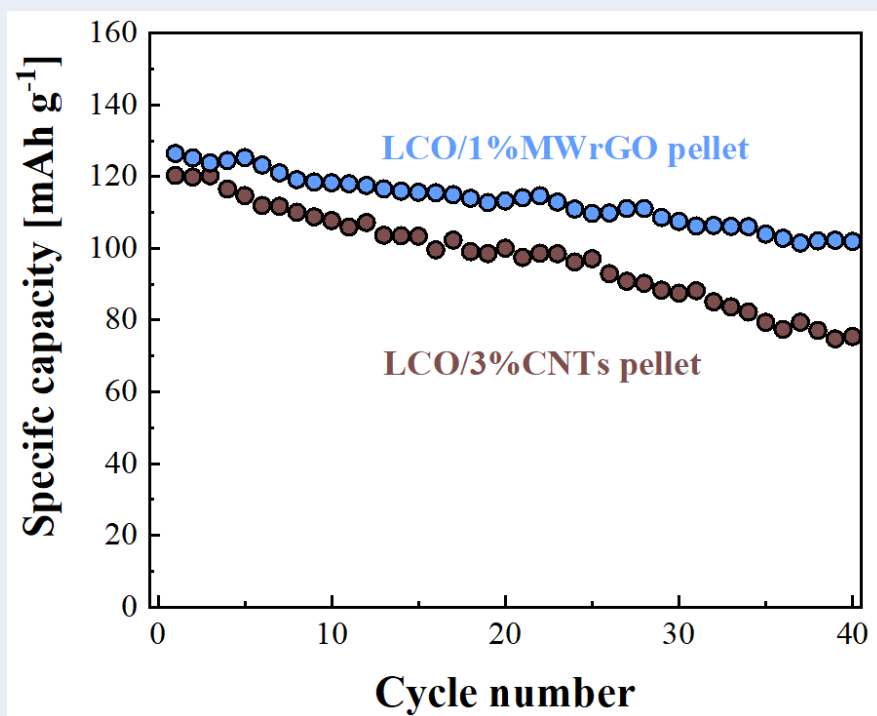
In the initial cycle, the LCO/1%MWrGO cathode delivered a gravimetric charge capacity of  $151 \text{ mAh g}^{-1}$  and a gravimetric discharge capacity of  $126 \text{ mAh g}^{-1}$ , yielding a coulombic efficiency of 83.4%. In consideration of the effective loading of LCO in the LCO/1%MWrGO cathode ( $4.02 \text{ g cm}^{-3} \times 99\%$ ), an extraordinary volumetric discharge capacity of  $\sim 501.5 \text{ mAh cm}^{-3}$  was obtained in the initial cycle which was superior to that of LCO/3%CNTs cathode ( $459 \text{ mAh cm}^{-3}$ ). Given that the discharge voltage was 3.88 V, the volumetric energy density of LCO/1%MWrGO cathode was determined to be  $1946 \text{ Wh L}^{-1}$ , which was greater than  $\sim 1764 \text{ Wh L}^{-1}$  for LCO/3%CNTs cathode. In closer inspection of Fig. 6-15, the LCO/1%MWrGO cathode exhibited definite potential plateaus at around 3.95 V and 3.88 V during galvanostatic charge and discharge process, which were ascribed to the single stage intercalation of Li ions from/into the octahedral sites [74]. Two small successive plateaus were also observed at 4.07 V and 4.18 V in the charge process. These steady potential plateaus are in good agreement with the abovementioned CV analysis.



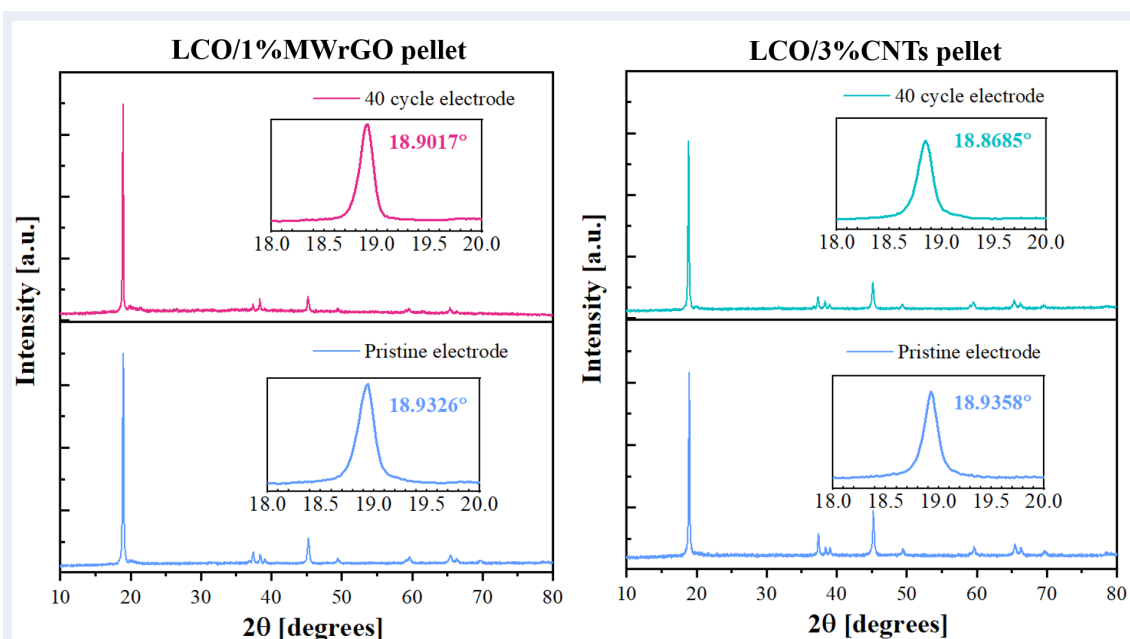
**Fig. 6-15.** The galvanostatic cycling curves of LCO/1%MWrGO pellet for 1<sup>st</sup>, 2<sup>nd</sup>, 5<sup>th</sup>, 10<sup>th</sup>, and 20<sup>th</sup> cycles at the current rate of 0.1 C.

Fig. 6-16 compares the cycling behaviour of LCO/1%MWrGO composite cathode and LCO/3%CNTs composite cathode over 40 cycles at the current rate of 0.1 C. With regard to LCO/1%MWrGO cathode, a reversible gravimetric discharge capacity of 101.9 mAh g<sup>-1</sup> can be retained after 40 cycles, corresponding to a capacity retention of 80.9%. This capacity retention was astonishingly higher than that of LCO/3%CNTs cathode (62% capacity retention) largely due to the use of porous graphene sheets in the rigid LCO matrix prepared by CSP. The presence of flexible graphene cushion was able to sufficiently buffer the repetitious volumetric change of LCO particles induced by first-order phase transition to some extent and mitigate the formation of micro-cracks in the densely packed primary particles. Generally speaking, the formation and the propagation of micro-cracks results in a loss of grain-to-grain connectivity among primary particles,

which is the main reason to cell degradation. In addition to the buffer effect, the wrapping architecture of LCO by graphene sheets can also suppress LCO particles from disintegrating from the main matrix, as confirmed in Fig. 6-5. The *ex situ* XRD results of LCO/1%MWrGO electrode and LCO/3%CNTs electrode at pristine state and after 40 cycles at full discharge state are shown in Fig. 6-17. It is easily recognised that the (003) peak of LCO/1%MWrGO cathode exhibited less shifting (from  $18.9326^\circ$  to  $18.9017^\circ$ ) than LCO/3%CNTs cathode (from  $18.9358^\circ$  to  $18.8685^\circ$ ) after 40 cycles, indicating the better structural integrity of LCO/1%MWrGO cathode during battery operation.



**Fig. 6-16.** Cyclability comparison of LCO/1%MWrGO pellet and LCO/3%CNTs pellet between 3.0 V and 4.2 V over 40 cycles at the constant rate of 0.1 C.



**Fig. 6-17.** X-ray diffractograms of (a) LCO/1%MWrGO cathode and (b) LCO/3%CNTs cathode at pristine state and after 40 cycles at full discharge state. The insets show the magnified view of (003) peak of each XRD result.

Fig. 6-18 (a) shows the discharge rate capabilities of LCO/1%MWrGO composite cathode in the current rates of 0.1 - 5 C in comparison with LCO/3%CNTs composite cathode. It is clearly found that the overall rate capability performance of LCO/1%MWrGO cathode was superior to LCO/3%CNTs cathode, especially at high current rates ( $> 1$  C). This could be attributed to the more abundant inter-planar tunnels which could enhance the absorption and retention of excess electrolyte solution for the diffusion of lithium ions across the thick solid electrode. At 0.1 C current rate, both cathodes delivered a comparable gravimetric capacity at  $\sim 120$  mAh g<sup>-1</sup>. Nevertheless, with the increasing current rates, LCO/3%CNTs cathode showed more rapid capacity loss from  $\sim 80$  mAh g<sup>-1</sup> at 0.2 C to almost 0 mAh g<sup>-1</sup> at 1 C. In contrast, the LCO/1%MWrGO cathode was still capable to deliver  $\sim 50$  mAh g<sup>-1</sup> at 1 C. At even higher current rate, the bulk-type LCO/1%MWrGO cathode can still release  $\sim 30$  mAh g<sup>-1</sup> at 2 C but it declined to merely  $\sim 10$  mAh g<sup>-1</sup> at 5 C. All the rate capabilities of the LCO/1%MWrGO cathode

and the LCO/3%CNTs cathode are clearly interpreted against C-rate in Fig. 6-18 (b), showing the advantages of MWrGO due to the excellent electrical conductivity and the high SSA. It is believed that a high SSA leads to a lower current density under the same current load and the lower current density is able to reduce the electrochemical polarisation, especially concentration polarisation, and facilitate the utilisation of electroactive materials. Provided that concentration polarisation is negligible, the distribution of current density across the bulk cathode can be described as:

$$\frac{i_{a,0} - i_{a,D}}{\alpha} - \frac{i_{c,0} - i_{c,D}}{\beta} = \frac{i_a^2 n F}{2 R T k \sigma S} \quad [\text{Equation 23}]$$

Where,  $i_{a,0}$ ,  $i_{a,D}$ ,  $i_{c,0}$  and  $i_{c,D}$  represent the oxidised current density and reduced current density at the cathode surface ( $x = 0$ ) and under the cathode surface at the depth ( $x = D$ );  $\alpha$  and  $\beta$  are the transfer coefficients;  $n$  represents the number of transfer electrons involved in the electrochemical reaction;  $F$  is the Faraday's constant,  $96485.33 \text{ C mol}^{-1}$ ;  $R$  is the gas constant;  $8.3145 \text{ J mol}^{-1} \text{ K}^{-1}$ ;  $T$  is the absolute temperature in the unit of K;  $k$  is the electrical conductivity;  $\sigma$  means the Warburg factor determined by  $Z_{re}$  and  $\omega^{-1/2}$  ( $Z_{re} \propto \sigma \omega^{-1/2}$ );  $S$  represents the SSA. It can be seen that higher electrical conductivity and SSA are beneficial to generating a more uniform distribution of current density. In this case, the electrical conductivity and SSA of MWrGO were measured to be  $761.4 \text{ S m}^{-1}$  and  $310.24 \text{ m}^2 \text{ g}^{-1}$ , respectively, which are all higher than  $528.2 \text{ S m}^{-1}$  and  $125.01 \text{ m}^2 \text{ g}^{-1}$  of CNTs, thereby leading to an improved accessibility of the cathode composite and better electrochemical dynamic performance at the same C rate.

Notably, when the current rate reversed back to 0.1 C immediately after 5 C, the discharge gravimetric capacity of LCO/1%MWrGO cathode remained much the same as the initial value whilst the discharge gravimetric capacity of LCO/3%CNTs was slightly lower than

the initial value, indicating the microstructural integrity of LCO/1%MWrGO cathode has been preserved.

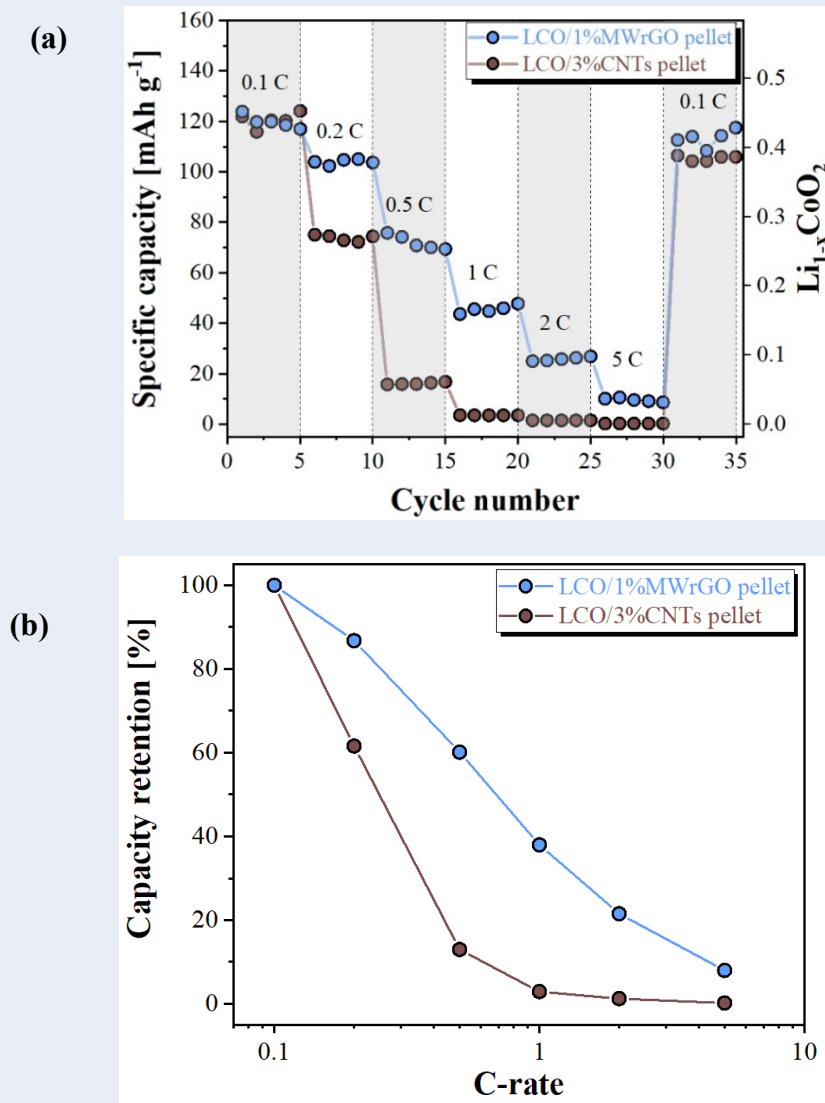


**Fig. 6-18. (a)** Rate capability comparison of LCO/1%MWrGO pellet produced by CSP and LCO/3%CNTs pellet produced by CSP. **(b)** The dependency of capacity retention on C-rate of LCO/1%MWrGO pellet and LCO/3%CNTs pellets in semi-logarithmic plots (normalised to first-cycle capacity).

Fig. 6-19 (a) shows the charge/discharge profiles of the LCO/1%MWrGO composite cathode at the rate range of 0.1 - 5 C within a cut-off window of 3.0 - 4.2 V. The potential plateaus appearing at around 3.95 V and 3.88 V during charge and discharge processes became less pronounced with increasing current rates, indicating that the first-order phase



transition was the diffusion-controlled process in the course of intercalation/deintercalation process. Close inspection of Fig. 6-19 (a) revealed that the discharge potential gradually declined with increasing current rates during discharge process, which is depicted in Fig. 6-19 (b). The phenomenon can be described by the relationship between discharge potential ( $\phi$ ), OCV ( $\phi^o$ ), polarisation potential ( $\eta$ ), and the internal resistance ( $R$ ) [209]:

$$\phi = \phi^o - (\eta + IR) \quad [\text{Equation 24}]$$

$\phi^o$  is a constant value determined by Gibbs free energy, as discussed in Equation 1;  $I$  represents the current flowing through the electrode; and the internal resistance  $R$  is determined by (i) the intrinsic LCO particle resistance, (ii) intrinsic graphene sheets resistance, as well as (iii) the contacting resistance between LCO particles and graphene sheets/electrolyte. That being the case, it can be readily understood that  $\phi$  is only affected by  $\eta$  and  $IR$ . Under constant internal resistance  $R$ , the higher  $I$  will result in the lower  $\phi$ . The large ohmic overpotentials  $IR$  could be one of the reasons leading to the reduced reversible capacities at high current rates due to the earlier voltage cut-off and thus the premature termination of intercalation/deintercalation process of Li ions into/from the host structure.

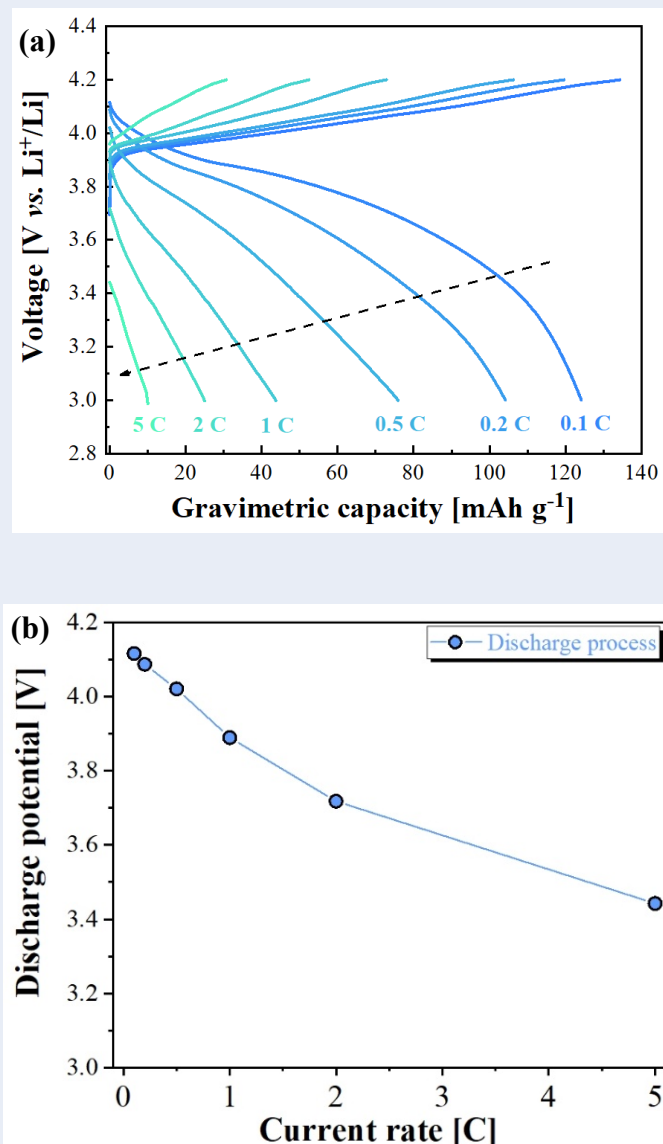


**Fig. 6-19. (a)** The electrochemical charge/discharge curves of the LCO/1%MWrGO composite cathode at varying current rates, **(b)** The plot of discharge potential versus current rates plot for the LCO/1%MWrGO cathode.

EIS measurement is the useful tool for obtaining battery dynamics information, especially the interfacial resistances between conductive fillers and active materials. It was conducted to investigate the reasons why LCO/1wt%MWrGO exhibited improved electrochemical properties and reaction kinetics over LCO/3wt%CNTs, particularly at tough charge/discharge rates. Fig. 6-20 interprets the Nyquist impedance spectrum obtained with a coin cell for LCO/1wt%MWrGO and LCO/3wt%CNTs over a frequency

range of 0.01 Hz to 10 kHz before and after the 40 cycles. All the curves comprise a single semicircle in the high-to-medium frequency regime and a quasi linear tail in the low-frequency regime. An intercept on the real axis  $Z_{\text{real}}$  at high frequency regime is associated to the electrolyte resistance. The semicircle represents the charge transfer process which is highly related to electrode conductivity and interfacial contact with organic electrolyte. The inclined straight line at low frequency regime is ascribed to Li ion diffusion in the solid phase of the electrode or so-called Warburg diffusion. The impedance spectrum were fitted with an equivalent electrical circuit composed of different components to study the underlying species transport and reaction kinetics of LCO. The simulation circuit is given in the inset and the fitted results are listed in Table 6-2.

After 40 cycles, the  $R_s$  for the LCO/3wt%CNTs exhibited greater increase (from 7.37 to 8.67  $\Omega$ ) than that for LCO/1wt%MWrGO (from 3.38 to 4.15  $\Omega$ ), which indicated the parasitic side reactions of the electrolyte happening on the LCO particles could be suppressed by the MWrGO and hence lower resistance was observed.  $R_{ct}$  is the main factor to affect the electrode kinetics during rate capability test, especially at high current rate. It is worth noting that the  $R_{ct}$  for LCO/1wt%MWrGO was much smaller than that of LCO/3wt%CNTs regardless of cycling test. The effectiveness of MWrGO in improving interfacial charge transfer kinetics manifests itself when comparing charge transfer resistances at solid particles. The small values of LCO/1wt%MWrGO can be attributed to the improved contact area of MWrGO and the electrolyte retention through the porous structure of MWrGO.

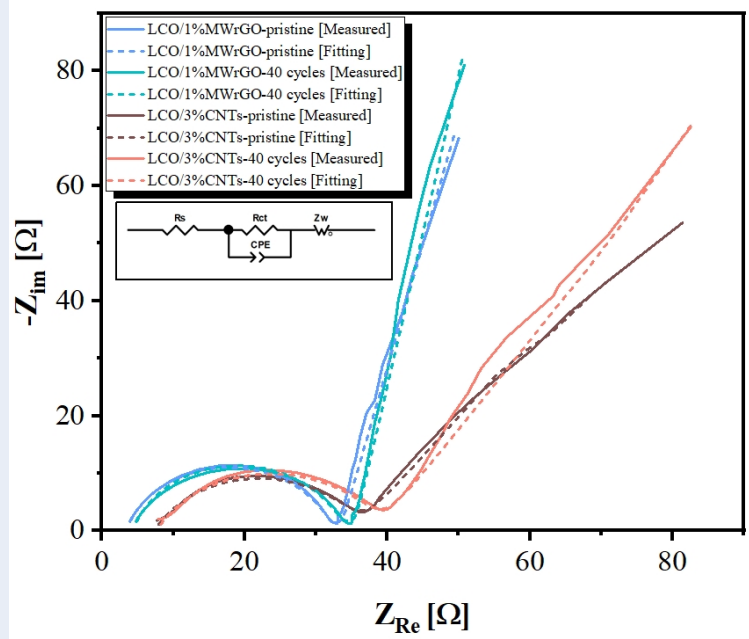


**Fig. 6-20.** Nyquist plots of LCO/1%MWrGO pellet and LCO/3%CNTs pellet before and after 40 cycles with the equivalent circuit in the inset, where  $R_s$  represents the electrolyte resistance,  $R_{ct}$  represents the charge transfer resistance, CPE stands for constant phase element for the electrode-electrolyte interface and  $Z_w$  is often referred to the Warburg impedance, which arises from the Li diffusion in LCO particles.

**Table 6-2.** Independent components of the LCO/1wt%MWrGO and LCO/3wt%CNTs electrodes deduced from the modelling of EIS data with the value uncertainty.

Sample	Pristine			After 40 cycles		
	$R_s$	$R_{ct}$	$Z_w$	$R_s$	$R_{ct}$	$Z_w$
<b>LCO-MWrGO</b>	3.38	18.27	5.45	4.15	18.84	6.47
<b>Uncertainty [%]</b>	1.8981	0.9539	19.688	1.8813	1.0952	19.292
<b>LCO-CNT</b>	7.37	28.53	19.72	8.67	31.19	34.11
<b>Uncertainty [%]</b>	1.3847	1.2744	16.247	1.6016	1.0667	19.956

To further understand the benefits induced by MWrGO, the diffusion coefficient ( $D_{Li}$ ,  $\text{cm}^2 \text{s}^{-1}$ ) of Li ions are estimated from the plots in the low-frequency region using the following equation [325, 326]:

$$D_{Li} = \frac{R^2 T^2}{2A^2 n^4 F^4 C_{Li}^2 \sigma^2} \quad [\text{Equation 25}]$$

Where,  $R$  is the gas constant ( $8.3145 \text{ J mol}^{-1} \text{ K}^{-1}$ ),  $T$  is the absolute temperature ( $298.15 \text{ K}$ ),  $A$  is the surface area of the electrode (unit:  $\text{cm}^2$ ),  $n$  is the charge transfer number ( $n=1$  for  $\text{LiCoO}_2$ ),  $F$  is the Faraday's constant ( $96485.33 \text{ C mol}^{-1}$ ),  $C_{\text{Li}}$  is the Li-ion concentration (unit:  $\text{mol cm}^{-3}$ ) and  $\sigma$  is the Warburg factor which can be determined using the following equation:

$$Z_{Re} = R_e + R_{ct} + \sigma \omega^{-1/2} \quad [\text{Equation 26}]$$

Where,  $R_s$  represents the electrolyte resistance;  $R_{ct}$  represents the charge transfer resistance and  $\omega$  is the angular frequency. Fig. 6-21 interprets the linear relationship between  $Z_{re}$  and  $\omega^{-1/2}$  in the low-frequency regime, from which  $\sigma$  can be calculated. The  $D_{\text{Li}}$  for LCO/1wt%MWrGO and LCO/3wt%CNTs pellets produced by CSP can be determined to be  $9.18 \times 10^{-13} \text{ cm}^2 \text{ s}^{-1}$  and  $1.71 \times 10^{-13} \text{ cm}^2 \text{ s}^{-1}$ , respectively, with the former 4 time than the latter. Thus, it can be seen that the MWrGO coating on the LCO particle surfaces can be helpful to improve the electrochemical kinetics.

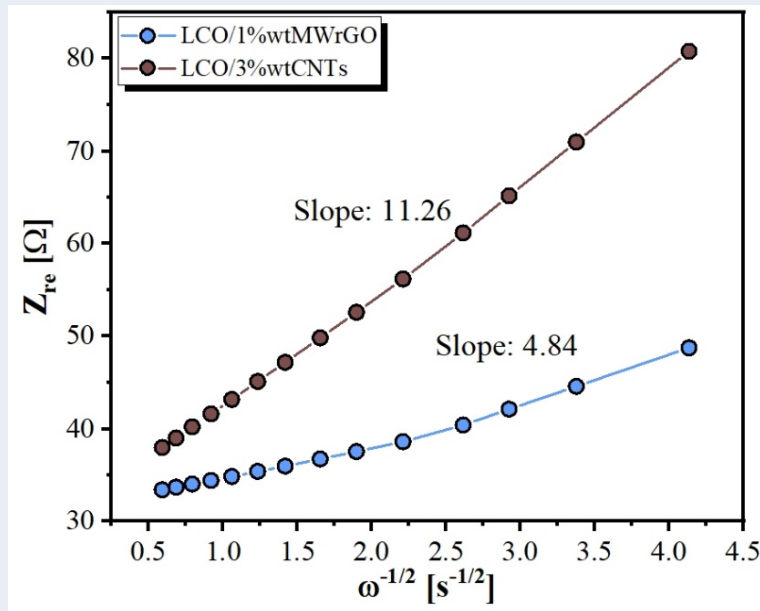


**Fig. 6-21.** The plots of  $Z_{re}$  and the reciprocal square root of frequency for LCO/1wt%MWrGO and LCO/3wt%CNTs pellets produced by CSP.

Based on the above analysis, despite that MWrGO and CNTs are the allotropes of carbon in different dimensions and are constructed by the same basic carbon blocks: hexagonal carbon lattice, they result in different enhancement to the performance of LIBs. The differences can be elucidated in the perspectives of their intrinsic physical properties, such as electrical conductivity and morphology, and their interaction/architecture with the surrounding LCO particles. With the demonstration in Fig. 6-22, the key differences in the following aspects can be highlighted:

(i) Morphology: MWrGO and CNTs are geometrically built by hexagonal carbon unit in 2D and 1D, respectively. The establishment of an interconnected carbon network by 1D nanotubes and 2D nanosheets is of critical importance to sustain abundant electron pathways in electrode. However, the direct contact between LCO particles and the surfaces of conductive fillers results in the different contact modes. The 2D planar characteristics of MWrGO generally provides a “plane-to-point” contact mode which is able to guarantee rapid electrode conduction as compared to the “line-to-point” contact mode achieved in CNTs network. This effective interfacial contact between LCO particles and graphitic sheets not only improves the utilisation of LCO active materials, but also facilitates the less use of conductive filler, even at ultrahigh LCO content (99%) in LCO/1wt%MWrGO pellet. Moreover, in the wrapping/encapsulation architecture, the layered graphitic nanosheets can serve as an effective protective “blanket” to reduce the undesired side reactions between LCO and organic electrolyte, as confirmed in the above EIS results.

(ii) Surface chemistry: due to the processing nature, MWrGO is likely to have more oxygen functional groups, as discussed in Chapter 5, on the surface compared to CNTs which is dominantly produced via CVD and has less oxygen functional groups. The

presence of oxygen functional groups endows MWrGO with a hydrophilic surface that promises strong polar-polar binding with organic electrolyte, thereby reducing the charge transfer resistance.

(iii) Physical properties: MWrGO has higher specific surface area than CNTs and exhibits abundant porous structure. The two physical attributes as well as ripple flake edges together help to facilitate the penetration of organic electrolyte, resulting in enhanced Li ion movement during cell cycling. In addition, MWrGO shows a promising electrical conduction in two dimensions whilst CNTs only show electrical conduction in uniaxial direction, which may lead to anisotropic polarisation in CNTs-reinforced electrode.

(iv) Void space: one of the major benefits induced by 3D interconnected porous structure formed by MWrGO is to introduce internal void space between LCO particles and MWrGO nanosheets, as schematically shown in Fig. 6-22 (b). The ample internal void space is of critical significance to relieve/alleviate repetitious volume expansion/contraction upon lithiation and delithiation to a large extent, thereby improving the structural integrity of dense and thick electrodes. Consequently, MWrGO retained a high volumetric energy density of  $405.5 \text{ mAh cm}^{-3}$  after 40 cycles, which was  $\sim 1.5$  times higher than that of LCO/3wt%CNTs ( $278 \text{ mAh cm}^{-3}$ ).

The abovementioned aspects are equally essential for improving the electronic/ionic conductivities of electrode, electrochemical utilisation of active materials, electrochemical reversibility, and packing density of high-performance electrode for LIBs.

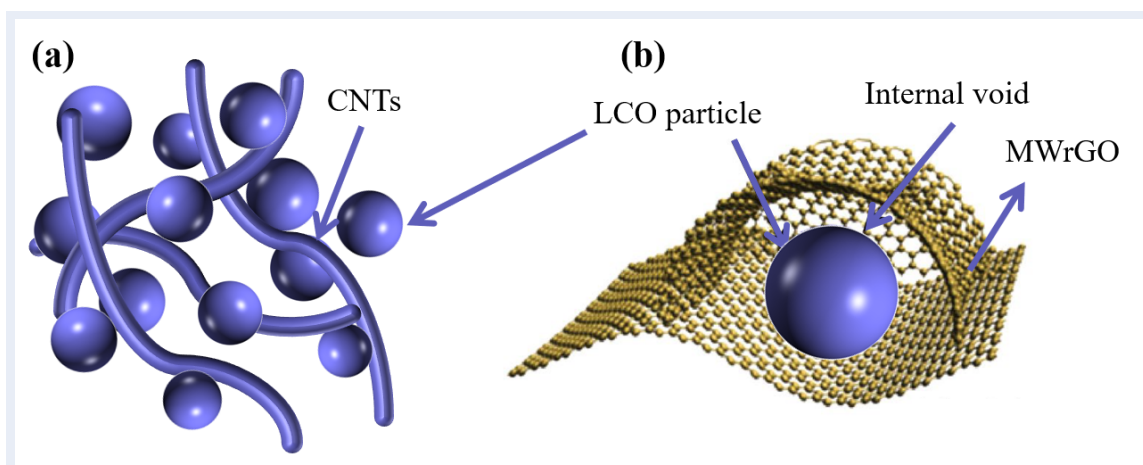


**Fig. 6-22.** The schematic representation of the architecture of LCO particles and **(a)** CNTs and **(b)** MWrGO.



## 6.5. Chapter conclusions

This chapter presents the successful fabrication of high-volumetric-capacity LCO composite cathode with MWrGO as conductive filler. The LCO/1%MWrGO cathode was produced at the CSP condition of 250 °C, 250 MPa and 1-hour duration time with 20 wt% 2 M LiOH solution. The LCO/1%MWrGO cathode was electrochemically characterised in half cell configuration and was compared with the LCO/3%CNTs counterpart.

- 1 wt% MWrGO inclusion in LCO composite cathodes ( $2.81 \text{ S cm}^{-1}$ ) was capable to provide a comparable electrical conductivity to 3 wt% CNTs inclusion in LCO composite cathodes ( $2.84 \text{ S cm}^{-1}$ ). The lower MWrGO inclusion in LCO/*x*MWrGO composite cathodes increased the material of LCO loading to as high as 99 wt% in a composite cathode. Meanwhile, the MWrGO established an effective 3D electrically conductive network due to (i) the large surface area and the porous structure; and (ii) the unique graphene-wrapping-particle architecture. As such, the electrochemical properties of LCO composite cathodes were improved with even lower content of conductive filler.
- The unique graphene-wrapping-particle architecture in electrodes not only preserves the original nanoscale characteristics of each constituent, but also provides synergism between different primary structures, thereby giving rise to better electrochemical properties under practical electrode conditions.
- The LCO/1%MWrGO composite cathode delivered a gravimetric discharge capacity of  $126 \text{ mAh g}^{-1}$  in the initial cycle, corresponding to an extraordinary volumetric discharge capacity of  $\sim 501.5 \text{ mAh cm}^{-3}$  and volumetric energy density of  $1946 \text{ Wh L}^{-1}$ . Moreover, the rate capability performance of LCO/1%MWrGO cathode was

superior to LCO/3%CNTs cathode, especially at high current rates ( $> 1\text{ C}$ ). The LCO/1%MWrGO composite electrode concurrently showed high volumetric energy density and promising rate performance at large mass loadings, which represented a critical step toward the practical application of high-energy-density LIBs.

- This study demonstrated a versatile approach to fabricate bulk-type electrode towards next-generation energy storage devices, including supercapacitor but not limiting to LIBs, on which the high volumetric capacity/energy is the primary concern.

## Chapter 7. Thesis conclusions

This thesis described the research works of the novel CSP technology for the fabrication of binder-free LCO cathodes with high volumetric energy density and enhanced electrochemical figures of merit, which enables a highly attractive application in miniature electronic devices, electric/hybrid vehicles, and grid-scale energy storage system. Due to the low-temperature nature of CSP ( $< 300\text{ }^{\circ}\text{C}$ ), the simultaneous sintering and integration of LCO and conductive fillers is achievable within short time, which has not been reported before. The conductive fillers used in this project were commercially available CNTs and MWrGO, the latter of which was synthesised via microwave-assisted reduction method. Several notable remarks on the project are listed as below:

1. Influences from CSP process variables such as uniaxial pressure, process temperature and process duration time have been studied for monolithic LCO pellets and have found that they all have nearly equivalent effects on the consolidation of LCO. With a systematic investigation, the CSP processing condition of  $250\text{ }^{\circ}\text{C}$ ,  $250\text{ MPa}$  and 1-hour duration time was selected as the standard CSP processing parameters to co-sinter LCO/carbon composite.
2. The one-step synthesis of LCO/carbon composite cathodes has been reported for the first time and also the electrical conductivities of LCO/carbon composite cathodes is able to be manipulated by varying the carbon content and carbon type. It is found in this project that the percolation thresholds of conductive fillers in CSP-ed LCO pellets were 3 wt% for CNTs and 1 wt% for MWrGO. The discrepancy in building continuous electrically conductive network in bulk LCO cathodes with CNTs and MWrGO was attributed to the nanoporous structure, planar character, and high

electrical conductivity of MWrGO. The successful fabrication of LCO/carbon composite demonstrates that CSP is a new approach to prepare composite cathode which compromised ingredients with large chemical/physical differences.

3. The major advantages of less addition of highly conductive MWrGO and the complete removal of the binder/current collector in LCO matrix translate into a  $\sim 10\%$  increase in volumetric energy density as compared to the use of CNT. That is,  $\sim 501.5 \text{ mAh cm}^{-3}$  for LCO/1%MWrGO and  $\sim 459 \text{ mAh cm}^{-3}$  for LCO/3%CNTs. These values are amongst previously reported highest volumetric energy densities for bulk LCO cathode.
4. The quality of MWrGO, mainly in terms of remaining oxygen functional groups, structural defects, surface area and electrical conductivity, can be manipulated through controlling the microwave powers and the inert gas atmosphere, which have not been reported before. Despite that the microwave power of 800 W and argon flushing time of 10 min were demonstrated to be the optimal MWrGO processing condition for the application of LIBs in this project, the microstructure and chemistry of MWrGO can be tuned for other application based on the realistic needs.
5. The microwave coupling effect of GO was shown to be highly dependent on the long-range  $\pi$ - $\pi$  conjugated networks because free  $\pi$  electrons are required to move in a long distance to generate sufficient Joule heating. Compared with the addition of secondary microwave susceptor which is believed only to locally reduce the surrounding GO, the strategy of restoring the GO conjugated network by annealing at  $250^\circ\text{C}$  is beneficial to boosting the microwave absorption, thereby leading to a uniform reduction of GO.

6. The contribution of D' peak to the apparent G peak likely give misinterpretation data of  $I_D/I_G$  and give misleading conclusions in the perspective of structural disorders in graphene. Therefore, by deducting the intensity contribution of D' peak from the apparent G peak, a more reliable  $I_D/I_{G-in}$  ratio was proposed in this project to characterise the structural evolutions of graphene. This modified  $I_D/I_{G-in}$  ratio could be applicable to other graphene-based materials prepared using other methods, such as thermal/chemical reduction, liquid/gas exfoliation or CVD approaches.

## Chapter 8. Future work

- Despite that the capacity retention was improved for LCO/1%MWrGO cathodes by using porous and conductive graphene, the gravimetric discharge capacity was still diminished from 126 mAh g<sup>-1</sup> to 101.9 mAh g<sup>-1</sup> after 40 cycles, corresponding to a capacity retention of 80.9%. The cycle to cycle capacity fading could be attributed to the small LCO particles which exhibited large surface areas. Although the small particle size can enhance the dissolution process of LCO species during CSP and conduce to the diffusion rate of Li ions, the large surface areas react strongly with electrolyte liquid, leading to the serious decomposition [281]. Henceforth, the perspective for future research endeavour could be focussed on cold sintering process of LCO particles with slightly larger particle size without the sacrifice in relative density of bulk LCO pellets.
- The concept of CSP on densification of LCO has been verified in this project for the first time, which enlarges the spectrum of cold-sintered ceramics for LIBs application. To date, bulk cathodes, such as LCO, LiFePO<sub>4</sub> [17, 18] and V<sub>2</sub>O<sub>5</sub> composite [106], and solid-state electrolyte, such as Na<sub>3.256</sub>Mg<sub>0.128</sub>Zr<sub>1.872</sub>Si<sub>2</sub>PO<sub>12</sub> solid electrolyte [102] and Li<sub>1.5</sub>Al<sub>0.5</sub>Ge<sub>1.5</sub>(PO<sub>4</sub>)<sub>3</sub> [105], have been reported using CSP technology. However, no report has been found for bulk anode. It is therefore worth pushing the boundaries of the CSP technology for fabricating full solid-state LIBs prototype which is demanded for its high safety. With further exploitation and multidisciplinary, there is no doubt that the development of CSP will bring about many advances in sintering technology and act to assist in the development of high safety energy storage devices.
- Whilst the electrochemical evaluation of LCO cathodes to date has predominantly

relied on half-cell configuration, the studies using full-cell configuration are rather limited. Some perceived problems which are not identified in half cells may become obstacles in full cells and thus deteriorate the overall electrochemical performance. The full cell containing bulk LCO composite cathodes can be constructed with commercial graphite powder or the high-capacity MWrGO powder synthesised in Chapter 5.

- The preparation of chemically doped graphene is normally achieved using high temperature CVD or heat treated at relative high temperature. However, this incorporation of dopants into the carbon framework of graphene sheets is generally not efficient and it may take up to several hours [327] and require high temperature [328]. Microwave-assisted heating is an efficient and homogenous heating method which can increase the reaction temperature within seconds. It would be interesting to make use of this unique heating strategy to produce chemically doped graphene with manipulating properties.

## References

- [1] G. Girishkumar, B. McCloskey, A. C. Luntz, S. Swanson, and W. Wilcke, "Lithium–air battery: promise and challenges", *The Journal of Physical Chemistry Letters*, Vol. 1, No. 14, pp. 2193-2203, **2010**.
- [2] WMO, "WMO Greenhouse Gas Bulletin (GHG Bulletin) - No. 15: The State of Greenhouse Gases in the Atmosphere Based on Global Observations through 2018," (Accessed November, 2019).
- [3] C. Mi, and M. A. Masrur, *Hybrid electric vehicles: principles and applications with practical perspectives*: John Wiley & Sons, **2017**.
- [4] Y. Liang, C. Z. Zhao, H. Yuan, Y. Chen, W. Zhang, J. Q. Huang, D. Yu, Y. Liu, M. M. Titirici, and Y. L. Chueh, "A review of rechargeable batteries for portable electronic devices", *InfoMat*, Vol. 1, No. 1, pp. 6-32, **2019**.
- [5] Z. P. Cano, D. Banham, S. Ye, A. Hintennach, J. Lu, M. Fowler, and Z. Chen, "Batteries and fuel cells for emerging electric vehicle markets", *Nature Energy*, Vol. 3, No. 4, pp. 279-289, **2018**.
- [6] T. S. Schmidt, M. Beuse, X. Zhang, B. Steffen, S. F. Schneider, A. Pena-Bello, C. Bauer, and D. Parra, "Additional emissions and cost from storing electricity in stationary battery systems", *Environmental Science & Technology*, Vol. 53, No. 7, pp. 3379-3390, **2019**.
- [7] J. W. Choi, and D. Aurbach, "Promise and reality of post-lithium-ion batteries with high energy densities", *Nature Reviews Materials*, Vol. 1, No. 4, pp. 16013, **2016**.
- [8] P. Russo, C. Di Barib, M. Mazzaroc, A. De Rosac, and I. Morriellod, "Effective fire extinguishing systems for lithium-ion battery", *Chemical Engineering Transactions*, Vol. 67, pp. 727-732, **2018**.
- [9] Y. Nishi, "The development of lithium ion secondary batteries", *The Chemical Record*, Vol. 1, No. 5, pp. 406-413, **2001**.
- [10] K. Ozawa, "Lithium-ion rechargeable batteries with LiCoO<sub>2</sub> and carbon electrodes: the LiCoO<sub>2</sub>/C system", *Solid State Ionics*, Vol. 69, No. 3, pp. 212-221, **1994**.
- [11] W. Lai, C. K. Erdonmez, T. F. Marinis, C. K. Bjune, N. J. Dudney, F. Xu, R. Wartena, and Y. M. Chiang, "Ultrahigh-energy-density microbatteries enabled by new electrode architecture and micropackaging design", *Advanced Materials*, Vol. 22, No. 20, pp. E139-E144, **2010**.
- [12] C. L. Cobb, and C. J. Bae, "Tortuosity of binder-free and carbon-free high energy density LiCoO<sub>2</sub> electrodes for rechargeable lithium-ion batteries", *ECS Transactions*, Vol. 58, No. 13, pp. 13-24, **2014**.



- [13] H. Yamada, T. S. Suzuki, T. Uchikoshi, M. Hozumi, T. Saito, and Y. Sakka, “Ideal design of textured LiCoO<sub>2</sub> sintered electrode for Li-ion secondary battery”, *APL Materials*, Vol. 1, No. 4, pp. 042110, **2013**.
- [14] J. P. Maria, X. Kang, R. D. Floyd, E. C. Dickey, H. Guo, J. Guo, A. Baker, S. Funihashi, and C. A. Randall, “Cold sintering: current status and prospects”, *Journal of Materials Research*, Vol. 32, No. 17, pp. 3205-3218, **2017**.
- [15] N. Yamasaki, K. Yanagisawa, M. Nishioka, and S. Kanahara, “A hydrothermal hot-pressing method: apparatus and application”, *Journal of Materials Science Letters*, Vol. 5, No. 3, pp. 355-356, **1986**.
- [16] H. Guo, J. Guo, A. Baker, and C. A. Randall, “Hydrothermal-assisted cold sintering process: a new guidance for low-temperature ceramic sintering”, *ACS Applied Materials & Interfaces*, Vol. 8, No. 32, pp. 20909-20915, **2016**.
- [17] J. H. Seo, K. Verlinde, J. Guo, D. S. B. Heidary, R. Rajagopalan, T. E. Mallouk, and C. A. Randall, “Cold sintering approach to fabrication of high rate performance binderless LiFePO<sub>4</sub> cathode with high volumetric capacity”, *Scripta Materialia*, Vol. 146, pp. 267-271, **2018**.
- [18] J. H. Seo, J. Guo, H. Guo, K. Verlinde, D. S. B. Heidary, R. Rajagopalan, and C. A. Randall, “Cold sintering of a Li-ion cathode: LiFePO<sub>4</sub>-composite with high volumetric capacity”, *Ceramics International*, Vol. 43, No. 17, pp. 15370-15374, **2017**.
- [19] K. R. Bullock, “Lead/acid batteries”, *Journal of Power Sources*, Vol. 51, No. 1-2, pp. 1-17, **1994**.
- [20] F. Feng, M. Geng, and D. Northwood, “Electrochemical behaviour of intermetallic-based metal hydrides used in Ni/metal hydride (MH) batteries: a review”, *International Journal of Hydrogen Energy*, Vol. 26, No. 7, pp. 725-734, **2001**.
- [21] T. Placke, R. Klopsch, S. Dühnen, and M. Winter, “Lithium ion, lithium metal, and alternative rechargeable battery technologies: the odyssey for high energy density”, *Journal of Solid State Electrochemistry*, Vol. 21, No. 7, pp. 1939-1964, **2017**.
- [22] T. Sasaki, Y. Ukyo, and P. Novák, “Memory effect in a lithium-ion battery”, *Nature Materials*, Vol. 12, No. 6, pp. 569, **2013**.
- [23] C. S. Rustomji, Y. Yang, T. K. Kim, J. Mac, Y. J. Kim, E. Caldwell, H. Chung, and Y. S. Meng, “Liquefied gas electrolytes for electrochemical energy storage devices”, *Science*, Vol. 356, No. 6345, pp. eaal4263, **2017**.
- [24] A. Manthiram, and J. Kim, “Low temperature synthesis of insertion oxides for lithium batteries”, *Chemistry of Materials*, Vol. 10, No. 10, pp. 2895-2909, **1998**.

- [25] D. Andre, S.-J. Kim, P. Lamp, S. F. Lux, F. Maglia, O. Paschos, and B. Stiaszny, "Future generations of cathode materials: an automotive industry perspective", *Journal of Materials Chemistry A*, Vol. 3, No. 13, pp. 6709-6732, **2015**.
- [26] B. J. Landi, M. J. Ganter, C. D. Cress, R. A. DiLeo, and R. P. Raffaele, "Carbon nanotubes for lithium ion batteries", *Energy & Environmental Science*, Vol. 2, No. 6, pp. 638, **2009**.
- [27] J. M. Tarascon, and M. Armand, "Issues and challenges facing rechargeable lithium batteries", *Materials for Sustainable Energy: A Collection of Peer-Reviewed Research and Review Articles from Nature Publishing Group*, pp. 171-179: World Scientific, **2011**.
- [28] S. J. Dillon, and K. Sun, "Microstructural design considerations for Li-ion battery systems", *Current Opinion in Solid State and Materials Science*, Vol. 16, No. 4, pp. 153-162, **2012**.
- [29] B. Ji, F. Zhang, M. Sheng, X. Tong, and Y. Tang, "A novel and generalized lithium-ion-battery configuration utilizing Al foil as both anode and current collector for enhanced energy density", *Advanced Materials*, Vol. 29, No. 7, pp. 1604219, **2017**.
- [30] M. Winter, and R. J. Brodd, "What are batteries, fuel cells, and supercapacitors?," ACS Publications, **2004**.
- [31] T. B. Reddy, and D. Linden, "Handbook of batteries", *David Linden*, Vol. 3, pp., **2001**.
- [32] B. Vijayaraghavan, D. R. Ely, Y.-M. Chiang, R. García-García, and R. E. García, "An analytical method to determine tortuosity in rechargeable battery electrodes", *Journal of the Electrochemical Society*, Vol. 159, No. 5, pp. A548, **2012**.
- [33] E. J. Cairns, and P. Albertus, "Batteries for electric and hybrid-electric vehicles", *Annual Review of Chemical and Biomolecular Engineering*, Vol. 1, pp. 299-320, **2010**.
- [34] F. Su, Y. He, B. Li, X. Chen, C. You, W. Wei, W. Lv, Q. Yang, and F. Kang, "Could graphene construct an effective conducting network in a high-power lithium ion battery?", *Nano Energy*, Vol. 1, No. 3, pp. 429-439, **2012**.
- [35] K. Xu, "Nonaqueous liquid electrolytes for lithium-based rechargeable batteries", *Chemical Reviews*, Vol. 104, No. 10, pp. 4303-4418, **2004**.
- [36] R. Kannan, D. Rajan, P. K. Terala, P. L. Moss, and M. H. Weatherspoon, "Analysis of the separator thickness and porosity on the performance of lithium-ion batteries", *International Journal of Electrochemistry*, Vol. 2018, pp., **2018**.
- [37] A. H. Whitehead, and M. Schreiber, "Current collectors for positive electrodes of lithium-based batteries", *Journal of the Electrochemical Society*, Vol. 152, No. 11, pp. A2105-A2113, **2005**.

- [38] C. X. Zu, and H. Li, “Thermodynamic analysis on energy densities of batteries”, *Energy & Environmental Science*, Vol. 4, No. 8, pp. 2614-2624, **2011**.
- [39] C. Julien, A. Mauger, K. Zaghib, and H. Groult, “Optimization of layered cathode materials for lithium-ion batteries”, *Materials*, Vol. 9, No. 7, pp. 595, **2016**.
- [40] C. Jiang, Z. Tang, S. Wang, and Z. Zhang, “A truncated octahedral spinel  $\text{LiMn}_2\text{O}_4$  as high-performance cathode material for ultrafast and long-life lithium-ion batteries”, *Journal of Power Sources*, Vol. 357, pp. 144-148, **2017**.
- [41] L. H. Hu, F. Y. Wu, C. T. Lin, A. N. Khlobystov, and L. J. Li, “Graphene-modified  $\text{LiFePO}_4$  cathode for lithium ion battery beyond theoretical capacity”, *Nature Communications*, Vol. 4, pp. 1687, **2013**.
- [42] A. Manthiram, “An outlook on lithium ion battery technology”, *ACS Central Science*, Vol. 3, No. 10, pp. 1063-1069, **2017**.
- [43] W. Zhang, “A review of the electrochemical performance of alloy anodes for lithium-ion batteries”, *Journal of Power Sources*, Vol. 196, No. 1, pp. 13-24, **2011**.
- [44] X. B. Cheng, and Q. Zhang, “Dendrite-free lithium metal anodes: stable solid electrolyte interphases for high-efficiency batteries”, *Journal of Materials Chemistry A*, Vol. 3, No. 14, pp. 7207-7209, **2015**.
- [45] H. Li, Z. Wang, L. Chen, and X. Huang, “Research on advanced materials for Li-ion batteries”, *Advanced Materials*, Vol. 21, No. 45, pp. 4593-4607, **2009**.
- [46] S. Natarajan, and V. Aravindan, “[Essay] An urgent call to spent LIB recycling: whys and wherefores for graphite recovery”, *Advanced Energy Materials*, pp. 2002238, **2020**.
- [47] P. Verma, P. Maire, and P. Novák, “A review of the features and analyses of the solid electrolyte interphase in Li-ion batteries”, *Electrochimica Acta*, Vol. 55, No. 22, pp. 6332-6341, **2010**.
- [48] X. B. Cheng, R. Zhang, C. Z. Zhao, F. Wei, J. G. Zhang, and Q. Zhang, “A review of solid electrolyte interphases on lithium metal anode”, *Advanced Science*, Vol. 3, No. 3, pp. 1500213, **2016**.
- [49] M. Winter, B. Barnett, and K. Xu, “Before Li ion batteries”, *Chemical Reviews*, Vol. 118, No. 23, pp. 11433-11456, **2018**.
- [50] R. Fong, U. Von Sacken, and J. R. Dahn, “Studies of lithium intercalation into carbons using nonaqueous electrochemical cells”, *Journal of the Electrochemical Society*, Vol. 137, No. 7, pp. 2009, **1990**.
- [51] S. Zhang, K. Xu, and T. Jow, “EIS study on the formation of solid electrolyte interface in Li-ion battery”, *Electrochimica Acta*, Vol. 51, No. 8-9, pp. 1636-1640, **2006**.

- [52] S. Zhang, M. S. Ding, K. Xu, J. Allen, and T. R. Jow, "Understanding solid electrolyte interface film formation on graphite electrodes", *Electrochemical and Solid-State Letters*, Vol. 4, No. 12, pp. A206-A208, **2001**.
- [53] K. Tatsumi, T. Kawamura, S. Higuchi, T. Hosotubo, H. Nakajima, and Y. Sawada, "Anode characteristics of non-graphitizable carbon fibers for rechargeable lithium-ion batteries", *Journal of Power Sources*, Vol. 68, No. 2, pp. 263-266, **1997**.
- [54] B. Gao, A. Kleinhammes, X. Tang, C. Bower, L. Fleming, Y. Wu, and O. Zhou, "Electrochemical intercalation of single-walled carbon nanotubes with lithium", *Chemical Physics Letters*, Vol. 307, No. 3-4, pp. 153-157, **1999**.
- [55] G. Wang, X. Shen, J. Yao, and J. Park, "Graphene nanosheets for enhanced lithium storage in lithium ion batteries", *Carbon*, Vol. 47, No. 8, pp. 2049-2053, **2009**.
- [56] D. Pan, S. Wang, B. Zhao, M. Wu, H. Zhang, Y. Wang, and Z. Jiao, "Li storage properties of disordered graphene nanosheets", *Chemistry of Materials*, Vol. 21, No. 14, pp. 3136-3142, **2009**.
- [57] B. Writer, "Anode materials, SEI, carbon, graphite, conductivity, graphene, reversible, formation", *Lithium-Ion Batteries*, pp. 1-71: Springer, **2019**.
- [58] X. Cai, L. Lai, Z. Shen, and J. Lin, "Graphene and graphene-based composites as Li-ion battery electrode materials and their application in full cells", *Journal of Materials Chemistry A*, Vol. 5, No. 30, pp. 15423-15446, **2017**.
- [59] Q. Li, J. Chen, L. Fan, X. Kong, and Y. Lu, "Progress in electrolytes for rechargeable Li-based batteries and beyond", *Green Energy & Environment*, Vol. 1, No. 1, pp. 18-42, **2016**.
- [60] E. Logan, E. M. Tonita, K. Gering, J. Li, X. Ma, L. Beaulieu, and J. Dahn, "A study of the physical properties of Li-ion battery electrolytes containing esters", *Journal of the Electrochemical Society*, Vol. 165, No. 2, pp. A21-A30, **2018**.
- [61] J. Xie, and Y. Lu, "A retrospective on lithium-ion batteries", *Nature Communications*, Vol. 11, No. 1, pp. 2499, **2020**.
- [62] T. R. Jow, K. Xu, O. Borodin, and M. Ue, *Electrolytes for lithium and lithium-ion batteries*: Springer, **2014**.
- [63] J. B. Goodenough, and Y. Kim, "Challenges for rechargeable Li batteries", *Chemistry of Materials*, Vol. 22, No. 3, pp. 587-603, **2010**.
- [64] K. Mizushima, P. Jones, P. Wiseman, and J. B. Goodenough, " $\text{Li}_x\text{CoO}_2$  ( $0 < x < 1$ ): a new cathode material for batteries of high energy density", *Materials Research Bulletin*, Vol. 15, No. 6, pp. 783-789, **1980**.
- [65] C. Julien, A. Mauger, K. Zaghib, and H. Groult, "Comparative issues of cathode materials for Li-ion batteries", *Inorganics*, Vol. 2, No. 1, pp. 132-154, **2014**.

- [66] F. Xiong, H. Yan, Y. Chen, B. Xu, J. Le, and C. Ouyang, "The atomic and electronic structure changes upon delithiation of  $\text{LiCoO}_2$ : from first principles calculations", *International Journal of Electrochemical Society*, Vol. 7, No. 10, pp., **2012**.
- [67] G. Amatucci, J. Tarascon, and L. Klein, " $\text{CoO}_2$ , the end member of the  $\text{Li}_x\text{CoO}_2$  solid solution", *Journal of the Electrochemical Society*, Vol. 143, No. 3, pp. 1114-1123, **1996**.
- [68] C. Daniel, D. Mohanty, J. Li, and D. L. Wood, "Cathode materials review", *AIP Conference Proceedings*, Vol. 1597, No. 1, pp. 26-43, **2014**.
- [69] E. Antolini, " $\text{LiCoO}_2$ : formation, structure, lithium and oxygen nonstoichiometry, electrochemical behaviour and transport properties", *Solid State Ionics*, Vol. 170, No. 3-4, pp. 159-171, **2004**.
- [70] K. Tan, M. Reddy, G. S. Rao, and B. Chowdari, "High-performance  $\text{LiCoO}_2$  by molten salt ( $\text{LiNO}_3\text{:LiCl}$ ) synthesis for Li-ion batteries", *Journal of Power Sources*, Vol. 147, No. 1-2, pp. 241-248, **2005**.
- [71] J. N. Reimers, and J. Dahn, "Electrochemical and *in situ* X-ray diffraction studies of lithium intercalation in  $\text{Li}_x\text{CoO}_2$ ", *Journal of the Electrochemical Society*, Vol. 139, No. 8, pp. 2091-2097, **1992**.
- [72] T. Ohzuku, and A. Ueda, "Solid-state redox reactions of  $\text{LiCoO}_2$  (R3m) for 4 volt secondary lithium cells", *Journal of the Electrochemical Society*, Vol. 141, No. 11, pp. 2972-2977, **1994**.
- [73] M. Nishizawa, and S. Yamamura, "Irreversible conductivity change of  $\text{Li}_{1-x}\text{CoO}_2$  on electrochemical lithium insertion/extraction, desirable for battery applications", *Chemical Communications*, No. 16, pp. 1631-1632, **1998**.
- [74] Q. Liu, X. Su, D. Lei, Y. Qin, J. Wen, F. Guo, Y. A. Wu, Y. Rong, R. Kou, and X. Xiao, "Approaching the capacity limit of lithium cobalt oxide in lithium ion batteries via lanthanum and aluminium doping", *Nature Energy*, Vol. 3, No. 11, pp. 936, **2018**.
- [75] M. Ménétrier, I. Saadoune, S. Levasseur, and C. Delmas, "The insulator-metal transition upon lithium deintercalation from  $\text{LiCoO}_2$ : electronic properties and  $^7\text{Li}$  NMR study", *Journal of Materials Chemistry*, Vol. 9, No. 5, pp. 1135-1140, **1999**.
- [76] S. Goriparti, E. Miele, F. De Angelis, E. Di Fabrizio, R. Proietti Zaccaria, and C. Capiglia, "Review on recent progress of nanostructured anode materials for Li-ion batteries", *Journal of Power Sources*, Vol. 257, pp. 421-443, **2014**.
- [77] G. T. K. Fey, C. Z. Lu, J. D. Huang, T. P. Kumar, and Y. C. Chang, "Nanoparticulate coatings for enhanced cyclability of  $\text{LiCoO}_2$  cathodes", *Journal of Power Sources*, Vol. 146, No. 1, pp. 65-70, **2005**.
- [78] A. Aboulaich, K. Ouzaouit, H. Faqir, A. Kaddami, I. Benzakour, and I. Akalay, "Improving thermal and electrochemical performances of  $\text{LiCoO}_2$  cathode at high

cut-off charge potentials by  $\text{MF}_3$  (M=Ce, Al) coating”, *Materials Research Bulletin*, Vol. 73, pp. 362-368, **2016**.

- [79] J. T. Lee, F. M. Wang, C. S. Cheng, C. C. Li, and C. H. Lin, “Low-temperature atomic layer deposited  $\text{Al}_2\text{O}_3$  thin film on layer structure cathode for enhanced cycleability in lithium-ion batteries”, *Electrochimica Acta*, Vol. 55, No. 12, pp. 4002-4006, **2010**.
- [80] Y. J. Kim, H. Kim, B. Kim, D. Ahn, J. G. Lee, T. J. Kim, D. Son, J. Cho, Y. W. Kim, and B. Park, “Electrochemical stability of thin-film  $\text{LiCoO}_2$  cathodes by aluminum-oxide coating”, *Chemistry of Materials*, Vol. 15, No. 7, pp. 1505-1511, **2003**.
- [81] Z. Wang, L. Liu, L. Chen, and X. Huang, “Structural and electrochemical characterizations of surface-modified  $\text{LiCoO}_2$  cathode materials for Li-ion batteries”, *Solid State Ionics*, Vol. 148, No. 3-4, pp. 335-342, **2002**.
- [82] J. Qian, L. Liu, J. Yang, S. Li, X. Wang, H. L. Zhuang, and Y. Lu, “Electrochemical surface passivation of  $\text{LiCoO}_2$  particles at ultrahigh voltage and its applications in lithium-based batteries”, *Nature Communications*, Vol. 9, No. 1, pp. 4918, **2018**.
- [83] X. Qin, X. Wang, J. Xie, and L. Wen, “Hierarchically porous and conductive  $\text{LiFePO}_4$  bulk electrode: binder-free and ultrahigh volumetric capacity Li-ion cathode”, *Journal of Materials Chemistry*, Vol. 21, No. 33, pp. 12444-12448, **2011**.
- [84] M. Park, X. Zhang, M. Chung, G. B. Less, and A. M. Sastry, “A review of conduction phenomena in Li-ion batteries”, *Journal of Power Sources*, Vol. 195, No. 24, pp. 7904-7929, **2010**.
- [85] J. Van Elp, J. Wieland, H. Eskes, P. Kuiper, G. Sawatzky, F. De Groot, and T. Turner, “Electronic structure of  $\text{CoO}$ , Li-doped  $\text{CoO}$ , and  $\text{LiCoO}_2$ ”, *Physical Review B*, Vol. 44, No. 12, pp. 6090, **1991**.
- [86] C. Julien, “Lithium intercalated compounds: charge transfer and related properties”, *Materials Science and Engineering: R: Reports*, Vol. 40, No. 2, pp. 47-102, **2003**.
- [87] S. P. Woo, S. H. Lee, and Y. S. Yoon, “Characterization of  $\text{LiCoO}_2$ /multiwall carbon nanotubes with garnet-type electrolyte fabricated by spark plasma sintering for bulk-type all-solid-state batteries”, *Composites Part B: Engineering*, Vol. 124, pp. 242-249, **2017**.
- [88] B. Tjaden, D. J. Brett, and P. R. Shearing, “Tortuosity in electrochemical devices: a review of calculation approaches”, *International Materials Reviews*, Vol. 63, No. 2, pp. 47-67, **2018**.
- [89] L. Li, R. M. Erb, J. Wang, J. Wang, and Y. M. Chiang, “Fabrication of low-tortuosity ultrahigh-area-capacity battery electrodes through magnetic alignment

- of emulsion-based slurries”, *Advanced Energy Materials*, Vol. 9, No. 2, pp. 1802472, **2019**.
- [90] S. Tintignac, R. Baddour-Hadjean, J. Pereira-Ramos, and R. Salot, “High performance sputtered LiCoO<sub>2</sub> thin films obtained at a moderate annealing treatment combined to a bias effect”, *Electrochimica Acta*, Vol. 60, pp. 121-129, **2012**.
  - [91] M. S. Park, S. H. Hyun, and S. C. Nam, “Characterization of a LiCoO<sub>2</sub> thick film by screen-printing for a lithium ion micro-battery”, *Journal of Power Sources*, Vol. 159, No. 2, pp. 1416-1421, **2006**.
  - [92] K. Striebel, C. Deng, S. Wen, and E. Cairns, “Electrochemical behavior of LiMn<sub>2</sub>O<sub>4</sub> and LiCoO<sub>2</sub> thin films produced with pulsed laser deposition”, *Journal of the Electrochemical Society*, Vol. 143, No. 6, pp. 1821-1827, **1996**.
  - [93] Y. Matsuda, N. Kuwata, and J. Kawamura, “Thin-film lithium batteries with 0.3–30 μm thick LiCoO<sub>2</sub> films fabricated by high-rate pulsed laser deposition”, *Solid State Ionics*, Vol. 320, pp. 38-44, **2018**.
  - [94] C. Chen, A. Buysman, E. Kelder, and J. Schoonman, “Fabrication of LiCoO<sub>2</sub> thin film cathodes for rechargeable lithium battery by electrostatic spray pyrolysis”, *Solid State Ionics*, Vol. 80, No. 1-2, pp. 1-4, **1995**.
  - [95] Y. H. Rho, and K. Kanamura, “Li<sup>+</sup>-ion diffusion in LiCoO<sub>2</sub> thin film prepared by the poly(vinylpyrrolidone) sol-gel method”, *Journal of the Electrochemical Society*, Vol. 151, No. 9, pp. A1406-A1411, **2004**.
  - [96] X. Wu, S. Xia, Y. Huang, X. Hu, B. Yuan, S. Chen, Y. Yu, and W. Liu, “High-performance, low-cost, and dense-structure electrodes with high mass loading for lithium-ion batteries”, *Advanced Functional Materials*, Vol. 29, No. 34, pp. 1903961, **2019**.
  - [97] H. Guo, A. Baker, J. Guo, and C. A. Randall, “Protocol for ultralow-temperature ceramic sintering: an integration of nanotechnology and the cold sintering process”, *ACS Nano*, Vol. 10, No. 11, pp. 10606-10614, **2016**.
  - [98] J. Guo, A. L. Baker, H. Guo, M. Lanagan, and C. A. Randall, “Cold sintering process: a new era for ceramic packaging and microwave device development”, *Journal of the American Ceramic Society*, Vol. 100, No. 2, pp. 669-677, **2017**.
  - [99] H. Guo, A. Baker, J. Guo, and C. A. Randall, “Cold sintering process: a novel technique for low-temperature ceramic processing of ferroelectrics”, *Journal of the American Ceramic Society*, Vol. 99, No. 11, pp. 3489-3507, **2016**.
  - [100] Y. Liu, Q. Sun, D. Wang, K. Adair, J. Liang, and X. Sun, “Development of the cold sintering process and its application in solid-state lithium batteries”, *Journal of Power Sources*, Vol. 393, pp. 193-203, **2018**.
  - [101] J. Guo, H. Guo, A. L. Baker, M. T. Lanagan, E. R. Kupp, G. L. Messing, and C. A. Randall, “Cold sintering: a paradigm shift for processing and integration of

- ceramics”, *Angewandte Chemie International Edition*, Vol. 55, No. 38, pp. 11457-11461, **2016**.
- [102] H. Leng, J. Huang, J. Nie, and J. Luo, “Cold sintering and ionic conductivities of  $\text{Na}_{3.256}\text{Mg}_{0.128}\text{Zr}_{1.872}\text{Si}_2\text{PO}_{12}$  solid electrolytes”, *Journal of Power Sources*, Vol. 391, pp. 170-179, **2018**.
- [103] S. Funahashi, J. Guo, H. Guo, K. Wang, A. L. Baker, K. Shiratsuyu, and C. A. Randall, “Demonstration of the cold sintering process study for the densification and grain growth of ZnO ceramics”, *Journal of the American Ceramic Society*, Vol. 100, No. 2, pp. 546-553, **2017**.
- [104] H. Guo, T. J. Bayer, J. Guo, A. Baker, and C. A. Randall, “Cold sintering process for 8 mol%  $\text{Y}_2\text{O}_3$ -stabilized  $\text{ZrO}_2$  ceramics”, *Journal of the European Ceramic Society*, Vol. 37, No. 5, pp. 2303-2308, **2017**.
- [105] S. S. Berbano, J. Guo, H. Guo, M. T. Lanagan, and C. A. Randall, “Cold sintering process of  $\text{Li}_{1.5}\text{Al}_{0.5}\text{Ge}_{1.5}(\text{PO}_4)_3$  solid electrolyte”, *Journal of the American Ceramic Society*, Vol. 100, No. 5, pp. 2123-2135, **2017**.
- [106] J. Guo, H. Guo, D. S. B. Heidary, S. Funahashi, and C. A. Randall, “Semiconducting properties of cold sintered  $\text{V}_2\text{O}_5$  ceramics and co-sintered  $\text{V}_2\text{O}_5$ -PEDOT:PSS composites”, *Journal of the European Ceramic Society*, Vol. 37, No. 4, pp. 1529-1534, **2017**.
- [107] H. Guo, J. Guo, A. Baker, and C. A. Randall, “Cold sintering process for  $\text{ZrO}_2$ -based ceramics: significantly enhanced densification evolution in yttria-doped  $\text{ZrO}_2$ ”, *Journal of the American Ceramic Society*, Vol. 100, No. 2, pp. 491-495, **2017**.
- [108] X. Zhao, J. Guo, K. Wang, T. Herisson De Beauvoir, B. Li, and C. A. Randall, “Introducing a ZnO–PTFE (Polymer) nanocomposite varistor via the cold sintering process”, *Advanced Engineering Materials*, Vol. 20, No. 7, pp. 1700902, **2018**.
- [109] Y. Jing, N. Luo, S. Wu, K. Han, X. Wang, L. Miao, and Y. Wei, “Remarkably improved electrical conductivity of ZnO ceramics by cold sintering and post-heat-treatment”, *Ceramics International*, Vol. 44, No. 16, pp. 20570-20574, **2018**.
- [110] P. Fragnaud, T. Brousse, and D. Schleich, “Characterization of sprayed and sputter deposited  $\text{LiCoO}_2$  thin films for rechargeable microbatteries”, *Journal of Power Sources*, Vol. 63, No. 2, pp. 187-191, **1996**.
- [111] H. S. Kim, Y. Oh, K. H. Kang, J. H. Kim, J. Kim, and C. S. Yoon, “Characterization of sputter-deposited  $\text{LiCoO}_2$  thin film grown on NASICON-type electrolyte for application in all-solid-state rechargeable lithium battery”, *ACS Applied Materials & Interfaces*, Vol. 9, No. 19, pp. 16063-16070, **2017**.



- [112] W. S. Kim, “Characteristics of LiCoO<sub>2</sub> thin film cathodes according to the annealing ambient for the post-annealing process”, *Journal of Power Sources*, Vol. 134, No. 1, pp. 103-109, **2004**.
- [113] K. J. Rao, H. Benqlilou-Moudden, B. Desbat, P. Vinatier, and A. Levasseur, “Infrared spectroscopic study of LiCoO<sub>2</sub> thin films”, *Journal of Solid State Chemistry*, Vol. 165, No. 1, pp. 42-47, **2002**.
- [114] J. Xie, N. Imanishi, T. Zhang, A. Hirano, Y. Takeda, O. Yamamoto, G. S. Cao, and X. B. Zhao, “Amorphous LiCoO<sub>2</sub> thin films on Li<sub>1+x+y</sub>Al<sub>x</sub>Ti<sub>2-x</sub>Si<sub>y</sub>P<sub>3-y</sub>O<sub>12</sub> prepared by radio frequency magnetron sputtering for all-solid-state Li-ion batteries”, *Electrochimica Acta*, Vol. 55, No. 19, pp. 5440-5445, **2010**.
- [115] J. Xie, N. Imanishi, T. Zhang, A. Hirano, Y. Takeda, and O. Yamamoto, “Li-ion transport in all-solid-state lithium batteries with LiCoO<sub>2</sub> using NASICON-type glass ceramic electrolytes”, *Journal of Power Sources*, Vol. 189, No. 1, pp. 365-370, **2009**.
- [116] H. Y. Park, S. C. Nam, Y. C. Lim, K. G. Choi, K. C. Lee, G. B. Park, J. B. Kim, H. P. Kim, and S. B. Cho, “LiCoO<sub>2</sub> thin film cathode fabrication by rapid thermal annealing for micropower sources”, *Electrochimica Acta*, Vol. 52, No. 5, pp. 2062-2067, **2007**.
- [117] J. Bates, N. Dudney, B. Neudecker, F. Hart, H. Jun, and S. Hackney, “Preferred orientation of polycrystalline LiCoO<sub>2</sub> films”, *Journal of the Electrochemical Society*, Vol. 147, No. 1, pp. 59-70, **2000**.
- [118] H. Nakaya, M. Iwasaki, T. H. de Beauvoir, and C. A. Randall, “Applying cold sintering process to a proton electrolyte material: CsH<sub>2</sub>PO<sub>4</sub>”, *Journal of the European Ceramic Society*, Vol. 39, No. 2, pp. 396-401, **2019**.
- [119] S. S. Berbano, M. Mirsaneh, M. T. Lanagan, and C. A. Randall, “Lithium thiophosphate glasses and glass–ceramics as solid electrolytes: processing, microstructure, and properties”, *International Journal of Applied Glass Science*, Vol. 4, No. 4, pp. 414-425, **2013**.
- [120] J. G. Pereira da Silva, M. Bram, A. M. Laptev, J. Gonzalez-Julian, Q. Ma, F. Tietz, and O. Guillon, “Sintering of a sodium-based NASICON electrolyte: a comparative study between cold, field assisted and conventional sintering methods”, *Journal of the European Ceramic Society*, Vol. 39, No. 8, pp. 2697-2702, **2019**.
- [121] S. Wang, S. Li, Y. Sun, X. Feng, and C. Chen, “Three-dimensional porous V<sub>2</sub>O<sub>5</sub> cathode with ultra high rate capability”, *Energy & Environmental Science*, Vol. 4, No. 8, pp. 2854-2857, **2011**.
- [122] Y. Zhao, S. S. Berbano, L. Gao, K. Wang, J. Guo, K. Tsuji, J. Wang, and C. A. Randall, “Cold-sintered V<sub>2</sub>O<sub>5</sub>-PEDOT:PSS nanocomposites for negative temperature coefficient materials”, *Journal of the European Ceramic Society*, Vol. 39, No. 4, pp. 1257-1262, **2019**.

- [123] M. Terrones, A. R. Botello-Méndez, J. Campos-Delgado, F. López-Urías, Y. I. Vega-Cantú, F. J. Rodríguez-Macías, A. L. Elías, E. Munoz-Sandoval, A. G. Cano-Márquez, and J.-C. Charlier, “Graphene and graphite nanoribbons: morphology, properties, synthesis, defects and applications”, *Nano Today*, Vol. 5, No. 4, pp. 351-372, **2010**.
- [124] A. K. Geim, and K. S. Novoselov, “The rise of graphene”, *Nature Materials*, Vol. 6, pp. 183, **2007**.
- [125] J. D. Bernal, “The structure of graphite”, *Proceedings of the Royal Society of London. Series A, Containing Papers of a Mathematical and Physical Character*, Vol. 106, No. 740, pp. 749-773, **1924**.
- [126] K. S. Novoselov, D. Jiang, F. Schedin, T. Booth, V. Khotkevich, S. Morozov, and A. K. Geim, “Two-dimensional atomic crystals”, *Proceedings of the National Academy of Sciences*, Vol. 102, No. 30, pp. 10451-10453, **2005**.
- [127] K. S. Novoselov, A. K. Geim, S. V. Morozov, D. Jiang, Y. Zhang, S. V. Dubonos, I. V. Grigorieva, and A. A. Firsov, “Electric field effect in atomically thin carbon films”, *Science*, Vol. 306, No. 5696, pp. 666-669, **2004**.
- [128] M. J. McAllister, J.-L. Li, D. H. Adamson, H. C. Schniepp, A. A. Abdala, J. Liu, M. Herrera-Alonso, D. L. Milius, R. Car, and R. K. Prud'homme, “Single sheet functionalized graphene by oxidation and thermal expansion of graphite”, *Chemistry of Materials*, Vol. 19, No. 18, pp. 4396-4404, **2007**.
- [129] A. Peigney, C. Laurent, E. Flahaut, R. Bacsá, and A. Rousset, “Specific surface area of carbon nanotubes and bundles of carbon nanotubes”, *Carbon*, Vol. 39, No. 4, pp. 507-514, **2001**.
- [130] C. Lee, X. Wei, J. W. Kysar, and J. Hone, “Measurement of the elastic properties and intrinsic strength of monolayer graphene”, *Science*, Vol. 321, No. 5887, pp. 385-388, **2008**.
- [131] Y. Zhu, S. Murali, W. Cai, X. Li, J. W. Suk, J. R. Potts, and R. S. Ruoff, “Graphene and graphene oxide: synthesis, properties, and applications”, *Advanced Materials*, Vol. 22, No. 35, pp. 3906-3924, **2010**.
- [132] R. R. Nair, P. Blake, A. N. Grigorenko, K. S. Novoselov, T. J. Booth, T. Stauber, N. M. Peres, and A. K. Geim, “Fine structure constant defines visual transparency of graphene”, *Science*, Vol. 320, No. 5881, pp. 1308-1308, **2008**.
- [133] A. Akturk, and N. Goldsman, “Electron transport and full-band electron-phonon interactions in graphene”, *Journal of Applied Physics*, Vol. 103, No. 5, pp. 053702, **2008**.
- [134] R. Hashemi, and G. J. Weng, “A theoretical treatment of graphene nanocomposites with percolation threshold, tunneling-assisted conductivity and microcapacitor effect in AC and DC electrical settings”, *Carbon*, Vol. 96, pp. 474-490, **2016**.

- [135] A. A. Balandin, "Thermal properties of graphene and nanostructured carbon materials", *Nature Materials*, Vol. 10, No. 8, pp. 569-581, **2011**.
- [136] H. Hu, Z. Zhao, Q. Zhou, Y. Gogotsi, and J. Qiu, "The role of microwave absorption on formation of graphene from graphite oxide", *Carbon*, Vol. 50, No. 9, pp. 3267-3273, **2012**.
- [137] R. Liu, Y. Zhang, Z. Ning, and Y. Xu, "A catalytic microwave process for superfast preparation of high-quality reduced graphene oxide", *Angewandte Chemie International Edition*, Vol. 56, No. 49, pp. 15677-15682, **2017**.
- [138] M. Ye, Z. Zhang, Y. Zhao, and L. Qu, "Graphene platforms for smart energy generation and storage", *Joule*, Vol. 2, No. 2, pp. 245-268, **2018**.
- [139] A. Anshuman, S. Saremi-Yarahmadi, and B. Vaidhyanathan, "Enhanced catalytic performance of reduced graphene oxide-TiO<sub>2</sub> hybrids for efficient water treatment using microwave irradiation", *RSC Advances*, Vol. 8, No. 14, pp. 7709-7715, **2018**.
- [140] Z. Wei, D. Wang, S. Kim, S. Y. Kim, Y. Hu, M. K. Yakes, A. R. Laracuente, Z. Dai, S. R. Marder, C. Berger, W. P. King, W. A. de Heer, P. E. Sheehan, and E. Riedo, "Nanoscale tunable reduction of graphene oxide for graphene electronics", *Science*, Vol. 328, No. 5984, pp. 1373-1376, **2010**.
- [141] S. Wang, P. K. Ang, Z. Wang, A. L. L. Tang, J. T. L. Thong, and K. P. Loh, "High mobility, printable, and solution-processed graphene electronics", *Nano Letters*, Vol. 10, No. 1, pp. 92-98, **2010**.
- [142] T. Kuilla, S. Bhadra, D. Yao, N. H. Kim, S. Bose, and J. H. Lee, "Recent advances in graphene based polymer composites", *Progress in Polymer Science*, Vol. 35, No. 11, pp. 1350-1375, **2010**.
- [143] Y. Wang, Z. Shi, Y. Huang, Y. Ma, C. Wang, M. Chen, and Y. Chen, "Supercapacitor devices based on graphene materials", *The Journal of Physical Chemistry C*, Vol. 113, No. 30, pp. 13103-13107, **2009**.
- [144] Y. Zhu, S. Murali, M. D. Stoller, A. Velamakanni, R. D. Piner, and R. S. Ruoff, "Microwave assisted exfoliation and reduction of graphite oxide for ultracapacitors", *Carbon*, Vol. 48, No. 7, pp. 2118-2122, **2010**.
- [145] W. Lv, D. M. Tang, Y. B. He, C. H. You, Z. Q. Shi, X. C. Chen, C. M. Chen, P. X. Hou, C. Liu, and Q. H. Yang, "Low-temperature exfoliated graphenes: vacuum-promoted exfoliation and electrochemical energy storage", *ACS Nano*, Vol. 3, No. 11, pp. 3730-3736, **2009**.
- [146] H. C. Schniepp, J. Li, M. J. McAllister, H. Sai, M. Herrera-Alonso, D. H. Adamson, R. K. Prud'homme, R. Car, D. A. Saville, and I. A. Aksay, "Functionalized single graphene sheets derived from splitting graphite oxide", *The Journal of Physical Chemistry B*, Vol. 110, No. 17, pp. 8535-8539, **2006**.

- [147] W.-K. Tse, E. Hwang, and S. Das Sarma, “Ballistic hot electron transport in graphene”, *Applied Physics Letters*, Vol. 93, No. 2, pp. 023128, **2008**.
- [148] Z. S. Wu, W. Ren, L. Gao, J. Zhao, Z. Chen, B. Liu, D. Tang, B. Yu, C. Jiang, and H. M. Cheng, “Synthesis of graphene sheets with high electrical conductivity and good thermal stability by hydrogen arc discharge exfoliation”, *ACS Nano*, Vol. 3, No. 2, pp. 411-417, **2009**.
- [149] A. C. Neto, F. Guinea, N. M. Peres, K. S. Novoselov, and A. K. Geim, “The electronic properties of graphene”, *Reviews of Modern Physics*, Vol. 81, No. 1, pp. 109, **2009**.
- [150] X. Y. Wang, A. Narita, and K. Muellen, “Precision synthesis versus bulk-scale fabrication of graphenes”, *Nature Reviews Chemistry*, Vol. 2, No. 1, pp. 0100, **2018**.
- [151] Y. Zhang, L. Gomez, F. N. Ishikawa, A. Madaria, K. Ryu, C. Wang, A. Badmaev, and C. Zhou, “Comparison of graphene growth on single-crystalline and polycrystalline Ni by chemical vapor deposition”, *The Journal of Physical Chemistry Letters*, Vol. 1, No. 20, pp. 3101-3107, **2010**.
- [152] L. Zhao, K. T. Rim, H. Zhou, R. He, T. F. Heinz, A. Pinczuk, G. W. Flynn, and A. N. Pasupathy, “Influence of copper crystal surface on the CVD growth of large area monolayer graphene”, *Solid State Communications*, Vol. 151, No. 7, pp. 509-513, **2011**.
- [153] D. Voiry, J. Yang, J. Kupferberg, R. Fullon, C. Lee, H. Y. Jeong, H. S. Shin, and M. Chhowalla, “High-quality graphene via microwave reduction of solution-exfoliated graphene oxide”, *Science*, Vol. 353, No. 6306, pp. 1413-1416, **2016**.
- [154] W. Zhao, M. Fang, F. Wu, H. Wu, L. Wang, and G. Chen, “Preparation of graphene by exfoliation of graphite using wet ball milling”, *Journal of Materials Chemistry*, Vol. 20, No. 28, pp. 5817-5819, **2010**.
- [155] Y. Hernandez, V. Nicolosi, M. Lotya, F. M. Blighe, Z. Sun, S. De, I. McGovern, B. Holland, M. Byrne, and Y. K. Gun'Ko, “High-yield production of graphene by liquid-phase exfoliation of graphite”, *Nature Nanotechnology*, Vol. 3, No. 9, pp. 563, **2008**.
- [156] X. Chen, J. F. Dobson, and C. L. Raston, “Vortex fluidic exfoliation of graphite and boron nitride”, *Chemical Communications*, Vol. 48, No. 31, pp. 3703-3705, **2012**.
- [157] N. W. Pu, C. A. Wang, Y. Sung, Y. M. Liu, and M. D. Ger, “Production of few-layer graphene by supercritical CO<sub>2</sub> exfoliation of graphite”, *Materials Letters*, Vol. 63, No. 23, pp. 1987-1989, **2009**.
- [158] W. S. Hummers, and R. E. Offeman, “Preparation of graphitic oxide”, *Journal of the American Chemical Society*, Vol. 80, No. 6, pp. 1339-1339, **1958**.

- [159] S. Stankovich, D. A. Dikin, R. D. Piner, K. A. Kohlhaas, A. Kleinhammes, Y. Jia, Y. Wu, S. T. Nguyen, and R. S. Ruoff, "Synthesis of graphene-based nanosheets via chemical reduction of exfoliated graphite oxide", *Carbon*, Vol. 45, No. 7, pp. 1558-1565, **2007**.
- [160] G. Kucinskis, G. Bajars, and J. Kleperis, "Graphene in lithium ion battery cathode materials: a review", *Journal of Power Sources*, Vol. 240, pp. 66-79, **2013**.
- [161] S. Park, J. An, J. R. Potts, A. Velamakanni, S. Murali, and R. S. Ruoff, "Hydrazine-reduction of graphite- and graphene oxide", *Carbon*, Vol. 49, No. 9, pp. 3019-3023, **2011**.
- [162] H. J. Shin, K. K. Kim, A. Benayad, S. M. Yoon, H. K. Park, I. S. Jung, M. H. Jin, H. K. Jeong, J. M. Kim, and J. Y. Choi, "Efficient reduction of graphite oxide by sodium borohydride and its effect on electrical conductance", *Advanced Functional Materials*, Vol. 19, No. 12, pp. 1987-1992, **2009**.
- [163] S. Pei, J. Zhao, J. Du, W. Ren, and H. M. Cheng, "Direct reduction of graphene oxide films into highly conductive and flexible graphene films by hydrohalic acids", *Carbon*, Vol. 48, No. 15, pp. 4466-4474, **2010**.
- [164] D. W. Boukhvalov, and M. I. Katsnelson, "Modeling of graphite oxide", *Journal of the American Chemical Society*, Vol. 130, No. 32, pp. 10697-10701, **2008**.
- [165] Y. Zhang, L. Guo, S. Wei, Y. He, H. Xia, Q. Chen, H. B. Sun, and F. S. Xiao, "Direct imprinting of microcircuits on graphene oxides film by femtosecond laser reduction", *Nano Today*, Vol. 5, No. 1, pp. 15-20, **2010**.
- [166] X. Gao, J. Jang, and S. Nagase, "Hydrazine and thermal reduction of graphene oxide: reaction mechanisms, product structures, and reaction design", *The Journal of Physical Chemistry C*, Vol. 114, No. 2, pp. 832-842, **2009**.
- [167] J. Menéndez, A. Arenillas, B. Fidalgo, Y. Fernández, L. Zubizarreta, E. G. Calvo, and J. M. Bermúdez, "Microwave heating processes involving carbon materials", *Fuel Processing Technology*, Vol. 91, No. 1, pp. 1-8, **2010**.
- [168] K. Ullah, S. Ye, L. Zhu, Z. D. Meng, S. Sarkar, and W. C. Oh, "Microwave assisted synthesis of a noble metal-graphene hybrid photocatalyst for high efficient decomposition of organic dyes under visible light", *Materials Science and Engineering: B*, Vol. 180, pp. 20-26, **2014**.
- [169] A. Fini, and A. Breccia, "Chemistry by microwaves", *Pure and Applied Chemistry*, Vol. 71, No. 4, pp. 573-579, **1999**.
- [170] A. M. Schwenke, S. Hoepfner, and U. S. Schubert, "Synthesis and modification of carbon nanomaterials utilizing microwave heating", *Advanced Materials*, Vol. 27, No. 28, pp. 4113-4141, **2015**.
- [171] D. Kumar, K. Singh, V. Verma, and H. S. Bhatti, "Microwave assisted synthesis and characterization of graphene nanoplatelets", *Applied Nanoscience*, Vol. 6, No. 1, pp. 97-103, **2016**.

- [172] P. Tang, G. Hu, Y. Gao, W. Li, S. Yao, Z. Liu, and D. Ma, "The microwave adsorption behavior and microwave-assisted heteroatoms doping of graphene-based nano-carbon materials" , *Scientific Reports*, Vol. 4, pp. 5901, **2014**.
- [173] S. Mao, K. Yu, S. Cui, Z. Bo, G. Lu, and J. Chen, "A new reducing agent to prepare single-layer, high-quality reduced graphene oxide for device applications", *Nanoscale*, Vol. 3, No. 7, pp. 2849-2853, **2011**.
- [174] J. Zhang, H. Yang, G. Shen, P. Cheng, J. Zhang, and S. Guo, "Reduction of graphene oxide via *L*-ascorbic acid", *Chemical Communications*, Vol. 46, No. 7, pp. 1112-1114, **2010**.
- [175] Y. Chen, X. Zhang, D. Zhang, P. Yu, and Y. Ma, "High performance supercapacitors based on reduced graphene oxide in aqueous and ionic liquid electrolytes", *Carbon*, Vol. 49, No. 2, pp. 573-580, **2011**.
- [176] Y. Liu, Y. Li, Y. Yang, Y. Wen, and M. Wang, "Reduction of graphene oxide by thiourea", *Journal of Nanoscience and Nanotechnology*, Vol. 11, No. 11, pp. 10082-10086, **2011**.
- [177] D. Kumar, C. Raghavan, C. Sridhar, J. H. Shin, S. H. Ryu, K. Jang, and D. S. Shin, "Microwave-assisted synthesis, characterization of reduced graphene oxide, and its antibacterial activity", *Bulletin of the Korean Chemical Society*, Vol. 36, No. 8, pp. 2034-2038, **2015**.
- [178] W. Chen, L. Yan, and P. R. Bangal, "Preparation of graphene by the rapid and mild thermal reduction of graphene oxide induced by microwaves", *Carbon*, Vol. 48, No. 4, pp. 1146-1152, **2010**.
- [179] A. F. Zedan, S. Sappal, S. Moussa, and M. S. El-Shall, "Ligand-controlled microwave synthesis of cubic and hexagonal CdSe nanocrystals supported on graphene. Photoluminescence quenching by graphene", *The Journal of Physical Chemistry C*, Vol. 114, No. 47, pp. 19920-19927, **2010**.
- [180] H. N. Tien, V. H. Luan, T. V. Cuong, B. S. Kong, J. S. Chung, E. J. Kim, and S. H. Hur, "Fast and simple reduction of graphene oxide in various organic solvents using microwave irradiation", *Journal of Nanoscience and Nanotechnology*, Vol. 12, No. 7, pp. 5658-5662, **2012**.
- [181] H. M. A. Hassan, V. Abdelsayed, A. E. R. S. Khder, K. M. AbouZeid, J. Turner, M. S. El-Shall, S. I. Al-Resayes, and A. A. El-Azhary, "Microwave synthesis of graphene sheets supporting metal nanocrystals in aqueous and organic media", *Journal of Materials Chemistry*, Vol. 19, No. 23, pp. 3832-3837, **2009**.
- [182] S. Liu, J. Tian, L. Wang, and X. Sun, "Microwave-assisted rapid synthesis of Ag nanoparticles/graphene nanosheet composites and their application for hydrogen peroxide detection", *Journal of Nanoparticle Research*, Vol. 13, No. 10, pp. 4539-4548, **2011**.

- [183] X. Li, G. Zhang, X. Bai, X. Sun, X. Wang, E. Wang, and H. Dai, “Highly conducting graphene sheets and Langmuir–Blodgett films”, *Nature Nanotechnology*, Vol. 3, pp. 538, **2008**.
- [184] W. Jiang, C. Yang, G. Chen, X. Yan, S. Chen, B. Su, Z. Liu, and J. Tian, “Preparation of high-quality graphene using triggered microwave reduction under an air atmosphere”, *Journal of Materials Chemistry C*, Vol. 6, No. 7, pp. 1829-1835, **2018**.
- [185] S. Park, S. Bak, K. Kim, J. Jegal, S. Lee, J. Lee, and K. Kim, “Solid-state microwave irradiation synthesis of high quality graphene nanosheets under hydrogen containing atmosphere”, *Journal of Materials Chemistry*, Vol. 21, No. 3, pp. 680-686, **2011**.
- [186] Z. Li, Y. Yao, Z. Lin, K. S. Moon, W. Lin, and C. Wong, “Ultrafast, dry microwave synthesis of graphene sheets”, *Journal of Materials Chemistry*, Vol. 20, No. 23, pp. 4781-4783, **2010**.
- [187] O. Taiwo, M. Jun, G. Yi, Z. Wei, J. Jian, X. S. Zhao, and Z. Zhonghua, “A new approach to nanoporous graphene sheets via rapid microwave-induced plasma for energy applications”, *Nanotechnology*, Vol. 25, No. 49, pp. 495604, **2014**.
- [188] S. Liu, J. Wu, Z. Zhou, L. Gao, S. Luo, X. Xu, and Z. M. Wang, “Influence of graphite oxide drying temperature on ultra-fast microwave synthesis of graphene”, *Journal of Materials Science: Materials in Electronics*, Vol. 24, No. 4, pp. 1298-1302, **2013**.
- [189] S. A. El-Khodary, G. M. El-Enany, M. El-Okr, and M. Ibrahim, “Preparation and characterization of microwave reduced graphite oxide for high-performance supercapacitors”, *Electrochimica Acta*, Vol. 150, pp. 269-278, **2014**.
- [190] Y. Shulga, S. Baskakov, E. Knerelman, G. Davidova, E. Badamshina, N. Y. Shulga, E. Skryleva, A. L. Agapov, D. N. Voylov, and A. P. Sokolov, “Carbon nanomaterial produced by microwave exfoliation of graphite oxide: new insights”, *RSC Advances*, Vol. 4, No. 2, pp. 587-592, **2014**.
- [191] K. MacKenzie, O. Dunens, and A. T. Harris, “A review of carbon nanotube purification by microwave assisted acid digestion”, *Separation and Purification Technology*, Vol. 66, No. 2, pp. 209-222, **2009**.
- [192] K. H. Kim, K. M. Cho, D. W. Kim, S. J. Kim, J. Choi, S. J. Bae, S. Park, and H. T. Jung, “The role of layer-controlled graphene for tunable microwave heating and its applications to the synthesis of inorganic thin films”, *ACS Applied Materials & Interfaces*, Vol. 8, No. 8, pp. 5556-5562, **2016**.
- [193] S. Kang, H. Choi, S. B. Lee, S. C. Park, J. B. Park, S. Lee, Y. Kim, and B. H. Hong, “Efficient heat generation in large-area graphene films by electromagnetic wave absorption”, *2D Materials*, Vol. 4, No. 2, pp. 025037, **2017**.

- [194] Q. Zhou, Z. Zhao, Y. Chen, H. Hu, and J. Qiu, “Low temperature plasma-mediated synthesis of graphene nanosheets for supercapacitor electrodes”, *Journal of Materials Chemistry*, Vol. 22, No. 13, pp. 6061-6066, **2012**.
- [195] I. Ogino, G. Fukazawa, S. Kamatari, S. Iwamura, and S. R. Mukai, “The critical role of bulk density of graphene oxide in tuning its defect concentration through microwave-driven annealing”, *Journal of Energy Chemistry*, Vol. 27, No. 5, pp. 1468-1474, **2018**.
- [196] T. Druzhinina, W. Weltjens, S. Hoepfner, and U. S. Schubert, “The selective heating of iron nanoparticles in a single-mode microwave for the patterned growths of carbon nanofibers and nanotubes”, *Advanced Functional Materials*, Vol. 19, No. 8, pp. 1287-1292, **2009**.
- [197] V. V. Chaban, and O. V. Prezhdo, “Microwave reduction of graphene oxide rationalized by reactive molecular dynamics”, *Nanoscale*, Vol. 9, No. 11, pp. 4024-4033, **2017**.
- [198] W. Yuan, Y. Zhang, L. Cheng, H. Wu, L. Zheng, and D. Zhao, “The applications of carbon nanotubes and graphene in advanced rechargeable lithium batteries”, *Journal of Materials Chemistry A*, Vol. 4, No. 23, pp. 8932-8951, **2016**.
- [199] L. Wen, F. Li, and H. M. Cheng, “Carbon nanotubes and graphene for flexible electrochemical energy storage: from materials to devices”, *Advanced Materials*, Vol. 28, No. 22, pp. 4306-4337, **2016**.
- [200] W. Lv, Z. Li, Y. Deng, Q.-H. Yang, and F. Kang, “Graphene-based materials for electrochemical energy storage devices: opportunities and challenges”, *Energy Storage Materials*, Vol. 2, pp. 107-138, **2016**.
- [201] R. Raccichini, A. Varzi, S. Passerini, and B. Scrosati, “The role of graphene for electrochemical energy storage”, *Nature Materials*, Vol. 14, No. 3, pp. 271, **2015**.
- [202] X. Yao, and Y. Zhao, “Three-dimensional porous graphene networks and hybrids for lithium-ion batteries and supercapacitors”, *Chem*, Vol. 2, No. 2, pp. 171-200, **2017**.
- [203] M. F. El-Kady, Y. Shao, and R. B. Kaner, “Graphene for batteries, supercapacitors and beyond”, *Nature Reviews Materials*, Vol. 1, No. 7, pp. 1-14, **2016**.
- [204] C. Nan, “Physics of inhomogeneous inorganic materials”, *Progress in Materials Science*, Vol. 37, No. 1, pp. 1-116, **1993**.
- [205] A. Skal, and B. Shklovskii, “Influence of the impurity concentration on the hopping conduction in semiconductors”, *Soviet Physics: Semiconductors*, Vol. 7, No. 8, pp. 1058-1061, **1974**.
- [206] P. De Gennes, “Scaling theory of polymer adsorption”, *Journal de Physique*, Vol. 37, No. 12, pp. 1445-1452, **1976**.



- [207] L. Feng, N. Xie, and J. Zhong, “Carbon nanofibers and their composites: a review of synthesizing, properties and applications”, *Materials*, Vol. 7, No. 5, pp. 3919-3945, **2014**.
- [208] X.-M. Liu, Z. dong Huang, S. woon Oh, B. Zhang, P.-C. Ma, M. M. Yuen, and J.-K. Kim, “Carbon nanotube (CNT)-based composites as electrode material for rechargeable Li-ion batteries: a review”, *Composites Science and Technology*, Vol. 72, No. 2, pp. 121-144, **2012**.
- [209] W. Guoping, Z. Qingtang, Y. Zuolong, and Q. MeiZheng, “The effect of different kinds of nano-carbon conductive additives in lithium ion batteries on the resistance and electrochemical behavior of the LiCoO<sub>2</sub> composite cathodes”, *Solid State Ionics*, Vol. 179, No. 7-8, pp. 263-268, **2008**.
- [210] Z. Ounaies, C. Park, K. Wise, E. Siochi, and J. Harrison, “Electrical properties of single wall carbon nanotube reinforced polyimide composites”, *Composites Science and Technology*, Vol. 63, No. 11, pp. 1637-1646, **2003**.
- [211] X. Feng, G. Liao, W. He, Q. Sun, X. Jian, and J. Du, “Preparation and characterization of functionalized carbon nanotubes/poly(phthalazinone ether sulfone ketone)s composites”, *Polymer Composites*, Vol. 30, No. 4, pp. 365-373, **2009**.
- [212] O. Regev, P. N. ElKati, J. Loos, and C. E. Koning, “Preparation of conductive nanotube–polymer composites using latex technology”, *Advanced Materials*, Vol. 16, No. 3, pp. 248-251, **2004**.
- [213] K. Sheem, Y. H. Lee, and H. S. Lim, “High-density positive electrodes containing carbon nanotubes for use in Li-ion cells”, *Journal of Power Sources*, Vol. 158, No. 2, pp. 1425-1430, **2006**.
- [214] W. Li, A. Garg, M. L. P. Le, C. Ruhatiya, and L. Gao, “Electrochemical performance investigation of LiFePO<sub>4</sub>/C<sub>0.15-x</sub> (x = 0.05, 0.1, 0.15 CNTs) electrodes at various calcination temperatures: experimental and intelligent modelling approach”, *Electrochimica Acta*, Vol. 330, pp. 135314, **2020**.
- [215] T. D. Duc, A. M.-T. Nguyen, T. N. Nguyen, H. T. La, and P. M. L. Le, “The impact of carbon additives on lithium ion diffusion kinetic of LiFePO<sub>4</sub>/C composites”, *Science and Technology Development Journal*, Vol. 22, No. 1, pp. 173-179, **2019**.
- [216] X. Li, Y. Zhang, H. Song, K. Du, H. Wang, H. Li, and J. Huang, “The comparison of carbon conductive additives with different dimensions on the electrochemical performance of LiFePO<sub>4</sub> cathode”, *International Journal of Electrochemical Science*, Vol. 7, No. 8, pp. 7111-7120, **2012**.
- [217] Z. Du, J. Li, M. Wood, C. Mao, C. Daniel, and D. L. Wood III, “Three-dimensional conductive network formed by carbon nanotubes in aqueous processed NMC electrode”, *Electrochimica Acta*, Vol. 270, pp. 54-61, **2018**.

- [218] H. Dai, “Carbon nanotubes: opportunities and challenges”, *Surface Science*, Vol. 500, No. 1-3, pp. 218-241, **2002**.
- [219] X. Li, F. Kang, X. Bai, and W. Shen, “A novel network composite cathode of  $\text{LiFePO}_4$ /multiwalled carbon nanotubes with high rate capability for lithium ion batteries”, *Electrochemistry Communications*, Vol. 9, No. 4, pp. 663-666, **2007**.
- [220] J. N. Coleman, S. Curran, A. Dalton, A. Davey, B. McCarthy, W. Blau, and R. Barklie, “Percolation-dominated conductivity in a conjugated-polymer-carbon-nanotube composite”, *Physical Review B*, Vol. 58, No. 12, pp. R7492, **1998**.
- [221] J. Y. Kwon, and H. D. Kim, “Preparation and properties of acid-treated multiwalled carbon nanotube/waterborne polyurethane nanocomposites”, *Journal of Applied Polymer Science*, Vol. 96, No. 2, pp. 595-604, **2005**.
- [222] S. Luo, K. Wang, J. Wang, K. Jiang, Q. Li, and S. Fan, “Binder-free  $\text{LiCoO}_2$ /carbon nanotube cathodes for high-performance lithium ion batteries”, *Advanced Materials*, Vol. 24, No. 17, pp. 2294-2298, **2012**.
- [223] H. Song, Y. Oh, N. Çakmakçı, and Y. Jeong, “Effects of the aspect ratio of the conductive agent on the kinetic properties of lithium ion batteries”, *RSC Advances*, Vol. 9, No. 70, pp. 40883-40886, **2019**.
- [224] S. Xie, Y. Liu, and J. Li, “Comparison of the effective conductivity between composites reinforced by graphene nanosheets and carbon nanotubes”, *Applied Physics Letters*, Vol. 92, No. 24, pp. 243121, **2008**.
- [225] C. Su, X. Bu, L. Xu, J. Liu, and C. Zhang, “A novel  $\text{LiFePO}_4$ /graphene/carbon composite as a performance-improved cathode material for lithium-ion batteries”, *Electrochimica Acta*, Vol. 64, pp. 190-195, **2012**.
- [226] J. Yang, J. Wang, D. Wang, X. Li, D. Geng, G. Liang, M. Gauthier, R. Li, and X. Sun, “3D porous  $\text{LiFePO}_4$ /graphene hybrid cathodes with enhanced performance for Li-ion batteries”, *Journal of Power Sources*, Vol. 208, pp. 340-344, **2012**.
- [227] Y. Zhang, W. Wang, P. Li, Y. Fu, and X. Ma, “A simple solvothermal route to synthesize graphene-modified  $\text{LiFePO}_4$  cathode for high power lithium ion batteries”, *Journal of Power Sources*, Vol. 210, pp. 47-53, **2012**.
- [228] H. Xu, J. Chang, J. Sun, and L. Gao, “Graphene-encapsulated  $\text{LiFePO}_4$  nanoparticles with high electrochemical performance for lithium ion batteries”, *Materials Letters*, Vol. 83, pp. 27-30, **2012**.
- [229] J. Dong, Y. Lin, H. Zong, H. Yang, L. Wang, and Z. Dai, “Three-dimensional architecture reduced graphene oxide- $\text{LiFePO}_4$  composite: preparation and excellent microwave absorption performance”, *Inorganic Chemistry*, Vol. 58, No. 3, pp. 2031-2041, **2019**.
- [230] H. Wang, Y. Yang, Y. Liang, L. F. Cui, H. Sanchez Casalongue, Y. Li, G. Hong, Y. Cui, and H. Dai, “ $\text{LiMn}_{1-x}\text{Fe}_x\text{PO}_4$  nanorods grown on graphene sheets for

- ultrahigh-rate-performance lithium ion batteries”, *Angewandte Chemie*, Vol. 123, No. 32, pp. 7502-7506, **2011**.
- [231] S.-M. Bak, K.-W. Nam, C.-W. Lee, K.-H. Kim, H.-C. Jung, X.-Q. Yang, and K.-B. Kim, “Spinel  $\text{LiMn}_2\text{O}_4$ /reduced graphene oxide hybrid for high rate lithium ion batteries”, *Journal of Materials Chemistry*, Vol. 21, No. 43, pp. 17309-17315, **2011**.
- [232] W. Zhang, Y. Zeng, C. Xu, N. Xiao, Y. Gao, L.-J. Li, X. Chen, H. H. Hng, and Q. Yan, “A facile approach to nanoarchitected three-dimensional graphene-based Li–Mn–O composite as high-power cathodes for Li-ion batteries”, *Beilstein Journal of Nanotechnology*, Vol. 3, No. 1, pp. 513-523, **2012**.
- [233] X. Tian, Y. Zhou, X. Tu, Z. Zhang, and G. Du, “Well-dispersed  $\text{LiFePO}_4$  nanoparticles anchored on a three-dimensional graphene aerogel as high-performance positive electrode materials for lithium-ion batteries”, *Journal of Power Sources*, Vol. 340, pp. 40-50, **2017**.
- [234] X. Wei, Y. Guan, X. Zheng, Q. Zhu, J. Shen, N. Qiao, S. Zhou, and B. Xu, “Improvement on high rate performance of  $\text{LiFePO}_4$  cathodes using graphene as a conductive agent”, *Applied Surface Science*, Vol. 440, pp. 748-754, **2018**.
- [235] R. Tang, Q. Yun, W. Lv, Y.-B. He, C. You, F. Su, L. Ke, B. Li, F. Kang, and Q.-H. Yang, “How a very trace amount of graphene additive works for constructing an efficient conductive network in  $\text{LiCoO}_2$ -based lithium-ion batteries”, *Carbon*, Vol. 103, pp. 356-362, **2016**.
- [236] Y. Shi, L. Wen, S. Pei, M. Wu, and F. Li, “Choice for graphene as conductive additive for cathode of lithium-ion batteries”, *Journal of Energy Chemistry*, Vol. 30, pp. 19-26, **2019**.
- [237] T. Liu, S. Sun, Z. Zang, X. Li, X. Sun, F. Cao, and J. Wu, “Effects of graphene with different sizes as conductive additives on the electrochemical performance of a  $\text{LiFePO}_4$  cathode”, *RSC Advances*, Vol. 7, No. 34, pp. 20882-20887, **2017**.
- [238] F. Chen, and N. Tao, “Electron transport in single molecules: from benzene to graphene”, *Accounts of Chemical Research*, Vol. 42, No. 3, pp. 429-438, **2009**.
- [239] Z. Ren, Z. Huang, J. Xu, J. Wang, P. Bush, M. Siegal, and P. Provencio, “Synthesis of large arrays of well-aligned carbon nanotubes on glass”, *Science*, Vol. 282, No. 5391, pp. 1105-1107, **1998**.
- [240] S. Iijima, “Helical microtubules of graphitic carbon”, *Nature*, Vol. 354, No. 6348, pp. 56-58, **1991**.
- [241] C. Journet, W. Maser, P. Bernier, A. Loiseau, M. L. de La Chapelle, d. S. Lefrant, P. Deniard, R. Lee, and J. Fischer, “Large-scale production of single-walled carbon nanotubes by the electric-arc technique”, *Nature*, Vol. 388, No. 6644, pp. 756-758, **1997**.

- [242] A. Rinzler, J. Liu, H. Dai, P. Nikolaev, C. Huffman, F. Rodriguez-Macias, P. Boul, A. H. Lu, D. Heymann, and D. Colbert, “Large-scale purification of single-wall carbon nanotubes: process, product, and characterization”, *Applied Physics A: Materials Science & Processing*, Vol. 67, No. 1, pp., **1998**.
- [243] Z.-S. Wu, G. Zhou, L.-C. Yin, W. Ren, F. Li, and H.-M. Cheng, “Graphene/metal oxide composite electrode materials for energy storage”, *Nano Energy*, Vol. 1, No. 1, pp. 107-131, **2012**.
- [244] M. Pumera, “Electrochemistry of graphene: new horizons for sensing and energy storage”, *The Chemical Record*, Vol. 9, No. 4, pp. 211-223, **2009**.
- [245] Y. Li, and M. Kröger, “A theoretical evaluation of the effects of carbon nanotube entanglement and bundling on the structural and mechanical properties of buckypaper”, *Carbon*, Vol. 50, No. 5, pp. 1793-1806, **2012**.
- [246] Z. Shen, M. Röding, M. Kröger, and Y. Li, “Carbon nanotube length governs the viscoelasticity and permeability of buckypaper”, *Polymers*, Vol. 9, No. 4, pp. 115, **2017**.
- [247] J. Xie, N. Imanishi, T. Matsumura, A. Hirano, Y. Takeda, and O. Yamamoto, “Orientation dependence of Li-ion diffusion kinetics in LiCoO<sub>2</sub> thin films prepared by RF magnetron sputtering”, *Solid State Ionics*, Vol. 179, No. 9-10, pp. 362-370, **2008**.
- [248] L. Gan, M. Dong, Y. Han, Y. Xiao, L. Yang, and J. Huang, “Connection-improved conductive network of carbon nanotubes in a rubber cross-link network”, *ACS Applied Materials & Interfaces*, Vol. 10, No. 21, pp. 18213-18219, **2018**.
- [249] E. Talaie, P. Bonnick, X. Sun, Q. Pang, X. Liang, and L. F. Nazar, “Methods and protocols for electrochemical energy storage materials research”, *Chemistry of Materials*, Vol. 29, No. 1, pp. 90-105, **2016**.
- [250] R. Dash, and S. Pannala, “Theoretical limits of energy density in silicon-carbon composite anode based lithium ion batteries”, *Scientific Reports*, Vol. 6, pp. 27449, **2016**.
- [251] D. C. Marcano, D. V. Kosynkin, J. M. Berlin, A. Sinitskii, Z. Sun, A. Slesarev, L. B. Alemany, W. Lu, and J. M. Tour, “Improved synthesis of graphene oxide”, *ACS Nano*, Vol. 4, No. 8, pp. 4806-4814, **2010**.
- [252] T. Placke, S. Rothermel, O. Fromm, P. Meister, S. F. Lux, J. Huesker, H. W. Meyer, and M. Winter, “Influence of graphite characteristics on the electrochemical intercalation of bis(trifluoromethanesulfonyl)imide anions into a graphite-based cathode”, *Journal of the Electrochemical Society*, Vol. 160, No. 11, pp. A1979-A1991, **2013**.
- [253] J. K. Hong, J. H. Lee, and S. M. Oh, “Effect of carbon additive on electrochemical performance of LiCoO<sub>2</sub> composite cathodes”, *Journal of Power Sources*, Vol. 111, No. 1, pp. 90-96, **2002**.

- [254] Z. Guo, A. Jones, and N. Li, "The effect of ultrasound on the homogeneous nucleation of BaSO<sub>4</sub> during reactive crystallization", *Chemical Engineering Science*, Vol. 61, No. 5, pp. 1617-1626, **2006**.
- [255] Z. Guo, M. Zhang, H. Li, J. Wang, and E. Kougoulos, "Effect of ultrasound on anti-solvent crystallization process", *Journal of Crystal Growth*, Vol. 273, No. 3-4, pp. 555-563, **2005**.
- [256] X. Qi, T. Zhou, S. Deng, G. Zong, X. Yao, and Q. Fu, "Size-specified graphene oxide sheets: ultrasonication assisted preparation and characterization", *Journal of Materials Science*, Vol. 49, No. 4, pp. 1785-1793, **2014**.
- [257] J. Liu, H. Yan, and K. Jiang, "Mechanical properties of graphene platelet-reinforced alumina ceramic composites", *Ceramics International*, Vol. 39, No. 6, pp. 6215-6221, **2013**.
- [258] A. J. Bard, L. R. Faulkner, J. Leddy, and C. G. Zoski, *Electrochemical methods: fundamentals and applications*: Wiley New York, **1980**.
- [259] L. Wang, B. Chen, J. Ma, G. Cui, and L. Chen, "Reviving lithium cobalt oxide-based lithium secondary batteries-toward a higher energy density", *Chemical Society Reviews*, Vol. 47, No. 17, pp. 6505-6602, **2018**.
- [260] Z. Wang, Y. Yin, Y. Ren, Z. Wang, M. Gao, T. Ma, W. Zhuang, S. Lu, A. Fan, and K. Amine, "High performance lithium-manganese-rich cathode material with reduced impurities", *Nano Energy*, Vol. 31, pp. 247-257, **2017**.
- [261] J. Qiu, D. He, M. Sun, S. Li, C. Wen, J. Hatrick-Simpers, Y. F. Zheng, and L. Cao, "Effects of neutron and gamma radiation on lithium-ion batteries", *Nuclear Instruments and Methods in Physics Research Section B: Beam Interactions with Materials and Atoms*, Vol. 345, pp. 27-32, **2015**.
- [262] P. Bouwman, B. A. Boukamp, H. J. Bouwmeester, H. Wondergem, and P. Notten, "Structural analysis of submicrometer LiCoO<sub>2</sub> films", *Journal of the Electrochemical Society*, Vol. 148, No. 4, pp. A311-A317, **2001**.
- [263] J. H. Shim, K. S. Lee, A. Missyul, J. Lee, B. Linn, E. C. Lee, and S. Lee, "Characterization of spinel Li<sub>x</sub>Co<sub>2</sub>O<sub>4</sub>-coated LiCoO<sub>2</sub> prepared with post-thermal treatment as a cathode material for lithium ion batteries", *Chemistry of Materials*, Vol. 27, No. 9, pp. 3273-3279, **2015**.
- [264] J. Cho, Y. J. Kim, and B. Park, "Novel LiCoO<sub>2</sub> cathode material with Al<sub>2</sub>O<sub>3</sub> coating for a Li ion cell", *Chemistry of Materials*, Vol. 12, No. 12, pp. 3788-3791, **2000**.
- [265] N. Pereira, J. Al-Sharab, F. Cosandey, F. Badway, and G. Amatucci, "Thermodynamically induced surface modification for the stabilization of high-capacity LiCoO<sub>2</sub>", *Journal of the Electrochemical Society*, Vol. 155, No. 11, pp. A831-A838, **2008**.
- [266] M. N. Rahaman, *Ceramic processing*: CRC press, **2017**.

- [267] M. N. Rahaman, *Ceramic processing and sintering*: CRC press, **2003**.
- [268] H. Tukamoto, and A. West, “Electronic conductivity of  $\text{LiCoO}_2$  and its enhancement by magnesium doping”, *Journal of the Electrochemical Society*, Vol. 144, No. 9, pp. 3164-3168, **1997**.
- [269] J. Molenda, A. Stokłosa, and T. Bąk, “Modification in the electronic structure of cobalt bronze  $\text{Li}_x\text{CoO}_2$  and the resulting electrochemical properties”, *Solid State Ionics*, Vol. 36, No. 1-2, pp. 53-58, **1989**.
- [270] N. Imanishi, M. Fujiyoshi, Y. Takeda, O. Yamamoto, and M. Tabuchi, “Preparation and  $^7\text{Li}$ -NMR study of chemically delithiated  $\text{Li}_{1-x}\text{CoO}_2$  ( $0 < x < 0.5$ )”, *Solid State Ionics*, Vol. 118, No. 1-2, pp. 121-128, **1999**.
- [271] M. Jo, S. Jeong, and J. Cho, “High power  $\text{LiCoO}_2$  cathode materials with ultra energy density for Li-ion cells”, *Electrochemistry Communications*, Vol. 12, No. 7, pp. 992-995, **2010**.
- [272] Y. Ding, P. Zhang, Y. Jiang, and D. Gao, “Effect of rare earth elements doping on structure and electrochemical properties of  $\text{LiNi}_{1/3}\text{Co}_{1/3}\text{Mn}_{1/3}\text{O}_2$  for lithium-ion battery”, *Solid State Ionics*, Vol. 178, No. 13-14, pp. 967-971, **2007**.
- [273] B. Wang, J. Bates, F. Hart, B. Sales, R. Zuhr, and J. Robertson, “Characterization of thin-film rechargeable lithium batteries with lithium cobalt oxide cathodes”, *Journal of the Electrochemical Society*, Vol. 143, No. 10, pp. 3203-3213, **1996**.
- [274] P. Nie, L. Shen, H. Luo, H. Li, G. Xu, and X. Zhang, “Synthesis of nanostructured materials by using metal-cyanide coordination polymers and their lithium storage properties”, *Nanoscale*, Vol. 5, No. 22, pp. 11087-11093, **2013**.
- [275] P. Jeevan-Kumar, K. Jayanth-Babu, O. Hussain, and C. Julien, “RF-sputtered  $\text{LiCoO}_2$  thick films: microstructure and electrochemical performance as cathodes in aqueous and nonaqueous microbatteries”, *Ionics*, Vol. 19, No. 3, pp. 421-428, **2013**.
- [276] W. Zhu, D. Liu, A. Paoletta, C. Gagnon, V. Gariepy, A. Vijh, and K. Zaghib, “Application of *operando* X-ray diffraction and Raman spectroscopies in elucidating the behavior of cathode in lithium-ion batteries”, *Frontiers in Energy Research*, Vol. 6, pp. 66, **2018**.
- [277] E. Quartarone, and P. Mustarelli, “Electrolytes for solid-state lithium rechargeable batteries: recent advances and perspectives”, *Chemical Society Reviews*, Vol. 40, No. 5, pp. 2525-2540, **2011**.
- [278] H. Lee, C. Wan, and Y. Wang, “Thermal stability of the solid electrolyte interface on carbon electrodes of lithium batteries”, *Journal of the Electrochemical Society*, Vol. 151, No. 4, pp. A542-A547, **2004**.
- [279] K. Dokko, S. Horikoshi, T. Itoh, M. Nishizawa, M. Mohamedi, and I. Uchida, “Microvoltammetry for cathode materials at elevated temperatures:

- electrochemical stability of single particles”, *Journal of Power Sources*, Vol. 90, No. 1, pp. 109-115, **2000**.
- [280] H. Wang, Y. I. Jang, B. Huang, D. R. Sadoway, and Y. M. Chiang, “Electron microscopic characterization of electrochemically cycled  $\text{LiCoO}_2$  and  $\text{Li(Al,Co)O}_2$  battery cathodes”, *Journal of Power Sources*, Vol. 81-82, pp. 594-598, **1999**.
- [281] J. G. Kim, B. Son, S. Mukherjee, N. Schuppert, A. Bates, O. Kwon, M. J. Choi, H. Y. Chung, and S. Park, “A review of lithium and non-lithium based solid state batteries”, *Journal of Power Sources*, Vol. 282, pp. 299-322, **2015**.
- [282] S. P. Woo, W. Lee, and Y. S. Yoon, “Composite cathode material using spark plasma sintering for bulk-type hybrid solid-state batteries”, *Journal of the Korean Physical Society*, Vol. 73, No. 7, pp. 1019-1024, **2018**.
- [283] C. Bao, S. Bi, H. Zhang, J. Zhao, P. Wang, C. Y. Yue, and J. Yang, “Graphene oxide beads for fast clean-up of hazardous chemicals”, *Journal of Materials Chemistry A*, Vol. 4, No. 24, pp. 9437-9446, **2016**.
- [284] M. Oksuz, and H. Y. Erbil, “Wet-spun graphene filaments: effect of temperature of coagulation bath and type of reducing agents on mechanical & electrical properties”, *RSC Advances*, Vol. 8, No. 31, pp. 17443-17452, **2018**.
- [285] S. Yang, X. Feng, S. Ivanovici, and K. Müllen, “Fabrication of graphene-encapsulated oxide nanoparticles: towards high-performance anode materials for lithium storage”, *Angewandte Chemie International Edition*, Vol. 49, No. 45, pp. 8408-8411, **2010**.
- [286] A. Y. S. Eng, Z. Sofer, P. Šimek, J. Kosina, and M. Pumera, “Highly hydrogenated graphene through microwave exfoliation of graphite oxide in hydrogen plasma: towards electrochemical applications”, *Chemistry—A European Journal*, Vol. 19, No. 46, pp. 15583-15592, **2013**.
- [287] J. M. Kim, D. Ko, J. Oh, J. Lee, T. Hwang, Y. Jeon, W. Hooch Antink, and Y. Piao, “Electrochemically exfoliated graphene as a novel microwave susceptor: the ultrafast microwave-assisted synthesis of carbon-coated silicon-graphene film as a lithium-ion battery anode”, *Nanoscale*, Vol. 9, No. 40, pp. 15582-15590, **2017**.
- [288] L. M. Malard, M. A. Pimenta, G. Dresselhaus, and M. S. Dresselhaus, “Raman spectroscopy in graphene”, *Physics Reports*, Vol. 473, No. 5, pp. 51-87, **2009**.
- [289] A. C. Ferrari, and D. M. Basko, “Raman spectroscopy as a versatile tool for studying the properties of graphene”, *Nature Nanotechnology*, Vol. 8, pp. 235, **2013**.
- [290] D. Yang, A. Velamakanni, G. Bozoklu, S. Park, M. Stoller, R. D. Piner, S. Stankovich, I. Jung, D. A. Field, C. A. Ventrice, and R. S. Ruoff, “Chemical analysis of graphene oxide films after heat and chemical treatments by X-ray

- photoelectron and Micro-Raman spectroscopy”, *Carbon*, Vol. 47, No. 1, pp. 145-152, **2009**.
- [291] A. A. K. King, B. R. Davies, N. Noorbehesht, P. Newman, T. L. Church, A. T. Harris, J. M. Razal, and A. I. Minett, “A new raman metric for the characterisation of graphene oxide and its derivatives”, *Scientific Reports*, Vol. 6, pp. 19491, **2016**.
- [292] K. N. Kudin, B. Ozbas, H. C. Schniepp, R. K. Prud'homme, I. A. Aksay, and R. Car, “Raman spectra of graphite oxide and functionalized graphene sheets”, *Nano Letters*, Vol. 8, No. 1, pp. 36-41, **2008**.
- [293] L. G. Cançado, A. Jorio, E. M. Ferreira, F. Stavale, C. A. Achete, R. B. Capaz, M. V. d. O. Moutinho, A. Lombardo, T. Kulmala, and A. C. Ferrari, “Quantifying defects in graphene via Raman spectroscopy at different excitation energies”, *Nano Letters*, Vol. 11, No. 8, pp. 3190-3196, **2011**.
- [294] M. M. Lucchese, F. Stavale, E. M. Ferreira, C. Vilani, M. V. d. O. Moutinho, R. B. Capaz, C. A. Achete, and A. Jorio, “Quantifying ion-induced defects and Raman relaxation length in graphene”, *Carbon*, Vol. 48, No. 5, pp. 1592-1597, **2010**.
- [295] K. Krishnamoorthy, M. Veerapandian, K. Yun, and S. J. Kim, “The chemical and structural analysis of graphene oxide with different degrees of oxidation”, *Carbon*, Vol. 53, pp. 38-49, **2013**.
- [296] N. Huang, H. Lim, C. H. Chia, M. A. Yarmo, and M. Muhamad, “Simple room-temperature preparation of high-yield large-area graphene oxide”, *International Journal of Nanomedicine*, Vol. 6, pp. 3443, **2011**.
- [297] M. F. R. Hanifah, J. Jaafar, M. Othman, A. Ismail, M. A. Rahman, N. Yusof, W. Salleh, and F. Aziz, “Facile synthesis of highly favorable graphene oxide: effect of oxidation degree on the structural, morphological, thermal and electrochemical properties”, *Materialia*, pp. 100344, **2019**.
- [298] N. Morimoto, T. Kubo, and Y. Nishina, “Tailoring the oxygen content of graphite and reduced graphene oxide for specific applications”, *Scientific Reports*, Vol. 6, pp. 21715, **2016**.
- [299] C. D. Zangmeister, “Preparation and evaluation of graphite oxide reduced at 220 °C”, *Chemistry of Materials*, Vol. 22, No. 19, pp. 5625-5629, **2010**.
- [300] V. Țucureanu, A. Matei, and A. M. Avram, “FTIR spectroscopy for carbon family study”, *Critical Reviews in Analytical Chemistry*, Vol. 46, No. 6, pp. 502-520, **2016**.
- [301] L. Shahriary, and A. A. Athawale, “Graphene oxide synthesized by using modified Hummers approach”, *International Journal of Renewable Energy and Environmental Engineering*, Vol. 2, No. 01, pp. 58-63, **2014**.
- [302] J. Yang, C. Zang, L. Sun, N. Zhao, and X. Cheng, “Synthesis of graphene/Ag nanocomposite with good dispersibility and electroconductibility via



- solvothermal method”, *Materials Chemistry and Physics*, Vol. 129, No. 1, pp. 270-274, **2011**.
- [303] M. Fathy, T. Abdel Moghny, M. A. Mousa, A. H. A. El-Bellihi, and A. E. Awadallah, “Absorption of calcium ions on oxidized graphene sheets and study its dynamic behavior by kinetic and isothermal models”, *Applied Nanoscience*, Vol. 6, No. 8, pp. 1105-1117, **2016**.
- [304] M. Ibrahim, and A. A. Mahmoud, “Computational notes on the reactivity of some functional groups”, *Journal of Computational and Theoretical Nanoscience*, Vol. 6, No. 7, pp. 1523-1526, **2009**.
- [305] W. Zhang, W. He, and X. Jing, “Preparation of a stable graphene dispersion with high concentration by ultrasound”, *The Journal of Physical Chemistry B*, Vol. 114, No. 32, pp. 10368-10373, **2010**.
- [306] K. Muthoosamy, R. G. Bai, I. B. Abubakar, H. N. Lim, H. S. Loh, N. M. Huang, C. H. Chia, and S. Manickam, “Exceedingly biocompatible and thin-layered reduced graphene oxide nanosheets using an eco-friendly mushroom extract strategy”, *International Journal of Nanomedicine*, Vol. 10, pp. 1505-1519, **2015**.
- [307] M. D. Stoller, S. Park, Y. Zhu, J. An, and R. S. Ruoff, “Graphene-based ultracapacitors”, *Nano Letters*, Vol. 8, No. 10, pp. 3498-3502, **2008**.
- [308] Y. Xu, H. Bai, G. Lu, C. Li, and G. Shi, “Flexible graphene films via the filtration of water-soluble noncovalent functionalized graphene sheets”, *Journal of the American Chemical Society*, Vol. 130, No. 18, pp. 5856-5857, **2008**.
- [309] X. Wang, W. Xing, B. Yu, X. Feng, L. Song, and Y. Hu, “A facile and cost-effective approach to the reduction of exfoliated graphite oxide using sodium hypophosphite under acidic conditions”, *Journal of Materials Chemistry C*, Vol. 1, No. 4, pp. 690-694, **2013**.
- [310] Z. Lei, L. Lu, and X. S. Zhao, “The electrocapacitive properties of graphene oxide reduced by urea”, *Energy & Environmental Science*, Vol. 5, No. 4, pp. 6391-6399, **2012**.
- [311] Y. Lei, Z. Tang, R. Liao, and B. Guo, “Hydrolysable tannin as environmentally friendly reducer and stabilizer for graphene oxide”, *Green Chemistry*, Vol. 13, No. 7, pp. 1655-1658, **2011**.
- [312] D. Luo, G. Zhang, J. Liu, and X. Sun, “Evaluation criteria for reduced graphene oxide”, *The Journal of Physical Chemistry C*, Vol. 115, No. 23, pp. 11327-11335, **2011**.
- [313] X. Zhou, J. Zhang, H. Wu, H. Yang, J. Zhang, and S. Guo, “Reducing graphene oxide via hydroxylamine: a simple and efficient route to graphene”, *The Journal of Physical Chemistry C*, Vol. 115, No. 24, pp. 11957-11961, **2011**.
- [314] M. Thommes, K. Kaneko, A. V. Neimark, J. P. Olivier, F. Rodriguez-Reinoso, J. Rouquerol, and K. S. Sing, “Physisorption of gases, with special reference to the

evaluation of surface area and pore size distribution (IUPAC Technical Report)", *Pure and Applied Chemistry*, Vol. 87, No. 9-10, pp. 1051-1069, **2015**.

- [315] J. Hassoun, F. Bonaccorso, M. Agostini, M. Angelucci, M. G. Betti, R. Cingolani, M. Gemmi, C. Mariani, S. Panero, V. Pellegrini, and B. Scrosati, "An advanced lithium-ion battery based on a graphene anode and a lithium iron phosphate cathode", *Nano Letters*, Vol. 14, No. 8, pp. 4901-4906, **2014**.
- [316] C. J. Smyth, A. J. Rennie, and B. J. Inkson, "Modification of graphene anode morphologies via wet and dry milling", *Energy Procedia*, Vol. 151, pp. 168-173, **2018**.
- [317] C. Wu, N. Pu, Y. Liu, C. Chen, Y. Peng, T. Cheng, M. Lin, and M. Ger, "Improving rate capability of lithium-ion batteries using holey graphene as the anode material", *Journal of the Taiwan Institute of Chemical Engineers*, Vol. 80, pp. 511-517, **2017**.
- [318] H. Wang, J. Xie, H. Almkhelfe, V. Zane, R. Ebini, C. M. Sorensen, and P. B. Amama, "Microgel-assisted assembly of hierarchical porous reduced graphene oxide for high-performance lithium-ion battery anodes", *Journal of Materials Chemistry A*, Vol. 5, No. 44, pp. 23228-23237, **2017**.
- [319] M. Endo, C. Kim, K. Nishimura, T. Fujino, and K. Miyashita, "Recent development of carbon materials for Li ion batteries", *Carbon*, Vol. 38, No. 2, pp. 183-197, **2000**.
- [320] F. Su, R. Tang, Y. He, Y. Zhao, F. Kang, and Q. Yang, "Graphene conductive additives for lithium ion batteries: origin, progress and prospect", *Chinese Science Bulletin*, Vol. 62, No. 32, pp. 3743-3756, **2017**.
- [321] Y. Takahashi, N. Kijima, K. Dokko, M. Nishizawa, I. Uchida, and J. Akimoto, "Structure and electron density analysis of electrochemically and chemically delithiated LiCoO<sub>2</sub> single crystals", *Journal of Solid State Chemistry*, Vol. 180, No. 1, pp. 313-321, **2007**.
- [322] M. Shibuya, T. Nishina, T. Matsue, and I. Uchida, "In situ conductivity measurements of LiCoO<sub>2</sub> film during lithium insertion/extraction by using interdigitated microarray electrodes", *Journal of the Electrochemical Society*, Vol. 143, No. 10, pp. 3157, **1996**.
- [323] X.-Y. Qiu, Q.-C. Zhuang, Q.-Q. Zhang, R. Cao, P.-Z. Ying, Y.-H. Qiang, and S.-G. Sun, "Electrochemical and electronic properties of LiCoO<sub>2</sub> cathode investigated by galvanostatic cycling and EIS", *Physical Chemistry Chemical Physics*, Vol. 14, No. 8, pp. 2617-2630, **2012**.
- [324] H. Sato, D. Takahashi, T. Nishina, and I. Uchida, "Electrochemical characterization of thin-film LiCoO<sub>2</sub> electrodes in propylene carbonate solutions", *Journal of Power Sources*, Vol. 68, No. 2, pp. 540-544, **1997**.

- [325] J. Zhao, L. Wang, X. He, C. Wan, and C. Jiang, "Kinetic investigation of  $\text{LiCoO}_2$  by electrochemical impedance spectroscopy (EIS)", *Internatinal Journal of Electrochemical Science*, Vol. 5, No. 4, pp. 478-488, **2010**.
- [326] G. Liu, H. Kuo, R. Liu, C. Shen, D. Shy, X. Xing, and J. Chen, "Study of electrochemical properties of coating  $\text{ZrO}_2$  on  $\text{LiCoO}_2$ ", *Journal of Alloys and Compounds*, Vol. 496, No. 1-2, pp. 512-516, **2010**.
- [327] Z. H. Sheng, H. L. Gao, W. J. Bao, F. B. Wang, and X. H. Xia, "Synthesis of boron doped graphene for oxygen reduction reaction in fuel cells", *Journal of Materials Chemistry*, Vol. 22, No. 2, pp. 390-395, **2012**.
- [328] X. Li, H. Wang, J. T. Robinson, H. Sanchez, G. Diankov, and H. Dai, "Simultaneous nitrogen doping and reduction of graphene oxide", *Journal of the American Chemical Society*, Vol. 131, No. 43, pp. 15939-15944, **2009**.

## Publication

Jianshen Wu, Jiawei Zhao, Bala Vaidhyanathan, Hongtao Zhang, Aashu Anshuman, Avias Nare, and Sina Saremi-Yarahmadi, “Rapid microwave-assisted bulk production of high-quality reduced graphene oxide for lithium ion batteries”, *Materialia*, vol. 13, pp. 100833, 2020. <https://doi.org/10.1016/j.mtla.2020.100833>